

**Application of Mobility Spectrum Analysis to
Modern Multi-layered IR Device Material**

BY

ALEXANDER EARL BROWN
B.S. Physics, Allegheny College, 2009
M.S. Physics, University of Illinois at Chicago, Chicago, 2012

THESIS

Submitted as partial fulfillment of the requirements
for the degree of Doctor of Philosophy in Physics
in the Graduate College of the
University of Illinois at Chicago, 2015

Chicago, Illinois

Defense Committee:

Sivalingam Sivananthan, Chair and Advisor
Christoph Grein, Physics
Zheng Yang, Electrical & Computer Engineering
Leo Almeida, U.S. Army
Jose Arias, U.S. Army

ACKNOWLEDGEMENTS

First and foremost, I would like to thank my advisor Professor Sivananthan, who ignited my interest in semiconductor physics and supported me throughout my studies. I am forever grateful for the opportunities you have given to me, and this accomplishment could only be realized through your continued belief in me as a researcher. I would like to thank Professor Grein for his incredible depth of knowledge and passion for understanding, and also Professor Yang for his interest and support.

I have so many people I would like to thank from Night Vision and Electronic Sensors Directorate: Dr. Joe Pellegrino for the project and opportunity, my committee members Dr. L.A. Almeida and Dr. Jose Arias for their endless assistance and level of expertise which I aspire to one day achieve, Dr. Craig Lennon for everything, I would have been lost many times without your help, Dr. Patrick Maloney who showed me the ways of electrical/optical characterization, Nathan Henry for his work on III-V materials and to everyone else who helped me get to where I am today.

To the many wonderful people at university: Dr. Stephen Fahey, Dr. Jin Hwan Park, Dr. Eric Colegrove, Benjamin Rickman, John van Dyke, Colin Hayes, Brian Stafford, Francisco Restrepo, Dr. Yong Chang, Dr. Suk-Ryong Hahn, and finally thank you to two irreplaceable individuals that do it all, Yesim Anter and Paola Caicedo.

Lastly, to those closest to me, Ruth and my parents Peggy and Earl, I am grateful for the unwavering support during this process, their patience, and for believing in me throughout.

TABLE OF CONTENTS

ACKNOWLEDGEMENTS	ii
LIST OF TABLES	vi
LIST OF FIGURES	vii
LIST OF ABBREVIATIONS	xiii
SUMMARY	xv
1. Introduction	1
1.1 Overview	1
1.2 History	1
1.3 Blackbody radiation	3
1.4 Principles of operation	4
1.4.1 Photon and thermal detectors	6
1.5 Figures of merit	8
1.5.1 Thermal generation	8
1.5.2 Quantum efficiency	9
1.5.3 R_0A product and dark current	10
2. Background	12
2.1 IR Materials Systems	12
2.1.1 HgCdTe	12
2.1.1.1 Introduction	12
2.1.1.2 Fundamental Properties	12
2.1.1.3 Band structure	12
2.1.1.4 Optical	14
2.1.1.5 Lifetime	19
2.1.1.5.1 Auger lifetime	20
2.1.1.5.2 Radiative lifetime	22
2.1.1.5.3 Shockley-Read-Hall	23
2.1.1.6 Mobility	25
2.1.1.7 MBE and epitaxial growth	28
2.1.1.7.1 Doping	29
2.1.1.7.2 Substrates	31
2.1.1.7.3 <i>In-situ</i> monitoring	33
2.1.1.7.4 Device considerations	34
2.1.1.7.5 p-n junction and dark current basics	35
2.1.2 III-V Superlattice	41
2.1.2.1 Introduction	41
2.1.2.2 Type overview	42

2.1.2.3	T2SLs and fundamental properties	43
2.1.2.4	Material Properties	44
2.1.2.5	Dark current	48
2.2	Electrical Transport and scattering	49
2.2.1	HgCdTe electron scattering	50
2.2.1.1	Ionized impurity scattering	50
2.2.1.2	Polar optical phonon scattering	53
2.2.1.3	Alloy scattering	55
2.2.1.4	Neutral impurity scattering	55
2.2.1.5	Dislocation scattering	56
2.2.1.6	Strain field scattering	57
2.2.2	HgCdTe hole scattering	58
2.2.2.1	Ionized impurity scattering	59
2.2.2.2	Acoustic phonon scattering	60
2.2.3	III-V superlattices – interface roughness scattering	61
2.3	Hall and Mobility Spectrum analysis	62
2.3.1	Mobility spectrum analysis	64
3.	Experimental	67
3.1	Hall measurement	67
3.1.1	Systems	67
3.1.2	Considerations (uniformity, geometry, contacts)	70
3.1.3	Sample test	72
3.2	Supplementary	84
3.2.1	PCD	84
3.2.2	SEM/EBIC	90
3.2.3	IV	91
3.2.4	Optical	92
4.	MSA studies of HgCdTe	94
4.1	Introduction	94
4.2	LW HgCdTe for planar devices	94
4.2.1	Experimental	94
4.2.1.1	CdTe growth	97
4.2.1.2	MCT growth and sample preparation	98
4.2.2	Results	100
4.2.2.1	MSA results	100
4.2.2.2	PCD and IV results	112
4.2.3	Summary	117
4.3	P+/n heterojunction HgCdTe	118
4.3.1	Experimental	118

4.3.2	Results.....	120
4.3.2.1	MCT/CdTe/Si.....	120
4.3.2.2	MCT/GaAs/Si.....	126
4.3.2.3	MCT/CZT.....	134
4.3.3	Discussion.....	142
4.4	Summary.....	145
5.	III-V studies.....	147
5.1	Bulk InAs, GaSb, and InAsSb.....	147
5.2	LW T2SL III-V.....	156
5.2.1	InAs/GaSb.....	156
5.2.2	InAs/InAsSb.....	166
5.3	Residual doping and annealing results.....	175
5.4	Surface passivation experiments.....	182
5.5	Summary.....	191
6.	Conclusions and future work.....	194
	CITED LITERATURE	198
	VITA	214

LIST OF TABLES

Table I: HgCdTe substrate properties.....	31
Table II: Hall test sample properties.....	76
Table III: QCL characteristics for lifetime measurement.....	88
Table IV: Injected carrier concentration calculations for PCD measurement.....	88
Table V: HgCdTe sample properties for LW planar study.....	98
Table VI: Summary of resolved parameters from LW HgCdTe planar layers.....	112
Table VII: Sample information of P+/n MW HgCdTe layers.....	119
Table VIII: Summary of resolved properties for uid bulk III-V materials.....	155
Table IX: Summary of surface (e3) and barrier-interface (e2) electron characteristics at 77 K.....	175
Table X: Summary of 77 K single-field Hall results on annealed bulk InAs and GaSb.....	177

LIST OF FIGURES

Figure 1: Experimental and theoretical absorption coefficient of a $\text{Hg}_{0.79}\text{Cd}_{0.21}\text{Te}$ sample at 80K. Inset shows the first derivative of the absorption coefficient, with the peak representing the optical bandgap E_0 . [26].	18
Figure 2: Absorption coefficient versus energy comparison of Chu, Schacham and Finkman (SF), and Price and Boyd (PB) expressions for $\text{Hg}_{0.775}\text{Cd}_{0.225}\text{Te}$ at 77 K.	19
Figure 3: Electron mobility in LW HgCdTe material versus carrier concentration, showing comparative mobility as majority (n-type) and minority (p-type) carrier [66].	27
Figure 4: Depiction of hybridization to ROIC using indium bump bonding process (a & b) and the resultant architecture after hybridization of the vertically integrated photodiode (c).	35
Figure 5: Relevant dark current mechanisms in HgCdTe.	40
Figure 6: Band structure calculation of LW InAs/GaSb using BANDS along the growth direction (left portion) and in-plane direction (right portion).	47
Figure 7: Relevant dark current mechanisms for T2SL diodes.	49
Figure 8: Lakeshore 9509 HMS.	68
Figure 9: Magnetic field plot of superconducting solenoid magnet used in Lakeshore 9509 HMS. Measurement shows $\pm 0.1\%$ homogeneity across 6 cm on central axis.	69
Figure 10: Sample mounting for 9509 HMS.	69
Figure 11: Voltage (a) and current density (b) of patterned test structure (Greek cross), simulated using finite difference method to solve Poisson's equation across grid. Voltage at terminal A is 1 V and terminal B is 0 V. Contour line spacing in (a) is 50 mV. [217]	72
Figure 12: IV characteristics of In contacts on p-type HgCdTe single layer showing ohmic behavior at 80 K.	73
Figure 13: Initial Hall test structures during testing. Grey areas indicated contact areas.	73
Figure 14: Greek cross structure with critical dimensions of arm length, A, and arm width, S.	74
Figure 15: Correction factor vs resistance ratio. Values of f below 0.9 typically indicate a measurement error.	75
Figure 16: SEM image of over-the-side (lateral) contacts deposited using e-beam. Sample, T1, is square p-on-n MW HgCdTe, with lighter areas indicating Au.	77
Figure 17: Correction factor f versus B-field for test samples. Measurements taken at 78 K (left figure) and 298 K (right figure).	78
Figure 18: Percent difference of R_H values using two Hall configurations plotted versus B-field for Hall test samples. Measurements taken at 78 K (left figure) and 298 K (right figure).	79
Figure 19: Spatial Dektak map of wet-etched Greek cross structure, sample T2	80
Figure 20: Spatial Dektak map of ICP etched Greek cross structure, sample T4.	80
Figure 21: Dektak profile of wet-etched Greek cross structure, sample T3.	81

Figure 22: Dektak profile of ICP etched Greek cross structure, sample T4.	81
Figure 23: Sample T2 temperature evolution of mobility Spectrum from 50 K to 293 K. Figure (a) for electron spectra and figure (b) for hole spectra.....	82
Figure 24: Sample T3 temperature evolution of mobility Spectrum from 50 K to 293 K. Figure (a) for electron spectra and figure (b) for hole spectra.....	83
Figure 25: Sample T4 temperature evolution of mobility Spectrum from 50 K to 293 K. Figure (a) for electron spectra and figure (b) for hole spectra.....	84
Figure 26: From top to bottom, spectral characteristics of 1.5, 4.6 and 8.3 μm QCL lasers.	87
Figure 27: Temporal pulse profile for 1.5 μm QCL and InGaAs reference detector response. QCL trigger width is ~ 80 ns while InGaAs detector width is ~ 100 ns. InGaAs detector highlights offset between trigger end and pulse end.	87
Figure 28: CdTe passivation testing on MW HgCdTe. Poor results are obtained on unpassivated and post-passivation annealed samples. Best results are obtained after CdTe passivation (no anneal), and slight improvement can be seen after 100 $^{\circ}\text{C}$ bake of unannealed CdTe.	90
Figure 29: RHEED pattern of GaAs substrate following oxide desorption.....	96
Figure 30: SE derived overlayer thickness of GaAs during preparation shown alongside surface temperature (a) and the real part of the dielectric function at 3.98 eV (b). The abrupt change in thickness coincides with a rapid change in the real part of the dielectric function [227].	96
Figure 31: Compositional profile of layer G1. SE composition represents as-grown profile, while solid-red line is derived from post-annealing SIMS, showing significant changes in the substrate-interfacial region.	100
Figure 32: Mobility spectrum of sample G1 at 50 K, showing three distinct carrier species.	101
Figure 33: Carrier concentration fitting results of electron carrier E1.....	102
Figure 34: G1 mobility spectrum temperature evolution.....	103
Figure 35: Mobility spectrum temperature evolution from samples S1 (a) and CZT1 (b).	104
Figure 36: Resolved carrier mobility (left column) and carrier concentration (right column) of LW samples CZT1, G1, and S1. Carrier E1 (bulk), E2, and E3 are shown from top to bottom.....	105
Figure 37: Mobility versus temperature of low conductivity hole peak in LW samples.	107
Figure 38: Extracted bulk electron and possible minority carrier hole concentration from sample CZT1. The experimentally determined intrinsic carrier concentration (blue triangle) matches well with theory at high temperature.	108
Figure 39: Experimental and theoretical mobility versus temperature of carrier E1 from MCT/CZT sample CZT1.....	109
Figure 40: Experimental and theoretical mobility versus temperature of carrier E1 from MCT/CdTe/GaAs sample G1.	110
Figure 41: Experimental and theoretical mobility versus temperature of carrier E1 from MCT/CdTe/Si sample S1.....	111
Figure 42: PCD lifetime data for sample G1. Theoretical calculations of radiative (Rad), Auger (Aug),	

and SRH are shown.....	113
Figure 43: Lifetimes of samples grown on CZT substrates, indicating intrinsic recombination.	114
Figure 44: Sample CZT1 dark IV on a 60 μm radius planar diode. Model includes 3D diffusion and GR currents.....	116
Figure 45: Sample G1 dark IV on a 7.5 μm radius planar diode. Model includes diffusion and tunneling currents.....	117
Figure 46: Typical P+/n structure in this work. The post-growth SIMS and SE profiles are for the MW MCT/Si sample S2_MW.....	119
Figure 47: Mobility spectrum temperature evolution of sample S2_MW. Figure (a) shows hole spectra, containing carrier H1 (light hole) and H2 (heavy hole), while Figure (b) shows electron spectra, containing carriers E1 (bulk), E2 (transitional), and E3/E4 (interface).	120
Figure 48: Mobility (left) and carrier concentration (right) versus temperature of all carriers in sample S2_MW.....	121
Figure 49: Comparison of cap hole mobility from sample S2_MW using MCF and MSA.	122
Figure 50: Mobility fitting results for bulk electron in sample S2_MW.	123
Figure 51: Lifetime fitting results of sample S2_MW.....	124
Figure 52: P-on-n mesa diodes fabricated from MCT/CdTe/Si sample S2_MW.....	125
Figure 53: Fitted IV-curves of a 20 x 20 μm mesa diode fabricated from sample S2_MW.....	126
Figure 54: SIMS profiles on samples G2_MW (solid line) and G3_MW (dashed line) for indium and x-value, from top to bottom, respectively.	127
Figure 55: G2_MW mobility spectrum showing electrons (red) and hole (blue) carriers.	128
Figure 56: Hole mobility from sample G2_MW with theoretically calculated mobility due to ionized impurity scattering.	129
Figure 57: Bulk electron mobility versus temperature in sample G2_MW with theoretical scattering mechanisms.....	130
Figure 58: G3_MW mobility spectrum temperature evolution.....	131
Figure 59: Lifetime versus temperature of G3_MW absorber layer.....	133
Figure 60: IV characteristics of sample G3_MW mesa diodes. Left figure is for a 50 μm circular diode, while right figure is for an 80 μm circular diode. Pronounced tunneling (thin solid black line) is evident in both diodes. GR (short dash red) and diffusion (long dash green) are also present in both cases at low reverse bias.....	134
Figure 61: SIMS profiles of CZT2_MW. Indium (dashed line) and arsenic (dotted line) are shown on the primary axis, while composition (solid line) is shown on the secondary axis.....	135
Figure 62: Mobility spectrum temperature evolution of electrons (left) and holes (right) from sample CZT2_MW.....	136
Figure 63: Bandgap versus temperature of sample CZT2_MW absorber as determined from first-derivative of spectral response measurement. Fitting of the bandgap temperature dependence yielded an	

x-value of ~ 0.2815 . Inset graph shows first derivative of spectral response at 80 K.....	137
Figure 64: Theoretical fitting of mobility versus temperature on the absorber electron (E1) from sample CZT2_MW.....	138
Figure 65: PCD lifetime versus temperature on CZT2_MW absorber. Two sets of PCD data are shown; lifetime with a narrow band-pass filter (filled circles) and lifetime using the same setup but without a filter (open circles). Dashed line represented theoretically intrinsic lifetime using these parameters. As can be seen, a much better fit is obtained after introducing the radiative lifetime enhancement factor $\beta = 6.5$	139
Figure 66: Lifetime results from sample CZT2_MW after various amounts of material were removed. The x-axis reflects the total sample thickness after etching.....	140
Figure 67: IVT plot for 30 μm square mesa diode from sample CZT2_MW.....	141
Figure 68: QE (left) and EBIC (right) results from CZT2_MW, indicating excellent diode performance and uniformity.....	142
Figure 69: P+/n dark current comparison to Rule 07. Figure on the left shows the best performing diode near operating temperature (no scaling), while the right figure shows spread of dark current across a number of processed diodes.....	143
Figure 70: Dynamic resistance-area product curves for diodes in this work near operating temperature.....	143
Figure 71: GaSb mobility spectrum at 77 K for uid (left) and Te-doped (right) samples.....	148
Figure 72: Heavy (open) and light (closed) hole mobility versus temperature for uid GaSb grown on GaAs.	149
Figure 73: Mobility versus temperature results from Te-doped GaSb sample showing conduction from Γ , L, and X conduction bands.	150
Figure 74: 77 K mobility spectrum of uid InAs sample.....	151
Figure 75: Bandgap versus temperature of $\text{InAs}_{0.91}\text{Sb}_{0.09}$ layer determined from spectral response.	152
Figure 76: Evolution of electron mobility spectra from $\text{InAs}_{0.91}\text{Sb}_{0.09}$ layer.....	153
Figure 77: Mobility versus temperature of bulk, surface, and back interface carriers present in $\text{InAs}_{0.91}\text{Sb}_{0.09}$ layer. Dashed line represented lattice scattering.	154
Figure 78: Bulk electron mobility and carrier concentration versus temperature. MSA data (filled) and single-field (open) are shown for comparison.	155
Figure 79: Characterization sample structure of LW InAs/GaSb SL.....	157
Figure 80: Mobility spectrum of three distinct layers in order to properly identify carriers in the <i>p</i> -type SL structure. From top to bottom: Absorber and back contact layers of <i>p</i> -type device structure, etched sample containing only the back contact layer, and characterization sample containing only the <i>p</i> -type absorber layer.	158
Figure 81: Mobility spectrum temperature evolution of Be-doped LW InAs/GaSb SL structure, with electrons (a) and holes (b).....	159
Figure 82: Temperature dependence of carriers e1 and e2 carrier concentration from Be-doped LW InAs/GaSb. Values are normalized to minimum resolved concentration to highlight change with temperature.	160

Figure 83: Mobility spectrum temperature evolution of uid LW InAs/GaSb SL structure, with electrons (a) and holes (b).	161
Figure 84: Mobility versus temperature for all resolved carriers in uid LW InAs/GaSb (top) and Be-doped LW InAs/GaSb. Mobility temperature behavior at higher temperatures is included.....	162
Figure 85: Activation energies of carriers h1 and h2 near room temperature. In both the uid and Be-doped case the activation energy of carrier h2 is larger.....	163
Figure 86: Carrier concentration versus 1000/T for all resolved carriers in uid LW InAs/GaSb (top) and Be-doped LW InAs/GaSb. Bulk carriers (E1 and H1+H2) are given in units of cm^{-3} while interfacial carriers (E2 and E3) are expressed as cm^{-2} . Fitting of bandgap in the intrinsic region and carrier activation at low temperature are included.	164
Figure 87: Single-field Hall results (solid black line and circle) are compared to bulk electron (open red markers) and bulk hole (open blue markers) from MSA. The mobility (a and b), carrier concentration (c and d), and conductivity percent (e and f) and shown for uid LW InAs/GaSb (left column, a,c and e) and Be-doped LW InAs/GaSb (right column, b, d, and e).	166
Figure 88: Mobility spectrum temperature evolution of 3.3 μm uid LW InAs/InAsSb SL showing distinct electron (a) and hole (b) peaks.....	168
Figure 89: Mobility (left) and concentration (right) of all peaks in uid LW InAs/InAsSb sample.....	169
Figure 90: Electron peak percent conductivity to overall conductivity versus temperature in uid LW InAs/InAsSb layer. The graph clearly shows peak mergers at 150 K and 200 K.	170
Figure 91: 77 K electron mobility spectrum of 0.5 μm and 3.3 μm thick InAs/InAsSb absorbers.	171
Figure 92: Mobility spectrum of Be-doped InAs/InAsSb at 77 K. Percent of overall conductivity values are included.	173
Figure 93: Electron (top) and hole (bottom) spectra comparison between uid and Be-doped InAs/InAsSb absorbers.	174
Figure 94: Nomarski images of surface morphology on GaAs (top) and InAs (bottom) samples. As-grown images are shown in the left column, while images after annealing at 560 $^{\circ}\text{C}$ are shown in the right column.	177
Figure 95: GaSb (left) and InAs (right) mobility spectrum at 77 K for as-grown (solid green), 530 $^{\circ}\text{C}$ annealed (red dot), and 560 $^{\circ}\text{C}$ annealed (blue dash).....	178
Figure 96: Bulk mobility (top) and concentration (bottom) for absorber electron and hole before and after post-growth anneal at 500 $^{\circ}\text{C}$ in uid LW InAs/GaSb.....	180
Figure 97: Bulk mobility (top) and concentration (bottom) for absorber electron and hole before and after post-growth anneal at 500 $^{\circ}\text{C}$ in Be-doped LW InAs/GaSb.	181
Figure 98: Percent conductivity of bulk electron (closed circle), surface electron (open circle), and bulk hole (open triangle) in Be-doped LW InAs/GaSb layer used for all surface passivation measurements. Surface electron conductivity contribution is seen to maximize at low temperature.....	183
Figure 99: 30 K mobility spectrum of surface electron after SiO_2 passivation with respect to electret charging. As-grown surface conductivity shown for comparison. Inset graph shows consistency of bulk hole spectra to verify measurement integrity.	185
Figure 100: Collection of electron surface conductivity data on all thiol surface treatments in this work.	

Results include attempts to shorten immersion time in thiol-solution, as well as stability studies after cryo-cycling and time lapse. 187

Figure 101: Dark current measurements of thiol passivated p-type barrier structure. Unpassivated and shallow etch results are shown for comparison. 189

Figure 102: Inverse dynamic resistance-area product versus perimeter-to-area plot for successful thiol passivations. The fitted slope from this data is used to determine the surface resistivity, as shown in inset-table..... 190

Figure 103: Rank plot of thiol passivated diodes from fabrication lots. 191

Figure 104: In-plane mobilities of bulk electrons (left figure) and bulk holes for all superlattice measurements..... 192

LIST OF ABBREVIATIONS

Atomic Layer Deposition (ALD)
Background Limited Performance (BLIP)
Band-to-Band (B2B) tunneling
Beam equivalent pressure (BEP)
Beattie-Landsberg-Blackmore (BLB)
Boltzmann Transport Equation (BTE)
Brooks-Herring (BH)
CdZnTe (CZT)
Chemical Vapor Deposition (CVD)
Conduction Band (CB)
Current-Voltage (IV)
Deep Level Transient Spectroscopy (DLTS)
Effective Medium Approximation (EMA)
Electron Beam Induced Current (EBIC)
Electron Cyclotron Resonance (ECR)
Empirical Pseudopotential Method (EPM)
Etch Pit Density (EPD)
Far Infrared (FIR)
Field of View (FOV)
Focal Plane Array (FPA)
Fourier Transform Infrared Spectroscopy (FTIR)
Free Carrier Absorption (FCA)
Full-Width Half-Maximum (FWHM)
Generation-Recombination (GR)
Heavy Hole (HH)
Heterojunction (HJ)
HgCdTe (MCT)
Infrared (IR)
Interface Roughness Scattering (IRS)
Kramers-Kronig (KK)
Light Hole (LH)
Liquid Phase Epitaxy (LPE)
Long-wave Infrared (LWIR)
Mercury Cadmium Telluride (MCT)
Metalorganic Vapour Phase Epitaxy (MOCVD)
Mid-wave Infrared (MWIR)
Mobility Spectrum Analysis (MSA)
Molecular Beam Epitaxy (MBE)
Multi-Carrier Fitting (MCF)
Multiple Quantum-Well (MQW)
Near Infrared (NIR)
Photoconductor (PC)

Photoluminescence (PL)
Photovoltaic (PV)
Polar Optical Phonon (POP)
Proportional-integral-derivative (PID) controller
Quantum Dot Infrared Photodetector (QDIP)
Quantum Efficiency (QE)
Quantum Well Infrared Photodetector (QWIP)
Readout Integrated Circuit (ROIC)
Reflection High-Energy Electron Diffraction (RHEED)
Resistance-area Product (RA)
Secondary Ion Mass Spectroscopy (SIMS)
Self-Assembled Monolayer (SAM)
Semiconductor (SC)
Sensor Chip Assembly (SCA)
Shockley-Read-Hall (SRH)
Short-wave Infrared (SWIR)
Signal-to-noise (S/N)
Spectroscopic Ellipsometry (SE)
Strained-Layer Superlattice (SLS)
Submillimeter (SubMM)
Superlattice (SL)
Thermal Cyclic Annealing (TCA)
Time Delay and Integration (TDI)
Time-Resolved Photoluminescence (TRPL)
Trap-Assisted tunneling (TAT)
Type-II Superlattice (T2SL)
Ultra High Vacuum (UHV)
Unintentionally Doped (uid)
Valence Band (VB)
Vertically Integrated Photodiode (VIP)
Very Long-wave Infrared (VLWIR)
Virtual Crystal Approximation (VCA)
X-Ray Diffraction (XRD)

SUMMARY

This work focuses on the characterization of two materials at the forefront of IR detectors; incumbent, tried and true, HgCdTe technologies and emergent III-V based superlattice structures holding much promise for future detector purposes. *Ex-situ* doped long-wave planar devices and *in-situ* doped mid-wave heterojunction (P+/n architecture) HgCdTe structures are explored with regards to substrate choice, namely lattice-matched CdZnTe and lattice-mismatched Si or GaAs. A detailed study of scattering mechanisms reveal that growth on lattice-mismatched substrates leads to dislocation scattering limited mobility at low temperature, correlating with extrinsically limited minority carrier lifetime and excessive diode tunneling current, resulting in overall lower performance. Mobility spectrum analysis proves to be an effective diagnostic on performance as well as providing insight in surface, substrate-interface, and minority carrier transport.

Two main issues limiting performance of III-V based superlattices are addressed; high residual doping backgrounds and surface passivation. Mobility spectrum analysis proves to be a reliable method of determining background doping levels. Modest improvements are obtained via post-growth thermal annealing, but results suggest future efforts should be placed upon growth improvements. Passivation efforts using charged electret dielectric show promise but further refinements would be needed. Thiol passivation is identified as a successful passivant of Be-doped *p*-type InAs/GaSb long-wave absorbers using mobility spectrum analysis, correlating with fabricated device dark current. Mobility spectrum analysis demonstrates it will be indispensable in future development of III-V material.

1. Introduction

1.1 Overview

Modern detector materials used for infrared (IR) imaging purposes contain complex multi-layered architectures, making robust characterization techniques necessary. In order to determine multi-carrier transport properties in the presence of mixed conduction, variable-field Hall characterization can be performed and then analyzed using mobility spectrum analysis to extract parameters of interest. Transport parameters are expected to aid in modeling and simulation and can be used for optimization purposes. The performance of IR devices ultimately depend on transport mechanisms, so an accurate determination becomes paramount.

This work focuses on characterization of two material systems at the forefront of IR detection; incumbent HgCdTe (MCT) technology and emergent III-V based superlattices. The applicability of variable-field Hall characterization and mobility spectrum analysis is demonstrated in a number of novel case studies for development of mid-wave and long-wave material.

1.2 History

IR radiation occupies the electromagnetic spectrum between the visible and microwave, at wavelengths ranging from approximately 0.7 μm out to 1000 μm . Herschel, a prominent astronomer in his time, first reported on the observation of IR radiation in 1800 when he noticed a thermometer response corresponding to radiation outside of the visible spectrum [1]. Using a monochromator and thermometer, he postulated the existence of an ‘invisible’ form of light, which was in fact IR radiation. Many critical discoveries followed that contributed to the state of modern IR technology, first among them was the thermoelectric effect, or the conversion of a temperature difference within a material to an electrical voltage, by Seebeck in 1821 [2]. The application of the Seebeck effect then led to the development of temperature sensing devices, more specifically the thermocouple in 1829 by Nobili and the thermopile in

1833 by Nobili-Melloni. Later, the photoconductive effect, which is an increase in conductivity with absorption of radiation, was discovered by Smith in 1873 in selenium [3], marking the first photon effect. Langley's bolometer followed shortly thereafter in 1881 [4], and utilized the temperature dependence of electrical resistance to measure the power of incident radiation. The IR photovoltaic (PV) effect was first seen by Bose in 1904 [5] and the first IR photoconductor (PC) followed in 1917 by Case [6], marking the beginning of modern IR devices.

The 20th century saw extensive research pertaining to IR photon detectors. Early detectors were made from single-element lead salts but suffered from poor reproducibility. In the 1950's, improvements of growth techniques allowed for extrinsic detectors using Ge to be made, exhibiting high-performance but requiring temperatures below 30 K for operation. The 1960's made way for alloy II-VI (HgCdTe), IV-VI (PbSnTe), and III-V (InAsSb) material systems, and introduced bandgap tunability through ternary composition control. Initially, PbSnTe detectors were favored, largely due to HgCdTe growth issues related to the high vapor pressure of Hg. Ultimately, PbSnTe was abandoned because of its high dielectric constant and thermal coefficient of expansion mismatch with Si, which created problems with silicon readout technology. Hence, HgCdTe became the material of choice for the first-generation scanning linear PC arrays.

Second-generation 2-D arrays of PV detectors came about in the 1980's and 1990's coupled with advancements in processing techniques. Large staring arrays saw circuits integrated onto the focal plane array (FPA) themselves. These arrays are frequently indium bump bonded to the readout integrated circuit (ROIC), creating a structure known as a sensor chip assembly (SCA). Systems today may be either 2-D arrays with linear formats and time delay and integration (TDI) implementation, or 2-D staring arrays. Pixel size has consistently decreased while pixel count has increased, a trend that is likely to continue. FPAs are commonly produced today in 1024 x 1024 or even 2K x 2K formats. HgCdTe has remained the material of choice for high performance IR application despite numerous competitors (PtSi Schottky barriers, InSb, PbSe, PbS, Si:Ga, Si:In, etc.) over the years. The 21st century has seen the demonstration of increasingly complex detector structures including two-color and hyperspectral detection structures.

The dominant objectives in the field today strive for smaller pixel pitch ($< 10 \mu\text{m}$), larger FPAs with higher yields, and raising operating temperatures (up to room temperature).

1.3 Blackbody radiation

Temperature is the basis of IR radiation detection. All materials above 0 K consist of continually vibrating atoms with energy dependent frequency. The resultant electromagnetic waves produced from these vibrations contain information about the temperature of the object in question. The spectral radiant exitance, M , measured in $\text{W}/(\text{cm}^2 \cdot \mu\text{m})$, of an ideal blackbody was correctly given by Plank in 1900 when he introduced the quantization of energy levels, a defining moment in modern physics. Plank's law is written as:

$$M(\lambda, T) = \frac{2\pi hc^2}{\lambda^5} \cdot \left[e^{\frac{hc}{\lambda k_B T}} - 1 \right]^{-1} \quad (1.1)$$

and the total radiance for a blackbody at temperature T is found by integrating over all wavelengths to obtain:

$$M(T) = \sigma T^4 \quad (1.2)$$

$$\sigma = \frac{2\pi^5 k_B^4}{15c^2 h^3}$$

where h is Plank's constant, c is the speed of light, λ is wavelength, k_B is Boltzmann's constant, T is temperature, and σ is Stefan's constant and has the approximate value of $5.67 \times 10^{-12} \text{ W}/(\text{cm}^2 \cdot \text{K}^4)$.

Equation 1.2 is known as the Stefan-Boltzmann law.

Wien's displacement law, which conveniently determines the wavelength at which maximum exitance occurs, is found by differentiating Equation 1.1 with respect to λ and setting the derivative equal

to zero giving:

$$\lambda_{\max} = 2898/T \text{ } \mu\text{m} \quad (1.3)$$

However, for imaging purposes, it is often important to instead determine the wavelength at which exitance changes most rapidly with temperature to determine the wavelength of maximum contrast.

This can be done by setting $d/d\lambda [d/dT (M(\lambda, T))] = 0$ and solving for λ to obtain:

$$\lambda_{\max \text{ contrast}} = 2410/T \text{ } \mu\text{m} \quad (1.4)$$

It can readily be seen from the equations above that objects near room temperature peak at $\sim 10 \text{ } \mu\text{m}$ while objects near 575 K peak at $\sim 5 \text{ } \mu\text{m}$. If a characteristic target temperature is known, integration of Equation 1.1 over a specific waveband determines the exitance across that interval so that the ideal detection window may be chosen for the desired application.

In practice, many thermal sources do not behave as perfect blackbodies, but act rather as graybodies or selective radiators. A wavelength dependent emissivity term, $\epsilon(\lambda, T)$, may be introduced to Equation's 1.1 - 1.3 to account for this effect. The emissivity of an object is simply the ratio between the spectral radiant exitance of the thermal source and that of an ideal blackbody, and is typically dependent on both temperature and wavelength.

1.4 Principles of operation

IR detectors are semiconductor devices made to respond to incident photons for sensing and imaging applications. Detector cut-offs must be strategically selected based upon desired application and operational environment. Most sensing purposes require transmission through atmosphere, thus creating a number of windows available for tactical imaging. Molecular and chemical absorption from water and CO_2 are the primary absorbers in the range of 1-30 μm . The most common division of IR bands and their

corresponding wavelength ranges are shown below, with the most prominently utilized today being the near IR (NIR), short-wave IR (SWIR), mid-wave IR (MWIR), and long-wave (LWIR).

Near infrared NIR: 0.7-1.0 μm

Short wave SWIR: 1.0-2.6 μm

Mid wave MWIR: 3.0-5.2 μm

Long wave LWIR: 8-14 μm

Very long wave VLWIR: 15-30 μm

Far infrared FIR 30-100 μm

Submillimeter (SubMM) (100-1000) μm

Each IR band differs substantially in regards to sensitivity, background flux, and contrast, amongst other parameters. As such, the most suitable band may be chosen after the intended application is well defined. For example, the NIR/SWIR has seen application in long distance fiber optics transmission and communication, as well as in active sensors. The MWIR band can be exploited when higher contrast is desired over higher sensitivity, and is generally more suitable for hotter objects, such as jet engines and missiles. Alternatively, the LWIR band is preferred for most situations demanding high performance because of the high sensitivity to near room temperature objects. The total radiance in the LWIR band is greater than in the MWIR band, but signal-to-noise (S/N) benefits are negated due to higher background flux levels. Noise in the form of thermally generated carriers requires photon detector cooling for intended detection $> 3 \mu\text{m}$, with LWIR detectors frequently cooled to liquid nitrogen (78 K) temperatures.

In real-world application, IR radiation is further attenuated by Rayleigh scattering and depends on the size of the scattering particles. If the particle is much larger than the wavelength, then scattering is independent of wavelength. This is the case for rain particles and larger aerosols. In contrast, for particles smaller than the wavelength, a strong wavelength dependence (λ^{-4}) is seen. It is important to note that IR therefore has the ability to penetrate further through smoke and mists as compared to visible radiation.

1.4.1 Photon and thermal detectors

IR detectors may be separated into two broad categories: thermal and photon detectors. Detector type is distinguishable by the principle operation mechanisms employed. In thermal detectors, absorbed photons create a temperature change in the active sensing element while a temperature dependent physical property is continuously monitored. Properties most commonly utilized for IR application include changes in electrical resistance, internal electrical polarization, or thermoelectric voltage. Operation requires an adequate heat sink so the desired resolution can be met. The most common examples of thermal detectors include thermopiles, bolometers, and pyroelectric devices.

Thermal detector systems are generally low cost and have achieved demonstration of good imagery in recent years. Thermal detectors suffer from slower response times due to the nature of detection and show wavelength independent response without the use of external filtering. In other words, a thermal detector depends only on incident power. One advantage of a thermal detector is that it may be operated at room temperature.

Photon detectors absorb incident radiation which in turn creates electron-hole pairs within the material. A change in the energy distribution of the semiconductor is observed in the form of an electrical signal output. The primary modes of operation are photovoltaic (PV) and photoconductive (PC), with other photoeffects (photoelectromagnetic, Demer, and photon drag) being less commonly exploited. PC detectors consist of a slab of radiation sensitive material that changes resistivity as absorption increases the free carrier population. PV detectors rely on built-in fields to separate photo-generated electron-hole pairs, thereby generating voltage.

During the development of IR detectors, it became apparent that high impedance materials were required for interfacing with high-input impedance silicon ROICs. This prerequisite favored PV devices rather than lower impedance PC devices. In addition, PV devices displayed lower power dissipation on an FPA compared to PC devices. Coupled with faster response times, resilience to trapping effects associated

with PC devices, and cost benefits, PV devices emerged as the favored device technology. Photodiodes, or an abrupt p-n junction PV detector, are the most widely used in MW and LW FPAs applications today.

The class of photon detectors can be further divided into majority carrier and minority carrier devices. The most important photon detector types include intrinsic (minority carrier) detectors, extrinsic (majority carrier), photoemissive (majority carrier) detectors, and quantum well/quantum dot (majority carrier) infrared photodetectors (QWIPs and QDIPs).

Intrinsic detectors exploit photon absorption across the fundamental bandgap of a semiconductor material. The semiconductor may be elemental (Si, Ge), binary (PbS, PbSe, InAs, InSb), ternary (PbSnTe, InGaAs, InAsSb, HgCdTe) or superlattice (InAs/InGaSb, InAs/GaSb, HgTe/CdTe, InAs/InAsSb) in nature. The relevant noise carrier is the minority carrier. Direct bandgap semiconductors have high optical absorption coefficients, and well-designed devices can achieve high quantum efficiencies (QE).

Extrinsic detectors absorb incident radiation via carriers at an impurity level located between the conduction band (CB) and valence band (VB) edges of a semiconductor. High doping levels are required and the specific energy levels depend on the choice of dopant. The thermal generation rate of carriers in extrinsic devices is roughly five orders of magnitude higher than in intrinsic detectors, and as such very low temperatures are required for operation. Typical material systems consist of heavily doped Si (As, Ga, or Sb doping), Ge (Hg or Ga doping), or GaAs. In general, intrinsic detectors are considered superior for most IR detection purposes, with extrinsic detectors employed only in VLWIR systems.

Photoemissive detectors are typically silicon Schottky barrier devices in which radiation is absorbed by carriers within the metal and transported across the metal-silicon Schottky barrier [7]. Typical materials used include PtSi, IrSi, or Pd₂Si. Quantum well IR (QWIP) photodetectors and quantum dot IR photodetectors are superlattice heterojunction structures in which free electrons in the conduction band undergo intersubband transitions. Type I GaAs/AlGaSb superlattices are a classic example of a QWIP material system.

Photon detectors typically exhibit high sensitivity and fast response times, and show a wavelength dependent response through the use of bandgap tailoring. Photon detectors are generally preferred for

their high performance capabilities. Thermal generation rates, and hence dark current, for a given temperature and bandgap are lowest in intrinsic detectors compared to the other detector types mentioned above. Furthermore, intrinsic detectors display the highest overall device QE, and for these reasons, will be the primary focus in this work.

1.5 Figures of merit

A number of processes must be considered when evaluating the performance of an IR photodetector. In an operational environment, multiple factors determine the effectiveness of a device under question. Numerous variables can make side-by-side comparisons oftentimes difficult, so care must be taken in order to fairly assess performance when different materials and detectors are under investigation. Figures of merit have therefore been adopted in the IR field to ease comparison, with those relevant to this work described in this section.

1.5.1 Thermal generation

One key component of performance is noise in the form of optical generation, or statistical fluctuations in the arrival rate of incident photons. Maximum detector performance is obtained under the condition that noise from optical generation exceeds noise as a result of the thermal generation of carriers within the material. This is known as background limited performance (BLIP). For a background flux, ϕ_B , incident on a detector, BLIP dictates that the rate of photo generated carriers per unit area must be greater than the rate of thermally generated carriers per unit area. Thus, we have the BLIP requirement:

$$QE \cdot \phi_B > n_{thermal} \cdot \frac{t}{\tau} \quad (1.5)$$

where QE here is the absorption quantum efficiency, n_{thermal} is the number of thermally generated carriers, t is the detector thickness, and τ is the minority carrier lifetime. The background flux is dependent on the situational environment, such as temperature and field of view (FOV).

Using an absorption coefficient α , we may consider the case when $\alpha \cdot t \ll 1$. Under this condition, we define a normalized thermal generation rate, G_{th}^* , as:

$$G_{\text{th}}^* = \frac{n_{\text{thermal}}}{\alpha\tau} \xrightarrow{\text{(for direct gap SC)}} = \frac{n_i^2}{n_{\text{maj}} \cdot \alpha \cdot \tau_{\text{min}}} \quad (1.6)$$

It clearly follows that G_{th}^* determines an upper limit on the operational temperature required to meet the BLIP criteria, namely $\varphi_B > G_{\text{th}}^*$. It is important to note that G_{th}^* can be calculated for any IR material, making it a useful metric for comparison of varying material systems.

1.5.2 Quantum efficiency

Device quantum efficiency (QE) represents the ability to convert incident radiation into useful signal output, and is a combination of photon absorption and subsequent electrical detection. Simply stated, QE is the percentage of targeted photons detected. In a well-designed intrinsic detector, this equates to the number of electron-hole pairs generated per photon. However, in some material systems, collection efficiency may not be unity. Ultimately, overall device QE is therefore a product of absorption efficiency and the internal efficiency of collection.

The most prominent factors that determine QE are diffusion length, absorption coefficient, and surface recombination velocity. High absorption coefficient is desired, but QE becomes strongly dependent on surface recombination velocity as carrier generation can be very shallow. This issue is typically eradicated through careful device design and adequate surface passivation.

Materials with low absorption coefficients may require thicker absorbing layers, but at the

expense of an increase in device dark current. Enhancements in absorption may be made through the use of a backside reflector, interference phenomena [8], or increasing the optical collection. Diffusion length varies with material quality, but is generally a function of temperature, doping, and material choice.

QE is a critical parameter when considering ultimate detector performance. In fact, both the responsivity, R , and normalized S/N detectivity, D^* both depend on QE. Responsivity is a measure of electrical output per optical input. For IR photodiodes, a relevant performance parameter is the detectivity, D^* , which is a normalized measure of S/N to allow ease of comparison, given in units of [$\text{cm Hz}^{1/2} \text{ W}^{-1}$]. For a photodiode with a gain of 1, the QE dependence for both R and D^* is linear and given by the equations:

$$R = \frac{J_{ph}}{\phi} = QE \cdot \frac{q}{h\nu} \quad (1.7)$$

$$D^* = QE \cdot \frac{\lambda}{hc} \sqrt{\frac{1}{2G_{th}}} \quad (1.8)$$

1.5.3 R_oA product and dark current

A commonly used figure of merit for a photodiode is the zero-bias resistance area product:

$$R_oA = \left[\frac{dJ_{dark}}{dV} \right]^{-1} \Big|_{V_b=0} \quad (1.9)$$

where J_{dark} is the dark current (no photogenerated current) density given in A/cm^2 . Photodiodes are typically operated at zero-bias or under a slight reverse bias. For the latter case, the dynamic resistance-area product

$$R_dA = \left[\frac{dJ_{dark}}{dV} \right]^{-1} \Big|_{V_b=V_d} \quad (1.10)$$

may be used for quality assessment. R_oA or R_dA products are experimentally determined from the IV-characteristics. High resistance-area products are desired, and experimentally determined values are often compared to ideal diffusion limited values calculated from device modeling. The R_oA of an ideal photodiode is given by:

$$R_oA = \frac{k_B T}{q J_s} = \frac{k_B T}{q^2 G_{th}} \quad (1.11)$$

where $J_s=qG_{th}$ is the saturation current of an ideal diode IV, t is the active region thickness. For a P-on-n photodiode structure, with contribution only from n -type region, we have:

$$R_oA(A1) = \frac{2k_B T \tau_{A1}}{q^2 N_d t} \quad (1.12)$$

Where N_d is the donor concentration, τ_{A1} is the Auger 1 lifetime, and t is the n -type region thickness.

The total current in any photodiode is given by

$$J_{tot} = J_{dark}(V) + J_{\phi}(flux) \quad (1.13)$$

where J_{dark} is routinely measured in the community. The IV-characteristics of a photodiode contain information on current-generating mechanisms within a photodiode and will be discussed in greater detail in Chapter 2. J_{dark} depends heavily on bandgap and temperature. A convenient rule of thumb referred to as ‘Rule 07’ [9, 10] estimates state-of-the-art dark current across a wide range of IR cutoff wavelengths and temperatures. ‘Rule 07’ will be used in this work to evaluate diode performance near operational temperature.

2. Background

This chapter will focus on the fundamental material properties that will be useful for modeling and analysis purposes. The focus of this work is on direct gap semiconductor materials for intrinsic devices, therefore this section is divided into two main material systems under consideration: HgCdTe and III-V Sb-based superlattice materials. Additional background will be given pertaining to carrier scattering and Hall measurement. The parameters and equations in this chapter will be used to analyze data in the subsequent results chapters.

2.1 IR Materials Systems

2.1.1 HgCdTe

2.1.1.1 Introduction

The highly favorable material properties of $\text{Hg}_{(1-x)}\text{Cd}_{(x)}\text{Te}$ (MCT) were first brought to attention in the 1959 publication by Lawson and coworkers [11]. Since then, HgCdTe has ignited a tremendous amount of research and development, subsequently proving to be the material of choice in second-generation IR systems. Today, HgCdTe is the most widely used semiconductor material for IR photodetectors, and remains unparalleled in terms of fundamental properties and performance. This section will encompass the current status of HgCdTe technology, including fundamental material properties, with attention paid to both growth methods and device considerations pertinent to this work.

2.1.1.2 Fundamental Properties

2.1.1.3 Band structure

$\text{Hg}_{(1-x)}\text{Cd}_{(x)}\text{Te}$ is a narrow-bandgap, zinc-blende, II-VI, semiconductor ternary alloy consisting of HgTe and CdTe, and frequently considered pseudo-binary due the weak Hg-Cd bond. The band structure

is direct gap at $k = 0$ Γ -point, with a spherical but non-parabolic conduction band. The bandgap is tunable across the IR spectrum ($\sim 1 \mu\text{m}$ to $> 20 \mu\text{m}$), from SWIR out to VLWIR. Bandgap increases with Cd composition from -0.30 eV for semimetallic HgTe up to 1.65 eV for CdTe at 4.2 K. The x-value and temperature dependent bandgap may be calculated according to Hansen et al. as [12]:

$$E_g(x, T) = -0.302 + 1.93x + 5.35 \cdot 10^4 T(1 - 2x) - 0.81x^2 + 0.832x^3 \quad (2.1)$$

where x is the Cd composition. Equation 2.1 is valid for $0 < x < 0.6$ and from 4.2 – 300 K.

Similar, but with more constricted x range, dependences are given by Finkman [13] and Lowney [14], but the Hansen expression remains the most commonly implemented today.

The corresponding intrinsic carrier concentration as a function of x and T is given by Hansen and Schmit [15]:

$$n_i(x, T) = (5.585 - 3.82x + 1.753 \cdot 10^{-3}T - 1.364 \cdot 10^{-3}xT) \cdot 10^{14} E_g^{3/4} T^{3/2} e^{-\frac{E_g}{2k_B T}} \quad (2.2)$$

where E_g is in eV and calculated according to Equation 2.1 The validity range of Equation 2.2 is $0.14 < x < 0.4$ and from 50 - 300 K. Intrinsic carrier concentration is critical in modeling numerous properties related to carrier transport in semiconductors.

Magneto-optical measurements performed by Weiler [16] determined the electron and hole effective masses in HgCdTe alloys. The electron effective mass, m_e^* , can be expressed in analytic form using the following equation provided by Weiler:

$$\frac{m_0}{m_e^*} = 1 + 2F + \frac{E_p}{3} \cdot \left(\frac{2}{E_p} + \frac{1}{E_g + \Delta} \right) \quad (2.3)$$

where $E_p = 19$ eV, Δ is the split off spin-orbit band energy and taken to be 1 eV, and $F = -0.8$.

The light hole effective mass may be taken to be that of m_e^* , as they are quite similar, or can be calculated by the Kane model using:

$$m_{lh}^* = -m_0 \left(\frac{1-4m_0P^2}{3\hbar E_g} \right)^{-1} \quad (2.4)$$

where P is the Kane momentum matrix element and taken to be $P = 8.49 \times 10^{-8}$ eV cm.

Weiler found that the heavy hole effective mass, m_{hh}^* , changed only slightly along different crystallographic planes, ranging from 0.4-0.53 m_0 . The heavy hole effective mass is not well defined but typically taken to be 0.55 m_0 for modeling purposes. Values used in the literature range from 0.28-0.71 m_0 and may depend on additional modelling parameters [17].

2.1.1.4 Optical

Optical parameters of HgCdTe show a Cd-compositional dependence. The complex dielectric function, $\tilde{\epsilon}$, (or complex refractive index \tilde{n}) is commonly written in terms of its real (ϵ_1 , n) and imaginary (ϵ_2 , κ) parts, and are related through the Kramers-Kronig (KK) relation. As a polar dielectric crystal, the complex dielectric function of HgCdTe has high-frequency, interband, intraband, and phonon contributions. The high frequency dielectric function, ϵ_∞ , and low frequency (static) dielectric function, ϵ_0 , are given by [17, 18]:

$$\epsilon_\infty = 15.2 - 15.6x + 8.2x^2 \quad (2.5)$$

$$\epsilon_0 = 20.5 - 15.6x + 5.7x^2$$

Temperature dependence in Equation 2.5 was found to be negligible. The refractive index n is

given in terms of ε_1 and ε_2 . The refractive index dispersion near and below bandgap was calculated by Lui et al. [19] from absorption spectra curves and using the KK-relation. The empirical fit was determined to be:

$$n(\lambda, T)^2 = A + \frac{B}{1 - \left(\frac{C}{\lambda}\right)^2} + D\lambda^2 \quad (2.6)$$

$$A = 13.173 - 9.852x + 2.909x^2 + 10^{-3}(300 - T)$$

$$B = 0.83 - 0.246x - 0.0961x^2 + 8 \cdot 10^{-3}(300 - T)$$

$$C = 6.706 - 14.437x + 8.531x^2 + 7 \cdot 10^{-4}(300 - T)$$

$$D = 1.953 \cdot 10^{-4} - 0.0128x + 1.853 \cdot 10^{-4} \cdot x^2$$

which is valid for $0.273 < x < 0.443$ in the range of $4.2 < T < 300$ K, and $0.205 < x < 1.0$ at 300 K. As HgCdTe detectors are typically passivated with CdTe to reduce surface recombination and leakage currents, an explicit refractive index with temperature and wavelength dependence is needed for CdTe and can be calculated according to Hlidek [20]. The loss due to reflectivity, $R = \left(\frac{n_2 - n_1}{n_1 + n_2}\right)^2$, for normal incident radiation at the air-to-CdTe surface interface is around 20%. Losses at the CdTe-HgCdTe interface are typically much smaller (~2%). The refractive index of CdZnTe is assumed to be the same as CdTe.

Absorption in HgCdTe is described by two distinct regions: below gap ($E_{\text{photon}} < E_{\text{go}}$) and above gap ($E_{\text{photon}} > E_{\text{go}}$) absorption, with E_{go} being the optical energy gap. Below gap absorption is due to transitions between localized band-tail states, and displays an exponential energy dependence. Urbach [21] described the general expression as:

$$\alpha_{\text{Urbach}} = \alpha_0 e^{\frac{E_{\text{photon}} - E_0}{W}} \quad (2.7)$$

where E_o is a reference energy with absorption coefficient α_o , E_{photon} is given by $\hbar\omega$, and W is the Urbach energy. This form of absorption is referred to as the Urbach tail, and is thought to be the result of random fluctuations within the material. Chu [22] provided the following empirically derived set of equations to describe the x -value and temperature dependence of the Urbach tail:

$$W = \frac{k_B T}{\sigma} = \frac{E_{g,C} - E_o}{\ln \alpha_g - \ln \alpha_o} \quad (2.8)$$

$$\ln \alpha_o = -18.5 + 45.68x$$

$$E_o = -0.355 + 1.77x$$

$$\alpha_g = -65 + 1.88T + (8694 - 10.31T)x$$

$$E_{g,C}(x, T) = -0.295 + 1.87x - 0.28x^2 + (6 - 14x + 3x^3)10^{-4} \cdot T + 0.35x^4$$

The samples were measured by Chu from 4.2 K to 300 K and had a composition x -value ranging from 0.165 to 0.443. Satisfactory fits can be made to experimental data when using $E_o = E_g + W/2$. Above bandgap absorption in the intrinsic (Kane) region for a direct bandgap semiconductor with parabolic bands follows the well-known square root dependence [23]:

$$\alpha = A\sqrt{\hbar\omega - E_g} \quad (2.9)$$

where A is a constant. Schacham and Finkman [24] applied such a square root rule to HgCdTe, but introduced x and T dependence according to:

$$\alpha = \beta\sqrt{\hbar\omega - E_g} \quad (2.10)$$

$$\beta = 2.109 \cdot 10^5 \sqrt{\frac{1+x}{81.9+T}}$$

This expression provides adequate fits to experimental data near the bandgap, but predicts a lower absorption coefficient at higher photon energies (> 100 meV above gap), particularly when considering thin-film photodiodes or PV materials. An alternative expression provided by Price and Boyd [25] maintains slightly higher absorption coefficient values in Kane region as compared to the Schacham and Finkman expression. The Price and Boyd expression in the intrinsic regime is given by the following:

$$\alpha = \beta \sqrt{E_{\text{photon}} - E_g} \quad (2.11)$$

$$E_g = \ln \left[\frac{\alpha_t}{\alpha_o \sqrt{e}} \right] \cdot \frac{T+81.9}{\sigma} + E_0$$

$$\beta = \frac{\alpha_t}{\sqrt{T+81.9/2\sigma}}$$

$$\alpha_o = e^{53.61x-18.88}$$

$$\alpha_t = 500 + 5600x$$

$$\sigma = 3.267 \cdot 10^4 (1 + x)$$

$$E_0 = 1.838x - 0.3424$$

More recent calculations performed by Chang, Grein, Sivananthan et al. [26] employed k·p calculations using a 14 x 14 matrix [27] giving hyperbolic conduction and light hole bands, and using a parabolic heavy hole band. Their derivations showed exceptional fitting to experimental data, well above the optical energy gap. Figure 1 shows absorption coefficient data and fitting results for $\text{Hg}_{0.79}\text{Cd}_{0.21}\text{Te}$ at 80 K. It can be seen that the Chu expression (dashed line) gives an adequate fit of the Urbach tail region. Meanwhile, the Kane region shows that the expressions given by Chang, Grein, Sivananthan et al. (solid line) using hyperbolic E_c and E_{lh} provide much better agreement compared to the parabolic bands used by Schacham and Finkman (dashed/dotted line).

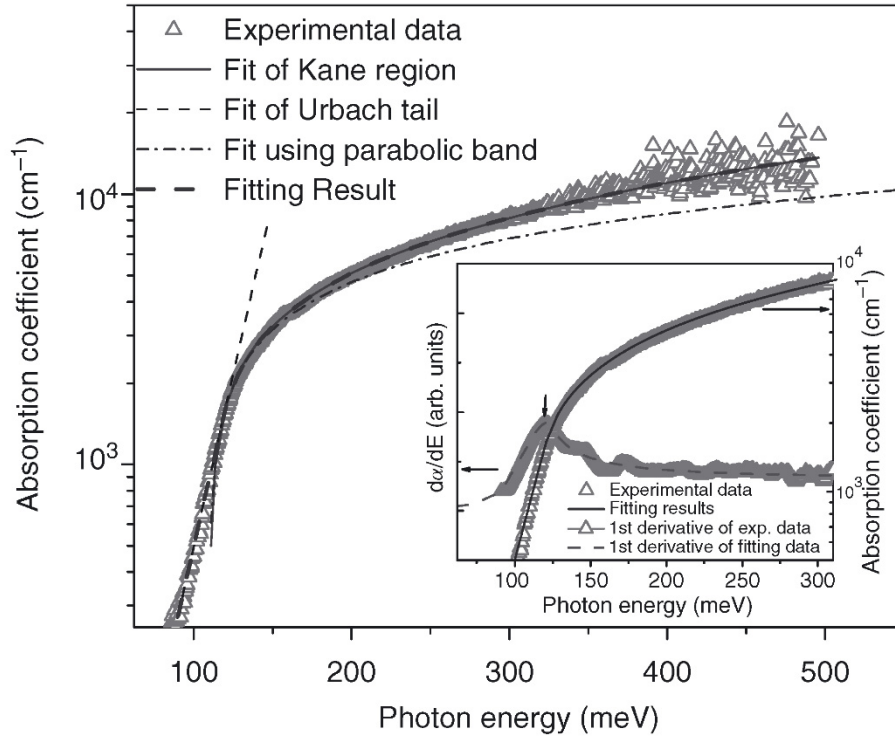


Figure 1: Experimental and theoretical absorption coefficient of a $\text{Hg}_{0.79}\text{Cd}_{0.21}\text{Te}$ sample at 80K. Inset shows the first derivative of the absorption coefficient, with the peak representing the optical bandgap E_0 . [26].

Figure 2 shows a comparison between the expressions given by Chu (Equation 2.8), Schacham and Finkman (Equation 2.10) and those provide by Price and Boyd (Equation 2.11) for $x = 0.225$ at 77 K. It can be seen that Price and Boyd maintains higher absorption coefficient values in the Kane region. For the purposes of this work, we are primarily concerned with near gap absorption. Therefore, we will employ the Price and Boyd expressions in the Kane region and the Chu treatment of the Urbach tail.

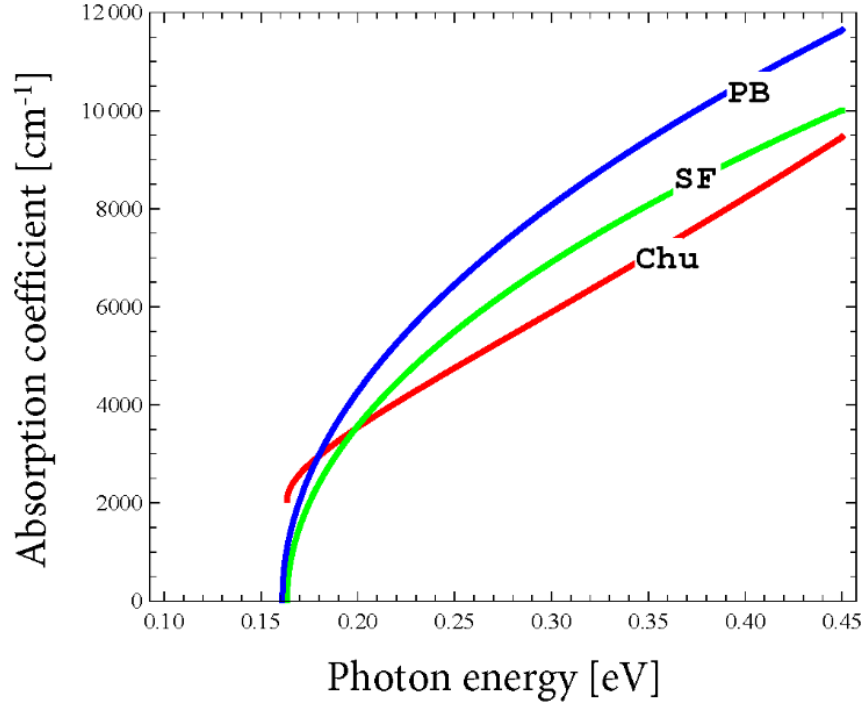


Figure 2: Absorption coefficient versus energy comparison of Chu, Schacham and Finkman (SF), and Price and Boyd (PB) expressions for $\text{Hg}_{0.775}\text{Cd}_{0.225}\text{Te}$ at 77 K.

The optical energy gap, E_0 , is defined to be the transition between the two optical regions. It may be determined experimentally as a peak in the first derivative of the absorption coefficient. The inset in Figure 1 shows both the absorption coefficient and its derivative with respect to photon energy, with the E_0 peak clearly highlighted.

2.1.1.5 Lifetime

HgCdTe carrier lifetime is determined by three bulk recombination mechanisms: Auger, radiative, and Shockley-Read-Hall (SRH). An additional recombination mechanism may result from the abrupt termination of lattice periodicity at the surface/interfaces which contain localized recombination states, characterized by a surface recombination velocity S . The effective lifetime is given by the Matthiessen's rule as:

$$1/\tau_{eff} = 1/\tau_{bulk} + 1/\tau_{surface} = 1/\tau_A + 1/\tau_R + 1/\tau_{SRH} + 2S/d \quad (2.12)$$

where τ_A is the Auger lifetime, τ_R is the radiative lifetime, τ_{SRH} is the SRH lifetime, and d is the sample thickness. Auger and radiative recombination are an intrinsic result of the electronic band structure, making them inherently unavoidable. In contrast, SRH and surface recombination are a result of unwanted defects and lattice imperfections. Defect related mechanisms limit detector performance and are theoretically avoidable under ideal growth and processing conditions.

2.1.1.5.1 Auger lifetime

Auger recombination is a photonless band-to-band mechanism involving three charge carriers. Of the many possible multi-carrier interactions in HgCdTe, two mechanisms dominate. The first is Auger 1, which consists of an electron and minority carrier heavy hole recombining and the excitation of a second electron in the CB. The second is Auger 7, which consists of a heavy hole and minority carrier electron recombining and the excitation of a light hole. Auger 1 is dominant in n -type HgCdTe, while conversely, Auger 7 is dominant in p -type HgCdTe.

The intrinsic Auger 1 recombination lifetime, τ_{A1}^i , in n -type HgCdTe is given by Beattie-Landsberg-Blackmore (BLB) [28, 29, 30] as:

$$\tau_{A1}^i = 3.8 \cdot 10^{-18} \cdot \epsilon_{\infty}^2 \frac{m_o}{m_e} \sqrt{(1 + \mu)} \cdot (1 + 2\mu) \left(\frac{E_g}{k_B T}\right)^{3/2} e^{\frac{(1+2\mu) \cdot E_g}{(1+\mu) k_B T}} (|F_1 F_2|^2)^{-1} \quad (2.13)$$

where $\mu = m_e/m_{hh}$ is the ratio of electron to hole effective masses, and $|F_1 F_2|$ is the overlap integral of Bloch functions. The Auger lifetime depends on carrier concentration according to:

$$\tau_{A1} = \frac{2n_i^2}{n_o(n_o+p_o)} \cdot \tau_{A1}^i \quad (2.14)$$

where n_i is the intrinsic carrier concentration, n_o is the free (equilibrium) electron concentration, and p_o is the free hole concentration. A similar expression may be written for the Auger 7 mechanism. The ratio of Auger 7 to Auger 1 is defined as:

$$\gamma = \frac{\tau_{A7}}{\tau_{A1}} \quad (2.15)$$

Krishnamurthy [31] calculated γ to be between 3 - 6 for LW at low temperature (40 - 80 K), while Casselman [32] estimated a range from 0.5 to 6 depending on x -value and temperature. More recent calculations suggest that γ is between 8 - 12 or larger [33, 34]. For this work we will use a gamma value of 10 throughout, consistent with calculations using the empirical pseudopotential method [35].

The calculation of $|F_1F_2|$ is difficult and assumptions are often made, with reported values ranging from 0.1-0.3 [36] in the literature. In practice, $|F_1F_2|$ has historically been treated as a fitting parameter when analyzing experimental data, yet a number of methodologies have been employed over the years. For example, Kinch [33, 37, 38] and Schacham [24] have suggested using fixed values of 0.2 or 0.22, while Blakemore suggests adjusting between 0.16 and 0.22.

The recombination rates of Beattie and Landsberg [28] have recently been calculated directly using both a 14 x 14 k - p method [39, 40] and separately using a hybrid pseudopotential tight-binding approach [41, 42] in LWIR HgCdTe. Calculations of the overlap integral varied between the models, in large part due to differences in the band structures employed. However, as pointed out by Grein et al. [40], the overlap integral was found to be strongly dependent on effective mass (see Figure 5 therein), which also aides in explaining the discrepancy. More recent calculations [35] using an empirical pseudopotential method (EPM) [43] were in good agreement with those presented by Grein et al., supporting a value of $|F_1F_2| = 0.16$ for LW HgCdTe. For these reasons, and the fact that MW HgCdTe has

a higher electron effective mass, values of $|F_1F_2| = 0.16$ for LW and $|F_1F_2| = 0.14$ for MW material will be used in this work unless otherwise specified.

2.1.1.5.2 Radiative lifetime

Radiative recombination refers to the annihilation of electron-hole pairs and subsequent emission of a photon. In the small modulation limit (negligible excess carrier population), the radiative lifetime for bands with spherical symmetry was presented by van Roosbroeck and Shockley [44] as:

$$\tau_R = \frac{1}{B_o(n_o+p_o)} \quad (2.16)$$

where B_o is the thermal equilibrium spontaneous generation rate and is dependent on the absorption coefficient. Using more refined expressions for the energy dependence of the absorption coefficient, Schacham and Finkman [24] calculated:

$$B_o = 5.8 \cdot 10^{-13} \sqrt{\epsilon_\infty} \left(\frac{m_o}{m_e^* + m_h^*} \right)^{3/2} \left(1 + \frac{m_o}{m_e^*} + \frac{m_o}{m_h^*} \right) \left(\frac{300}{T} \right)^{3/2} (E_g^2 + 3k_B T E_g + 3.75 \cdot (k_B T)^2) \quad (2.17)$$

Radiative recombination in HgCdTe was critically re-evaluated by Humpreys [45, 46], arguing that previous treatments largely underestimated lifetimes related to this mechanism due to the process of photon reabsorption, also known as photon recycling. An enhancement factor, $\beta > 20$, was calculated for thin HgCdTe samples. The work by Humpreys suggested that for thicker samples, nearly all photons emitted through this process were quickly reabsorbed within the material. Grein [47] expanded the theory to include non-parabolic effects and explicitly determined absorption coefficients. It was shown that by

averaging over the entire free carrier population an enhancement factor $\beta = 26.1$ at 293 K and $\beta = 12.9$ at 77 K was determined for a 3 μm sample thickness giving credence to the importance of photon recycling.

In this work, we allow for the possible effects of photon recycling by introducing the enhancement factor β as:

$$\tau_R = \beta \tau_{R,o} \quad (2.18)$$

where $\tau_{R,o}$ is calculated from Equations 2.16 and 2.17. The effective form of radiation recombination given by Humpreys has the form:

$$\tau_R = \frac{t}{2 \cdot QE \cdot \phi_B} \cdot \frac{n_i^2}{n+p} \quad (2.19)$$

As pointed out by Humpreys, the effect did not strictly apply to diodes under sufficient reverse bias as a result of carrier sweep out, reducing the number of photons generated. Detailed modeling by Jozwikowski [48] examined the processes of carrier exclusion and photon suppression as related to photon recycling in a MW p-on-n diode, and determined that at a reverse bias of 0.2 V, the net generation rate was roughly four orders of magnitude lower than that predicted by van Roosbroeck and Shockley. Furthermore, they showed a radiative lifetime enhancement in both MW and LW p-on-n diodes operating at 80K and 300K, with the smallest enhancement occurring at 80K in the MW diode. Despite this, the enhancement was roughly an order or magnitude, and resulted in lifetime limited by a combination of Auger, radiative, and SRH, when the classical treatment predicts only radiative limited lifetime. For these reasons, the effects of photon recycling will be considered when experimentally measuring carrier lifetime and current-voltage characteristics.

2.1.1.5.3 Shockley-Read-Hall

Lattice imperfection and/or crystalline defects can give rise to unwanted energy states within the forbidden energy gap, referred to as SRH-centers, or traps. Generation-recombination mechanisms through a concentration of SRH-centers, N_t , at an energy level E_t above the VB give minority carrier lifetime expressions written as [36, 49, 50]:

$$\tau_{SRH} = \frac{(n_o + n_1)\tau_{po} + (p_o + p_1)\tau_{no}}{n_o + p_o} \quad (2.20)$$

$$\tau_{po} = 1/V_p \sigma_p N_t$$

$$\tau_{no} = 1/V_n \sigma_n N_t$$

where n_o and p_o are the equilibrium carrier concentrations, $V_{n,p}$ are the electron and hole thermal velocities, $\sigma_{n,p}$ are the capture cross sections for electrons and holes, τ_{no,p_o} are the capture time constants, and p_1 and n_1 are the thermal free hole and electron concentrations due to traps located at E_t :

$$p_1 = p_o e^{(E_f - E_t)/k_B T} = N_v e^{(E_v - E_t)/k_B T} \quad (2.21)$$

$$n_1 = n_o e^{(E_t - E_f)/k_B T} = N_c e^{(E_t - E_c)/k_B T}$$

$$N_c = 2 \left(\frac{2\pi m_e^* k_B T}{h^2} \right)^{3/2}$$

$$N_v = 2 \left(\frac{2\pi m_h^* k_B T}{h^2} \right)^{3/2}$$

where E_f is the Fermi level, N_v is the VB effective density of states, and N_c is the CB effective density of states. The above expressions are valid for low excess carrier concentrations and under the condition that N_t is less than the carrier concentration. N_t , E_t , and τ_{no,p_o} are determined by fitting temperature-dependent

experimental data, but exact characterization often requires advanced techniques such as deep level transient spectroscopy (DLTS). For the simplified case of low-temperature n -type HgCdTe, the equations reduce to:

$$\tau_{SRH} = \left(1 + \frac{n_1}{n_o}\right) \tau_{po} \quad (2.22)$$

It is expected that SRH mechanisms will be most relevant in lightly doped n -type and p -type materials. Further simplifications may be made by setting $\tau_{no} = \tau_{po}$ and fixing E_t to be either mid-gap or at the intrinsic energy level E_i . Having $\tau_{no} = \tau_{po}$ makes no assumptions about whether a trap is acceptor-like or donor-like. It also follows from the equations above that traps located near mid-gap (either $E_t = E_i$ or $E_t = E_g/2$) will produce the most effective recombination states, and will be modeled as such in this work.

2.1.1.6 Mobility

HgCdTe is categorized by high mobility electrons and relatively low mobility, low conductivity holes. A small electron effective mass is the cause of high electron mobility values, which routinely exceed $10^5 \text{ cm}^2\text{V}^{-1} \text{ s}^{-1}$ in high quality LWIR material. The electron effective mass is dependent on x -value, while the hole effective mass is largely independent of x -value. A number of scattering mechanisms control mobility in HgCdTe and shall be discussed in more theoretical detail in Section 2.2. Broadly speaking, it can be said that mobility depends primarily on the x -value, doping, temperature, and quality of material in question. Mobility is generally seen to decrease with increasing temperature and doping.

For modeling purposes, it is not always convenient to directly measure certain structures and/or layers of interest. Therefore, simple models that predict expected mobilities become valuable. Rosbeck et al. [51] generated a formula to approximate electron mobility based on available Hall data taken by Scott [52] and Schmit et al. [53]. The expression has the following form:

$$\mu_e = 9 \cdot 10^8 \cdot \frac{b}{z^{2a}} [cm^2V^{-1}s^{-1}] \quad (2.23)$$

$$a = \left(\frac{0.2}{x}\right)^{0.6}$$

$$b = \left(\frac{0.2}{x}\right)^{7.5}$$

$$z = \begin{cases} T, & T > 50 K \\ \frac{1.18 \cdot 10^5}{(2600 - |T - 35|^{2.07})}, & T < 50 K \end{cases}$$

and was intended for compositions of $0.2 < x < 0.6$. Care must be exercised when using Equation 2.23, as no distinction is made concerning doping concentration. Ionized impurity scattering tends to dominate mobility at low temperature [54], and Equation 2.23 is not accurate, particularly below 150 K, when donor concentrations exceed $5 \times 10^{15} \text{ cm}^{-3}$.

The heavy hole mobility is much lower than the electron, and can often be modeled as 100 times smaller than the more readily obtainable electron mobility. An empirical expression for the hole mobility at 77 K with respect to acceptor concentration was given by Dennis et al. [55]:

$$\mu_{hh} = 440 \cdot \left(1 + \frac{p}{1.8 \cdot 10^{17}}\right)^{-1/4} [cm^2V^{-1}s^{-1}] \quad (2.24)$$

The light hole concentration is approximately 100 times less than that of the heavy hole concentration, making measurement difficult. Analysis of magnetotransport data has been used to determine the light hole mobility in *p*-type HgCdTe [56-62], with a wide range of values ($1,000 - 40,000 \text{ cm}^2V^{-1} s^{-1}$) reported at low temperature. As Grill pointed out [63], different Hall scattering factors between heavy and light holes can complicate analysis, which Yadava noted was particularly evident at low temperature [64]. Gold [56] speculated that interband coupling effects were the cause for different

scattering rates at higher temperatures. For simplicity, we estimate light hole mobilities to be between 5 to 50 times those of heavy hole mobilities, and carrier concentrations 50 - 500 times less.

Minority carrier mobility is of great importance, being a critical parameter pertaining to device performance. Measurements of minority carrier electrons are more favorable due to their high mobility and resultant conductivity contributions. A number of studies have been performed, finding that minority carrier electron mobilities are comparable with majority carrier electron mobilities [56, 65, 66], as long as acceptor doping is kept below mid- 10^{16} cm^{-3} , at which point a sharp decrease can be seen as illustrated in Figure 3. Discrepancies are typically not seen between n -type electron mobility and p -type electron mobility above 200 K, while the largest mobility reductions are seen at lowest temperature.

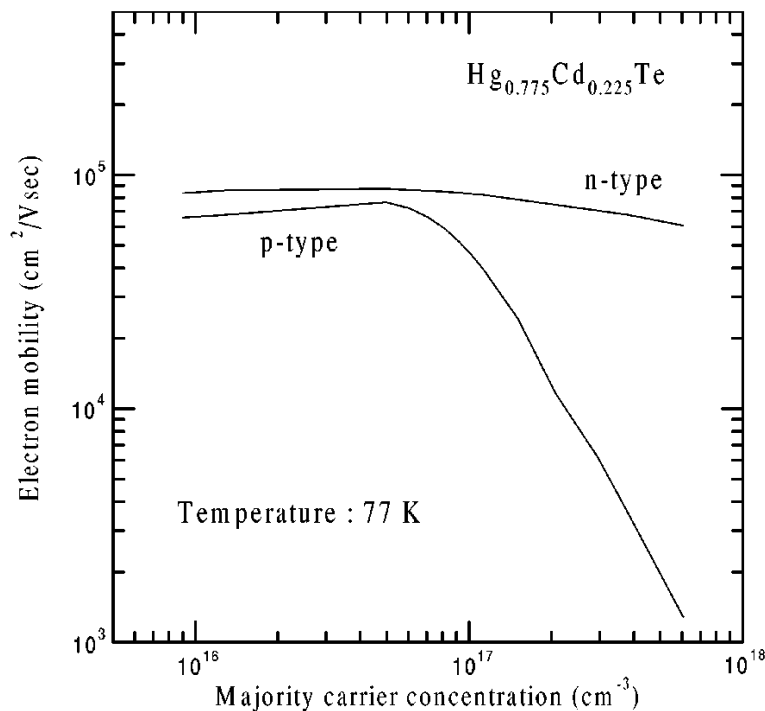


Figure 3: Electron mobility in LW HgCdTe material versus carrier concentration, showing comparative mobility as majority (n -type) and minority (p -type) carrier [66].

The measurement of hole mobility in n -type HgCdTe is quite challenging, yet results have been obtained using the Haynes-Shockley method [67, 68] and extracted from diffusion length measurements

with electron-beam induced current (EBIC) [69, 70]. Results appear to indicate that the minority carrier hole mobility is comparable to similarly doped majority carrier material, with values in excess of $500 \text{ cm}^2\text{V}^{-1}\text{s}^{-1}$ being reported at 77 K.

2.1.1.7 MBE and epitaxial growth

The archetypal issue with the growth of HgCdTe has been the high vapor pressure of Hg. Early HgCdTe growth utilized bulk growth techniques, but later gave way to more preferred epitaxial methods such as molecular beam epitaxy (MBE), liquid phase epitaxy (LPE), and metalorganic chemical vapor phase epitaxy (MOCVD). Epitaxial growth afforded greater control over impurities while requiring much lower growth temperatures, thus reducing the amount of native as-grown material defects. Ideal characteristics of HgCdTe films today include low defects, high uniformity, versatility in growth structure, possibility of large-area growth, and affordability. This section will describe the basics of growth technology pertaining to this work.

MBE growth is performed under ultra-high vacuum (UHV) and non-equilibrium conditions. Epitaxial (layer by layer) 2-D growth is realized by generating thermally evaporated molecular fluxes from high purity source materials that subsequently condense on a single crystal substrate. UHV ($\sim 10^{-7}$ – 10^{-9} torr) reduces the amount of unwanted contaminants within the HgCdTe material and ensures the molecular fluxes have nearly collision-free paths. Precise control of beam flux ratios (Hg, CdTe, and Te₂) is crucial as it determines the alloy composition and crystalline quality.

While MBE growth of HgCdTe offers the lowest temperature growth (~ 185 - 190 °C), device quality material requires a very stringent substrate temperature window. Even minor deviance (± 1 °C) from ideal substrate temperature can lead to degraded material. Notably, low temperature growth leads to the formation of micro-twins, surface hillocks, and dislocations. Conversely, high temperature growth increases micro-voids, and Te precipitates due to Hg deficiency. Crystalline defects have shown adverse effects on a number of transport properties which can contribute to poor performance. Therefore, *in-situ*

monitoring techniques have been developed which allow real-time, non-destructive observation of the growth process.

MBE growth is performed under Te-rich conditions as Hg-rich growth results in poor structural quality. The most common growth orientation today takes place on (211)B vicinal substrates, under a 2-D step-flow process, with adatoms at step bottoms. Kinetic and quasi-equilibrium theories have been used to better understand MBE growth. Quasi-equilibrium theory is useful since structural quality depends on whether partial equilibrium is achieved on thermodynamic time scales. Alternatively, the low temperature and slow MBE growth rate mean that surface kinetics and chemistry are vitally important too in understanding the growth process.

An MBE chamber typically consists of loading, buffer, and growth chambers separated by locking mechanisms. The loading chamber executes rough pumping and easy introduction of sample substrates into the system. The buffer chamber provides higher vacuum levels for sample storage and outgassing if needed, and is kept under constant vacuum. The growth chamber itself is a sophisticated collection of effusion cells, pumps, gauges, thermocouples, characterization tools, and sample manipulation tools. The walls of the growth chamber are cooled using liquid nitrogen so that unincorporated source material and other contaminants are collected. The sample itself is rotated during growth to improve uniformity, and its temperature is closely monitored and controlled via proportional-integral-derivative (PID) feedback loops.

A major advantage of MBE over alternative techniques is the ability to rapidly change the impinging flux constitutes through shutter control. This attribute has propelled MBE to be the preferred method for advanced multi-layered structures.

2.1.1.7.1 Doping

Intrinsic HgCdTe grows *p*-type due to metal lattice vacancies. The Hg-vacancies are doubly ionized in nature [71-74], and their concentration depends on growth temperature, Hg partial pressure,

and Cd-composition. Although low concentrations are possible, vacancy-doping is generally not perceived as an ideal *p*-type doping option due to insufficient control of doping profile and rapid diffusion through interstitials. Furthermore, vacancies have been seen to reduce carrier mobilities [75] and act as recombination centers [76].

Extrinsic *p*-type doping using Group I or Group V ions have therefore been pursued. Doping may be either *in-situ* or *ex-situ* via ion implant or in-diffusion, with *in-situ* being the preferred method. Group I elements (Cu, Ag, Au) exhibit very high diffusion coefficients in HgCdTe, even at room temperatures, rendering them precarious for stable junction formation. Of the Group V elements (P, As, Sb), arsenic proved to be the superior candidate. Arsenic has a relatively low diffusivity and can be incorporated over a sufficiently wide range (10^{15} - 10^{19} cm⁻³) for various applications.

The amphoteric nature of arsenic has been established [77], as it may be incorporated as a donor (As_{Hg}) on a metal site or as an acceptor (As_{Te}) on a Te site [78]. As-grown samples typically show compensated *n*-type behavior inferred from Hall measurements [79]. Post-growth annealing is required in order to assure desired electrical activation with 100 % activation being reported up to 2×10^{18} cm⁻³ [80]. Activation of As-doped MBE material requires two-stage annealing at $T > 300$ °C followed by a Hg-vacancy fill ~ 200 - 250 °C, both under Hg overpressure. The former anneal electrically activates the As [77] by creating Te vacancies which are then occupied by As. The latter anneal step fills unwanted Hg vacancies formed during growth or annealing. Proper conditions can result in Hg-vacancy concentrations of 10^{13} cm⁻³ or lower. The higher temperature anneal is short in duration, typically less than 10 minutes, but unfortunately negates some of the benefits that low temperature MBE growth offers.

As₄ is only physisorbed on the MCT surface. The sticking coefficient is low and very temperature dependent, often leading to poor reproducibility. As₄ incorporates as a tetramer [81], severely distorting the surrounding lattice. Therefore, As cracking (As₄ → As₂) is commonly implemented to increase incorporation during MBE growth [82]. However, care must be taken not to expose the substrate to excess heat from the As-cracking cell.

In-situ n-type and *p*-type doping are therefore routinely performed by incorporating indium and

arsenic into the lattice, respectively. Low p -type doping ($< \text{mid-}10^{15} \text{ cm}^{-3}$) remains an ongoing challenge [83], and the precise mechanisms of incorporation and activation are still under investigation [84, 85]. Indium donor concentrations of $10^{14} - 10^{19} \text{ cm}^{-3}$ are readily demonstrated and no activation is required, being a fully ionized shallow donor. Very low n -type doping (low 10^{14}) has to contend with compensating Hg-vacancy acceptors and other impurities. Standard practice entails vacancy removal through post-growth annealing under Hg over-pressure, as Hg diffuses easily through interstitial sites.

It should be noted that Hg-vacancies are present even in n -type doped samples, and a post-growth annealing treatment is necessary to reduce their concentration. Details on annealing will be given in Chapter 4.

2.1.1.7.2 Substrates

The ideal substrate for HgCdTe growth has the following properties: transparent, high resistivity, available in large-areas, close lattice and thermal coefficient of expansion matching HgCdTe, low impurities and defects, straightforward surface preparation, high thermal conductivity, and high uniformity. Substrates act as a template for subsequent growth, so quality is paramount, as defects and impurities may propagate into the epilayer. A summary of some substrate properties used for HgCdTe growth are shown in Table I.

Table I: HgCdTe substrate properties.

	a (Å)	α [$\times 10^6 \text{ K}^{-1}$] Near 300K	Cost [US \$ cm^{-2}]	Size Available [cm^2]	Surface Defects [cm^{-2}]	Thermal Conductivity [$\text{mW cm}^{-1} \text{ K}^{-1}$]	MCT EPD [cm^{-2}]
Si	5.43	~ 2.6	~ 1	~ 700	10^2	1235	$\sim 10^6$
GaAs	5.65	~ 6.7	$\sim 3-5$	~ 180	5×10^3	500	$\sim 10^6$
CdTe	6.482	~ 4.8	~ 30 (GaAs) ~ 3 (Si)		10^5 (GaAs and Si)	55	
$\text{Cd}_{0.96}\text{Zn}_{0.04}\text{Te}$	6.466	~ 4.8	~ 400	~ 50	10^4	55	$\sim 10^4$

According to the work of [86], the lattice parameter, a , of $\text{Hg}_{1-x}\text{Cd}_x\text{Te}$ at room temperature is given by:

$$a(\text{\AA}) = 6.4815x + 6.46152(1 - x) \quad (2.25)$$

which gives $a = 6.46602$ ($x = 0.225$) and $a = 6.46751$ ($x = 0.3$). It is readily apparent that $\text{Cd}_{0.96}\text{Zn}_{0.04}\text{Te}$ provides the best lattice matching ($< 0.1\%$), and CdTe is also quite suitable with a mismatch less than 1%. Si and GaAs both exhibit large mismatches, $\sim 19\%$ and $\sim 15\%$ respectively, and consequently require the growth of a thick CdTe buffer layer before HgCdTe epi-growth. Therefore, the CdTe-substrate interface plays an important role in lattice defect formation, with the CdTe-Si interface mismatch exceeding that of CdTe-GaAs. However, this can be reduced somewhat by the introduction of a thin layer of ZnTe growth on Si before the CdTe buffer [87, 88], which has the added benefit of preserving substrate 211 orientation.

Lattice mismatching results in the formation of threading dislocations to reduce lattice strain, and are well known to adversely affect HgCdTe device transport properties and performance [89-93]. Such dislocations can be quantified using a decoration etch [94, 95] and recorded as etch pit densities (EPD). EPD values of 10^5 cm^{-2} or lower are required for acceptable performance, and can be accomplished with growth on CdZnTe. Growth on CdTe/Si and CdTe/GaAs both result in EPD values exceeding 10^6 cm^{-2} , but may be reduced after thermal cyclic annealing (TCA) [96-99] to values in the low- 10^5 range. The possibility of dislocation passivation using hydrogen has been explored with some promising results [75]. Hydrogen conceptually attaches to dangling bonds associated with dislocation induced SRH-centers, and thus improves electrical properties of the material. However, both approaches introduce additional issues, namely TCA annealing can blur junction sharpness due to diffusion, while hydrogen passivation elicits long-term stability concerns.

It follows that arguments based purely on lattice and thermal matching alone make $\text{Cd}_{0.96}\text{Zn}_{0.04}\text{Te}$ the preferred substrate for high quality HgCdTe epilayers. Although the highest performance is achieved

on CdZnTe, substrates are expensive and are available in limited size, thus impacting the total number of pixels on an FPA. Furthermore, CdZnTe provides a thermal expansion match to HgCdTe but has a large thermal expansion mismatch with Si-based ROICs, reducing its practicality somewhat. Additional growth uniformity concerns due to low thermal conductivity have led to the extensive investigation of growth on alternatively substrates, with the most notable being Si and GaAs.

Si and GaAs substrates are much less expensive, readily available, and are commercially offered in larger areas. Si is the lowest cost and largest area substrate available, but alternatively, has the largest thermal and lattice mismatches with HgCdTe of the possible substrate choices discussed. The thermal mismatch with HgCdTe is a major concern during cryogenic treatments, as irreversible cracking damage may occur. The benefits of GaAs are similar to those of Si, but substrates are slightly more expensive and available in smaller areas. Wafers are available epi-ready leading to straight forward surface preparation as compared to the more laborious procedures for Si and CdZnTe. Both the thermal and lattice mismatch of GaAs are slightly better than Si, and while cryogenic concerns may be less, dislocation formation remains analogous.

No substrate is preferred for every device application today, with each offering its own distinct advantages and disadvantages. Substrate research is ongoing, with CdZnTe focus centered on production; i.e. reducing quality variability while increasing area and driving down costs. Meanwhile, research on alternative substrates continue to focus on dislocation reduction via novel growth techniques (silicon-on-insulator growth or selective area growth using nanopatterned substrates) and/or post-growth treatments.

2.1.1.7.3 *In-situ* monitoring

MBE growth of HgCdTe is a delicate process with a large number of dynamic features exhibiting run-to-run variability. Chamber and effusion cell conditions may change significantly over time, so routine monitoring is necessary. Aside from thermocouple and flux gauge readings, the primary *in-situ* tools at disposal are reflection high-energy electron diffraction (RHEED), spectroscopic ellipsometry

(SE), pyrometer, and absorption-edge spectroscopy. The most heavily relied upon being RHEED and SE.

RHEED is a surface analysis technique, sensitive to as little as one monolayer of crystalline material. The technique does not cause material damage or interfere with growth but prolonged exposure may cause localized heating and should be avoided. RHEED is particularly useful for monitoring undesirable growth conditions, such as twin formation or 3-D growth. The initial growth stages are crucial to subsequent layer quality, and are continuously monitored using RHEED. Periodic surface quality assessments are made with RHEED throughout a growth run.

SE is well calibrated tool based on the manipulation of a known polarization state, and measures the frequency-dependent dielectric function. A robust SE system can be used to monitor Cd-composition, growth rate, surface temperature, and roughness [100, 101]. The accuracy of extracted parameters ultimately depends on the strength of the library used [102]. Therefore, an expansive collection of experimentally determined dielectric function values with respect to temperature and composition is needed. In this work, SE has been used to monitor surface roughness and temperature during CdTe growth and x-value and surface roughness during HgCdTe growth. Surface roughness is treated according to the Bruggeman effective medium approximation (EMA) with 50% taken to be void and 50% material [103].

2.1.1.7.4 Device considerations

Device architectures currently in practice today implement HgCdTe photodiode arrays in scanning or staring hybrid FPAs. Junction formation can be accomplished through extrinsic doping during growth or any number of post-growth techniques (ion implant, in-diffusion or out-diffusion, plasma induced conversion, etc.). Hybridization to the ROIC is done using indium bumps, or by etching vias through the HgCdTe to landing pads on the Si in an architecture referred to as the vertically integrated photodiode (VIP) [104]. The two hybridization methods described are shown in Figure 4. VIP architectures are outside the scope of this work, and we therefore draw attention to indium bump-bonded

architectures, specifically either delineated mesa diodes or planar structures formed by ion implantation.

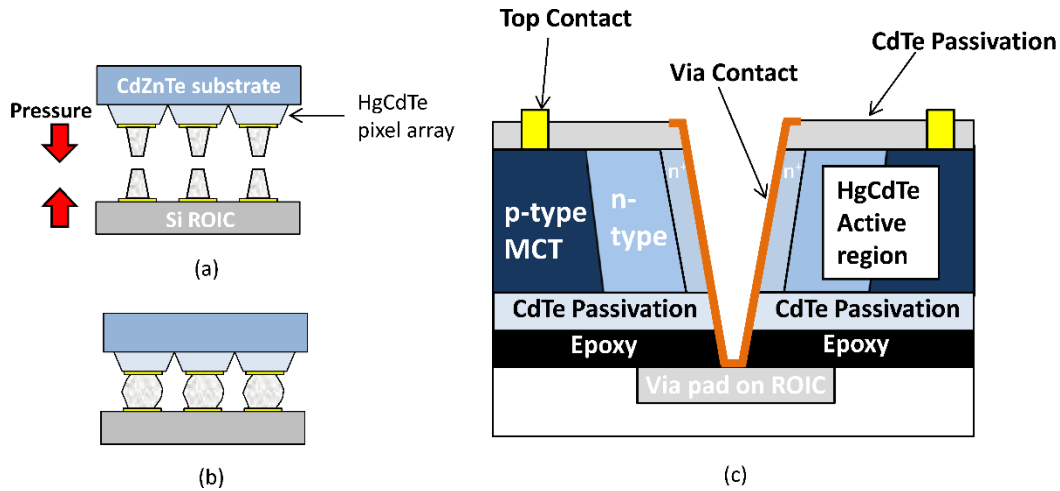


Figure 4: Depiction of hybridization to ROIC using indium bump bonding process (a & b) and the resultant architecture after hybridization of the vertically integrated photodiode (c).

In this work, we consider only mesa and planar diodes, the basic building blocks of device FPAs. This section will outline the basic properties of HgCdTe p-on-n junction photodiodes, particularly the P+/n heterojunction design. Diode performance in this work will be assessed through I-V characteristics, with related dark current mechanisms discussed herein.

2.1.1.7.5 p-n junction and dark current basics

The p-n junction is formed when *n*-type and *p*-type semiconductor regions are brought together. The sudden gradients in charge carrier concentrations cause diffusion across the metallurgical junction. Specifically, holes will diffuse to the *n*-type region while electrons will simultaneously diffuse to the *p*-type region. This process leaves behind complementary regions of fixed ions devoid of mobility carriers, known as the depletion, or space-charge, region. The resultant electric field generates drift currents that exactly cancel the diffusion currents under steady-state conditions, such that there is zero total current across the junction at thermal equilibrium. A large electrostatic potential difference exists across the

junction known as the built-in voltage, V_{bi} , and is found using Poisson's equation [105]:

$$V_{bi} = \phi_n - \phi_p = \frac{k_B T}{q} \cdot \ln\left(\frac{N_a N_d}{n_i^2}\right) = \frac{k_B T}{q} \cdot \ln\left(\frac{n_o}{n_{po}}\right) = \frac{k_B T}{q} \cdot \ln\left(\frac{p_o}{p_{no}}\right) \quad (2.26)$$

where $\phi_{n,p}$ is the electrostatic potential of the n and p regions respectively, n_{po} is the electron concentration in the p-region, and p_{no} is the hole concentration in the n-region. The equilibrium electron carrier concentration n_o is given by:

$$n_o = \frac{N_d - N_a}{2} + \sqrt{\left(\frac{N_d - N_a}{2}\right)^2 + n_i^2} \quad (2.27)$$

and related to the equilibrium hole concentration p_o through the mass action law, $n_o \cdot p_o = n_i^2$, for non-degenerate conditions.

The total depletion region width, W_{dep} , for an abrupt junction is the sum of depletion widths in the n -type and p -type regions [106]:

$$W_{dep} = x_n + x_p = \sqrt{\frac{2 \epsilon_s \epsilon_0 (N_A + N_D)(V_{bi} - V)}{q N_A N_D}} \quad (2.28)$$

where V is the applied bias and dopants are assumed fully ionized. The depletion region can be made smaller under forward-bias conditions, and likewise larger under reverse-bias conditions. For unequal n -type and p -type doping the depletion region extends further into the lightly doped region. For a one-sided junction ($N1_{doping} \gg N2_{doping}$) the depletion region can be approximated by the depletion region in the lightly doped side.

The rectifying behavior of p-n junctions dictates that current only flow easily in one direction. Forward-biasing results in minority carrier injection, and current rises rapidly with voltage. Alternatively, reverse-biasing produces very small currents. The relevant mechanism in an ideal diode is due to

diffusion current from the quasi-neutral regions. Assuming low-injection [107],

$$\begin{aligned}
J_{diff} &= J_s \exp\left(\frac{qV}{KT} - 1\right) \\
J_s &= q \left(\frac{n_{p0} D_n}{L_n} \zeta_p + \frac{p_{n0} D_p}{L_p} \zeta_n \right) \\
\zeta_p &= \frac{S_p \cosh \frac{W_p}{L_n} + \frac{D_n}{L_n} \sinh \frac{W_p}{L_n}}{\frac{D_n}{L_n} \cosh \frac{W_p}{L_n} + S_p \sinh \frac{W_p}{L_n}} \\
\zeta_n &= \frac{S_n \cosh \frac{W_n}{L_p} + \frac{D_p}{L_p} \sinh \frac{W_n}{L_p}}{\frac{D_p}{L_p} \cosh \frac{W_n}{L_p} + S_n \sinh \frac{W_n}{L_p}}
\end{aligned} \tag{2.29}$$

where $S_{n,p}$ is the surface recombination velocity and $W_{n,p}$ is the width of the neutral region. Surface recombination is typically not an issue for larger passivated HgCdTe diodes, and $S_{n,p}$ may be set to zero, simplifying the above expressions. The diffusion lengths $L_{n,p}$, and diffusion coefficients $D_{n,p}$, are given according to:

$$L_{n,p} = \sqrt{D_{n,p} \cdot \tau_{n,p}} = \sqrt{\frac{k_B T}{q} \cdot \mu_{n,p} \cdot \tau_{n,p}} \tag{2.30}$$

For a diffusion limited diode, the resistance-area product is then given as:

$$R_o A = \frac{k_B T}{q J_s} \tag{2.31}$$

Additional dark current contributions arise from generation-recombination (GR) in the depletion region, band-to-band (B2B) tunneling, and trap-assisted tunneling (TAT) across the forbidden gap. GR

current is particularly relevant in narrow-gap semiconductors at lower temperatures. The expression for depletion region GR in a one-sided abrupt junction is given as [108, 109, 110]:

$$J_{GR-SRH} = \frac{q n_i W_{dep} \sinh\left(\frac{qV}{2KT}\right)}{\sqrt{\tau_{p0} \tau_{n0}} \left(\frac{q(V_{bi} - V)}{2KT}\right)} f(b) \quad (2.32)$$

$$f(b) = \int_{z_1}^{z_2} \frac{dz}{z^2 + 2bz + 1}$$

$$b = \exp\left(-\frac{qV}{2KT}\right) \cosh\left[\frac{(E_t - E_{Fi})}{KT} + \frac{1}{2} \ln\left(\frac{\tau_{p0}}{\tau_{n0}}\right)\right]$$

$$z_1 = \sqrt{\frac{\tau_{p0}}{\tau_{n0}} \left(\frac{n_i}{p_{p0}}\right)} \exp\left(\frac{qV}{2KT}\right)$$

$$z_2 = \sqrt{\frac{\tau_{p0}}{\tau_{n0}} \left(\frac{n_{n0}}{n_i}\right)} \exp\left(-\frac{qV}{2KT}\right)$$

Then, if $b < 1$:

$$f(b) = \frac{1}{\sqrt{1-b^2}} \left[\operatorname{atan}\left(\frac{z_2 + b}{\sqrt{1-b^2}}\right) - \operatorname{atan}\left(\frac{z_1 + b}{\sqrt{1-b^2}}\right) \right]$$

If $b = 1$:

$$f(b) = \frac{1}{z_1 + b} - \frac{1}{z_2 + b}$$

And if $b > 1$:

$$f(b) = \frac{1}{2\sqrt{b^2-1}} \left[\ln \frac{z_2 + b - \sqrt{b^2-1}}{z_2 + b + \sqrt{b^2-1}} - \ln \frac{z_1 + b - \sqrt{b^2-1}}{z_1 + b + \sqrt{b^2-1}} \right]$$

The voltage dependence of GR current roughly follows the voltage dependence of the depletion region, namely $J_{GR-SRH} \sim \sqrt{V}$ for an abrupt junction and $J_{GR-SRH} \sim (V)^{1/3}$ for a linearly graded junction. This is comparatively different than the voltage independent diffusion current in Equation 2.29. The temperature dependence of GR current is also notable, in that it varies as n_i , while diffusion current follows n_i^2 . This makes GR current most pronounced at lower temperatures, giving way to the more

rapidly rising diffusion current as temperature increases. The crossover from GR dominated to diffusion dominated dark current should be considered during a temperature dependent IV analysis.

Direct band-to-band tunneling through a depletion region with a uniform electric field is given by [105]:

$$J_{B2B} = \frac{\sqrt{2m^*} \cdot q^3 \cdot E \cdot V}{h^2 \sqrt{E_g}} \cdot \text{Exp} \left[\frac{-8\pi\sqrt{2m^*} \cdot E_g^{3/2}}{3qhE} \right] \quad (2.33)$$

Likewise, TAT through a mid-gap state located at E_t is given by [111]:

$$J_{TAT} = \frac{q^2 \pi^2 m^* \cdot M^2 \cdot N_t \cdot V}{h^3 (E_g - E_t)} \cdot \text{Exp} \left[\frac{-8\pi\sqrt{2m^*} \cdot (E_g - E_t)^{3/2}}{3qhE} \right] \quad (2.34)$$

where E is the uniform field in the space-charge region, V is the applied bias, M is the matrix element associated with the trap potential, and N_t is the trap density. For convenience, we follow the assumptions of Kinch [38] to simplify the above expressions for B2B and TAT tunneling with $E_t = E_g/2$ as:

$$J_{TAT} = \frac{10^{-13} \cdot N_t \cdot V}{E_g} \cdot \text{Exp} \left[f \cdot \frac{-1.5 \cdot 10^{10} \cdot \pi m_e^{*1/2} \cdot E_g^{3/2}}{\sqrt{N(E_g + V)}} \right] \quad (2.35)$$

$$J_{B2B} = 1.2 \cdot 10^{-2} \cdot V \sqrt{N(E_g + V)} \cdot \text{Exp} \left[f \cdot \frac{-9.43 \cdot 10^{10} m_e^{*1/2} E_g^{3/2}}{\sqrt{N(E_g + V)}} \right]$$

where $m_e^* = 7 \cdot 10^{-2} E_g$ [37], E_g is calculated according to Equation 2.1 in eV, V is the applied bias in volts, N_t is the SRH trap density, and N is the absorber doping level. These expressions qualitatively reproduce the bias dependence of tunneling for abrupt junctions and will be used to obtain satisfactory fitting results. Any overestimations are accounted for by introducing the factor f , which varies between 1-2. As can be seen, doping plays a critical role in determining B2B tunneling currents, and must be kept

low enough to suppress related dark current. Likewise, excessive mid-gap traps increase TAT significantly and must be minimized. It should be noted that in general it is difficult to distinguish between the two forms of tunneling and no attempt will be made here to do so.

The total dark current is simply the sum of all contributing mechanisms. An example in which contributions from all of the expressions above are relevant is represented in Figure 5. As can be seen, diffusion current exhibits voltage-independent reverse bias behavior, while GR goes as \sqrt{V} . Tunneling mechanisms become noticeable at appreciable bias, and are often not observed in well-designed, high quality diodes.

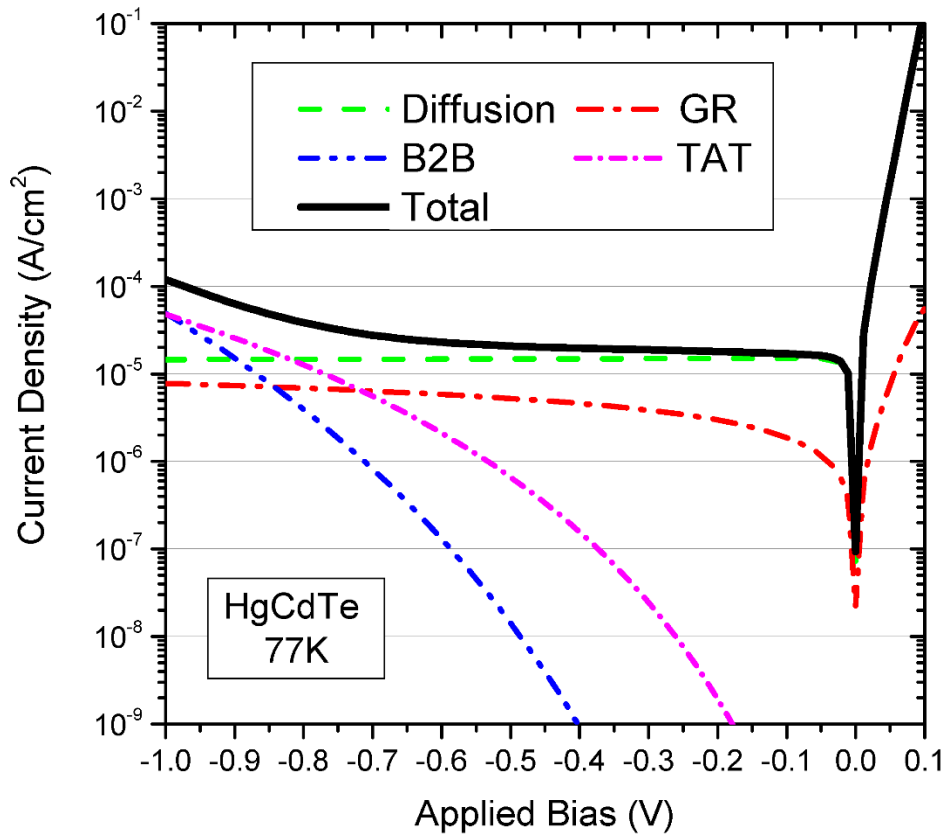


Figure 5: Relevant dark current mechanisms in HgCdTe.

Forward bias characteristics are described by:

$$J_{forward} = A \cdot e^{\frac{qV}{nk_B T}} \quad (2.36)$$

where A is a user determined constant and n is known as the diode ideality factor. An ideality factor $n = 1$ corresponds to diffusion current limited and $n = 2$ for GR current limited, giving insight into the relative contributions present.

A heterojunction consists of two different semiconductor materials, which may not necessarily have the same bandgap, dielectric permittivity, work function, or electron affinity. Analogous diodes expressions pertaining to heterojunctions can be derived accordingly. HgCdTe diodes in this work are based on the P+/n heterojunction design. Here we have used capital letters to designate wider band gap, and (+) to signify much higher doping levels. In the P+/n design, the wider gap P+ cap effectively eliminates thermal dark current contributions from this region, and the doping disparity leads to a depletion region extending only into the lightly doped n -type absorbing base. The corresponding R_oA for an Auger limited lifetime in the n -type base is given as:

$$R_oA = \frac{2k_B T \cdot \tau_{A1}}{q^2 N_d t} \quad (2.37)$$

where N_d is the extrinsic doping and t is the base thickness in μm . This expression is valid for short-based diodes limited by diffusion current at low temperature. The base region is typically doped to $\sim 10^{15} \text{ cm}^{-3}$ levels to suppress tunneling. While an n-on-p design was first demonstrated [112] and offers potential performance benefits, the low p -type doping issues mentioned in Section 2.1.1.7.1, along with difficulty forming ohmic contacts make this configuration less desirable. Wang [113] also showed generally larger R_oA values for P+/n polarity versus N+/p polarity in LW LPE material.

2.1.2 III-V Superlattice

2.1.2.1 Introduction

A wealth of research on the optical and electrical properties of superlattices (SLs) followed their original proposal in 1970 by Esaki and Tsu [114]. The great potential of this material system for IR detectors was quickly realized, due in large part to the unique properties attributable to III-V based SL detectors. This material system offers tremendous flexibility in material combinations as well as device design, and is well suited for absorption across the IR spectrum. Today, SLs are an attractive alternative to incumbent HgCdTe systems, with theoretical performance predicted to exceed that of HgCdTe technologies. Some distinct material advantages of III-V SLs include; suppression of tunneling due to larger effective masses [115], higher lateral growth uniformity, possibility of greatly reducing Auger recombination [116, 117], and better manufacturability and durability. High uniformity and Auger suppression are particularly attractive for LWIR and VLWIR capabilities.

Despite their obviously attractive properties, III-V SL materials suffer from characteristically low lifetimes due to parasitic SRH-centers. Additional problems persist as regards to low mobility, high background carrier concentration, surface leakage currents, passivation, and weak absorption leading to low overall QE. However, many advances have propelled this material system to be a serious contender for use in future IR systems. This section will summarize the fundamental properties of III-V Sb-based SLs, with the emphasis being type-II superlattice (T2SL) properties.

2.1.2.2 Type overview

It is convenient to categorize SL heterostructures according to the respective band alignments of constitute semiconductor materials and carrier confinement schemes. The three basic types of SLs all utilize quantum confinement by introducing alternating thin layers ($<100 \text{ \AA}$) such that energy levels are quantized (1-D) in the growth direction. The SL structure differs from QW or multiple quantum-well (MQW) structures in that the periodicity is short enough that electron wave functions in neighboring wells overlap with one another, forming allowable and forbidden energy bands [114]. To first order, the effective bandgap is then determined by the dimensions of the stacked layers.

The type I SLs, typified by the GaAs/AlGaAs system, consist of approximately aligned nested

bandgaps, with an energy gap given by $\Delta E_g = \Delta E_c + \Delta E_v$. Electron and hole carriers are confined to the same layer. Type I SLs have found application in QWIP PC detectors, but are extrinsic detectors with lower performance than HgCdTe detectors, and therefore not considered in this work.

Type II superlattices (T2SLs) may be either staggered or broken gap alignments. CBs and VBs overlap in adjacent layers, with the energy gap given by $\Delta E_g = |\Delta E_c + \Delta E_v|$. Electrons and holes are confined in different layers, with optical matrix elements dependent on the degree of overlap. In the broken-gap [118] InAs/GaSb system, the InAs CB edge lies below the GaSb VB edge, resulting in electrons confined in the InAs layers and holes confined in the GaSb layers.

Type III SLs were first proposed as IR detectors by Schulman and McGill [119] in 1979 using the HgTe/CdTe system. Layers exhibit different band symmetry, with bandgap decreasing by means of increasing HgTe layer thickness [120]. Electrons are primarily located in the semi-metal HgTe layers but holes are dispersive. Despite the attractive properties of type III SLs, this system will not be considered in this work due to significant interdiffusion [121], rendering them unstable under typical device processing temperatures.

2.1.2.3 T2SLs and fundamental properties

Application of T2SLs for IR detection was met with initial concern over the small optical matrix elements associated with spatially separated carriers [119]. Optical calculations by Chang and Schulman [122] showed the oscillator strength in InAs/GaSb T2SLs was inversely proportional to the product of InAs and GaSb monolayers, as absorption was mainly restricted to near the hetero-interfaces, meaning directly dependent on the number of interfaces. The strained-layer-superlattice (SLS) was proposed in 1987 by Smith and Mailhot [123] by incorporating indium into the GaSb, resulting in tensile-strained InAs and compressive-strained GaInSb layers. InAs/GaInSb SLSs allowed for deeper wells and shorter SL periods, resulting in absorption coefficients comparable to that of HgCdTe [124]. Additionally, strain induced splitting of the light hole and heavy hole bands [125], dramatically reducing Auger recombination rates. Indeed, instrumental theoretical work by Grein et al. [116, 117] showed a 3-5 order

of magnitude reduction of Auger recombination rates in LW InAs/GaInSb SLSs as compared to HgCdTe at the same bandgap, with experimental confirmation shortly thereafter in 1994 [126].

Development of the InAs/Ga(In)Sb SL system has continued since, with large advancements being made concerning proper growth conditions, particularly the advantages of a forced InSb-like interface [127]. High performance FPAs have been reported in the MWIR [128, 129], LWIR [130, 131], and VLWIR [132, 133]. Barrier devices, notably the nBn [134], CBIRD [135], M-structure [136], and W-structure [137], have been introduced to impede excessive SRH-center induced GR and surface leakage while allowing photocurrent signal. While barrier devices have shown improved performance the theoretical potential of T2SLs has yet to be reached.

Research today is focused on improving material properties, such as carrier lifetime and mobility. A recent study by Svennson et al. [138] measured lifetimes in InAs/GaSb T2SLs with the same bandgap but varied the period thicknesses, finding that lifetimes improved as GaSb content decreased, suggesting the culprit native defect was associated with the GaSb layers. This prompted the investigation of InAs/InAsSb SLs (Ga-free SLs) as an alternative material system, and indeed, time-resolved photoluminescence (TRPL) measurements by Steenbergen et al. [139] showed a lifetime > 412 ns for LW Ga-free material at 77 K, a significant enhancement from the ~ 30 ns typically reported [140, 141] in LW InAs/GaSb binary T2SLs. MW InAs/InAsSb lifetimes of ~ 9 μ s have been reported [142], and even more recent work shows a lifetime of 10 μ s by increasing overall Sb content [143]. This represents a vast improvement of roughly two orders of magnitude over binary InAs/GaSb SLs. Still, the origin of the relatively short lifetimes in InAs/GaSb is not clearly understood, and current research is focused on methods of improvement, including residual background concentration reduction through growth methods and post-growth annealing [144-146].

2.1.2.4 Material Properties

The binary zincblende semiconductors InAs, GaSb, and AlSb are an important group of materials

nearly latticed around 6.1 Å. Heterostructures based on the 6.1 Å family are significant today due to their band alignments [147], particularly the InAs/GaSb and InAs/InAsSb systems. AlSb possesses the largest bandgap (~1.6 eV) and alloys such as AlAsSb frequently act as electrical insulators in heterostructures. Compared to II-VI HgCdTe technology, the III-V materials possess smaller lattice constants, and are more mechanically robust due to the more covalent nature of chemical bonds. Superlattice materials are MBE grown at temperatures above 400 °C, and commonly make use of readily available GaSb substrates, but are at times grown on lattice mismatched GaAs [148].

Although general guidelines exist while bandgap engineering (for example, SL designs comprised of (14, 7)-InAs/GaSb monolayers for LW and (8, 6)-InAs/GaSb for MW), the T2SL bandgap must be experimentally determined using photoluminescence (PL) or spectral response data. The bandgap is maximized at zero Kelvin, and decreases with increasing temperature, in contrast to HgCdTe. This temperature dependence may be fitted according to the expressions provided by Varshni [149] and Passler [150]:

$$E_g(T)_{Varshni} = E_0 - \frac{\alpha T^2}{\beta + T} \quad (2.38)$$

$$E_g(T)_{Passler} = E_0 - \frac{\alpha \Theta_p}{2} \cdot \left[\sqrt[p]{1 + \left(\frac{2T}{\Theta_p}\right)^p} - 1 \right] \quad (2.39)$$

where E_0 is the bandgap at zero Kelvin, α , β , and Θ_p are fitting parameters. A fixed value of $\beta = 270$ is used in this work and the Varshni expression will be used unless otherwise specified.

The intrinsic carrier concentration for SL materials is then given by:

$$n_i = \sqrt{N_c N_v} \cdot e^{-E_g/2k_B T} \quad (2.40)$$

$$N_c = 2 \left(\frac{2\pi m_e^* k_B T}{h^2} \right)^{3/2}$$

$$N_v = \frac{4\pi k_B T}{h^2}$$

where N_c and N_v are the effective density of states for a 3-D conduction band and 2-D valence band. The formula for N_v must be divided by the SL period in order to be expressed in the proper units. The dimensionality of the valence band has been shown to be neither 3-D nor 2-D [151], but rather is of a quasi-two dimensional form. The precise behavior may also change with temperature, favoring 2-D behavior at low temperature and more 3-D like behavior at high temperature as more dispersive states become available.

Band structure calculations are performed using the 8 x 8 k·p model software known as Naval Research Laboratory (NRL) BANDS TM [152], which provides effective medium band properties for SL devices, such as in-plane and out-of-plane (z-direction) effective masses and zone center bandgap. SL eigenstates are calculated using the envelop function approximation of z-dependent Bloch waves for a reduced Brillouin zone, and bandgap is taken to be the lowest energy separation between electron and hole sub-bands for both in-plane and z-direction axes.

The derived dispersion relations reveal highly anisotropic hole bands, resulting in differing in-plane and out-of-plane effective masses. Figure 6 shows a nearly dispersionless heavy hole band in the growth (z) direction, leading to very low vertical hole mobility and isolated quantized well states. Depending on design, the CB may lie within the broken gap region, resulting in nearly isotropic bands as tunneling is not required for transport in the z-direction. Alternatively, the CB may lie within the GaSb bandgap, greatly increasing the electron effective mass and exhibiting anisotropic behavior.

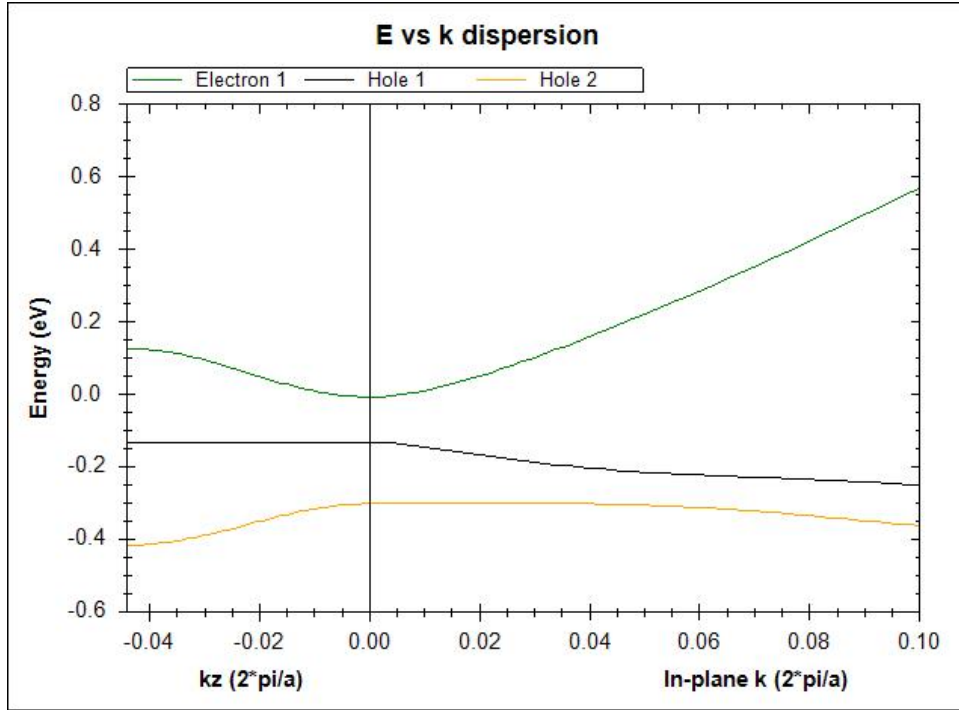


Figure 6: Band structure calculation of LW InAs/GaSb using BANDS along the growth direction (left portion) and in-plane direction (right portion).

The absorption spectrum for T2SLs can also be calculated using NRL BANDS, and characteristically shows softer absorption edges and absorption coefficients in the low-to-mid 10^3 cm^{-1} range. Absorption coefficient measurements may be taken by Fourier transform infrared spectroscopy (FTIR), but care must be exercised in transmission measurements, due to the effects of significant free carrier absorption (FCA) in GaSb substrates[153], as well as absorption in contact and/or buffer layers. Recent reports indicate that absorption coefficients are characteristically weaker in InAs/InAsSb LW T2SLs versus InAs/GaSb [154], resulting in decreased QE.

Lifetime and mobility characteristics follow from the band descriptions outlined above. As previously stated, lifetimes are primarily dominated by SRH recombination. Auger and radiative recombination may also contribute but are generally not limiting in InAs/GaSb [140, 141]. Alternatively, the InAs/InAsSb system lifetime may be influenced by radiative recombination at low temperature in some cases [155], but is too generally limited by SRH recombination [156]. The radiative lifetime

enhancement factor, β , in III-V based materials is much lower in comparison to HgCdTe [47, 157], due in large part to the lower absorption coefficient values.

Mobility values are dependent on transport direction, with in-plane mobility exceeding mobility in the growth direction. The dominant mechanisms for InAs/GaSb SLs are expected to be interface roughness scattering (IRS) [158] at low temperature and optical phonon scattering at higher temperature [159]. It has previously been reported that in-plane mobility limited by the IRS mechanism is proportional to the well width, L , to the sixth power [160]. Persistent-photoconductivity measurements performed on n -type and p -type samples showed that in-plane electron and hole mobility decrease with carrier concentration consistent with IRS limited behavior in InAs/GaSb SLs [161], and further studies have confirmed the dominance of this scattering mechanism in T2SL materials [162, 163].

Theoretical relationships between in-plane and out-of-plane mobilities have been calculated for the InAs/GaSb system [164], and experimental comparisons have also been made [165, 166]. Results show a strong yet complex dependence on the lateral correlation length of interface fluctuations Λ . IRS-limited horizontal mobilities have been shown to be double-valued functions of Λ while the vertical mobilities are monotonically dependent, making it possible to ascertain interface roughness parameters from temperature dependent data [167]. In principle, mobility values will change with specific sample details in question, and no general expressions exist for widespread application.

2.1.2.5 Dark current

The same dark current mechanisms outlined in Section 2.1.1.7.5 apply in T2SL materials, namely diffusion, generation-recombination, trap-assisted tunneling, and band-to-band tunneling. An additional current mechanism associated with surface leakage will be considered for SL material. This is known as shunt current, and will be given according to:

$$J_{shunt} = \frac{V}{R_S \cdot A} \quad (2.41)$$

where R_s is the surface sheet resistance. This form of current may be eliminated in barrier device designs due to the electrically insulating properties of the barrier. An appropriately designed barrier device also has the advantage of reducing SRH-induced dark current and is commonly used today. An example of dark current mechanisms relevant to III-V based SLs is shown in Figure 7.

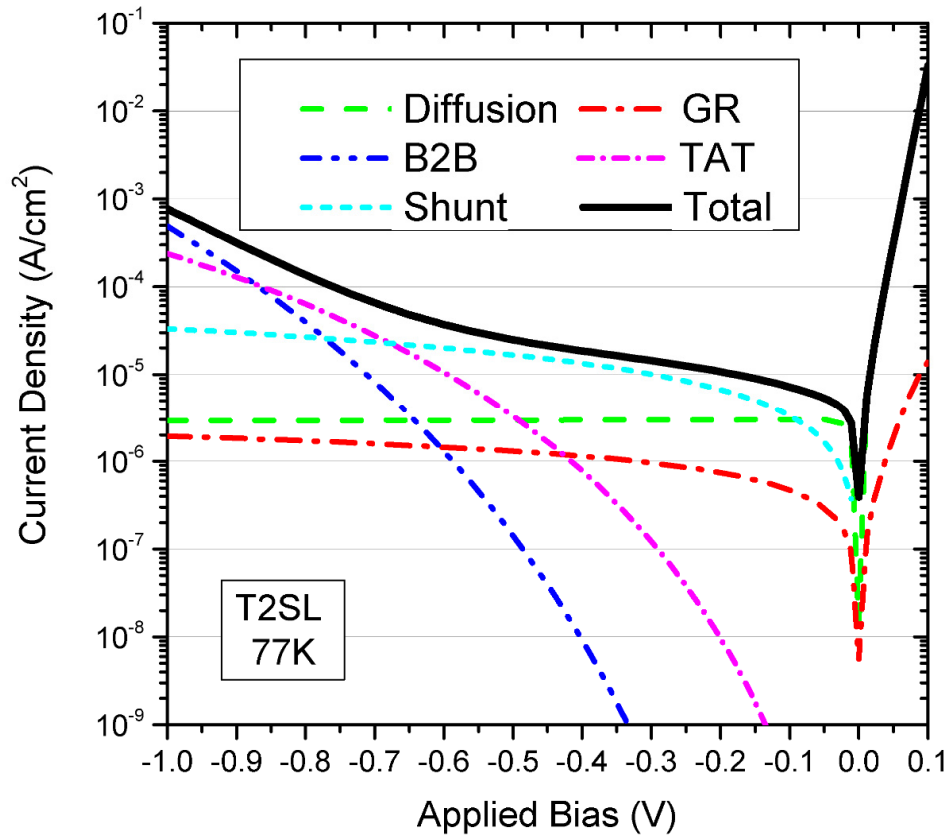


Figure 7: Relevant dark current mechanisms for T2SL diodes.

2.2 Electrical Transport and scattering

This section describes the scattering mechanisms most pertinent to electron and hole majority carrier scattering in *n*-type and *p*-type HgCdTe, respectively. Electron scattering will be determined by considering ionized impurity, polar optical phonon, alloy, neutral impurity, dislocation, and static-strain

scattering. Alternatively, the dominant mechanism for holes in p -type material include ionized impurity (heavy hole) and phonon scattering of the light hole.

2.2.1 HgCdTe electron scattering

2.2.1.1 Ionized impurity scattering

In high quality material, ionized impurity scattering becomes the dominant scattering mechanism at low temperatures for typical doping levels used in n -type HgCdTe. Not only do impurities distort the periodicity of the lattice through the creation of donor-like or acceptor-like bond states, they also influence the electronic behavior of carriers by scattering. Corresponding mobilities decrease with decreasing temperature as a result of a smaller thermal velocity, and thus experience a greater change in momentum during interaction with a charge center.

The potential radius of the Coulombic interaction with a fixed charge center is infinite, and therefore simplifications must be introduced to mathematically treat the scattering cross-section, the most common being the Conwell-Weisskopf (CW) [168] and Brooks-Herring (BH) [169] treatments. In determining transport properties using the Boltzmann transport equation (BTE), the problem reduces to the determination of a transition probability associated with impurity scattering. The Born approximation simplifies the evaluation to the first order of the interaction potential, but is only valid when certain conditions are met, namely that the doping is not excessively high and that the temperature is not extremely low. In the CW treatment, scattering is assumed to take place only between the carrier and the nearest charge center with potential given as:

$$V(r) = \frac{Zq}{4\pi\epsilon r} \quad (2.42)$$

where ϵ is the static permittivity, r is radius of separation, and Z is the charge of the impurity. The CW approximation then utilizes a cutoff radius of influence defined as half the average distance between

impurities. Furthermore, the standard Coulombic scattering cross-section is cut off at a minimum angle since near zero-angle scattering cases are much more likely to interact with other centers, which simplifies divergent integrals in the approach. The relaxation time in the CW treatment is obtained as:

$$\frac{1}{\tau_{CW}} = \frac{NZ^2q^4E^{-3/2}}{16\sqrt{2}\pi\epsilon^2m^{*1/2}} \cdot \ln\left(\csc^2\left(\frac{\beta_0}{2}\right)\right) \quad (2.43)$$

where N is the density of ionized impurities with charge Zq and β_0 is related to the upper bound of the scattering angle integrand. After approximations and plugging into $\mu = \frac{q\langle\tau\rangle}{m^*}$ the CW mobility due to ionized impurity scattering is given by:

$$\mu_{CW} = \frac{128\sqrt{2}\pi\epsilon^2(k_B T)^{3/2}}{\sqrt{m^*}NZ^2q^3} \cdot \left[\ln\left(1 + \frac{144\pi^2\epsilon^2(k_B T)^2}{Z^2q^4N^{2/3}}\right)\right]^{-1} \quad (2.44)$$

The CW treatment received criticism for utilizing cut-off radii and neglecting electron screening effects. Such screening effects reduce the Coulomb potential at greater distances, thus addressing the issue of low-angle scattering. Screening will then depend on the concentration at a distance r, $n(r)$, given by Dingle [170] as:

$$n(r) = \frac{1}{2\hbar^3} \left(\frac{m^*k_B T}{\pi}\right)^{3/2} \mathcal{F}_{1/2}\left(\frac{E_f + qV(r)}{k_B T}\right) \quad (2.45)$$

where E_f is the Fermi energy and $\mathcal{F}_{1/2}$ is the Fermi-Dirac integral of order $1/2$. Following the BH treatment, a screened Coulomb potential is then derived after linearization of Poisson's equation and retaining only first order terms as:

$$V(r) = \frac{Zq}{4\pi\epsilon r} e^{-\beta_s r} \quad (2.46)$$

where β_s is defined as the inverse screening length, typically referred to as Thomas-Fermi screening length, and may be taken as $1/\lambda_D$. The derived mobility of an electron in a non-degenerate gas is found to be:

$$\mu_{BH} = \frac{128\sqrt{2\pi}\epsilon^2(k_B T)^{3/2}}{\sqrt{m^*}NZ^2q^3} \cdot \left[\ln \left(\frac{24m^*\epsilon(k_B T)^2}{nq^2\hbar^2} \right) \right]^{-1} \quad (2.47)$$

which differs the CW expression only in the logarithmic term. It should be noted that both approaches utilize a maximum potential defined at a given distance and fixed for all such distances shorter so as to eliminate an infinite potential as $r \rightarrow 0$. Despite the similarities between the treatments [171], the BH expression has received the most attention in the literature.

Refinements to the BH treatment of importance to HgCdTe include the effects of electron-electron scattering [172] and inclusion of the non-parabolic band structure [173] which act to reduce the mobility calculated by the BH treatment. For the case of Takimoto screening [174], in which the interacting electron subsequently polarizes and weakens the strength of the screening field, modifications can be made to the screening potential used in the BH treatment. However, Takimoto showed that the incorporation of the effect was only considerable for doping greater than 10^{16} cm^{-3} , and thus negligible for typical HgCdTe *n*-type doping levels.

Care must also be taken when considering temperatures below $\sim 25 \text{ K}$, as the Born approximation may no longer be valid. This is typically the case at very low temperatures and or very high doping levels. Strictly speaking, the validity of the Born approximation mandates that the following condition be met [175]:

$$\frac{1}{2} ka_0 \gg 1 \quad (2.48)$$

where $a_0 = \frac{\hbar^2 \kappa_0}{m^* Z q^2}$ is the effective Bohr radius, k is the electron wave vector, and κ_0 is the static dielectric constant. If the Born approximation becomes invalid, the BH treatment could lead to appreciable errors in the mobility calculation. One such recourse is the partial-wave phase-shift technique to more accurately determine transition rates. For the case of HgCdTe, Meyer [54] solved the BTE using Kohler's variational method, which fully incorporates the non-parabolic nature of the band structure and includes inelastic processes as well, which are thought to be of significant importance. In HgCdTe at typical doping levels, Meyer found that the phase-shift analysis agreed with the BH treatment down to temperatures ~ 30 K, at which point the Born approximation was deemed invalid and considerable disagreement was observed, congruent with calculations done by Schenk [176]. To summarize, both studies indicate that the BH treatment should be satisfactory for moderately doped ($10^{14} - 10^{16} \text{ cm}^{-3}$) HgCdTe samples above ~ 30 K, greatly simplifying calculations.

2.2.1.2 Polar optical phonon scattering

The next most significant scattering mechanism in *n*-type HgCdTe is polar optical phonon (POP) scattering, which is likely to dominate at high temperatures. The weak-coupling approximation can be used across the composition range [52]. The longitudinal optical-phonon frequencies of HgCdTe alloys exhibit two-mode behavior associated with CdTe and HgTe modes [54, 177]. Therefore, a weighted contribution of modes must be determined based on composition, which has been shown to vary linearly for values less than $x = 0.5$ [178].

The relaxation time associated with POP scattering is not well defined except for in low ($T \ll \theta$) and high ($T \gg \theta$) temperature limits [173], where θ is the Debye temperature and is around 200 K for HgCdTe. At very high temperatures, average electron energies are high enough to treat the process as

elastic. Alternatively, the very low temperature limit is of little practical importance in this work due to the expected prominence of other scattering mechanisms, namely defect related scattering. The intermediate range of interest makes calculation more difficult as processes must be treated as inelastic. In this case, the electron interaction with the lattice comes in the form of absorption or emission of a phonon of characteristic frequency ν_0 , making it unnecessary to integrate over lattice frequency. Collisions in which energy changes are large must be taken into account via Kohler's variational principle, which also allows the user to specify the desired accuracy of calculations by expansion into higher order terms.

For high desired accuracy, Howarth [179] derived the collision operator using the BTE then applied the Kohler's variational principle to find numeric solutions in a number of cases. For the non-degenerate case the electrical conductivity σ is given as:

$$\sigma = 16a^3 m^* \nu_0 (k_B T)^2 \cdot (e^z - 1) \cdot \frac{G(\xi, z)}{3q^2 \hbar^2} \quad (2.49)$$

where $z = \theta/T$ and $G(\xi, z)$ is a weakly temperature dependent expression given by Howarth.

For non-pronounced interelectronic collisions at low temperature [180], momentum and energy transfer will be transferred to the lattice, and for low-energy the associated mobility may be written as:

$$\mu_{POP} = \sqrt{\frac{k\theta}{2m^*}} \cdot \frac{1}{N_o F_o} \quad (2.50)$$

where $k\theta$ is the optical phonon energy, $N_o = [e^{\theta/T} - 1]^{-1}$, $F_o = \left(\frac{1}{\epsilon_{hf}} - \frac{1}{\epsilon_s}\right)^{-1} \cdot m^* q k\theta / \hbar^2$, and $\gamma_o =$

θ/T with T being the lattice temperature. Discrepancies near room temperature may be expected [181].

Additional phonon scattering, such as acoustic-mode phonon scattering, is negligible for electron due to the s-like symmetry of the wave functions [177].

2.2.1.3 Alloy scattering

Random alloy fluctuations within $\text{Hg}_{1-x}\text{Cd}_x\text{Te}$ are treated as perturbations within the virtual crystal approximation (VCA). The distribution of alloying atoms is averaged into a potential sum over lattice sites with differing atomic potentials. Early on, the initial expressions were formalized by Nordheim [182] and Brooks [unpublished, see 183] for the case of electrons in metals and semiconductors, respectively. The expression derived by Brooks for parabolic, spherical, non-degenerate bands:

$$\mu_{\text{alloy}} = \frac{\sqrt{2\pi} \cdot q \hbar^4 \cdot N_0}{3m^{*5/2} \sqrt{k_B T} \cdot x(1-x) \Delta E^2} \quad (2.51)$$

where N_0 is the density of atoms and ΔE is an adjustable parameter associated with alloy potential fluctuations. There is no clear consensus on the value to be used for ΔE . It is often taken to be the energy band edge difference between HgTe and CdTe (~ 1.5 eV). Calculations using the tight-binding method have revealed this to be an overestimate as Hass [184] arrived at a value of $\Delta E \sim 1.1$ eV, which will be used unless otherwise specified. The Brooks formula above is suitable for MW HgCdTe at reasonable doping levels, but for lower x -values non-parabolic effects may be more pronounced. Although the impact of alloy scattering is significantly lessened by the $x(1-x)$ and m^* terms in the denominator of Equation 2.51, non-parabolic effects may be incorporated following the treatment by Kossut [185].

2.2.1.4 Neutral impurity scattering

Early treatments of scattering via neutral impurities assumed an immersed hydrogen atom within a dielectric medium [186], arriving at a temperature independent relaxation time for low energy electrons. Due to the slight attractive force between the hydrogen atom and a free electron, a weakly bound state was added to the scattering calculation resulting in a $\mu \sim T^{1/2}$ temperature dependence [175] given by:

$$\mu_{neutral} = 0.82 \frac{8\pi\epsilon_s\epsilon_0 E_b}{20N_I\hbar q} \cdot \left(\frac{2}{3} \sqrt{\frac{k_B T}{E_b}} + \frac{1}{3} \sqrt{\frac{E_b}{k_B T}} \right) \quad (2.52)$$

where N_I is the density of neutral impurities and E_b is the binding energy. A more recent calculation using phase shifts calculated between electrons and neutral hydrogen atoms removed approximations from earlier treatments, ultimately finding the treatments to be equivalent at higher temperatures [187]. Overall, neutral impurity scattering is not considered to be pronounced at any temperature for HgCdTe material.

2.2.1.5 Dislocation scattering

It is known that edge and screw dislocation lines produce large lattice distortions in diamond and zincblende semiconductors. Much work has been done on the electrical impact of dislocations, particularly in III-V materials [89, 188]. This mechanism has been important in understanding mobilities in a number of materials and particularly important for materials with low electron effective masses, such as in InAsSb [189].

Dislocations are often described as cylindrical acceptor centers embedded within semiconductor materials. For dislocations with an edge component, dangling bonds along the dislocation are introduced. Subsequently, electrons are attracted to the surrounding area until a space charge region is formed. The resultant potential field then interacts with free electrons in the material and may affect carrier mobility if dislocation density is high.

Scattering via dislocation lines is very directionally dependent, strongly affecting carriers moving perpendicular to the line while having little to no effect on parallel currents. At large distances the screened potential from a dislocation line was determined to be [190]:

$$V(r) = \frac{qf}{2\pi\epsilon d} K_0\left(\frac{r}{\lambda_D}\right) \quad (2.53)$$

where d is spacing between broken bonds, f is the occupation rate, K_0 is the modified Bessel function of zero order, and λ_D is the screening parameter given as $\lambda_D = \sqrt{\frac{\epsilon k_B T}{q^2 n'}}$ with $n' = n + (n + N_a) \left[1 - \frac{(n + N_a)}{N_d}\right]$.

The distance d may be taken to be on the order of the lattice parameter, or in the case of (211)B HgCdTe a value between 6.45-10 Å may be used. After appropriate distribution averaging, an expression for the mobility has been determined to be [191]:

$$\mu_{dislocations} = \frac{30\sqrt{2\pi}\epsilon^2 d^2 (k_B T)^{3/2}}{N_{disl} q^3 f^2 \lambda_D \sqrt{m_e^*}} \quad (2.54)$$

where N_{disl} is the dislocation density perpendicular to electron motion (may be taken as conventional EPD). The functional dependence follows a $\mu \sim T^{3/2} m^{-1/2}$ behavior.

For HgCdTe material, dislocation etching is common practice, making N^{disl} readily determined. The radius of the space charge region using typical HgCdTe doping is $< 1 \mu\text{m}$, meaning nearest dislocation lines are not expected to overlap for EPD values less than 10^8 cm^{-2} . As dislocation etching is common practice, the remaining unknown parameter is the occupation rate f , which has previously been taken as $f = 0.05$ for LW HgCdTe [192], unity in InAsSb [189], and $\sim 0.4-0.6$ for GaN [193]. For this work, we model a shallow acceptor trap with energy $E_t = 5 \text{ meV}$ and employ the minimization of free energy approach given by Weimann [193]. For $N_d = 2 \times 10^{15} \text{ cm}^{-3}$ and $N_{disl} = 10^6 \text{ cm}^{-2}$, occupation fractions of $f(\text{LW}) = 0.101$, $f(\text{MW}) = 0.171$, and $f(\text{SW}) = 0.282$ are obtained. The temperature dependence of f is seen to be weak, in agreement with previous findings.

2.2.1.6 Strain field scattering

It is ultimately the piezoelectric coupling coefficient e_{14} which will dictate the importance of this mechanism. CdTe has a reported value of $e_{14} \sim 0.034 \text{ C/m}^2$ [194], while LW HgCdTe has been measured using a cantilever beam technique to be 0.0136 C/m^2 [195]. As expected, the piezoelectric constant decreases with x-value as the material becomes less polar.

Scattering occurs in two forms. First, the partially ionic bonds in HgCdTe produce polarization associated with acoustic phonons. Carriers then interact with the dipole field produced, known as piezoelectric scattering. Alternatively, point defects producing localized lattice strain in zinc-blende semiconductor materials may scatter carriers due to piezoelectric potential fields, which will be referred to as strain scattering. The orientation and size of strain centers will play a heavy role in determining the overall strength of this scattering.

In this work we will only consider strain scattering, as piezoelectric scattering has been shown to be negligible in HgCdTe [52], largely due to the small coupling constant. Since point defects come in many forms, the expressions of Fedders [196] will be used for HgCdTe with excessive defects. The dependence is of the form $\mu \sim T^{1/2} \left[m_e^{3/2} e_{14}^2 N_s \beta \right]^{-1}$ where N_s is the density of point defects and β is associated with the scattering strength of those strain centers. The product $N_s \cdot \beta$ can be taken as a fitting parameter.

There is, however, very little information concerning static strain fields in HgCdTe, but electronic properties of III-V materials have been influenced by this scattering. Overall, strain scattering is expected to be a minor mobility correction for HgCdTe samples in this work.

2.2.2 HgCdTe hole scattering

The scattering mechanisms of the heavy and light holes in HgCdTe will be outlined in this section. There is considerably less work in the literature on the subject. Expressions for alloy disorder, static strain, and polar-optical scattering follow from the preceding section on electron scattering rates

with the appropriate effective mass and crystal potential fluctuation (ΔE_v) corrections.

Band-structure calculations of ΔE_v predict values < 0.1 eV [184], but theoretical mobilities were much higher than those measured [197]. Improved agreement with experiment [198] was achieved after incorporating the natural valence-band offset between HgTe and CdTe [199] with $\Delta E_v = 0.3-0.35$ eV and including static strain scattering to account for the temperature dependence of mobility [64, 197]. It remains unclear if the discrepancy between theory and experiment can be attributed to the calculation of ΔE_v , or m_{hh} .

Ionized impurity scattering is generally dominant in heavy holes, except for at high temperatures where polar-optical scattering may become important. The light hole is largely determined by acoustic phonon scattering but also experiences scattering contributions from ionized impurities, strain, and polar-optical phonons.

2.2.2.1 Ionized impurity scattering

Ionized impurity scattering of majority carrier holes follows the same screened Coulomb potential outlined above. For a doubly-ionized acceptor in HgCdTe, the Debye screening length takes the form:

$$\frac{1}{\lambda_D^2} = \frac{q^2}{\epsilon_s \epsilon_0 k_B T} \left[p + n - N_{a(-)} + \frac{(N_{a(-)} + 2N_{a(--)}) \cdot (N_{a(-)} + 2N_{a0})}{N_a} \right] \quad (2.55)$$

where $N_a = N_{a(-)} + N_{a(--)} + N_{a0}$ is the total concentration with $N_{a(-)}$, $N_{a(--)}$, N_{a0} being the singly ionized, doubly ionized, and neutral states, respectively. The effective concentration of impurities follows is then given as:

$$N_{eff} = \sum_j Z_j^2 N_j \quad (2.56)$$

which simplifies when only singly ionized acceptors are present but can also be used to treat the more general case of both single ($Z = 1$) and doubly ionized ($Z = 2$) states. The Fermi energy is calculated after Yadava [64], in which the doubly ionized vacancy acceptor model is solved using fourth order polynomial expressions described in Appendix A therein. The model can be simplified to accommodate a monovalent acceptor state with characteristic ionization energy, as is the case for As-doped HgCdTe. The mobility expression for ionized impurity scattering is given by Yadava [64] as:

$$\mu_{ll,h} = \frac{256}{9} \cdot \sqrt{\frac{2}{\pi}} \cdot \frac{\varepsilon_0^2 \varepsilon_s^2 (k_B T)^{3/2}}{q^3 \sqrt{m_{hh}^*/m_0} N_{eff}} \cdot \int_0^\infty \frac{y^3 e^{-y}}{F_{hh}^{intra} + b F_{hh}^{inter}} dy \quad (2.57)$$

$$F_{hh}^{intra} = (2 + Y) \ln \left(\frac{Y}{4 + Y} \right) + \frac{32}{3Y(4 + Y)} + 4$$

$$F_{hh}^{inter} = \frac{1 + Y + b^2}{b} \ln \left(\frac{Y + (1 + b)^2}{Y + (1 - b)^2} \right) - 4$$

where $F_{hh}^{inter, intra}$ refer to intra- and inter-valence scattering rates, respectively, and $Y = \hbar^2/2m_{hh}\lambda_D^2 k_B T y$, $y = \epsilon/k_B T$, and $b = \sqrt{m_{lh}/m_{hh}}$.

2.2.2.2 Acoustic phonon scattering

After considering intra- and intervalence transitions [200], the mobility of the light hole due to acoustic phonon scattering is readily written as:

$$\mu_{AC} = \frac{4q}{3m_0\sqrt{\pi}} \cdot \frac{\rho \bar{v}}{E_{AC}^2 T^{3/2} (m_{hh}/m_0)^{5/2} (1+b^4)} \quad (2.58)$$

where $b = (m_{hh}/m_{lh})^{1/2}$ in this expression, ρ is the mass density, \bar{v} is the average velocity of sound in the material, and E_{AC} is the acoustic deformation potential, which may be quite different than the deformation

potential for the heavy hole and is roughly ~ 13 eV.

2.2.3 III-V superlattices – interface roughness scattering

Small fluctuations in the uniformity of layer widths vary the associated electronic energy levels of a SL structure. Roughness on the order of only a monolayer can lead to appreciably strong scattering, making interface roughness scattering (IRS) the primary mechanism limiting mobility in SL structures for IR detection at typical operating temperatures [162].

For the case of electrons confined within a thin (<100 Å) quantum well with infinite barrier height, the in-plane mobility depends critically on the well width, a , as $\mu \sim a^6$ [158]. The classic $\mu \sim a^6$ dependence is successfully recovered in wide-gap systems such as GaAs/ $\text{Al}_{(x)}\text{Ga}_{(1-x)}\text{As}$ [160] and has also been observed in HgTe-CdTe [159] and InAs-AlSb [201] systems containing sufficiently thick barriers.

However, the classic a^6 dependence is not always experimentally observed. As Meyer [159] points out, modifications are required when modeling narrow-gap heterostructures due to strong interactions between bands. This is specifically true in SLs designed for IR application in which thin wells and thin barriers are often present, making IRS sensitive to variations in both, but also via introducing the possibility of electron wave function penetration across barriers. This penetration, or leakage, is believed to be the cause of less rapid dependences on well width observed in InAs/ $\text{Ga}_{(1-x)}\text{In}_{(x)}\text{Sb}$ ($\mu \sim a^{2.4}$) [162], GaAs- $\text{Al}_{(x)}\text{Ga}_{(1-x)}\text{As}$ ($\mu \sim a^{3.4}$) [202], and AlAs/GaAs ($\mu \sim a^{4.7-4.8}$) [203]. It is not entirely clear if leakage is solely responsible for the decreased dependence or if it is rather a combination of effects, such as substrate choice, absorber doping, strain, alloy scattering in the barrier, and other possible complications.

Still, the assertion that IRS dominates low temperature mobility in SL structures is undisputed. In fact, a recent study of InAs/GaSb in-plane mobility concluded that MW and LW structures were not only limited by IRS, but that the mobility dependence on InAs well width followed the classic $\mu \sim a^6$ behavior [163]. It appears that the quantitative dependence on well width should be considered on a case by case basis, but IRS will ultimately determine the in-plane mobility of SL structures in this work.

The relationship between horizontal (μ_{\parallel}) and vertical (μ_{\perp}) mobilities in InAs/GaSb have been modeled [164, 167] and determined experimentally [165, 166, 204]. The results indicate significant anisotropy, with electron horizontal/vertical mobility ratios typically ranging from ~ 2 -5 depending on material properties.

Changes in the confinement energy are characterized by a lateral correlation length, Λ , and by the height of roughness fluctuations, Δ . Finally, the general mobility expression is written as:

$$\mu_{IRS}^{-1} \sim g(\Lambda, A) \Delta^2 A \Lambda^2 \left(\frac{\partial E}{\partial a} \right)^2 \quad (2.59)$$

where A is the SL period width, a is the well width, g is a function incorporating screening effects and relating electron wavelength and correlation length, and E is the electron energy.

2.3 Hall and Mobility Spectrum analysis

Hall measurements are routinely used to determine resistivity, carrier concentration, and mobility in semiconductor materials. The characterization is widely used in the field to monitor growth quality and determine conductivity type. In fact, in a 1993 MCT industrial survey, Hall effect measurements were deemed to be the second most important and third most frequently used measurement out of 72 techniques under consideration [205].

The Hall effect, discovered in 1879 by Edwin Hall [206], is a direct result of the Lorentz force, given by:

$$F = q(\bar{E} + \bar{v} \times \bar{B}) \quad (2.60)$$

in which charge carriers experience a force when moving in the presence of a perpendicular component in

magnetic field. Subsequently, in an appropriate Hall measurement, charge carriers of differing signs within a conductor will accumulate on opposite sides of the material, giving rise to a voltage difference known as the Hall voltage. The Hall coefficient, R_H , is then defined as the ratio of electric field across the sample to the perpendicular current density magnetic field product. In the typical experimental setup this can be written as:

$$R_H = \frac{E_y}{J_x B_z} \quad (2.61)$$

In 1948, van der Pauw derived expressions for the resistivity, mobility, and carrier concentration utilizing four contacts on an arbitrarily shaped thin electrical conductor [207]. The derivations required sufficiently uniform thickness across the sample, and the absence of any non-conductive regions. Contacts were to be placed on the perimeter and made as small as possible, as non-infinitesimal contact size is a major proponent in the introduction of measurement error. The resistivity can then be written as:

$$\rho = f \cdot \frac{\pi t}{\ln(2)} \cdot \frac{R_{12,34} + R_{23,14}}{2} \quad (2.62)$$

$$R_{AB,CD} = \frac{V_D - V_C}{I_{AB}}$$

where the notation $R_{AB,CD}$ indicates current measured between contacts A and B and voltage measured across contacts C and D. The form factor f , is a function of the resistance ratios using different contact configurations. The form factor is determined by a transcendental equation, and depends on sample uniformity and symmetry. Form factor values range from 0 - 1, with highest precision measurements obtained at $f = 1$. Carrier concentration and mobility can be determined from the following equations:

$$V_H = \frac{V_{13} + V_{31} + V_{24} + V_{42}}{8} \quad (2.63)$$

$$n = \frac{IB}{qt|V_H|}$$

$$R_H = \frac{1}{qn}$$

$$\mu = \frac{|R_H|}{\rho}$$

where V_{AB} denotes the difference in Hall voltage across A and B measured under different polarity. The sign of R_H is then indicative of the conductivity type. If sample thickness is known, bulk concentration and resistivity values may be calculated, otherwise only sheet values will be obtained. To reduce error, all measurements are taken at positive and negative magnetic fields and current biases, as well as averaged between the two configurations. Agreement between measurements must be monitored to assure sample and processing are sufficiently homogenous.

2.3.1 Mobility spectrum analysis

Single-field measurement using the van der Pauw technique is adequate when a single carrier dominates conduction within a sample. In this case, a single carrier species with a particular mobility and concentration may be resolved at any non-zero magnetic field, as the quantities will be field-independent. In practice, this simplified approach is rarely adequate, and care must be taken if interpretation from a single magnetic field is utilized. Mobility and carrier concentration much more commonly exhibit magnetic field dependence, indicating the presence of more than a single carrier species. Therefore, a more robust analysis becomes necessary to extract the appropriate parameters in the presence of mixed conduction.

Mixed conduction effects have long been discussed in the literature. Anomalous Hall effects, surface conduction, interface contributions, and parallel conduction are amongst the topics receiving attention over the years. A number of layer models have been introduced to better analyze experimental

data in the presence of multiple carriers [208, 209], but typically only address a number of complicating factors, thus limiting their scope.

A much more robust and elegant approach was introduced by Beck and Anderson [210] to indiscriminately analyze magnetic field-dependent Hall data using expressions that relate ρ and R_H to the longitudinal and transverse elements of the conductivity tensor σ_{xx} and σ_{xy} . For a Hall sample the relation is given as:

$$R_H(B) = \frac{\sigma_{xy}/B}{\sigma_{xx}^2 + \sigma_{xy}^2} \quad (2.64)$$

$$\rho(B) = \frac{\sigma_{xx}}{\sigma_{xx}^2 + \sigma_{xy}^2}$$

The technique harnesses the magnetic field dependence of the conductivity tensor elements, writing them as an integral over a continuous conductivity density functions $S_n(\mu)$ and $S_p(\mu)$:

$$\sigma_{xx}(B) = \int_0^\infty \frac{S_p(\mu) + S_n(\mu)}{1 + (\mu B)^2} \cdot d\mu \quad (2.65)$$

$$\sigma_{xy}(B) = \int_0^\infty \frac{(S_p(\mu) - S_n(\mu)) \cdot (\mu B)}{1 + (\mu B)^2} \cdot du$$

where $S_n(\mu) = qn(\mu)\mu$ and $S_p(\mu) = qp(\mu)\mu$ are the conductivity density functions for electrons and holes, respectively, and contain the concentration density functions $n(\mu)$ and $p(\mu)$. Experimental measurements do not uniquely define $S_{n,p}(\mu)$, but rather a unique envelope (or upper-bound) containing only physical sets of solutions can be obtained.

Changes to the initial model proposed by Beck and Anderson were made by introduction of a discrete grid of mobility points [211]. In this approach the tensor elements are written as:

$$\sigma_{xx}(B_j) = \sum_{i=1}^m \frac{S_p(\mu_i) + S_n(\mu_i)}{1 + (\mu_i B_j)^2} \cdot \Delta\mu_i \quad (2.66)$$

$$\sigma_{xy}(B_j) = \sum_{i=1}^m \frac{[S_p(\mu_i) - S_n(\mu_i)] \cdot \mu_i B_j}{1 + (\mu_i B_j)^2} \cdot \Delta\mu_i$$

For this approach, the envelope function acts as a trial function and solutions are obtained using the Jacobi iterative procedure in order to find the spectra with the best fit to experimental data at all magnetic field points. A number of refinements, such as the introduction of pseudo-data through splining, the separate alteration of electron and hole spectra, and the minimization of error with regards to the derivative of the conductivity tensor, have been made in order to eliminate unphysical erroneous artifacts and ultimately boost resolution [212-214].

The fitting of experimentally determined σ_{xx} and σ_{xy} in this model allows the treatment of multiple bands in addition to non-parabolic effects. A notable feature of this approach which makes it favorable over preceding models is that no assumptions about the type or number of carriers are required. The experimental data is first converted into the appropriate input format and analyzed accordingly. Distinct carriers readily manifest as conductivity peaks when plotting conductivity as a function of mobility, making the method of carrier identification intuitively straight-forward. Such a technique is commonly referred to as mobility spectrum analysis (MSA).

In essence, the accuracy of the model depends on measurement limitations, which include measurement error and maximum magnetic-field strength, but also on the sophistication of the fitting algorithm. The mobility spectrum analysis technique has found application in a multitude of research fields due to its flexibility and potential to extract information from a wide variety of structures.

3. Experimental

This chapter will describe the primary equipment and experimental procedures most pertinent to this work. A large focus will be placed on variable-field Hall measurement, including sample preparation specifics. Additional characterization techniques will be outlined and procedural information given.

3.1 Hall measurement

3.1.1 Systems

Hall measurements are taken on one of three systems: a commercial MMR technologies system, Ecopia HMS-3000, or Lakeshore 9509 HMS. The MMR system has a constant field of 0.34 T and is capable of temperature control between 77 K and room temperatures. Alternatively, the Ecopia HMS-3000 has a permanent magnet of fixed strength 0.55 T but measurements are only taken at either 77 K or room temperature. The Ecopia and MMR systems are used primarily for their speed and ease of operation, often as a means of verification or quality control while more detailed measurements are taken on the Lakeshore 9509 HMS, which is shown in Figure 8.



Figure 8: Lakeshore 9509 HMS.

The only system with variable-field capability is the Lakeshore 9509 HMS. The system dewar hosts a custom superconducting solenoid magnet provided by American Magnetics, Inc. The magnet consists of fine niobium-titanium and niobium-tin filaments wound tightly around its core and embedded in a copper matrix. Protective over-wrapping plus a combination of electrical insulation and epoxy ensure the windings are stable and protected. The solenoid is immersed in liquid helium during operation with sample insert module placed along its central axis.

The field strength has a rated field ranging from 0 to 9 T, and is controlled via a Lakeshore 620 magnetic power supply (MPS) using the calibrated field/current ratio of 2029.3 Gauss/Amp. Magnetic field is ramped using a predetermined charging voltage to reduce the risk of stress or other malfunctions, taking roughly 10 minutes to ramp all the way up to 9 T. A calibrated field strength measurement along the central axis is shown in Figure 9, revealing a +/- 0.1 % homogeneity over 6 cm. Protective diode caps on the magnet circuit act to reduce the risk of damage associated with magnet quenching. Additional precautions are programmed into the MPS to more safely drain the magnet in the event of a quench. The MPS is run through an APC Smart-UPS 3000 XL to protect the magnet from surges or sudden power

loss.

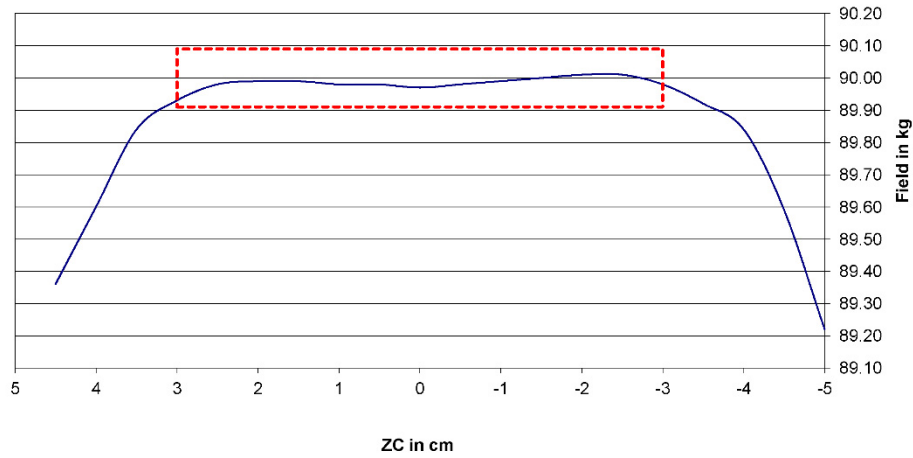


Figure 9: Magnetic field plot of superconducting solenoid magnet used in Lakeshore 9509 HMS. Measurement shows $\pm 0.1\%$ homogeneity across 6 cm on central axis.

The sample insert module is shown in Figure 10, and supports a maximum sample size of $\sim 13 \times 15$ mm. Samples are mounted on a non-conductive sapphire plate using Apiezon N Cryogenic high vacuum grease. With 6 contact posts, measurements can be made using either the Hall bar or van der Pauw configuration. The 6 posts lead to triaxial connectors which run to a Keithley 7001 switch matrix. The custom electrical setup consists of two 6514 Keithley electrometers, one 6485 Keithley picoammeter, one Keithley 220 programmable current source, and one 2182 Keithley nanovoltmeter. An IEEE-488 bus connects all electrical equipment to an external computer for automated control.

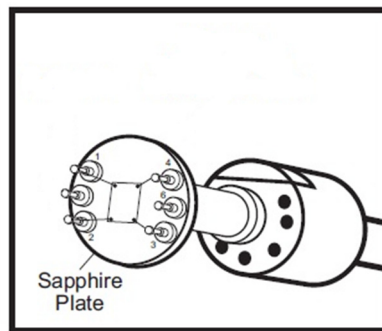


Figure 10: Sample mounting for 9509 HMS.

The system dewar contains a 40 L belly to reservoir liquid helium during measurements. The liquid helium level is monitored using a Lakeshore 241 which has a superconducting sensing element. Pre-cooling with liquid nitrogen greatly reduces the amount of liquid helium needed in order to fill the system.

A needle-valve between the helium reservoir and sample space regulates a small amount of gas flow from helium blow-off. The sample space is pumped through a solenoid valve assembly attached to an Agilent Technologies DS-402 rotary vane pump. The sample temperature range is as low as 2 K and as high as 400 K and controlled using the Lakeshore 340 temperature controller. The controller balances the regulated helium gas flow with two sensor readings that couple to resistive heating elements. The two sensor and resistor combinations are located on the backside of the sapphire mounting plate and right below a temperature block located midway along the sample insert stem. Temperature control in the system is very precise but long settle times are typically required to ensure equilibrium has been reached.

3.1.2 Considerations (uniformity, geometry, contacts)

The information you extract using MSA can be viewed as an alternative expression of experimentally obtained data, implying that the integrity of extracted parameters depends directly on measurement quality. Therefore, all efforts should be focused on eliminating or reducing errors to maximize resolution. For van der Pauw test structures, the primary sources of error have been shown to be non-ideal contacts and sample non-uniformity [207, 215, 216].

The van der Pauw technique requires four sufficiently small ohmic contacts to be placed on the perimeter of the test structure. Linear IV characteristics are used to verify contacts are ohmic and systematic offsets in voltmeter and current meters readings are eliminated using current reversal. Oftentimes, the most unwanted source of measurement error is a misalignment voltage, or non-zero Hall voltage at zero magnetic field. This, too, can be eliminated by taking measurements utilizing two Hall

configurations and current reversal. In fact, implementing current reversal, field reversal, and both Hall configurations removes many intrinsic sources of error, such as thermoelectric voltage effects, Ettingshausen effect voltages, and Nerst effect voltages, and are therefore utilized for all measurements in this work.

Contact quality is not the only concern, as contact size and placement can also have a large impact on measurement quality. As van der Pauw showed, the impact of non-infinitesimal contacts can be alleviated with sample patterning [207]. Even a simple square geometry with corner contacts can greatly reduce the impact of contact placement and size [215, 216]. The exact sample geometry is user chosen, with many variations implemented over the years.

Unfortunately, patterning has the potential to enhance the impact of sample non-uniformities. This is largely due to the fact that sample patterning reduces the physical area under test. Depending on geometry and location, fluctuations in resistivity and thickness may be over or under represented when averaging across a test structure. Since measurement will be skewed towards regions experiencing higher electric field, any fluctuations in those regions can have a considerable impact on measurement integrity. Most structures are designed to reduce contact effects by focusing on a smaller, centralized test area, and in the process eliminate deleterious contact effects. To highlight the effects of sample patterning, Figure 11 shows simulated voltage contour lines and current density of a patterned structure. As can be clearly seen, patterning reduces the sample area under test considerably while substantially increasing current density in some regions. Non-uniformity in these areas must be handled with care, and low biases must be chosen to avoid Joule heating in regions of high current. If sample resistivity is known, current is often chosen so power dissipation is $\sim 1\text{mW}$ or less.

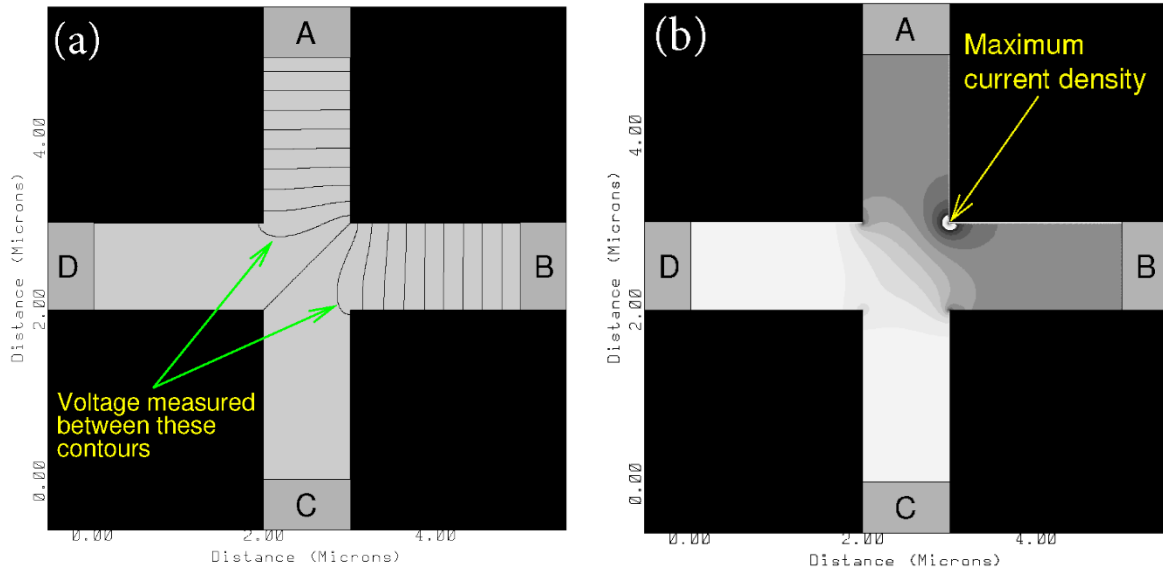


Figure 11: Voltage (a) and current density (b) of patterned test structure (Greek cross), simulated using finite difference method to solve Poisson's equation across grid. Voltage at terminal A is 1 V and terminal B is 0 V. Contour line spacing in (a) is 50 mV. [217]

3.1.3 Sample test

To better understand the impact of contacts, geometry, and non-uniformities, a series of LPE p -on- n MW HgCdTe samples were fabricated to investigate sample preparation. LPE samples were chosen since the high lateral growth uniformity best matches the assumptions of the van der Pauw method. The p -type layer better replicates future experiments that will undoubtedly contain p -type layers, traditionally more difficult when it comes to ohmic contact formation. In initial testing, combinations of Ag, Pt, Ti, In and Au were deposited on p -type single-layers to assess contact quality. It was found that Au was the most suitable, and that In worked quite well if the layer was sufficiently doped. Figure 12 shows the ohmic IV characteristics of In contacts on a $\sim 10^{17} \text{ cm}^{-3}$ As p -type HgCdTe sample at 80 K.

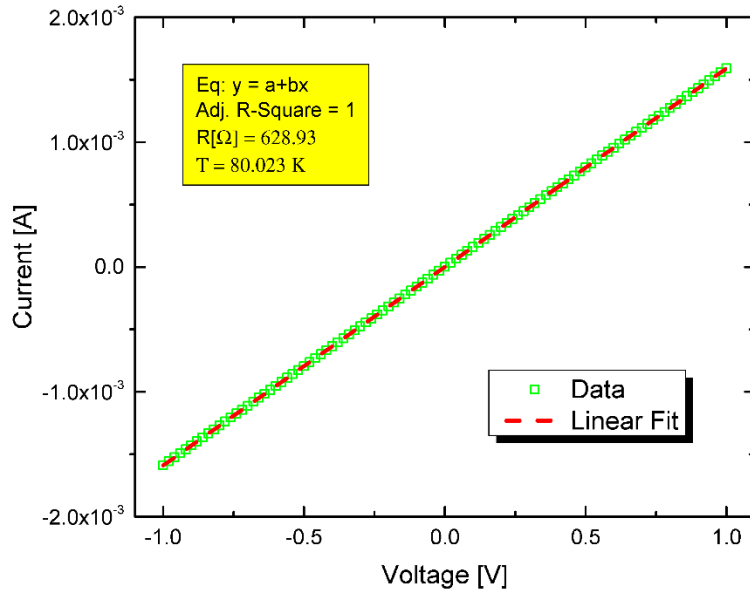


Figure 12: IV characteristics of In contacts on *p*-type HgCdTe single layer showing ohmic behavior at 80 K.

The test structures investigated are shown in Figure 13. Initial testing showed inconsistent patterning results for all structures except the square and Greek cross structures, possibly related to processing error. Since reproducible results were obtained for square and Greek cross structures (structures 1 and 2 counting from left to right in Figure 13), we will continue with these geometries.

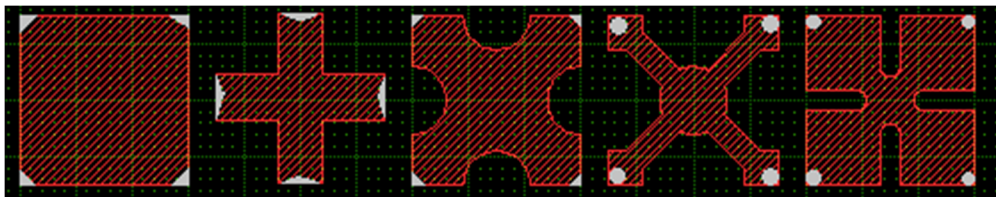


Figure 13: Initial Hall test structures during testing. Grey areas indicated contact areas.

The Greek cross initially emerged as feasible in terms of processing and effective in terms of error reduction. The critical dimensions of the Greek cross, shown in Figure 14, are the arm length, A , and the arm width, S , with error being proportional to the ratio A/S . Numerical calculations show that the normalized sheet resistance error, E , for a Greek cross structure is given as [218]:

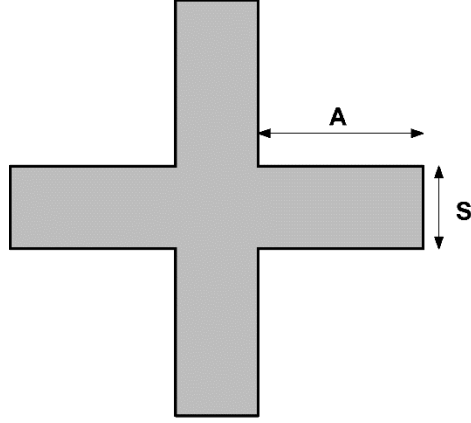


Figure 14: Greek cross structure with critical dimensions of arm length, A, and arm width, S.

$$E = 1 - \frac{\rho_0}{\rho} = (0.59 \pm 0.006) \cdot \exp\left[-(6.23 \pm 0.02) \cdot \frac{A}{S}\right] \quad (3.1)$$

where ρ_0 represents the actual resistivity. Equation 3.1 gives an error of approximately 0.1% for an A/S ratio of 1. It is generally recommended that $A/S > 2$, which is easily fabricated with modern processing techniques. Further calculations by de Mey [219] have shown that the associated error in mobility is given as:

$$\frac{\Delta\mu}{\mu_0} \cong 1.045 \cdot \exp\left[-\pi \cdot \frac{A}{S}\right] \quad (3.2)$$

To assess which geometry and contact methods perform best, we look at correction factor, f , the Hall coefficient difference between two configurations, and the parameters extracted from MSA. The correction factor, f , is a function of the ratio $R = R_{12,34}/R_{23,41}$ and can be found by solving the following transcendental equation:

$$\frac{R-1}{R+1} = \frac{f}{\ln(2)} \cosh^{-1} \left\{ \frac{1}{2} \exp \left[\frac{\ln(2)}{f} \right] \right\} \quad (3.3)$$

Plotted in Figure 15 is the correction factor, f , as a function of $R_{12,34}/R_{23,41}$. The correction factor is indicative of sample uniformity and geometrical symmetry. Best results are obtained when $R = 1$ and $f = 1$. Ideally, measurements should only be taken when $f > 0.9$.

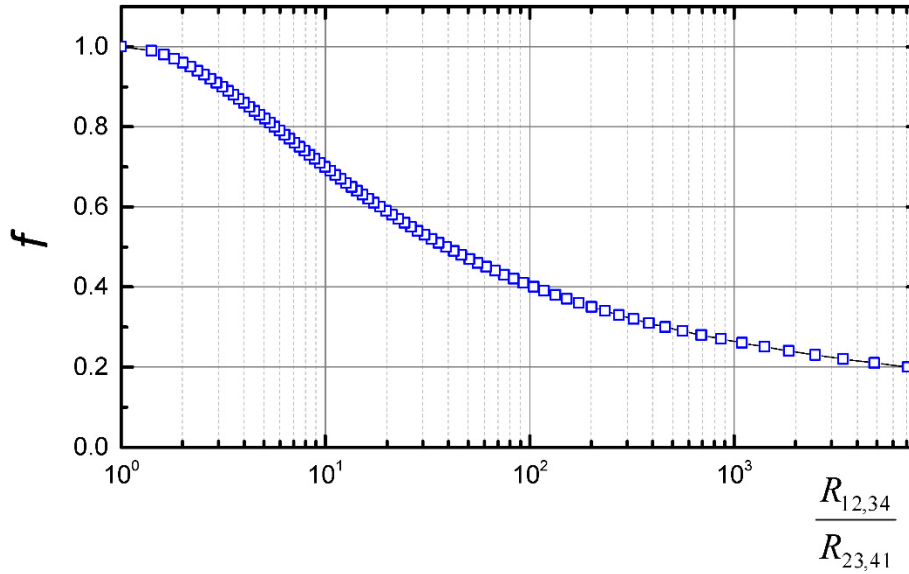


Figure 15: Correction factor vs resistance ratio. Values of f below 0.9 typically indicate a measurement error.

For a p-on-n structure, lateral contacts are preferred over top surface contacts so the equivalent circuit diagram contains fully connected layers in parallel, thus each layer is biased to the same degree [220]. This can be accomplished by scribing the sample or employing an over-the-side contact method. The challenge is finding a suitable technique for ohmic contacts on layers of both carrier type over a range of experimentally common x -values and doping concentrations.

As previously stated, we find that Au contacts are most reliably ohmic for p -type HgCdTe samples. A natural and ubiquitous choice for n -type HgCdTe is In, which can be soldered or wire-bonded. For highly doped p -type samples, In was found to be suitable for ohmic contacts. This makes In a particularly enticing option if ohmic contacts can be routinely formed on both n -type and p -type layers of the p-on-n structure. In this work, soldering temperatures are kept at a minimum to reduce in-diffusion or

material damage. Wire-bonding was performed on a K&S Model 4522 manual bonder with Leica S6 optical system attachment. Bonding settings are tailored for either HgCdTe or III-V material.

Four samples from the LPE MW HgCdTe p-on-n sample are prepared and summarized in Table II, with sample identifiers T1, T2, T3, and T4. Over-the-side contacts were accomplished on the square sample, T1, with electron beam deposition and can be seen in Figure 16. For this sample, T1, line of sight allowed for adequate sidewall coverage, followed by top-surface wire-bonding. The H_{Au}Cl₄ contacts of sample T2 are deposited in liquid droplet form, leaving a thin layer after evaporation. Cross structures T3 and T4 accomplished over-the-side contacts via soldering. All samples experienced identical post-growth arsenic activation (~ 9 minutes at 400 °C) and vacancy reduction (~ 24 hours at 233 °C) annealing under Hg overpressure. Brief etching in dilute 0.15% Br/MeOH solution was utilized to remove the native oxide layer prior to contact formation.

Cross structures T2, T3, and T4 have an A/S ratio of 1.375. Samples T2 and T3 were wet-etched using a 1% Br in HBr solution, giving an etch rate of roughly ~1,000 Å/s. Inductively coupled plasma (ICP) etching was performed on sample T4 using a Versaline Unaxis ICP system. The systems primary inductor is driven at 2 MHz while the RF-coupled DC source is held at 40.68 MHz, each operating on 300 W of input power. The argon to hydrogen ration was set at 16:1, with 8.0 sccm Ar and 0.5 sccm H₂, maintained at a process pressure of 0.4 mtorr. Total etch depth using the ICP system was ~18 μm of material, taking approximately 110 minutes to perform while at a constant temperature of -10° C. Dektak step-scanning was used to confirm that all patterns were etched entirely through the HgCdTe layer.

Table II: Hall test sample properties.

<u>Sample</u>	<u>Sample Geometry</u>	<u>Contacts</u>	<u>Patterning etch</u>
T1	Square	Au	n/a
T2	Cross	H _{Au} Cl ₄	Wet(Br/HBr)
T3	Cross	In	Wet(Br/HBr)

T4	Cross	In	ICP
----	-------	----	-----

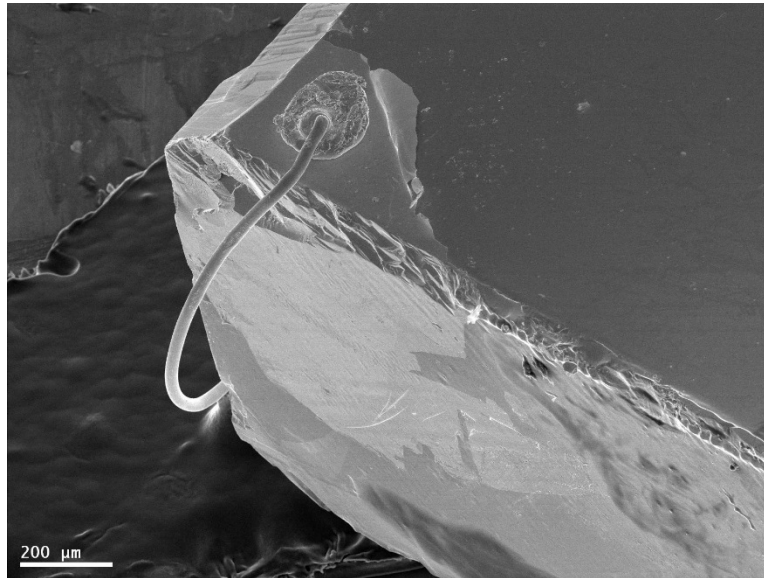


Figure 16: SEM image of over-the-side (lateral) contacts deposited using e-beam. Sample, T1, is square p-on-n MW HgCdTe, with lighter areas indicating Au.

According to Equation 2.66 ($\sigma_{xx}(B)$, $\sigma_{xy}(B)$), care should be taken when choosing the number and magnitude of magnetic field points. Too many magnetic field points can overcomplicate the fitting process while too few can forfeit valuable information when conductivity tensor elements are rapidly changing. For most practical applications, field points should be weighted towards lower magnetic fields when $\sigma_{xx}(B)$ and $\sigma_{xy}(B)$ are most dynamic. Therefore, we employ quasi-logarithmic B-field spacing with $\sim 25 - 32$ total field points ranging from $\sim 200 - 90,000$ gauss.

The correction factor results at 78 and 298 K obtained from all structures as a function of B-field can be seen in Figure 17. Correction factors are generally good ($f > 0.90$), with the only clear outlier being T1. The results indicate an advantage of the Greek cross structure over a simple square structure, as all three Greek cross structures are nearly unity throughout the test range.

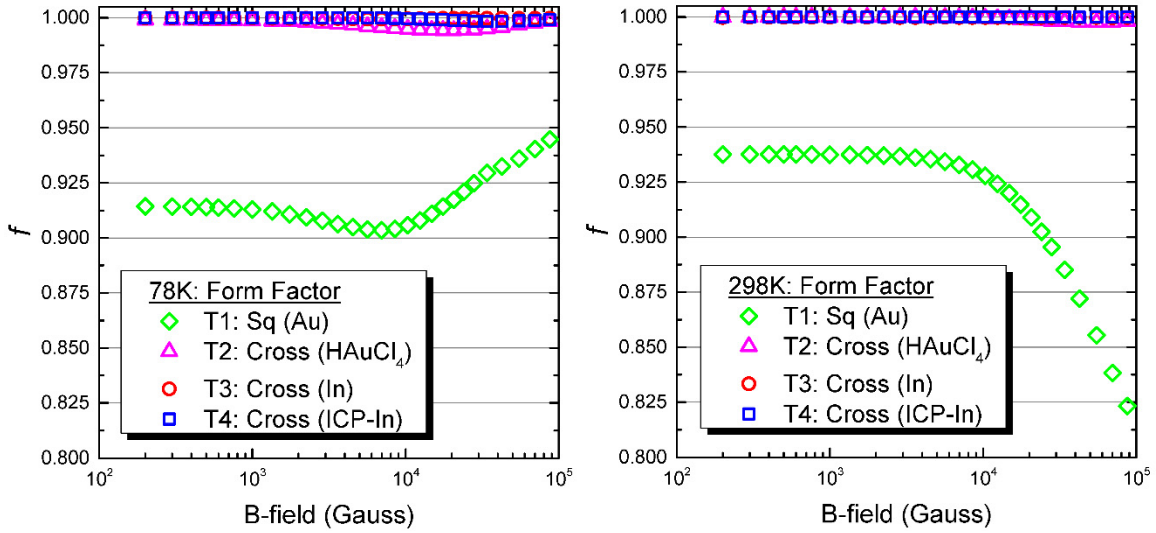


Figure 17: Correction factor f versus B-field for test samples. Measurements taken at 78 K (left figure) and 298 K (right figure).

Hall measurements were taken using both configurations to determine Hall coefficients, R_{HA} and R_{HB} , for all samples. The percent difference between configurations for test samples at 78 K and 298 K are shown in Figure 18. Percent differences of 10% or less are considered normal, while higher differences may be deemed unreliable. It is evident once again that the square sample T1 displays the poorest results, suffering the largest discrepancies between configurations. Amongst the Greek cross structures, there is no clear preference, but it should be noted that low B-field measurements near room temperature show significant inconsistency and may be removed in further analysis. At low temperatures, cross structures utilizing In contacts appear more consistent as compared to Au-based contacts.

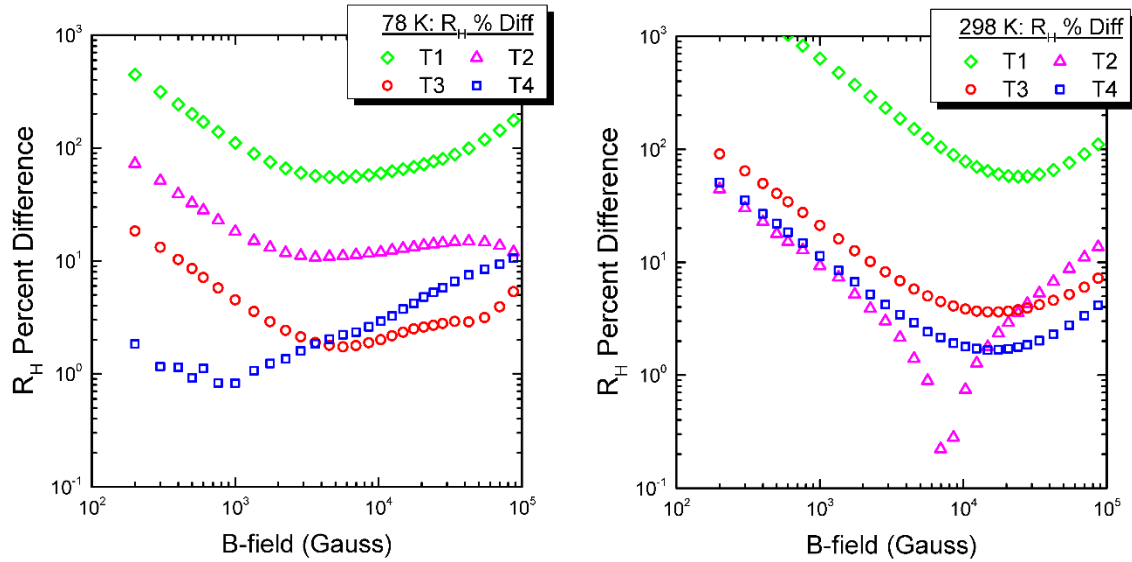


Figure 18: Percent difference of R_H values using two Hall configurations plotted versus B-field for Hall test samples. Measurements taken at 78 K (left figure) and 298 K (right figure).

The results above indicate that from a measurement error perspective, sample patterning appears to be a worthwhile endeavor. However, we observe variability between patterning techniques. Uniformity disparity is highlighted in Figures 19 and 20, which show topographical scans of samples T2 and T4, respectively, using a Bruker DektakXT stylus profilometer. The detailed scans reveal inhomogeneities in sample T2 in the form of sloped sidewalls and a processing error located at an inner corner. Despite the large protrusion of sample T2, the correction factor remains near unity in testing, and the Hall coefficient is reasonably consistent. Although this particular non-uniformity is avoidable, it is reassuring that even an egregious error such as this does not entirely compromise the measurement. Furthermore, cross-sectional and top-down profiles of samples T2 and T4 are given in Figures 21 and 22, respectively. Again, the presence of significantly sloped sidewalls, trenching, and dishing, while not desirable, have not compromised the Hall results.

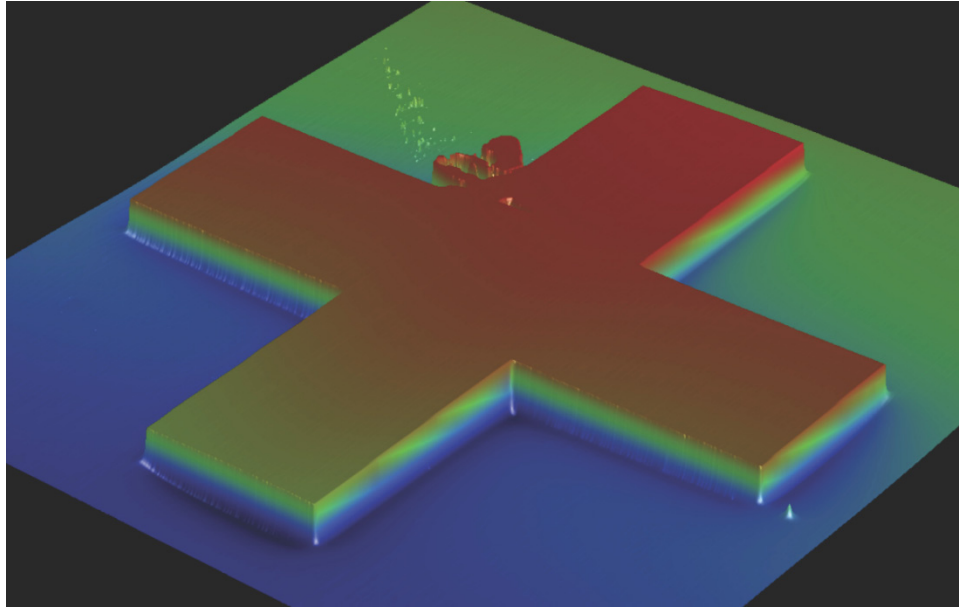


Figure 19: Spatial Dektak map of wet-etched Greek cross structure, sample T2

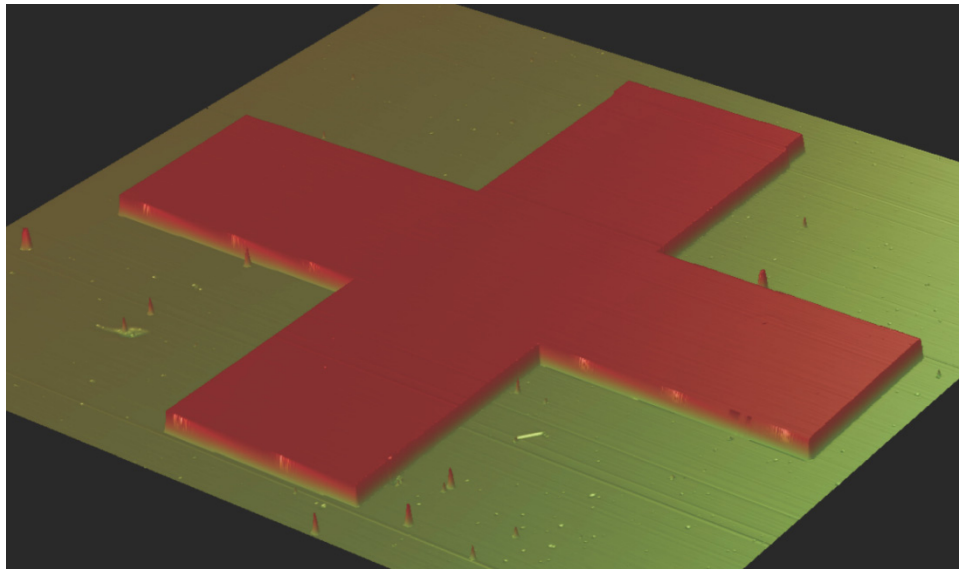


Figure 20: Spatial Dektak map of ICP etched Greek cross structure, sample T4.

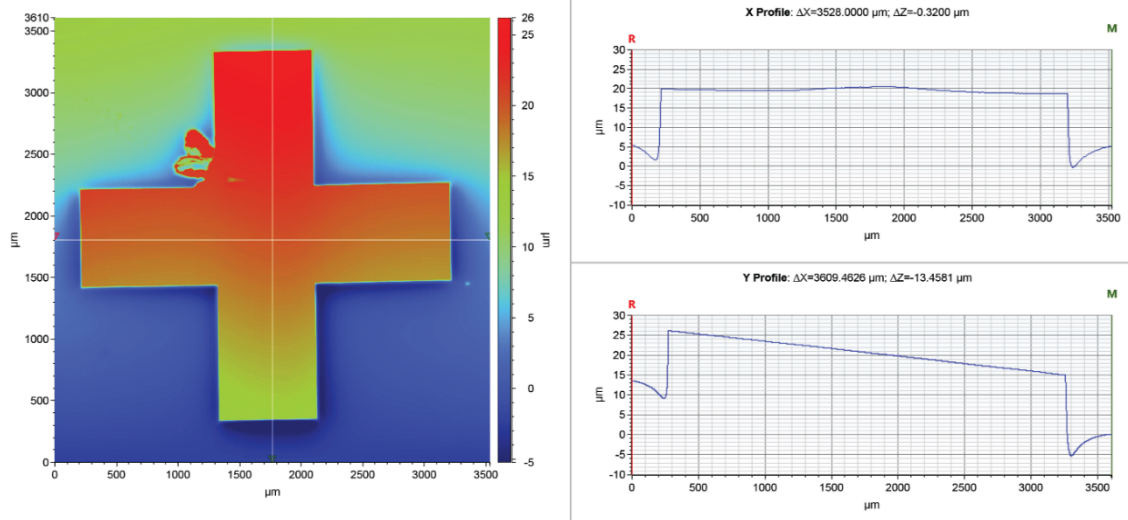


Figure 21: Dektak profile of wet-etched Greek cross structure, sample T3.

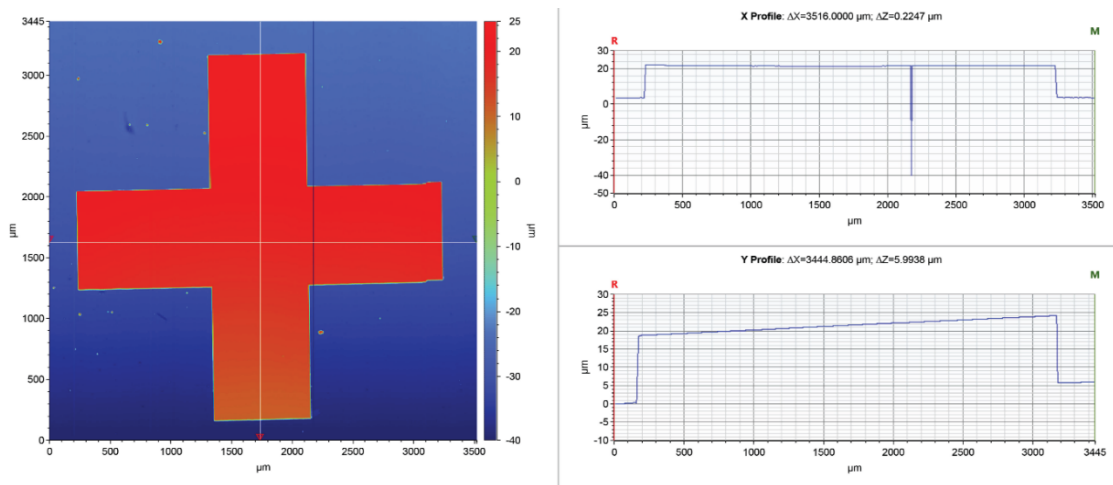


Figure 22: Dektak profile of ICP etched Greek cross structure, sample T4.

The temperature evolution of MSA fitting for Greek cross structures T2, T3, and T4 are shown in Figures 23, 24, and 25, respectively. Each line represents the mobility spectrum at a different temperature, and are collectively shown with a constant arbitrary offset between them. This allows one to easily see how the mobility spectrum evolves with temperature. For each figure, the electron spectra is shown in red on the left while the hole spectra is shown in blue on the right.

Qualitatively, the spectra contain much of the same information: a dominant electron species

identified as the bulk carrier in the n -type layer (e1), two lesser electron species (e2 and e3), one dominant hole species belonging to the p -type layer (h2), and one minor hole peak (h1), most likely a light hole in the p -type layer. The mobility spectra from T3 and T4 are quite consistent, but spectra from T2 is more distorted, especially at higher temperature. The dominant hole peak (h2) from sample T2 is quite pronounced, but it is harder to extract valuable information from the electron spectra. In addition, h1 is unrealistically high for a light hole carrier, suggesting a ghost peak. Ghost peaks are unwanted by-products of the MSA fitting algorithm, and generally related to measurement error or poor contacts. It is unclear if these results are due to the processing error or to the contact choice, or a combination of both.

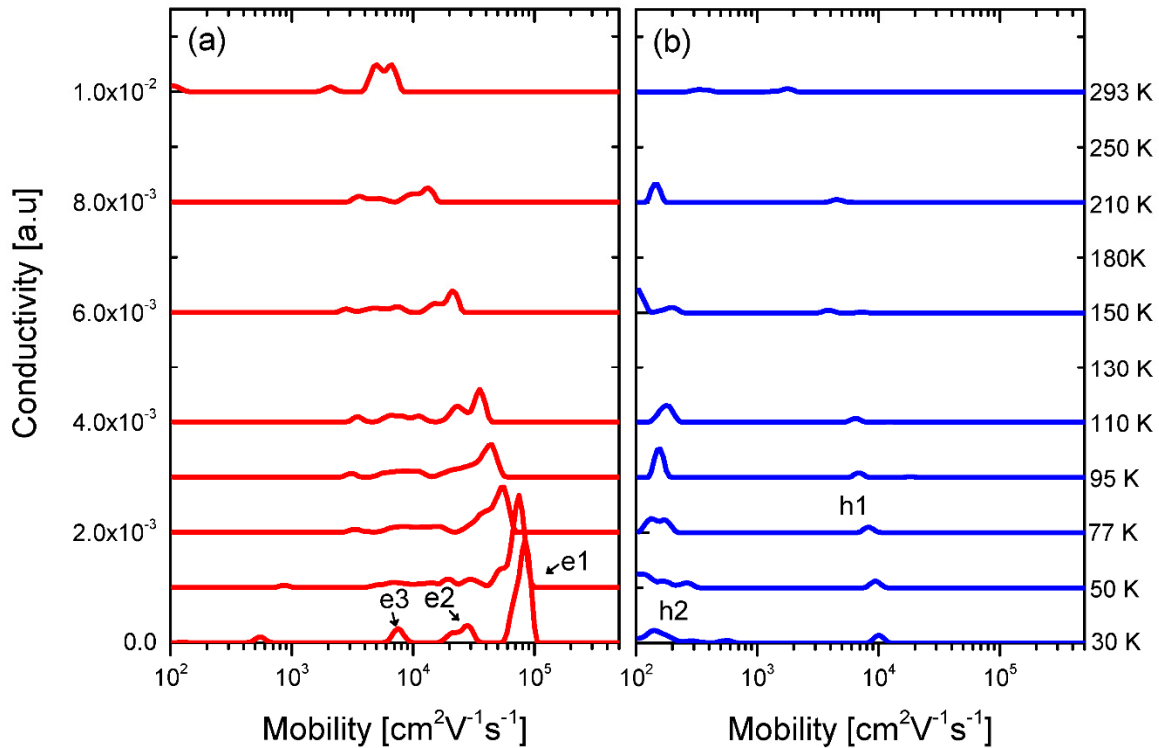


Figure 23: Sample T2 temperature evolution of mobility Spectrum from 50 K to 293 K. Figure (a) for electron spectra and figure (b) for hole spectra.

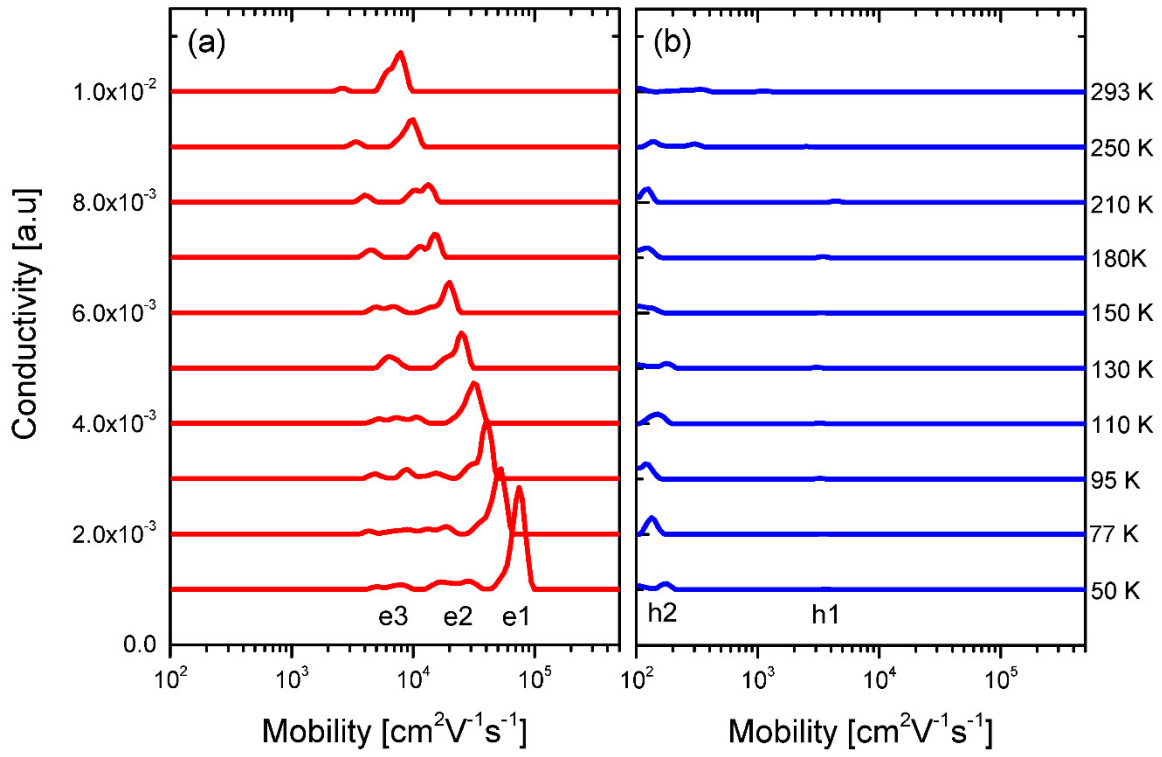


Figure 24: Sample T3 temperature evolution of mobility Spectrum from 50 K to 293 K. Figure (a) for electron spectra and figure (b) for hole spectra.

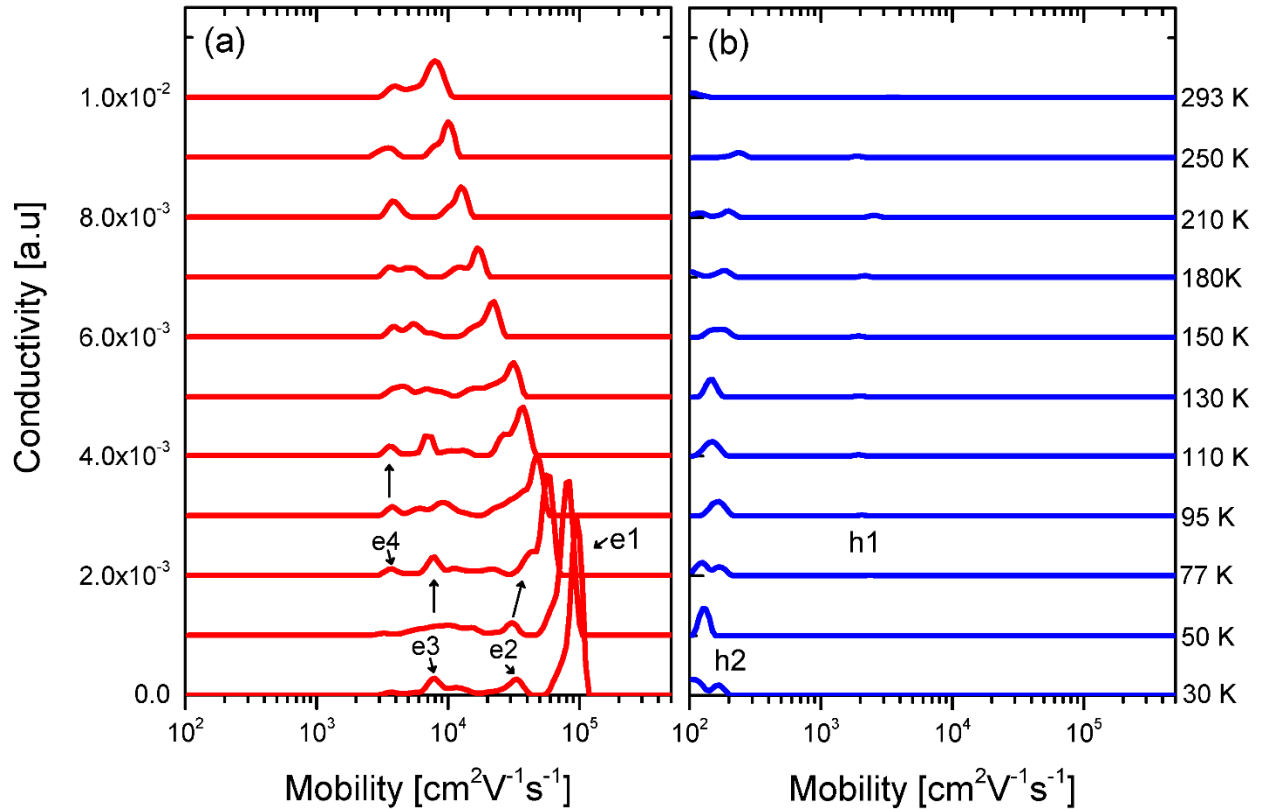


Figure 25: Sample T4 temperature evolution of mobility Spectrum from 50 K to 293 K. Figure (a) for electron spectra and figure (b) for hole spectra.

In summary, initial testing has shown better consistency and resolution using patterned samples, particularly the Greek cross structure utilizing lateral In contacts. That said, we observe degraded mobility spectra in the presence of processing abnormalities, specifically the protruded corner in structure T2. The spectra from structures T3 and T4 indicate that structures may be processed using either wet or dry etching processes, as the results are comparable. Moving forward, we conclude that sample patterning will provide the best measurement results, as long as major preparation errors are avoided. It is not decisively evident if Au-based or In-based contacts are preferable, but due to ease of application and satisfactory results obtained thus far, we will proceed with the In-based contact method.

3.2 Supplementary

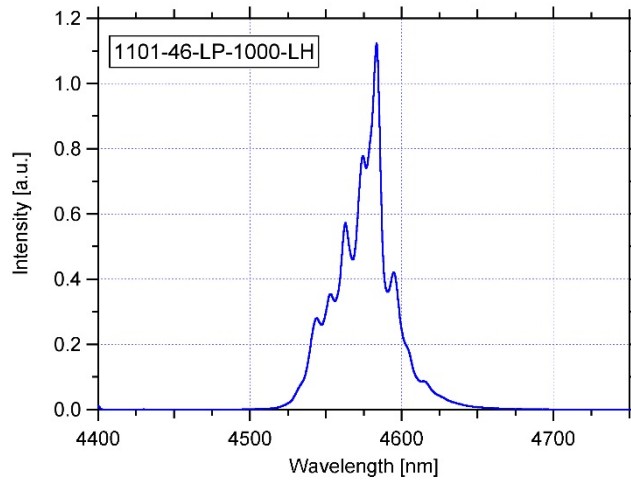
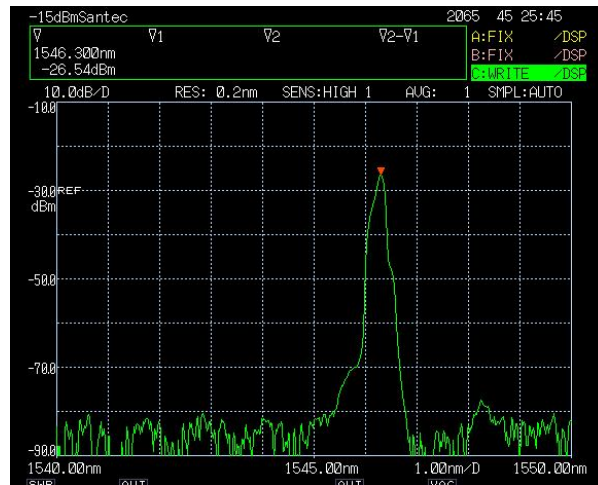
3.2.1 PCD

Minority carrier lifetime measurements using photoconductivity decay (PCD) method have long been performed on semiconductor materials [221, 36 and references therein]. Lifetime measurement techniques are typically divided into two categories depending on whether electrical contacts are required and a further two divisions if the measurement is done under transient or steady-state conditions. PCD is a contact method that monitors the conductivity change of a sample under optical excitation that produces an excess carrier population. The excitation may be pulsed or continuous. In this work, transient PCD method shall be performed using a pulsed laser source. The subsequent conductivity decay back to equilibrium is recorded and fitted to extract a minority carrier lifetime.

The basic setup of the PCD measurement begins with a laser source of known pulse width, energy per pulse, and rise/fall time which can be obtained by sampling the laser with a beamsplitter and reference detector. The remaining laser pulse impinges on the device under test (DUT) inside a custom designed Janis dewar pumped down to vacuum pressure via a Varian mini-task AG81 turbo and dry scroll ensemble. The dewar may be cooled using liquid nitrogen or liquid helium depending on temperature of interest. Temperature is monitored and controlled using a Lakeshore 331 temperature controller, allowing ample time for stabilization at each temperature point. A constant bias is held between two contacts placed at opposite sides of the sample along the perimeter. The circuit continues through a simple resistor-capacitor acting as a filter with time constant in excess of decay lifetime. After passing through an amplifier, the circuit connects to a Tetrax DPO 4104 oscilloscope. The oscilloscope is capable of performing 512 measurement averages internally. All electronic equipment is automated externally using LabView.

All lasers used in this work have pulse widths of approximately 100 ns with rise/fall times equal to 5 ns or less. The three quantum cascade lasers (QCL) used have characteristic wavelengths centered at 1.5 μm , 4.6 μm , and 8.3 μm , and are shown in Figure 26, and general characteristics listed in Table III. The repetition rate is chosen such that the sample returns to equilibrium between excitation pulses. Repetition rate may also be varied so as to determine the energy per pulse from a power (W) versus rate

(Hz) plot. Additional spatial characterization of beam profiles are carried out using a Spiricon Pyrocam III and knife-edge technique. A temporal profile for the 1.5 μm laser is shown in Figure 27, highlighting the offset between trigger and pulse.



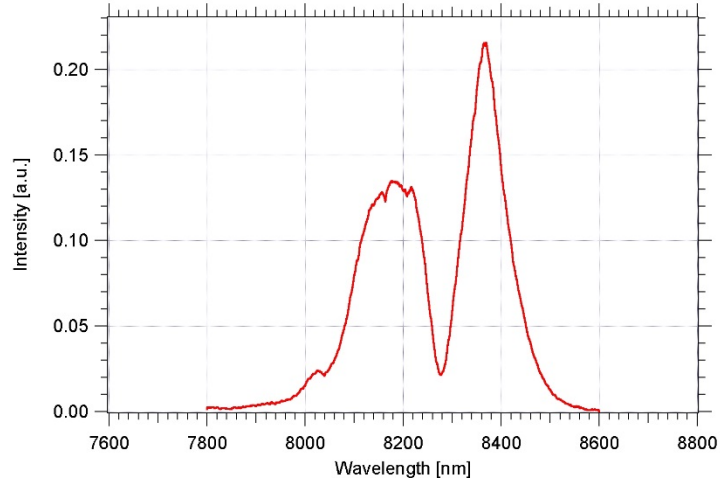


Figure 26: From top to bottom, spectral characteristics of 1.5, 4.6 and 8.3 μm QCL lasers.

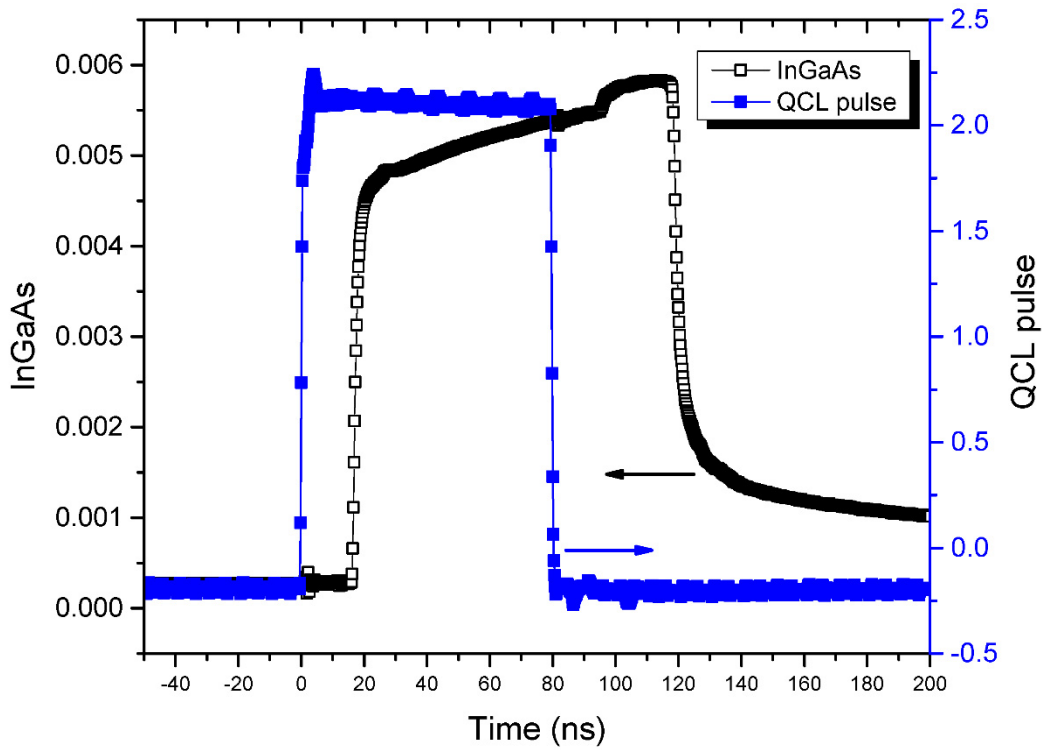


Figure 27: Temporal pulse profile for 1.5 μm QCL and InGaAs reference detector response. QCL trigger width is ~ 80 ns while InGaAs detector width is ~ 100 ns. InGaAs detector highlights offset between trigger end and pulse end.

Table III: QCL characteristics for lifetime measurement.

Wavelength (μm)	E/pulse (nJ)	Area (cm^{-2})
1.5	1.12	0.0064
4.6	95.7	0.0822
8.3	22.3	0.175

When using the PCD method, it is paramount to determine the injected carrier concentration in order to ensure measurements are taken in the low-injection regime. Taking all windows and filters into account, the injection level can be determined if the absorption coefficient and sample thickness are known. Neutral density filters may be used in the event that carrier injection exceeds the sample doping level. As an example, a summary of calculations are presented in Table IV.

Table IV: Injected carrier concentration calculations for PCD measurement.

<u>Wavelength (μm)</u>	<u>Photons/pulse</u>	<u>ND filter</u>	<u>α (cm^{-1})</u>	<u>Inj. Carrier Conc</u> (cm^{-3})
1.5	8.31×10^9	none	15,000	6.13×10^{14}
4.6	2.22×10^{12}	2.0	7,000	9.59×10^{13}
8.3	9.32×10^{11}	1.45	3,000	1.21×10^{14}

All calculations assume a sample thickness of 5 μm and beam spot sizes from Table IV, although further spot size reduction is commonly performed. The absorption coefficient is taken to represent the worst-case scenario, i.e. strongest absorption and most likely to compromise the low injection regime condition. The calculations include transmission through a ZnSe window on the Janis dewar and reflection at the air-CdTe interface. Beam splitters are routinely used on 4.6 and 8.3 μm QCLs and reduce

the number of photons by half. Finally, each calculation includes the transmission loss from Spectrogon narrow bandpass filters using values provided by the manufacturer. As can be seen in the final column of Table IV, the injected carrier concentration is well under typical doping levels.

Further considerations for proper measurement quality involve contact linearity, carrier sweep-out, trapping, and surface recombination. A simple IV performed with an SMU quickly assures that only ohmic contacts will be used in this work. Best results are achieved using In contacts on HgCdTe samples and thin (~ 50 Å) degenerately doped contact pads on SL material, using either Si, Te, or Be.

Carrier sweep-out occurs when electron-hole pairs form a distance on the order of a diffusion/drift length away from a contact. Under these conditions, a fraction of carriers will statistically make their way to a contact. If carriers leave the sample from sweep-out, the extracted lifetime will be artificially lowered due to the prevention of bulk recombination. While diffusion length is fixed according to material parameters, the drift length is proportional to the applied voltage bias, and therefore excessive voltages should be avoided. A diffusion length may be approximated or determined, but will normally be much smaller than the distance between location of photoexcitation and contact. For best results, the distance between excitation and contact should be greater than four times the drift/diffusion length, whichever is larger. Repeating measurements at increased bias is a quick way to determine if sweep-out is occurring.

Lifetimes associated with surface recombination are typically much shorter than in the bulk. In strongly absorbing materials, this implies that a significant amount of recombination takes place near the surface. If too much signal is lost in this manner, it becomes increasingly difficult to extract the bulk lifetime due to excessive conductivity loss and double decay features. Therefore, surface passivation is routinely performed to reduce near-surface states. In the event of two decays corresponding to the surface and bulk, double exponential fitting may be used. Passivation of HgCdTe samples in this work are deposited using thermal evaporation of CdTe. An optimization study, summarized by Figure 28, showed best results after CdTe deposition, and showed significant issues after post-passivation annealing.

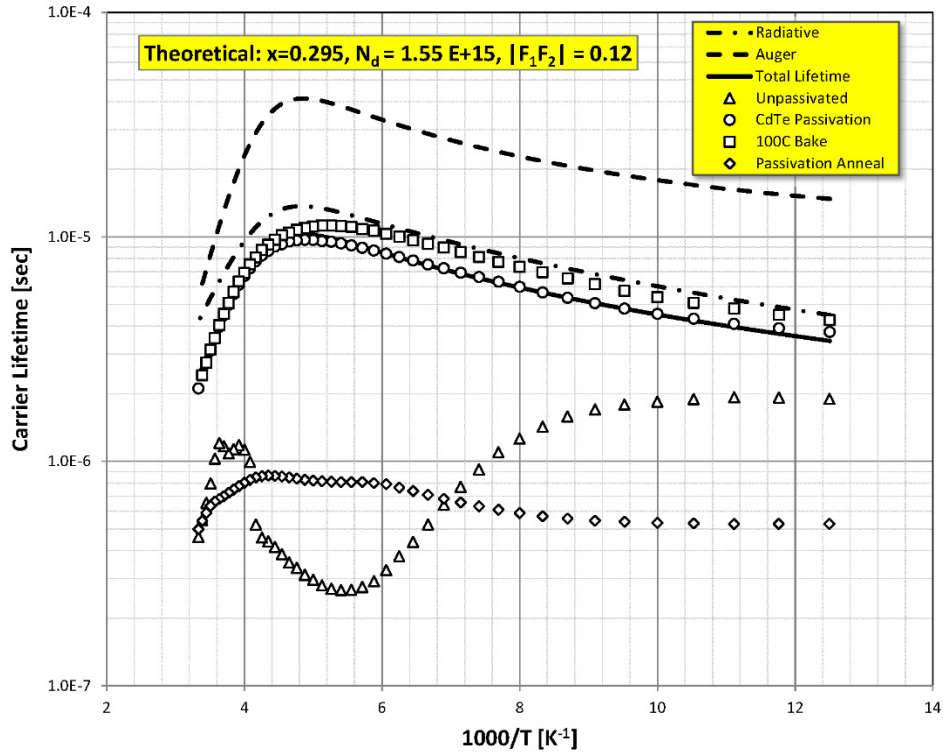


Figure 28: CdTe passivation testing on MW HgCdTe. Poor results are obtained on unpassivated and post-passivation annealed samples. Best results are obtained after CdTe passivation (no anneal), and slight improvement can be seen after 100 °C bake of unannealed CdTe.

Lastly, carrier trapping can greatly alter PCD lifetime values due to persistent photoconductivity. Accurate lifetime using PCD cannot be measured in the presence of excessive trapping. If measured lifetimes greatly exceed theoretical expectations, it is a good indication that trapping is at play, and the measurement compromised.

3.2.2 SEM/EBIC

The scanning electron microscope (SEM) is a ubiquitous and indispensable tool in the field of materials science. SEM images of surface topography and composition are routinely obtained by raster scanned bombardment of the sample surface with a focused electron beam. One additional application of an SEM is the electron beam induced current (EBIC) method. The EBIC method boils down to three basic

steps: generation of electron-hole pairs via electron beam, segregation of carriers due to an internal electric field, and signal sensing in an external circuit.

The first step is simply a result of electron bombardment. The generation profile is roughly bulb-like and the penetration depth will depend on the accelerating voltage. There exists a trade-off between spatial resolution and penetration depth, as an increase in accelerating voltage results in larger lateral excitation as well. Once electron-hole pairs have been created, they diffuse randomly in the absence of an internal electric field. However, an internal electric field will result in charge collection and forms the basis of the imaging process. An internal field is typically supplied by a p-n junction.

As such, the EBIC method provides unique characterization of semiconductor materials, particularly for the case of diodes. The powerful technique has been used to accurately determine diffusion length, the location of p-n junctions, surface recombination velocity, and defect energy levels [69, 70, 222]. Additionally, top-down spatial mapping across a sample elucidate electrical inhomogeneities, giving unique insight into sample uniformity and junction defect effects.

All imaging is performed on a Hitachi S-4500 SEM equipped with Gatan MonoCL and SmartEBIC systems and controlled through a modern computer interface. The microscope allows for rapid transition between SEM imaging and EBIC imaging modes so comparison can be made. The SmartEBIC system also contains a Stanford Research Systems SR570 low-noise current preamplifier and may be operated at zero-bias, or small forward and reverse biases, but most images are taken at or near zero-bias. The system contains a cryogenic stage to lower sample temperature and improve image quality. The accelerating voltage for most EBIC images is between 5 - 20 keV, with preference towards lower voltages.

3.2.3 IV

Current-voltage (IV) measurements are performed as a function of sample temperature on photodiodes in this work. A cryogenic test dewar with 68-pin leadless chip carrier (LCC) holder allows a

variety of diodes to be tested simultaneously. The dewar is pumped and cooled using liquid helium or nitrogen, and temperature controlled via Lakeshore 336 unit. Additionally, a standard SMU Keithley 236 and switch matrix are automated using LabView to collect IV data on all diodes at select temperature points.

3.2.4 Optical

Fourier transform infrared (FTIR) spectroscopy is used to estimate the thickness and compositional x-value of MCT layers. FTIR spectra are obtained with ease at room temperature in only a matter of minutes, making the measurement commonplace. A Michelson interferometer is used to determine transmission or reflection across the IR spectrum. In this approach, step scan is used to first determine the IR transmission spectra, followed by model fitting to extract the parameters of x-value and thickness.

In its simplest form, the separation of interference peaks relates to sample thickness, while the spectra cut-off relates to the sample composition. The optical model harnesses well established properties of MCT at room temperatures, such as the absorption coefficient and refractive index [13, 223]. An optical transfer matrix is first calculated for the system, which includes properties pertaining to the substrate choice and buffer layer. A non-linear model simultaneously fits experimental data to the parameters of interest. For layers grown on alternative substrates, an additional fitting parameter for the thickness of the CdTe buffer layer is added.

FTIR measurements are taken on a Thermo Nicolet Nexus 870 with IR globar source, potassium bromide beam splitter and pyroelectric DTGS detector. The system also has a fast MCT detector, multiple exit ports, external source port, and nitrogen purging capability. The spectral resolution is 0.125 cm^{-1} across a range of $400 - 12000 \text{ cm}^{-1}$, but experimental resolution is typically on the order of $2 - 4 \text{ cm}^{-1}$. Spectral scans are averaged by default, and may be increased for less strongly absorbing materials. FTIR measurements are used in conjunction with secondary-ion mass spectroscopy (SIMS) and SE to

better understand HgCdTe sample properties. The system is also used to conduct spectral measurements that determine the cut-off wavelength of HgCdTe and III-V materials as a function of temperature. To do so, the spectral response of the DUT must be normalized to the calibrated pyroelectric DTGS detector, which is particularly useful as its spectral response is flat. However, the normalization process is complicated somewhat by the limited bandwidth of the DTGS detector, which reduces response at lower wavelengths. Once corrected for frequency, normalization will then yield the appropriate spectral response.

4. MSA studies of HgCdTe

4.1 Introduction

This chapter is devoted to the HgCdTe material system. Two modern device architectures will be considered; *ex-situ* doped planar devices, and *in-situ* doped P+/n mesa devices. Growth and preparation details will be outlined and transport results reported. The goal of this section is to determine the utility of mobility spectrum analysis on an established material system to explore what can be determined and the limitations that exist. An emphasis will be placed upon effects of growth on different substrates. Supplementary characterization will be used for correlation purposes.

4.2 LW HgCdTe for planar devices

Experimental investigations begin with *n*-type LW HgCdTe, which is expected to have the highest electron mobility of all material in this work. From a MSA perspective, this is a great starting place as high mobility electrons should be more easily resolved due to the high field sensitivity of mobile carriers. It also allows us to explore conductivity contributions that might arise from the surface and substrate-interface regions. To do so, variable-field, variable-temperature measurements are performed on three LW *n*-type HgCdTe samples. Variable-temperature results will aid in carrier identification process and in extracting additional material information. Each sample will be MBE grown on a different substrate, namely CZT, Si, and GaAs, for comparison of fundamental transport properties.

4.2.1 Experimental

Direct HgCdTe growth on lattice-mismatched alternative substrates produces high threading dislocation densities ($\sim 10^6 - 10^8 \text{ cm}^{-2}$), severely degrading device performance. Therefore, it is common practice to growth a thick ($\sim 10 \mu\text{m}$) CdTe buffer layer over the Si or GaAs substrate to reduce dislocation density via annihilation in the buffer. The CdTe layer ultimately acts as a template for HgCdTe growth

and must be of the highest quality possible. Successful epitaxial growth of CdTe on Si and GaAs substrates has been achieved despite the large lattice mismatch [224] and devices fabricated with MCT/CdTe/Si [225] and MCT/CdTe/GaAs [226] have been promising, generating a vast amount of interest in the community due to the production benefits.

The growth of single-crystalline CdTe epilayers requires the removal of native oxides, with procedure implemented tailored to substrate choice. For Si wafers, the tenacious native oxide can be overcome after light etching in an HF solution, producing a hydrogen passivated surface. After loading in UHV, the passivation is removed at much more modest temperatures (~ 550 °C) before epitaxial growth occurs, rather than the normally excessive temperatures (> 900 °C) required to remove the native oxide. The temperature reduction in oxide desorption also reduces outgassing from various MBE components, potentially reducing contamination issues.

GaAs wafers are purchased as epi-ready, meaning no chemical treatments are necessary before loading. Oxide desorption occurs thermally within a very similar temperature range (~ 550 - 600 °C) and is monitored *in-situ* using SE and RHEED. An As_4 over flux is maintained throughout the desorption process to reduce damage to the surface of the GaAs. The desorption process can readily be observed using SE or RHEED. Figure 29 shows the RHEED pattern of a clean GaAs surface shortly after oxide desorption while Figure 30 shows the discontinuities in SE derived overlayer thickness and the real peak of the dielectric function. The abrupt changes in the EMA model parameters signify successful oxide desorption.



Figure 29: RHEED pattern of GaAs substrate following oxide desorption.

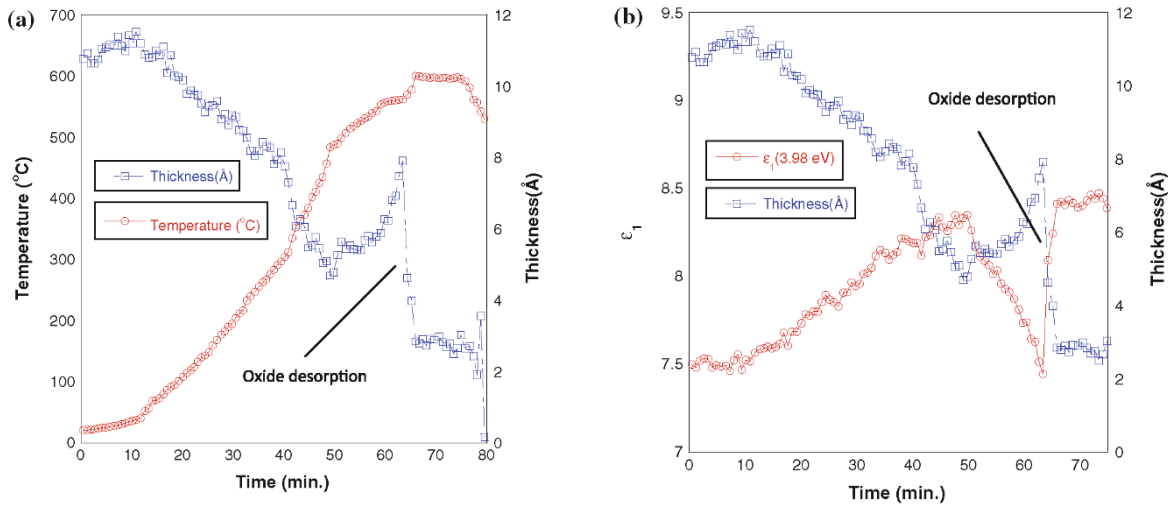


Figure 30: SE derived overlayer thickness of GaAs during preparation shown alongside surface temperature (a) and the real part of the dielectric function at 3.98 eV (b). The abrupt change in thickness coincides with a rapid change in the real part of the dielectric function [227].

Alternatively, HgCdTe growth begins immediately on the lattice matched CZT substrate. Wafer preparation consists of light etching in a dilute (< 1%) Br/MeOH solution, after which the CZT surface is Te-rich. The advantages of having a Te-rich surface are twofold: the surface becomes less prone to rapid oxidation and the near-surface Te will desorb more easily, leaving a clean CZT surface. The first advantage lowers the probability of an unwanted oxide layer, while the second simplifies procedures

before epitaxy, as the Te-rich surface desorbs at lower temperatures than those at which HgCdTe growth takes place.

4.2.1.1 CdTe growth

The growth of the CdTe buffer layer itself requires optimization. An oft used figure of merit for crystal quality is x-ray diffraction (XRD) full-width at half-maximum (FWHM). The system used in this work is the Bede D1 XRD with sealed tube K_{α} source, utilizing a two-bounce Ge crystal to isolate the $K_{\alpha 1}$ line.

Lattice imperfections such as curvature, defects, and dislocations, all act to broaden the FWHM, meaning the more narrow the diffracted beam the better the crystal quality is. While FWHM values of CZT substrates can be < 10 arcsec, values reported for CdTe on alternative substrates (Si/GaAs) are generally > 50 arcsec [228], but may be as low as ~ 30 arcsec [229]. The Dunn/Ayers model, which relates FWHM to dislocation density, is useful in explaining the broadening of the FWHM due to dislocations. Although the relative difference between FWHM values for HgCdTe grown on CZT versus alternative substrates seems small, it implies orders of magnitude differences in dislocation density. Experimental studies confirm that dislocations are the primary contributor to FWHM broadening for CdTe on alternative substrates [230].

One means of reducing dislocation values in CdTe and improving FWHM values is via *in-situ* thermal cyclic annealing [231]. A standard growth is initiated at $\sim 320^{\circ}\text{C}$ and immediately slow ramped ($< 1^{\circ}\text{C s}^{-1}$) to 350°C , with substrate temperature monitored by a noncontact thermocouple located near the substrate backside. The lower growth initiation temperature is required to ensure growth occurs in the (211) orientation, while growth at 350°C is found to improve crystallinity. After a desired amount of buffer growth, typically in $\sim 1\ \mu\text{m}$ intervals, growth is suspended and the sample temperature is ramped at $\sim 10^{\circ}\text{C s}^{-1}$ to the desired cyclic annealing temperature. The annealing process take place under a Te_2 flux, as partial sublimation may occur. A dwell time of 5 minutes at an annealing temperature is determined to

minimize sublimation while simultaneously providing crystallinity benefits.

Anneal temperatures ranging from $\sim 490^\circ\text{C}$ to $\sim 550^\circ\text{C}$ (thermocouple) were investigated, with comparisons made to a control receiving no annealing treatments. Typical buffer thickness was $\sim 10\ \mu\text{m}$. Annealing temperatures appeared to have the largest impact on surface morphology, with the $\sim 550^\circ\text{C}$ annealed sample being the smoothest. Surface defects of samples not receiving an anneal were well in excess of $10^7\ \text{cm}^{-2}$. Comparatively, samples experiencing cyclic annealing significantly improved to the point that an optical smooth surface was achieved using the 550°C anneal cycle. Other annealed samples ($490\text{-}530^\circ\text{C}$) displayed levels in the mid- $10^6\ \text{cm}^{-2}$ range, a marked improvement.

EPD and FWHM values were also seen to improve with cyclic annealing, with the most benefit coming from the 550°C . EPD of the control sample was in excess of $10^8\ \text{cm}^{-2}$, while 490°C , 530°C , 550°C annealed samples had values of 2×10^7 , 5×10^6 , and $4 \times 10^6\ \text{cm}^{-2}$, respectively. FWHM values of ~ 60 arcsecs were obtained on annealed samples with excellent uniformity across the 3" wafer. Cyclic annealing improves surface morphology and crystallinity and will be implemented in this work.

4.2.1.2 MCT growth and sample preparation

The MBE grown samples were doped *in-situ* n-type using indium, and grown in the (211) B orientation. The (211) B orientation is preferred because it most effectively suppresses twin-formation and has superior Hg incorporation [232]. General sample properties are shown in Table V.

Table V: HgCdTe sample properties for LW planar study.

<u>Sample</u>	<u>Substrate</u>	<u>Thickness</u> [μm]	<u>x-value</u> (FTIR)	<u>N_d</u> [cm^{-3}]	<u>Cap</u>
G1	GaAs	4.64	0.208	$\sim 3 \times 10^{15}$	No
S1	Si	9.82	0.233	$\sim 2 \times 10^{15}$	Yes
CZT1	CdZnTe	> 10	0.220	$\sim 4 \times 10^{14}$	Yes

All samples experienced identical p-type arsenic activation (~ 9 minutes at 400°C) and vacancy reduction (~ 24 hours at 233°C) annealing under an Hg overpressure to replicate processing procedures

typical for advanced structures. Brief etching in dilute 0.15% Br/MeOH solution was utilized to remove the native oxide layer prior to the formation of ohmic indium contacts. The contacts were made at the corners of the square van der Pauw configuration, with side lengths of approximately 5 mm. Hall and resistivity measurements were taken on the Lakeshore 9509 HMS at ~ 35 magnetic-field points ranging from ~300 gauss to 9 T and subsequently analyzed using MSA. Measurements were taken across 8 different temperature points ranging from 50 K to 293 K.

Due to the self-diffusivities of constituent elements, MCT is expected to exhibit compositional interdiffusion at elevated temperature such as those experienced during post-growth annealing. Major changes in the spatial composition of epilayer material can have a dramatic impact on the mobility distribution throughout the thin film. Figure 31 shows a comparison between SE derived compositional x-value and that derived from SIMS on layer G1. The SE profile is indicative of the as-grown profile, while SIMS was performed after annealing. Major changes within the substrate-interfacial region are expected to manifest in the mobility spectrum results.

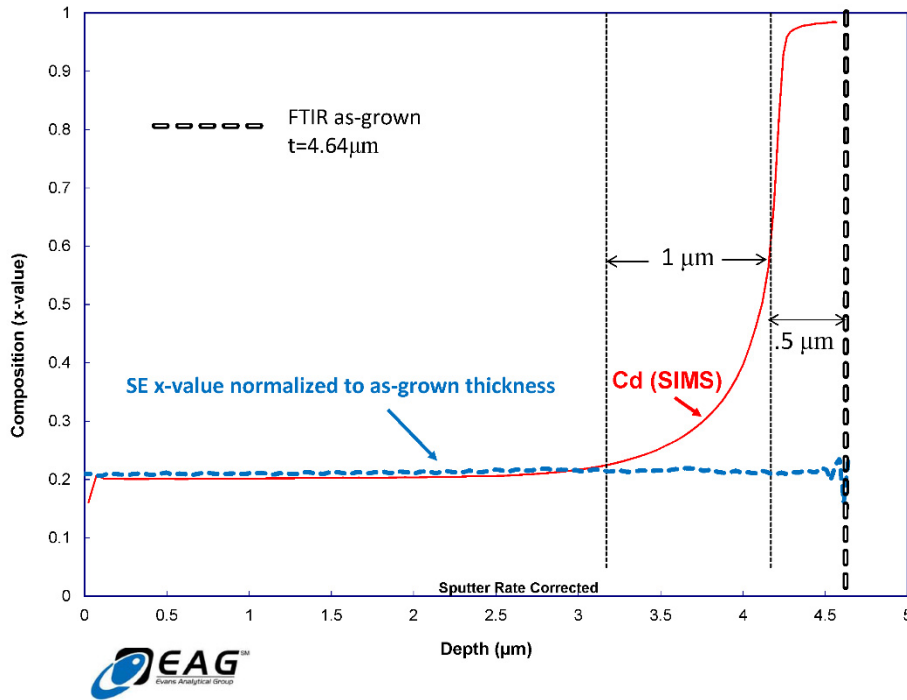


Figure 31: Compositional profile of layer G1. SE composition represents as-grown profile, while solid-red line is derived from post-annealing SIMS, showing significant changes in the substrate-interfacial region.

4.2.2 Results

4.2.2.1 MSA results

Mobility spectrum results for MCT/GaAs sample G1 at 50 K are shown in Figure 32, with three electron species labeled in decreasing order of mobility as E1 ($\sim 225,000 \text{ cm}^2\text{V}^{-1}\text{s}^{-1}$), E2 ($\sim 66,000 \text{ cm}^2\text{V}^{-1}\text{s}^{-1}$), and E3 ($\sim 16,000 \text{ cm}^2\text{V}^{-1}\text{s}^{-1}$). The spectrum at 50 K has been used for identification of species since it is expected that distinct carrier mobility will differ more at low temperature, thus making resolution of peaks most reliable. Carrier freeze-out of electrons is not expected as In is known to be a shallow donor, so obtained carrier concentrations will reflect doping levels. An additional electron peak at a mobility of approximately $5,000 \text{ cm}^2\text{V}^{-1}\text{s}^{-1}$ is seen in Figure 32, but is not conclusive due to the exceedingly low conductivity.

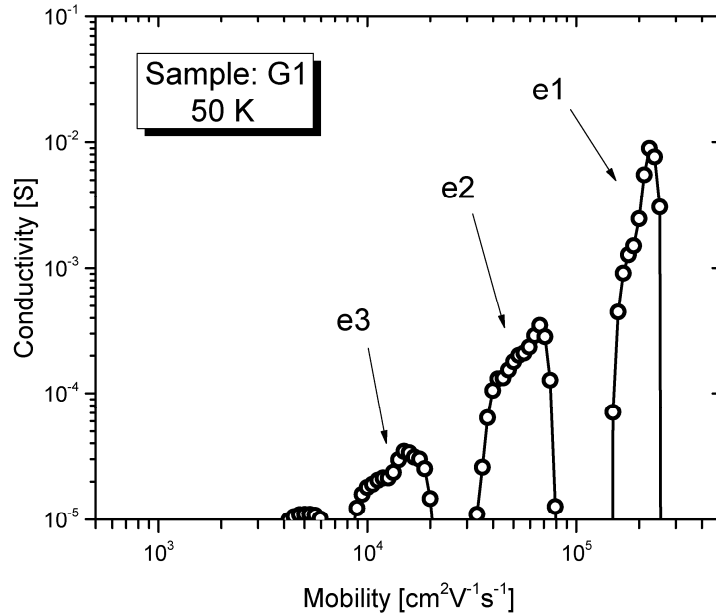


Figure 32: Mobility spectrum of sample G1 at 50 K, showing three distinct carrier species.

At 50 K, the conductivity in the MCT/GaAs sample is dominated by the E1 carrier, contributing $\sim 92\%$ of the total conductivity. E2 is the next most prominent at $\sim 7\%$, with E3 showing the smallest contribution of $\sim 1\%$. Carriers E2 and E3 are observed to make larger contributions at a temperature of 125 K, with contributions of $\sim 14\%$ and $\sim 2\%$ respectively. The high mobility and conductivity contribution of E1 suggest the carrier be identified as the bulk LW electron. The concentration of E1 was found to saturate to $\sim 2.85 \times 10^{15} \text{ cm}^{-3}$ at low temperatures, matching the bulk extrinsic *n*-type In doping concentration of $2.83 \times 10^{15} \text{ cm}^{-3}$ obtained from SIMS measurement. Fitting of the temperature dependence of equilibrium electron carrier concentration incorporating the Hansen and Schmit intrinsic behavior (Equation 2.2) is shown in Figure 33. The derived carrier concentration and *x*-value are in agreement with parameters derived from FTIR ($x = 0.208$) and SIMS ($N_d = 2.83 \times 10^{15} \text{ cm}^{-3}$), further validating the identification of carrier E1 as the bulk electron.

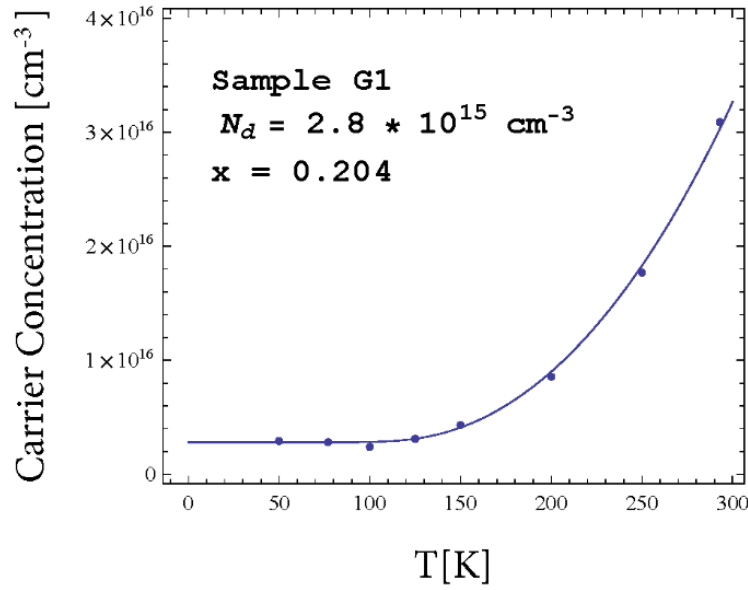


Figure 33: Carrier concentration fitting results of electron carrier E1.

Sheet concentration values were experimentally determined for each carrier peak. If a constant indium doping level is assumed throughout the sample, we may estimate the thickness associated with each specific carrier given the carrier does not originate from a 2D region. The assumption of a nominally constant doping level is supported by a flat In profile obtained from SIMS. Under this assumption the sheet concentration of carrier E2 corresponds to a region of $\sim 0.9 \mu\text{m}$ thick while carrier E3 corresponds to a region $\sim 0.5 \mu\text{m}$ thick. Upon reinvestigation of Figure 31, we can intuitively assign these carriers to the near-substrate interfacial region. Specifically, carrier E2 agrees well with a carrier originating within the lower transitional region (labelled as $1 \mu\text{m}$ thick). The x -value ranges from ~ 0.2 to ~ 0.6 with an average value of 0.32 within this region. The strong x -value mobility dependence in HgCdTe adequately explains the reduced mobility of carrier E2 as compared to carrier E1.

Carrier E3's estimated thickness ($\sim 0.5 \mu\text{m}$) agrees with that of the upper transitional region ($x = 0.6$ - 1.0 at a depth of 4.1 - $4.6 \mu\text{m}$) and may originate there. However, as E3's mobility and carrier concentration are in agreement with previous values on accumulation/inversion layers on HgCdTe [233, 234, 235], it is not clear if this carrier is solely due to conduction near the substrate-interface, or a rather

an amalgamation comprised of populations from both surface and substrate-interface regions.

The temperature evolution of the G1 mobility spectrum is shown in Figure 34, with each line representing a different temperature starting from the lowest temperature at the origin (50K). The results are linearly spaced so the temperature evolution is convenient to visualize. No scaling amongst spectra is performed. Due to the overwhelming conductivity of carrier E1, much of the spectra is dominated by this peak. At 50 K, carrier E2 is readily seen at $\sim 65,000 \text{ cm}^2\text{V}^{-1}\text{s}^{-1}$ and is observed to merge with carrier E1 for temperatures $\geq 200 \text{ K}$, producing a double peak. Carrier E3 is observable only at elevated temperature on this scale and is therefore marked for identification.

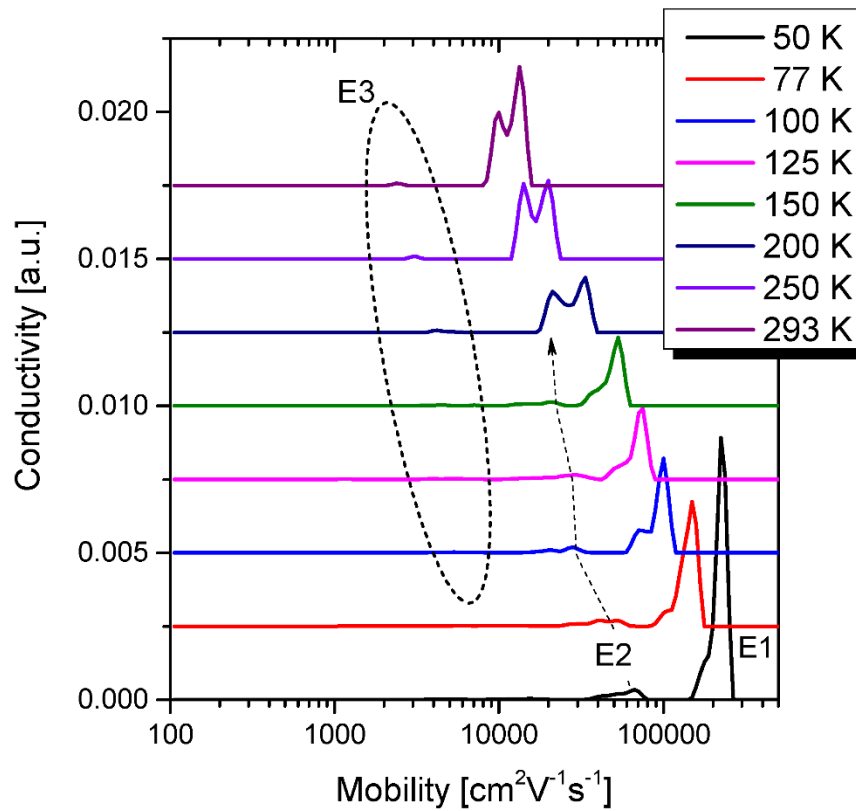


Figure 34: G1 mobility spectrum temperature evolution.

The temperature evolution of samples S1 and CZT1 are shown in Figure 35 (a) and (b), respectively. A similar carrier identification process on samples S1 and CZT1 also reveal three distinct

electron species, E1, E2, and E3, indicating that conduction within these layers is fundamentally similar despite changes in substrate. Peak merging of E1 and E2 is also seen in samples S1 and CZT1 for $T > 150$ K.

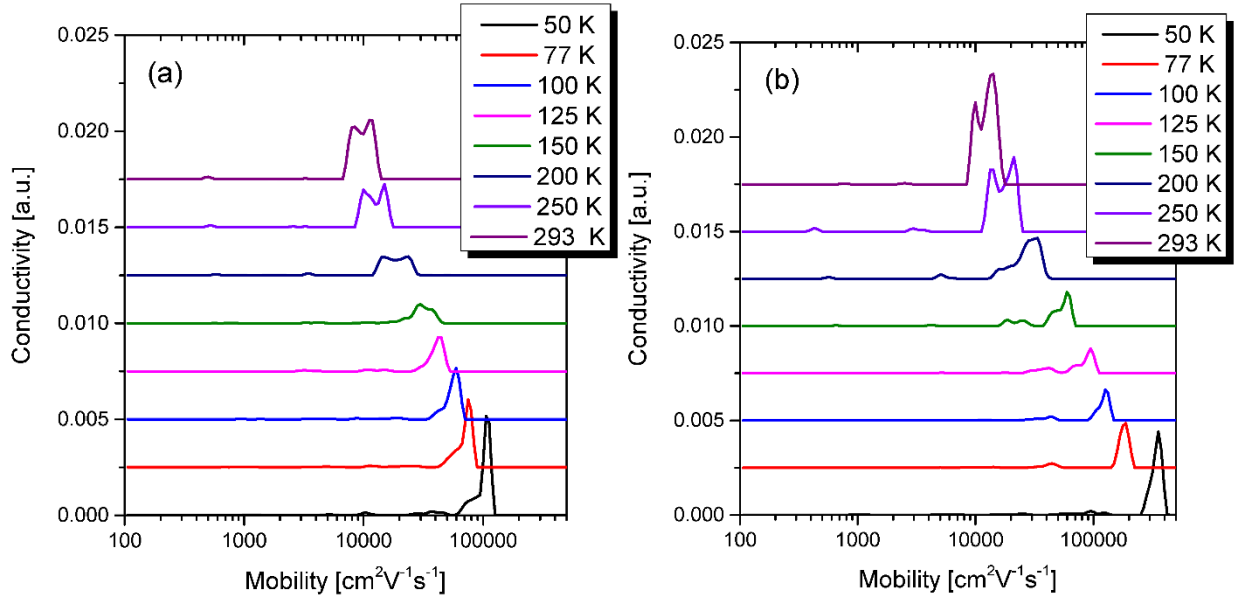


Figure 35: Mobility spectrum temperature evolution from samples S1 (a) and CZT1 (b).

To test if carrier E2 originates from higher x -value regions as speculated, sample CZT1 was etched in a Br/MeOH solution to effectively remove the cap layer and retested at 77 K. After etching, the percent conductivity of carrier E2 was found to drop from 11% to 9%, equating to a conductivity drop of 38%, the largest change in any resolved carrier. This finding suggests that the E2 peak contains carriers within the cap region. However, the peak is not eliminated after etching likely because E2 is a combination of higher x -value regions, namely the cap layer and the transitional region near the substrate-interface in the CZT1 layer.

Electron mobility and carrier concentration for all MBE grown n -type LW MCT samples are shown in Figure 36, with the left column depicting mobility and the right carrier concentration. Carrier E1 is expressed as a volume density, while carriers E2 and E3 are given as sheet concentrations as the exact

thickness of their respective regions are unknown. The mobility of carriers E1 roughly follow a classic $\mu \propto T^{-3/2}$ dependence associated with phonon scattering regime [209]. A similar temperature dependence is seen for carrier E2 in all samples, before the peak eventually merges with E1 above 150 K.

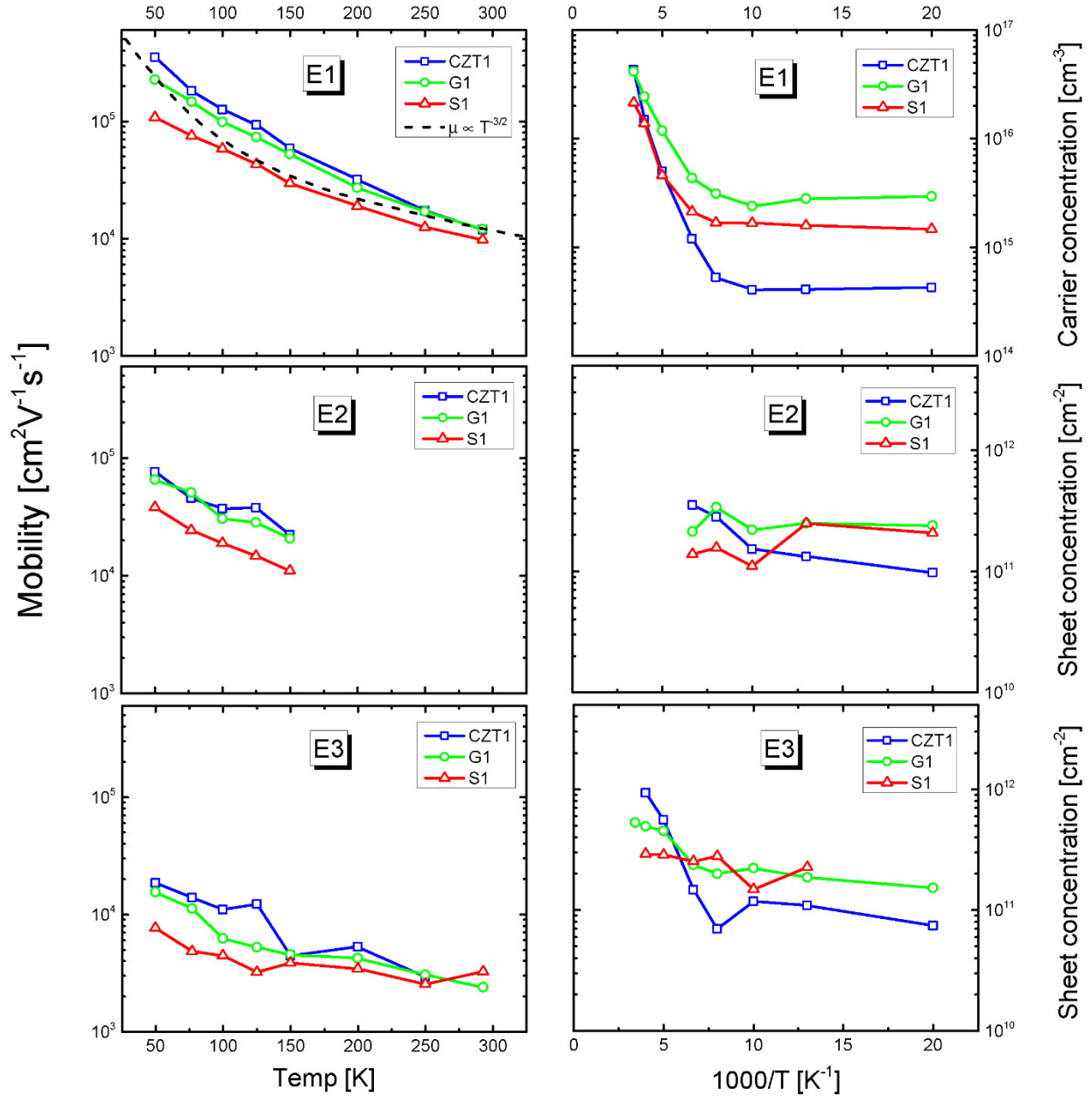


Figure 36: Resolved carrier mobility (left column) and carrier concentration (right column) of LW samples CZT1, G1, and S1. Carrier E1 (bulk), E2, and E3 are shown from top to bottom.

Carrier E3 displays the weakest temperature dependence, again suggesting a more 2D-like nature. However, below 150 K, there exists a slight temperature dependence in the mobility of E3, as well as an increasing discrepancy amongst samples. If the substrate-interface is in fact contributing to the E3 peak at 50 K, it is worth noting the superior mobility of samples CZT1 and G1 when compared to that of S1, a possible indication of material quality in that region.

An interesting feature that is ubiquitous in all three samples is a low mobility hole peak that emerges with increasing temperature, typically above 125 K. For an x-value of 0.22 and In doping level of $1 \times 10^{15} \text{ cm}^{-3}$, a minority carrier hole concentration of $6.4 \times 10^{14} \text{ cm}^{-3}$ is predicted at 150 K, which could realistically manifest in the mobility spectrum. Although the resolved carriers reported here possess very low conductivity, the mobility and carrier concentration match expected minority carrier hole parameters. Figure 37 shows the the MSA peak values of low mobility hole carriers in all samples versus temperature with comparison to a modeled hole mobility using an x-value of 0.22, appearing in good agreement with predicted values. The low conductivities ($< 2\%$ of overall conductivity) ultimately prevent definitive conclusions to be made due the potential introduction of artifacts from measurement error such as sample non-uniformities or non-ideal contacts, but the consistency amongst samples and the temperature behavior compared with theory are compelling.

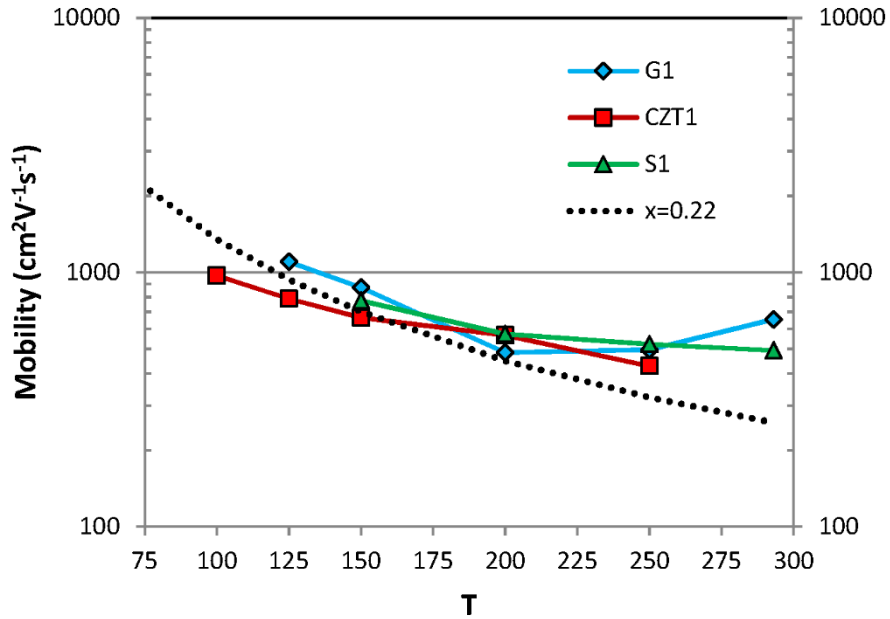


Figure 37: Mobility versus temperature of low conductivity hole peak in LW samples.

Sample CZT1 presents a particularly enticing opportunity to characterize a minority carrier hole as a result of the low overall n -type doping (mid- 10^{14} cm^{-3}). The temperature dependence of the experimentally determined electron, hole, and calculated intrinsic $n_i = \sqrt{n \cdot p}$ concentrations for sample CZT1 are shown in Figure 38, with comparison to the Hansen and Schmitt equation. For an x -value of 0.22, fitting in the intrinsic region is quite accurate. As temperature drops, the overall conductivity contribution of the hole peak drops dramatically and agreement with theory worsens. Still, the correct temperature behavior is observed for 150 K and above. Although not conclusive, the hole peak at higher temperature appears to be physical.

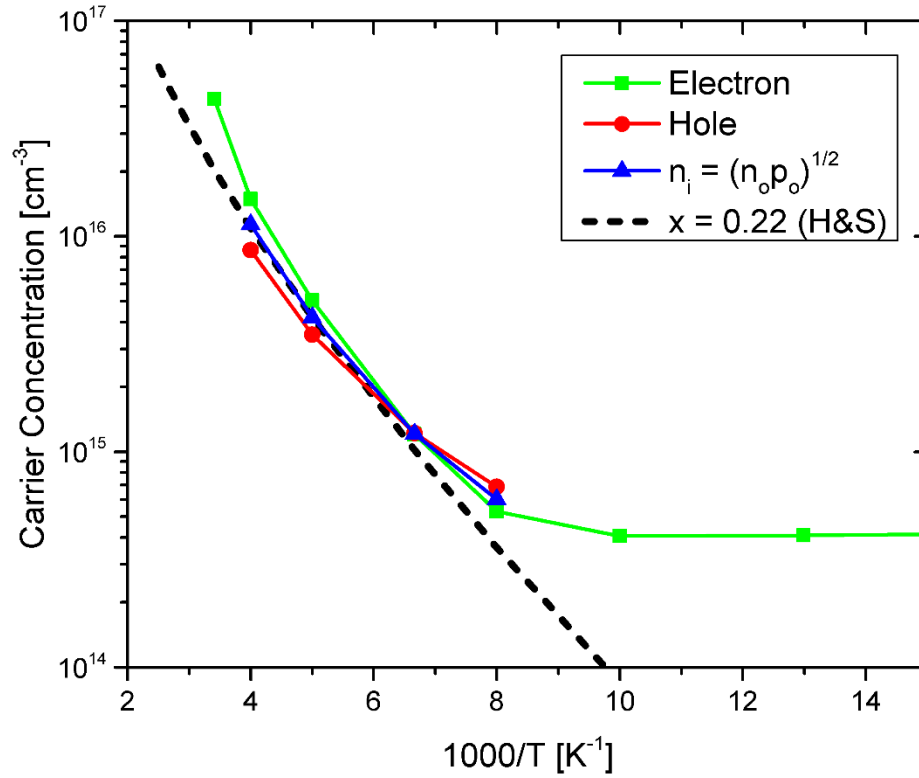


Figure 38: Extracted bulk electron and possible minority carrier hole concentration from sample CZT1. The experimentally determined intrinsic carrier concentration (blue triangle) matches well with theory at high temperature.

Fitting of bulk electron E1 mobility was done following the theoretical scattering mechanisms detailed in Section 2.2. The scattering mechanisms used include polar optical phonon (POP), dislocation, strain field, alloy disorder, ionized impurity, and neutral impurity scattering. The fitting results for samples CZT1, G1, and S1 are shown in Figures 39 - 41, respectively.

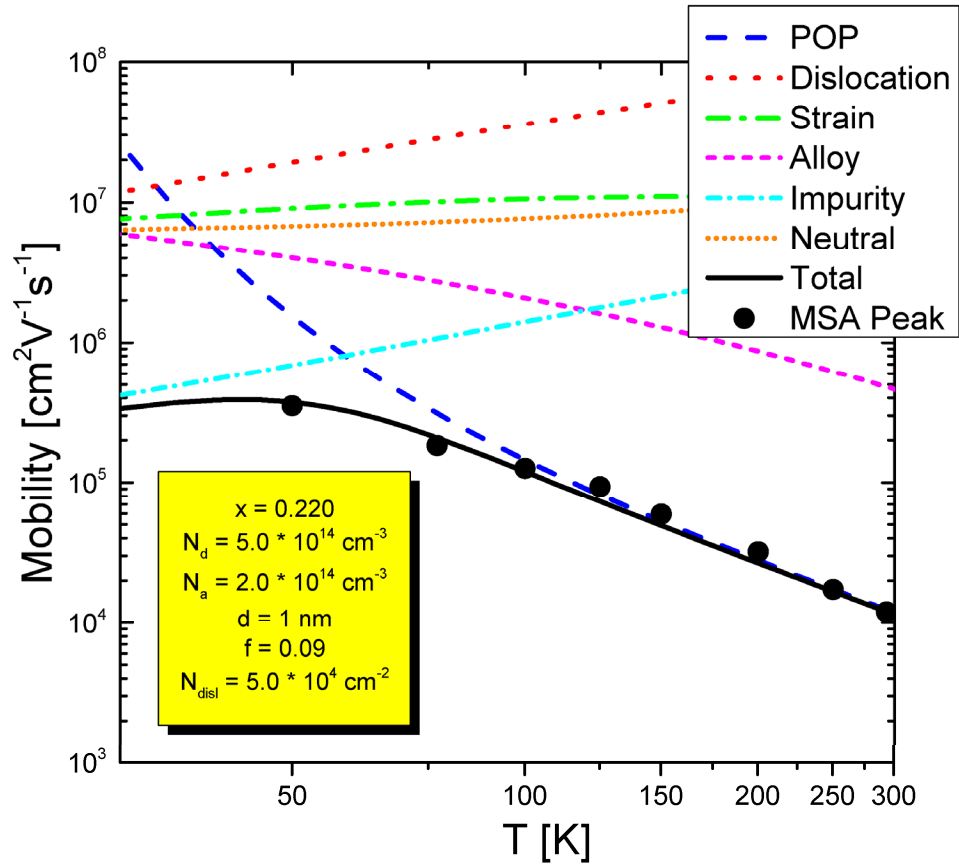


Figure 39: Experimental and theoretical mobility versus temperature of carrier E1 from MCT/CZT sample CZT1.

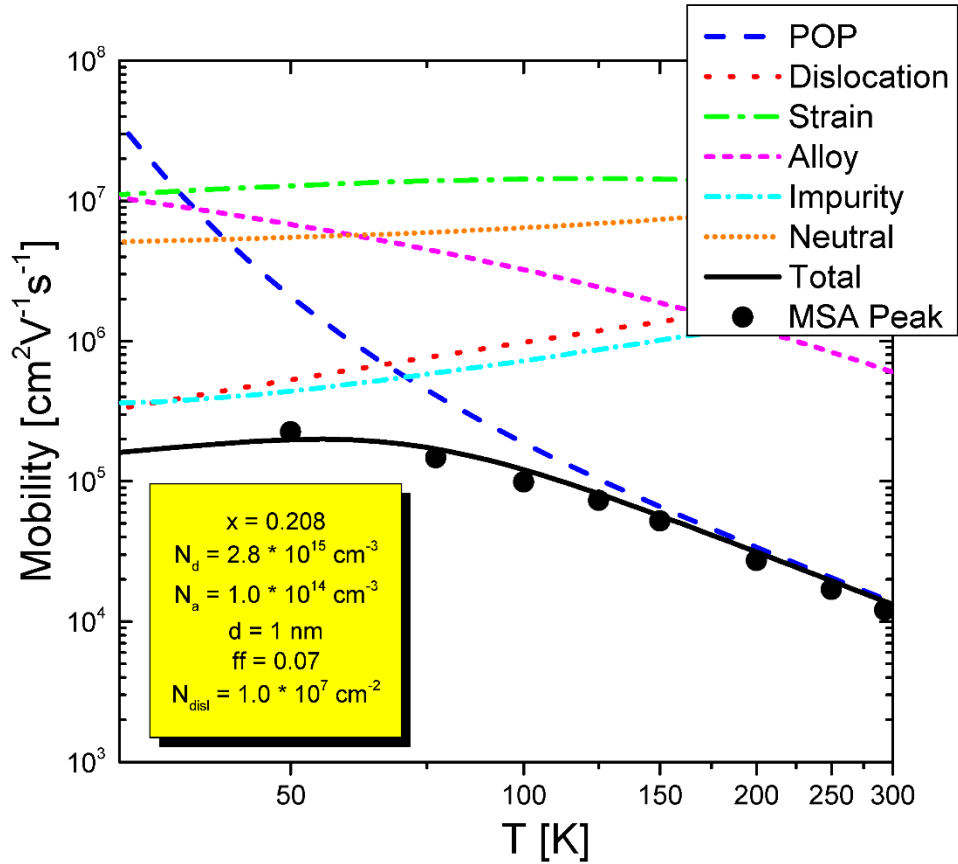


Figure 40: Experimental and theoretical mobility versus temperature of carrier E1 from MCT/CdTe/GaAs sample G1.

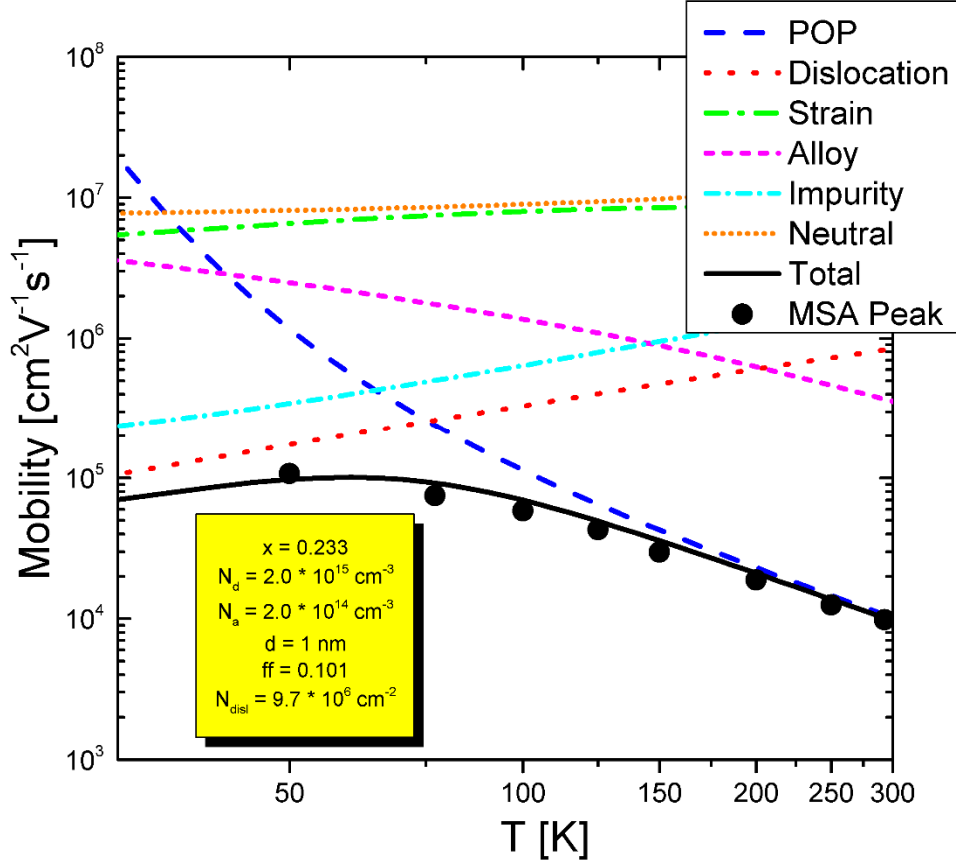


Figure 41: Experimental and theoretical mobility versus temperature of carrier E1 from MCT/CdTe/Si sample S1.

Satisfactory mobility fits were obtained for all samples, with fitting parameters closely matching supplemental measurements. Polar optical phonon scattering dominates for $T > 100$ K in all samples, as expected. Below 100 K, samples G1 and S1 were influenced largely by ionized impurity, POP, and dislocation scattering. Alternatively, sample CZT was dependent on a combination of POP and ionized impurity scattering below 100 K, consistent with previous results on LPE grown LW HgCdTe on CZT [198]. Overall, scattering from neutral impurities, static strain, and alloy disorder were not found to be limiting in LW material.

The occupation rate, f , obtained from the fitting of dislocation scattering agrees nicely with calculations in Section 2.2.1.5, which employ the minimization of free energy approach, and exhibits the proper x -value dependence, namely sample G1 has both the lowest occupation rate ($f = 0.07$) and x -value

($x = 0.208$) of samples in this study. A value of $f = 0.101$ was obtained for sample S1, which is exactly the occupation rate predicted for a LW sample with a dislocation density of $N_{\text{disl}} = 10^6 \text{ cm}^{-2}$ and $N_d = 2 \times 10^{15} \text{ cm}^{-3}$. Despite the difference in x -value between samples S1 and CZT1, results here are consistent with previous observation of a rise in occupation rate with increasing carrier concentration [193], as the carrier concentration of S1 is substantially higher than that of CZT1. The mobility fitting of the bulk electron indicates the importance of dislocation density as both S1 and G1 experience a significant reduction in mobility at low temperature. Calculations at 77 K show that mobility is a factor of 1.3 - 1.5 lower with the inclusion of dislocation scattering for samples grown on alternative substrates.

A summary of sample parameters derived from MSA data is shown in Table VI.

Table VI: Summary of resolved parameters from LW HgCdTe planar layers.

Sample	x-value (FTIR)	x-value (H&S fit)	$\mu_{E1} \propto T^{-a}$	$\mu_{E2} \propto T^{-a}$	$n(77\text{K}) [10^{15} \text{ cm}^{-3}]$	EPD [measured]	EPD [fit] cm^{-2}
CZT1	0.220	0.217	2.1	1.0	0.5	2×10^4	5×10^4
G1	0.208	0.204	1.9	1.0	2.8	1.3×10^7	1×10^7
S1	0.233	0.228	1.6	1.1	2.0	9.7×10^6	9.7×10^6

The MSA results have shown that dislocations act as effective scattering centers, reducing mobility at lower temperatures. The fitting of experimental data with relevant scattering mechanisms was determined to be an effective means of assessing the impact dislocations have on bulk electron mobility. To better understand the impact of dislocations on transport, PCD measurements were made to examine if SRH recombination centers associated with dislocations are present [236].

4.2.2.2 PCD and IV results

The temperature dependent minority carrier lifetime of sample G1 is shown in Figure 42, with Auger and radiative recombination representing the intrinsic lifetime. When combined, the expected

lifetime at 77 K is 163 ns, substantially higher than the measured lifetime of 30 ns. In order to properly model the lifetime an SRH component is included and is expected to decrease with increasing dislocation density [92]. The trap level is assumed to be mid-gap for simplicity. Using $\tau_{p0} = 50 \text{ ns}$, a satisfactory fit to the experimental data is obtained.

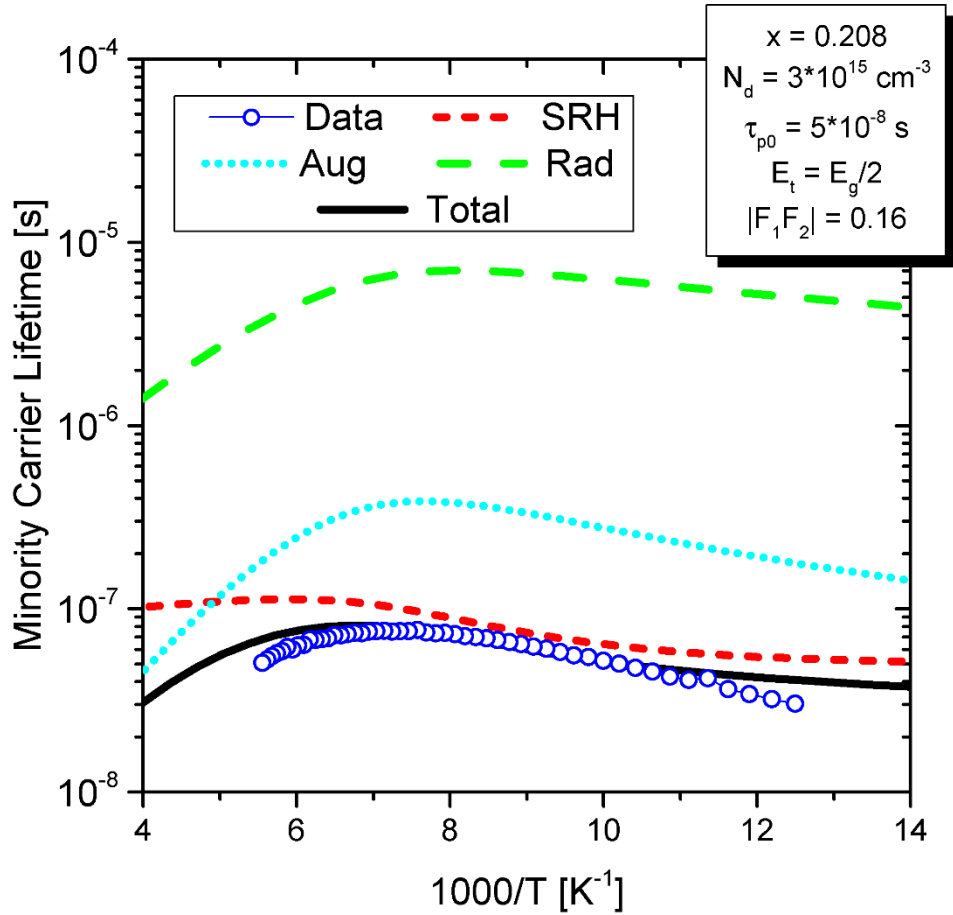


Figure 42: PCD lifetime data for sample G1. Theoretical calculations of radiative (Rad), Auger (Aug), and SRH are shown.

Previous correlation between minority carrier lifetime and dislocations in LW MBE-grown HgCdTe have shown a reduction in lifetime at 77 K for EPD values greater than 10^6 cm^{-2} [91]. The study suggests that for an EPD of $\sim 10^7 \text{ cm}^{-2}$, a factor of ~ 7 reduction in lifetime can be expected, which compares nicely with the factor ~ 5 reduction seen in G1. Another study measured the lifetime before and

after hydrogen passivation using an electron cyclotron resonance (ECR) plasma on samples with an EPD $\sim 10^7 \text{ cm}^{-2}$, finding that both low temperature mobility and lifetime were improved after passivation of dangling bonds [75]. In that study, the lifetime at 77 K was also observed to be a factor of ~ 5 lower for samples receiving no hydrogen passivation, supporting the notion that dislocations are responsible for the SRH lifetime in sample G1.

Comparatively, lifetimes of samples grown on CZT substrates at various doping levels are shown in Figure 43. Theoretical curves are obtained with the sole inclusion of Auger recombination, implying that $\tau_{SRH} > \tau_{intrinsic}$, as all low temperature results fall within the predicted range.

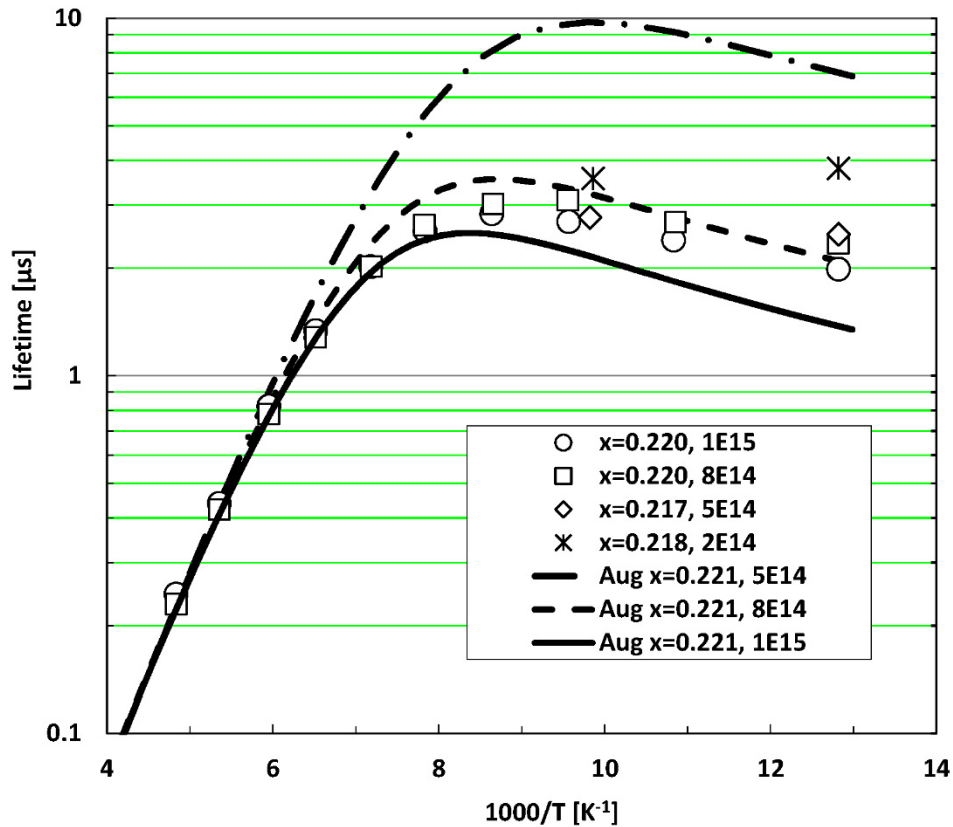


Figure 43: Lifetimes of samples grown on CZT substrates, indicating intrinsic recombination.

Lifetime values are used to analyze IV curves on planar devices measured at 78 K. Junction formation is achieved via ion-implantation of arsenic to produce a heavily doped p -type region

($N_a \sim 10^{17} \text{ cm}^{-3}$) such that the depletion region exists almost exclusively within the low doped n -type absorber region [237]. Lateral-diffusion current [238, 239] associated with the device architecture must be taken into account via the following equations:

$$J_{diff,3D} = J_{diff,1D} \left(1 + G_r(x_j) \right) \quad (4.1)$$

$$G_r(x_j) = \left(\frac{2}{x_j} \right) \frac{K_1(x_j)}{K_0(x_j)}$$

where $x_j = \frac{L_h}{R_j}$ is the ratio between the hole diffusion length L_h and the junction radius R_j , and K_i is the modified Bessel function of the i -th order. Figure 44 shows the theoretical and measured dark current of a 60 μm radius diode, assuming a hole diffusion length of 39 μm and a lifetime of 3.5 μs . Excellent agreement between measured and modelled dark current is achieved including only 3D diffusion and GR currents, with the primary contribution coming from diffusion. At 125 K, successful fitting is obtained for a diffusion length of $L_h = 44 \mu\text{m}$. It is interesting to note that if we take the lifetime to be intrinsically limited (2.9 μs at 125K), this result corresponds to a minority carrier hole mobility of 620 $\text{cm}^2\text{V}^{-1}\text{s}^{-1}$, which agrees reasonably well with the MSA resolved value of 787 $\text{cm}^2\text{V}^{-1}\text{s}^{-1}$, which again supports the notion that the hole peak is physically relevant.

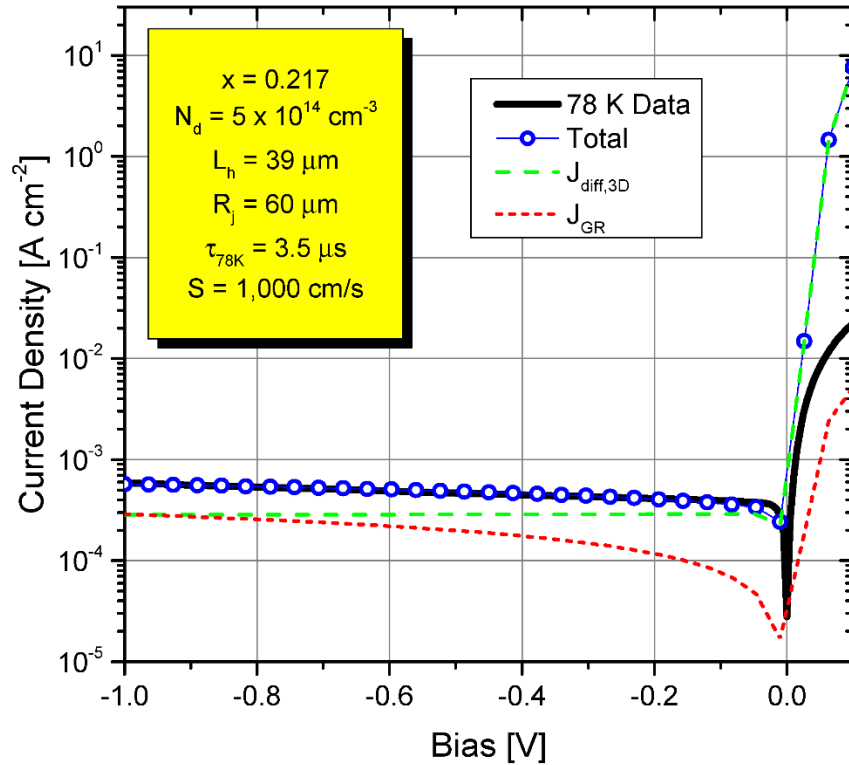


Figure 44: Sample CZT1 dark IV on a 60 μm radius planar diode. Model includes 3D diffusion and GR currents.

Comparative planar diodes on sample G1 displayed very different results and are almost entirely dominated by tunneling currents. Figure 45 shows the dark current of a 15 μm diode at 78 K. The tunneling current [239, 240] is a simplified two-parameter equation that makes no discrimination between B2B and TAT tunneling. The bias-dependence of dark current was not seen to match shunt or GR current. It should be noted that the extent of tunneling present in sample G1 far exceeds the B2B tunneling contribution predicted based on x -value and doping, suggesting the excesses tunneling current is extrinsic in nature.

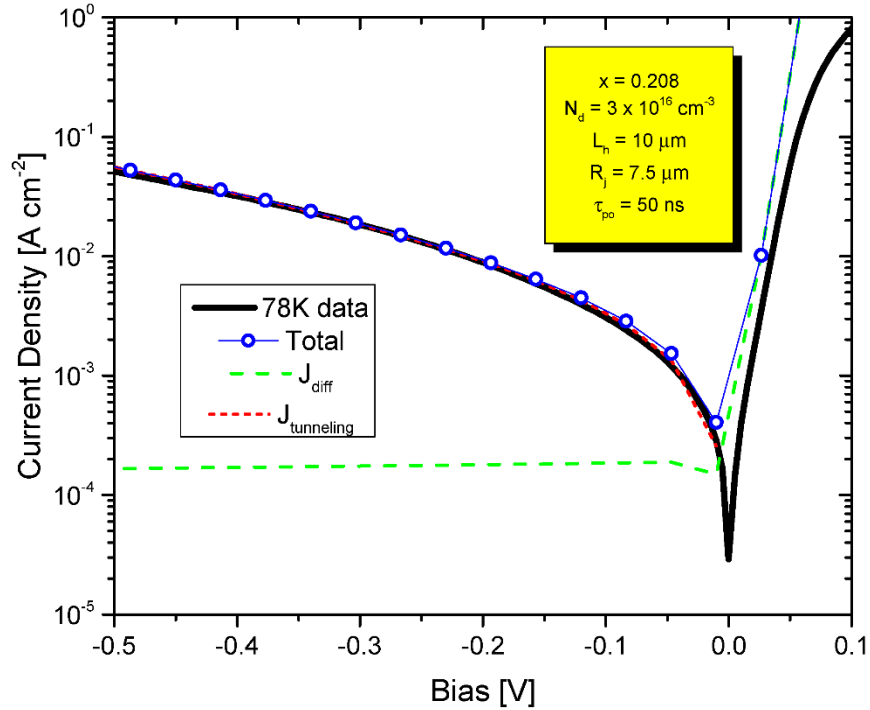


Figure 45: Sample G1 dark IV on a 7.5 μm radius planar diode. Model includes diffusion and tunneling currents.

4.2.3 Summary

In this section we have determined the mobility spectrum of LW n -type HgCdTe grown by MBE. Transport properties were explored in regards to substrate choice, with results presented for growth on CZT, GaAs, and Si. It was shown that the layers possess similar fundamental carrier species regardless of substrate.

Experimental data was used to accurately quantify x -value, doping concentration, and dislocation density in the bulk. All results were in agreement with supplementary characterization data. Bulk electron mobility was limited by ionized impurity scattering at low temperature for growth on CZT, while dislocation scattering was seen to influence low temperature mobility for growth on GaAs and Si. Higher x -value regions, such as wider-gap caps or transitional regions near the substrate-interface, manifest as an

additional carrier peak at a characteristically lower mobility than that of the bulk electron. This carrier species was seen to merge with the bulk electron at elevated temperatures.

Low conductivity hole peaks were observed in all samples at elevated temperatures. Although not conclusive, the resolved carrier concentration and mobilities appear in agreement with theory of a minority carrier hole species. Fitting the lateral diffusion component of IV curves at 125 K also supported the MSA characterization of a minority hole, as seen in the mobility agreement between the two methodologies.

PCD measurements showed a correlation between dislocation scattering limited mobility and SRH-limited minority carrier lifetime, suggesting dislocations to be effective scattering and recombination centers. Intrinsically limited lifetimes were obtained for growth on CZT and were successfully used to fit dark current of planar devices. Alternatively, planar devices on alternative substrates displayed pronounced tunneling currents, which may correlate to dislocation induced mid-gap trap states.

4.3 P+/n heterojunction HgCdTe

4.3.1 Experimental

Experimental growth techniques and sample preparation follow those outlined in Section 4.2, with the largest exceptions being the method of *p*-type doping and Hall sample patterning. Previously, planar devices were doped *ex-situ* via ion implantation, whereas heterojunction (HJ) layers in this section are doped *in-situ* via an arsenic cracker cell. The Hall patterning is a reaction to the increased complexity of the samples under test. In order to improve results Greek cross structures ($A/S \sim 3$) are patterned for Hall measurement. Lateral contacts are made on all Hall samples to ensure conductive layers are connected in parallel.

The typical P+/n heterojunction consists of a lightly *n*-type doping absorber region and a wider-gap highly doping *p*-type cap, as can be seen in the compositional profile of Figure 46. The cap is grown

at higher x -value in order to reduce dark current contributions from this region, and highly doped to ensure the depletion region extends primarily into the n -type absorber. The four samples grown for this study possess MW ($x \sim 0.30$) absorbers and are grown on lattice-matched CZT, and lattice-mismatched CdTe/GaAs and CdTe/Si. Details and sample identifiers are given in Table VII.

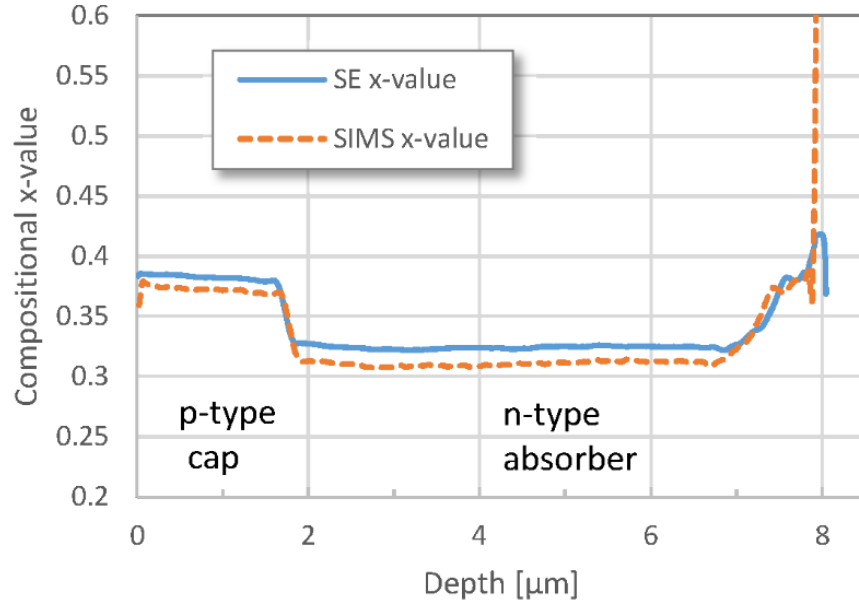


Figure 46: Typical P+/n structure in this work. The post-growth SIMS and SE profiles are for the MW MCT/Si sample S2_MW.

Table VII: Sample information of P+/n MW HgCdTe layers.

Sample	Substrate	Growth	t [μm]	Cap t [μm]	x-value (SIMS)	Δx (cap)	N_d [cm^{-3}] (SIMS)	EPD [cm^{-2}]
S2_MW	Si	MBE	8.0	1.8	0.310	0.061	3.0×10^{15}	9.4×10^6
G2_MW	GaAs	MBE	3.9	0.9	0.312	0.051	2.4×10^{15}	1.9×10^7
G3_MW	GaAs	MBE	4.3	1.1	0.301	0.048	2.3×10^{15}	1.8×10^7
CZT2_MW	CdZnTe	LPE	17.3	1.7	0.264	0.034	1.8×10^{15}	n/a

4.3.2 Results

4.3.2.1 MCT/CdTe/Si

Figure 47 shows the mobility spectrum results from sample S2_MW, and contains the expected carriers; a light hole (H1), heavy hole (H2), bulk electron (E1), transitional region electron (E2), and interfacial electrons (E3/E4). The hole activation in the cap appears to be successful, with H2 corresponding to a concentration of $\sim 1 \times 10^{17} \text{ cm}^{-3}$ at 95 K and displays temperature independent behavior. The mobility of H2 is inherently difficult to resolve as the carrier falls well below $1/B_{\text{max}} \sim 1,100 \text{ cm}^2\text{V}^{-1}\text{s}^{-1}$, meaning it is never fully quenched. Additionally, the overall conductivity contribution of H2 is low, ranging between 4-10 %. The primary conductivity contribution comes from the combined E1 and E2 peak, which maintains a high contribution ($\sim 90 \%$) throughout the entire temperature range.

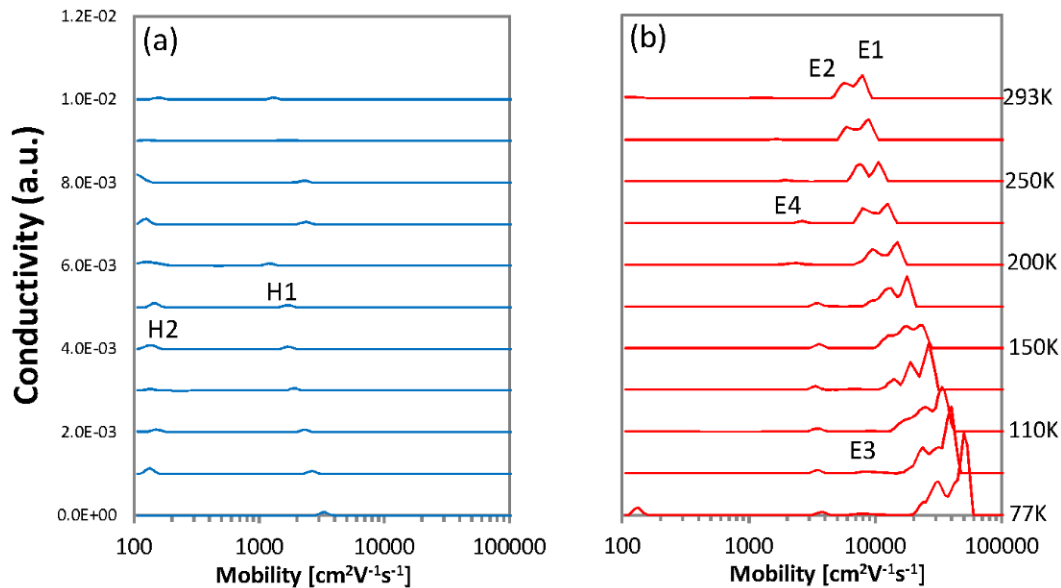


Figure 47: Mobility spectrum temperature evolution of sample S2_MW. Figure (a) shows hole spectra, containing carrier H1 (light hole) and H2 (heavy hole), while Figure (b) shows electron spectra, containing carriers E1 (bulk), E2 (transitional), and E3/E4 (interface).

The mobility and concentration of all carriers resolved in sample S2_MW are shown in Figure 48. Peaks E1 and E2 are combined as they are so tightly spaced, and produce a carrier concentration of $3.5 \times 10^{15} \text{ cm}^{-3}$ after dividing by the absorber thickness. The thicknesses associated with carriers E3, E4, and H1 are not definitively known and are therefore shown as sheet concentration values that fall within a range of $10^{11} - 10^{12} \text{ cm}^{-2}$.

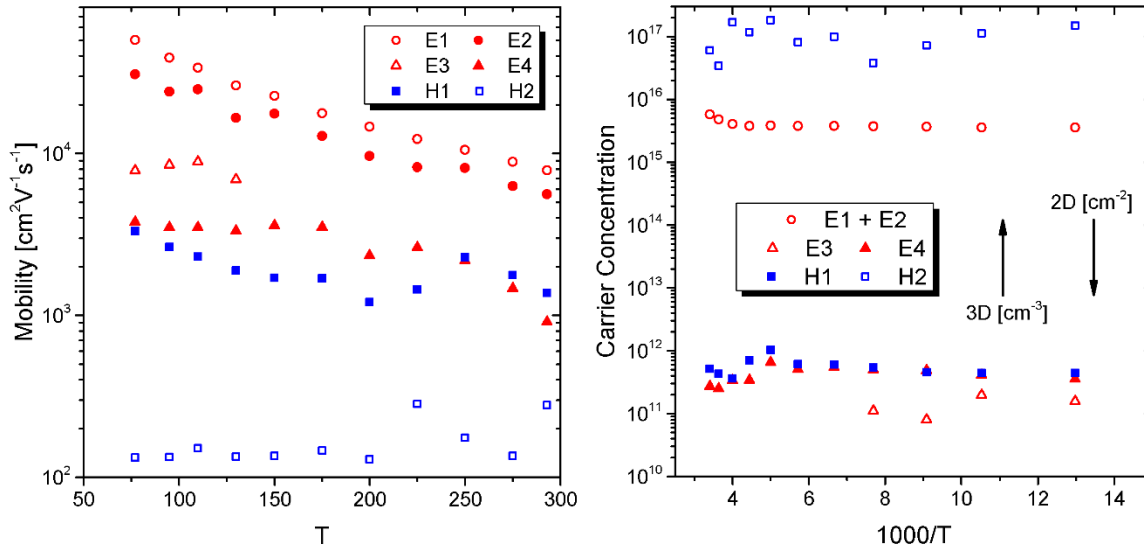


Figure 48: Mobility (left) and carrier concentration (right) versus temperature of all carriers in sample S2_MW.

The mobility of the bulk hole, H2, does not appear to be reliably resolved using MSA. Instead we use the multi-carrier fitting (MCF) [56] procedure, whereby the conductivity tensor and Hall measurements are fitted using the Levenberg-Marquardt algorithm after a predetermined number of carriers is assumed. A comparison between the methods is shown in Figure 49, with the 77 K MCF hole mobility in better agreement with expected values and theoretical calculation shown here [55].

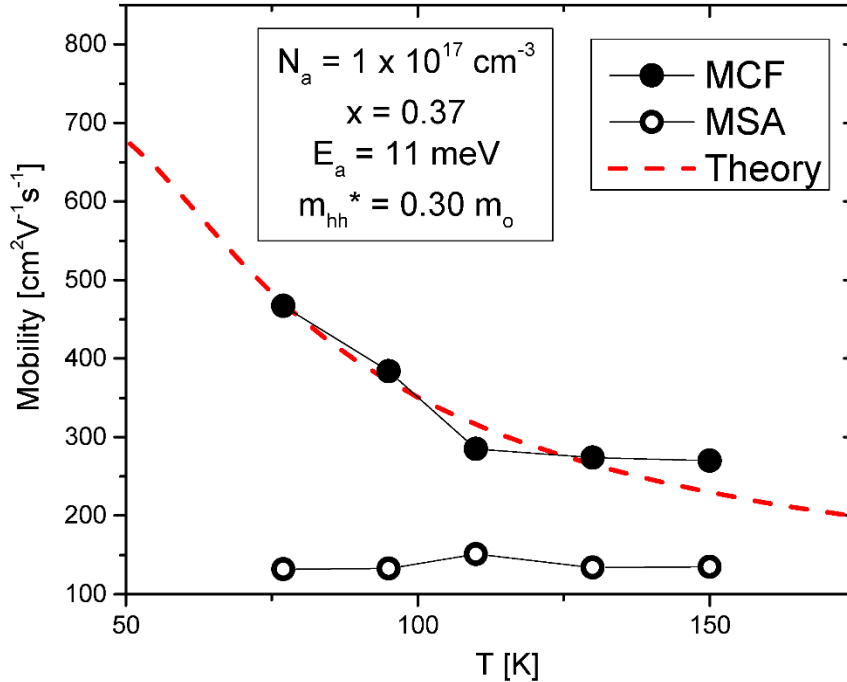


Figure 49: Comparison of cap hole mobility from sample S2_MW using MCF and MSA.

Upon analysis of the bulk electron mobility, it was found that satisfactory fits were only possible after averaging of peaks E1 and E2. The x-value used in fitting the mobility reflected a reduction in the compositional x-value versus that obtained from SIMS measurement, utilizing a value of 0.29 rather than ~0.31. A possible explanation of this result is a real drop in absorber Cd composition during activation/vacancy fill annealing, as SIMS was performed on as-grown material. An alternate interpretation would suggest the SIMS x-value to be unreliable, potentially a result of improper calibration. Regardless, FTIR fitting post-annealing supports the mobility derived x-value, returning an x-value of 0.2905, in excellent agreement with the mobility fitting result. Mobility versus temperature results are shown in Figure 50, predominantly limited by lattice scattering mechanisms except for a significant contribution from dislocation scattering at low temperature. The dislocation density closely matches the measured EPD value of $9.4 \times 10^6 \text{ cm}^{-2}$.

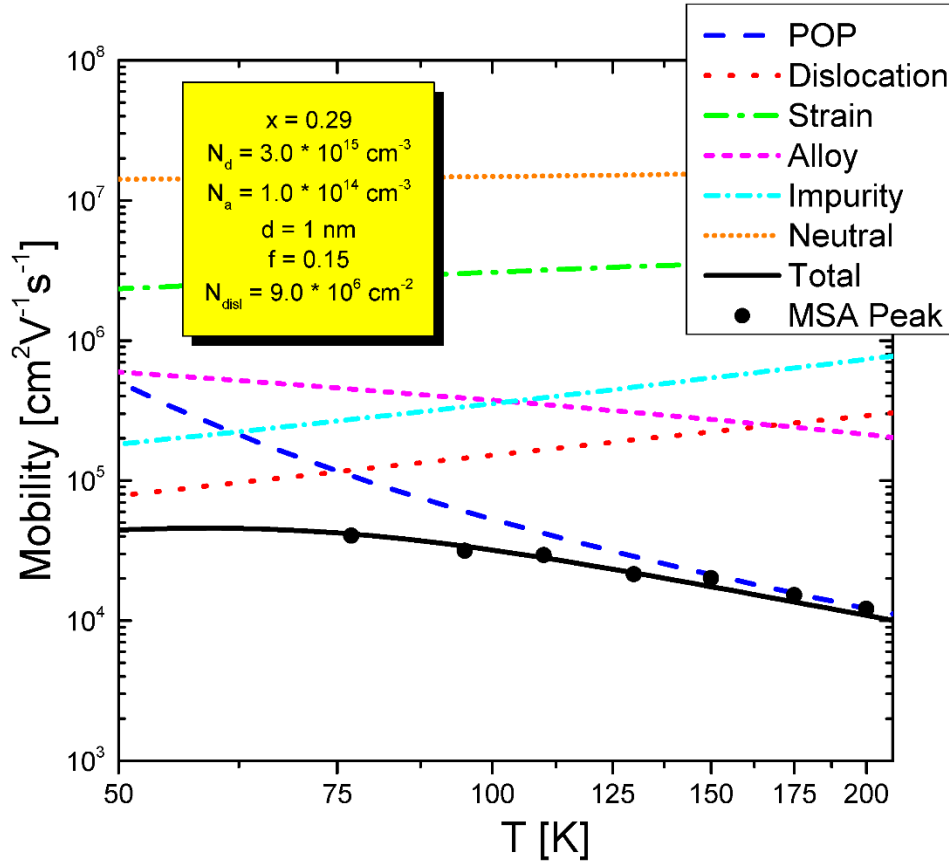


Figure 50: Mobility fitting results for bulk electron in sample S2_MW.

PCD measurements were performed after removing the *p*-type cap and depositing a polycrystalline-CdTe passivation layer. Low temperature results indicate intrinsically limited lifetime values, and are shown in Figure 51. Only a minor SRH-component was necessary in fitting the lifetime. The *x*-value and carrier concentration from mobility-fitting was seen to accurately predict lifetime in this sample. Due to a signal decrease at higher temperatures, lifetime values above 135 K could not be recorded.

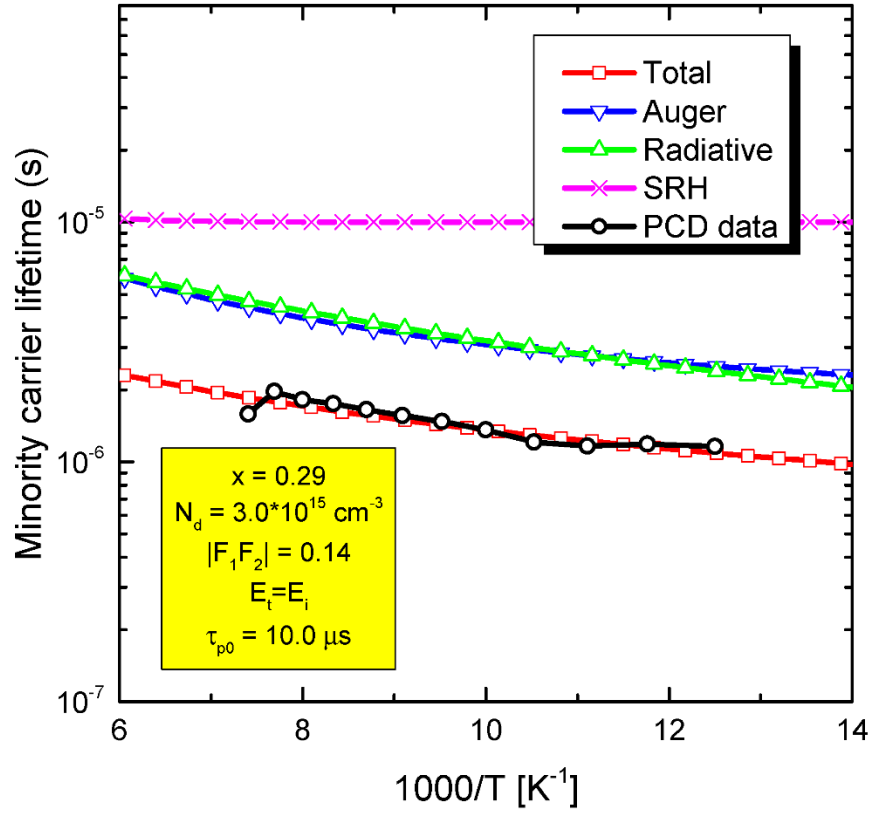


Figure 51: Lifetime fitting results of sample S2_MW.

An array of mesa detectors were fabricated from this material so that IV-characteristics could be determined. Contacts were made to the p -type cap layer using alloyed gold while contacts to the n -type base layer were made using In. A Nomarski image of mesa delineated diodes (pre-contact formation) is shown in Figure 52.

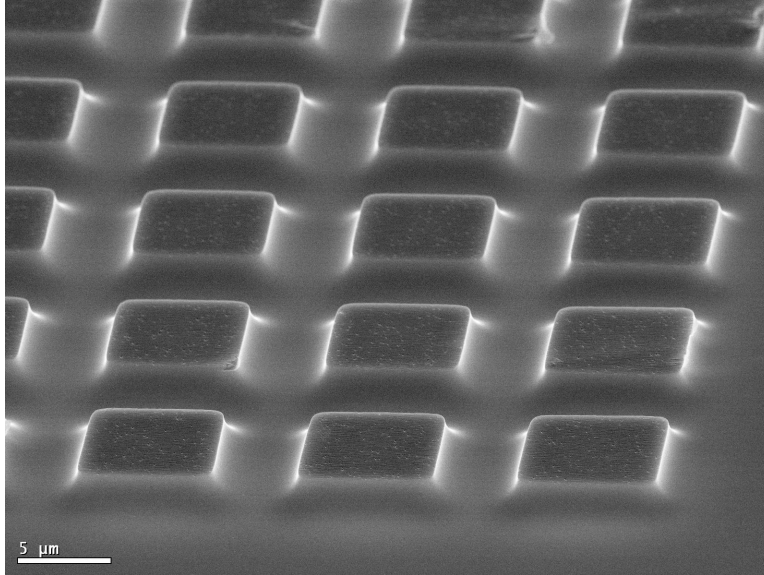


Figure 52: P-on-n mesa diodes fabricated from MCT/CdTe/Si sample S2_MW.

The x -value, p -type and n -type doping concentrations, and lifetimes from MSA/PCD measurements were used to fit IV curves of a $20 \times 20 \mu\text{m}$ mesa diode, with results from 130 K and 150K shown in Figure 53. Consistent fits show the dominate contributions to dark current are via diffusion and tunneling. The SRH-component did not exert a major influence on either PCD lifetime or GR dark current. Forward-bias characteristics indicate mostly diffusion-limited behavior with only a slight GR-component. The mean density of electrical junction defects determined from EBIC measurement was $2.64 \times 10^4 \text{ cm}^{-2}$, and may explain why reliable results were not obtained on larger diodes.

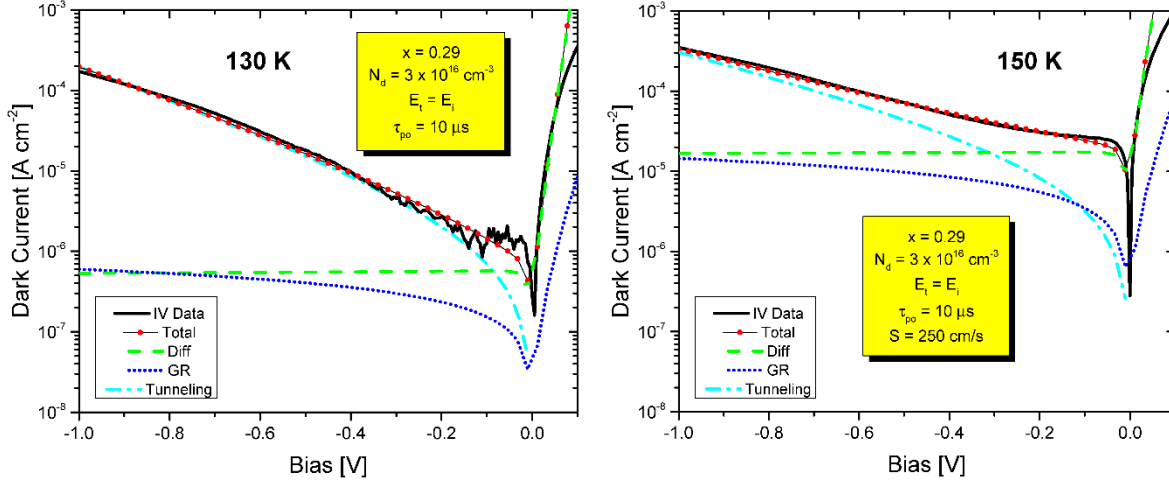


Figure 53: Fitted IV-curves of a 20 x 20 μm mesa diode fabricated from sample S2_MW.

The temperature dependent dark current at -50 meV indicates diffusion limited performance above 130 K with an estimated cut-off of 4.7 μm . Measurements below 130K were system limited. R_0A was measured to be 609 Ω cm^2 at 150K, in reasonable agreement with a modelled value of 695 Ω cm^2 . The presence of tunneling appears to correlate once again with a pronounced contribution from dislocation scattering in the mobility behavior.

4.3.2.2 MCT/GaAs/Si

Two nominally similar MW P+/n devices grown on CdTe/GaAs were investigated. These devices were grown with shorter absorbers (~ 3 μm) at doping concentrations of roughly 2×10^{15} cm^{-3} . A basic overview of the In and Cd (x-value) profiles are shown in Figure 54. Targeted As-doping levels in the cap were low-mid- 10^{17} cm^{-3} .

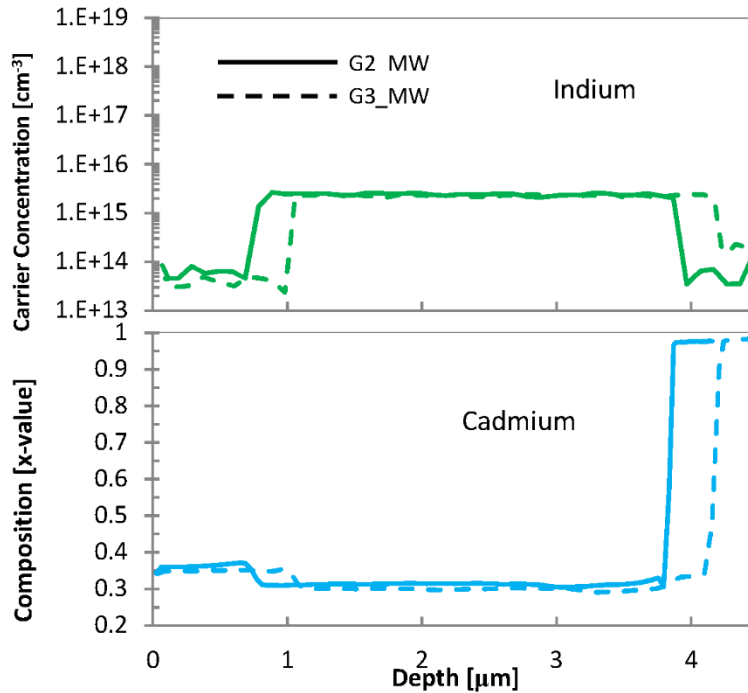


Figure 54: SIMS profiles on samples G2_MW (solid line) and G3_MW (dashed line) for indium and x-value, from top to bottom, respectively.

Figure 55 shows the temperature evolution of sample G2_MW, with linearly spaced spectra to give a more general sense of the conductivity. It is immediately apparent that there is a surprising low amount of *p*-type conduction. After accounting for the cap thickness, the low-temperature hole concentration comes out to be $\sim 2 \times 10^{15} \text{ cm}^{-3}$, which is a significant reduction compared to the value of $\sim 1 \times 10^{17} \text{ cm}^{-3}$ in sample S2_MW. It is difficult to remedy the cause of the low hole conductivity. In the case of sample G2_MW, annealing took place in the exact same tube as S2_MW, which displayed proper activation behavior. Witness samples in the ampoule also showed no indication that annealing had gone awry, as post-annealing Hall results matched previous values.

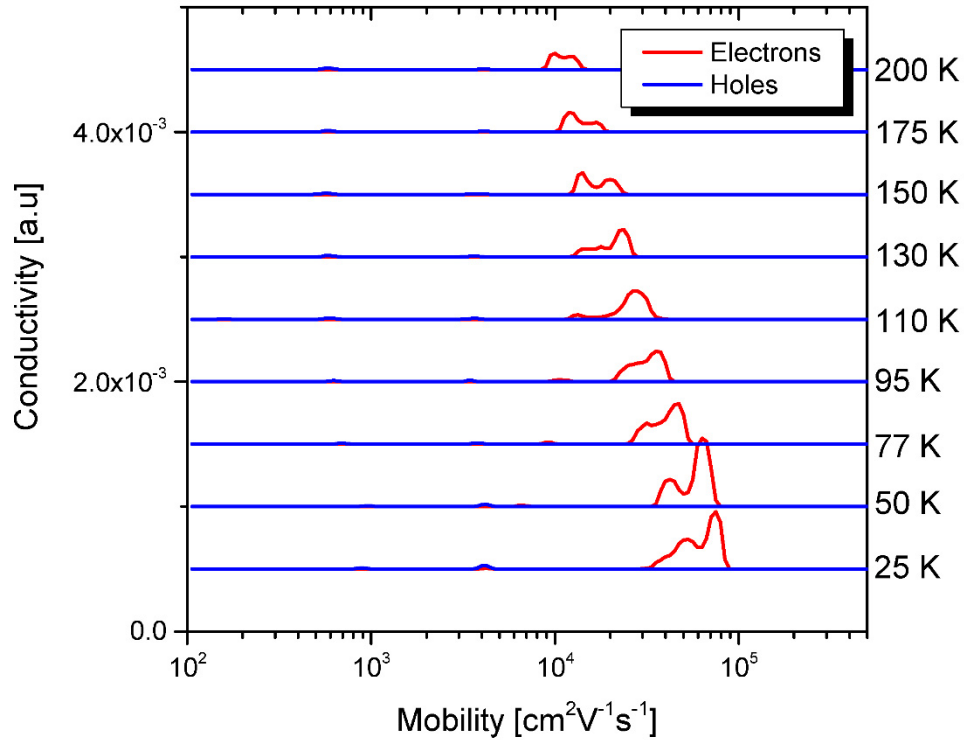


Figure 55: G2_MW mobility spectrum showing electrons (red) and hole (blue) carriers.

Aside from the low *p*-type conduction, the mobility of the bulk hole carrier in sample G2_MW appears well-behaved. The mobility versus temperature of the cap hole is shown in shown in Figure 56, with theoretical mobility from ionized impurity scattering. A doping level of $N_a = 2 \cdot 10^{15} \text{ cm}^{-3}$ was successfully used in fitting the low temperature mobility. A slight deviation between theory and experiment is seen for $T > 150 \text{ K}$ and interpreted as a contribution from polar optical scattering. The fact that the mobility is well-behaved suggests the overall incorporation of As in this layer is far below targeted values rather than insufficient activation during annealing. If insufficient activation was present, conduction in the cap would likely be compensated *n*-type. Furthermore, high levels of inactive As would distort the surrounding lattice, lowering mobility in the cap. Since neither are observed, it is safe to conclude that the cap was grown under improper conditions and that the true doping level is reflected in both the MSA obtained concentration and mobility fitting result.

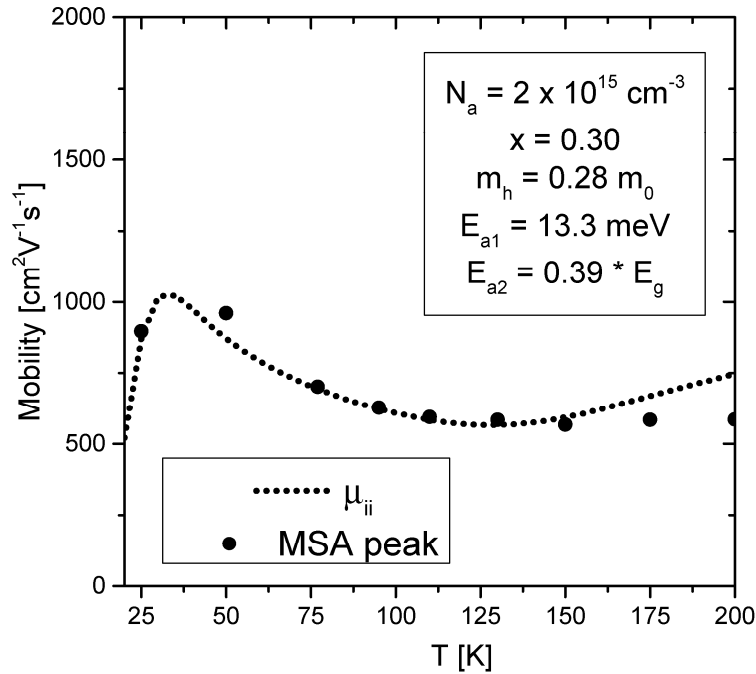


Figure 56: Hole mobility from sample G2_MW with theoretically calculated mobility due to ionized impurity scattering.

The bulk electron mobility fitting of sample G2_MW is shown in Figure 57, and shows no signs of compensation. The low temperature mobility is largely limited by dislocation scattering, with an occupation rate of $f = 0.12$ and a density of $9 \times 10^6 \text{ cm}^{-2}$. As measured EPD values of $1.9 \times 10^7 \text{ cm}^{-2}$ differ somewhat from those used in mobility fitting, but this discrepancy may be explained by the fact that EPD was measured on the As-doped cap layer, which has been demonstrated to possess larger EPDs as compared to absorber layers for MBE growth on alternative substrates [241].

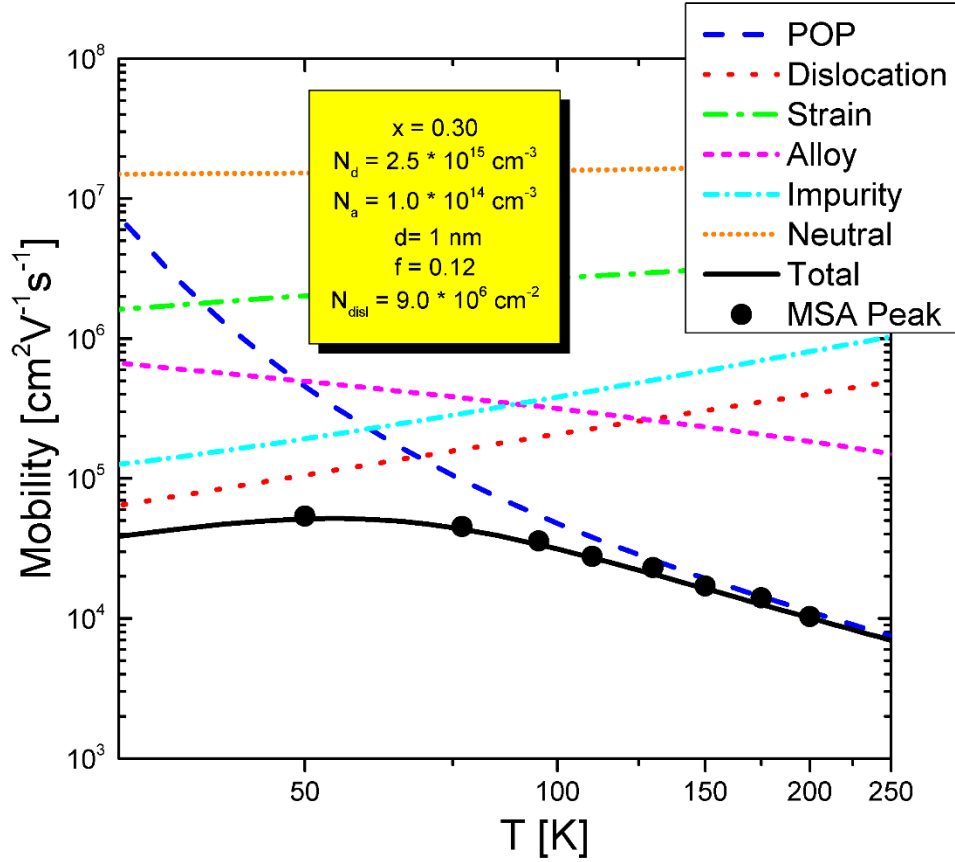


Figure 57: Bulk electron mobility versus temperature in sample G2_MW with theoretical scattering mechanisms.

Attempts to fabricate diode devices from G2_MW were unsuccessful. This is believed to be related to the low effective doping concentration in the cap layer. The low As level implies any device fabricated could no longer be treated as a one-sided junction and could display excessive dark current. More practical difficulties arise from the process of making contacts to the cap, as ohmic contacts on low doped *p*-type material are historically problematic. To reiterate, the cause of the low doping is not thought to be related to improper activation during annealing. Additional samples in the ampoule showed proper activation and the mobility fitting of the hole carrier reflected low doping levels. Although the bulk transport properties in G2_MW are favorable, MSA successfully identified a low effective doping concentration in the cap, immediately rendering this sample as a poor device candidate.

The temperature evolution of sample G3_MW is shown in Figure 58. It is worth noting the

change in scale as compared to the spectra of G2_MW in Figure 55, as G3_MW is much more conductive overall. Although these layers are similar, the mobility spectrum results are in reality quite different. Due to the change in conductivity scale, the bulk hole in the cap layer is not readily visible in Figure 58. A more detailed analysis finds that the low temperature carrier concentration in the cap of sample G3_MW to be $\sim 4 \times 10^{16} \text{ cm}^{-3}$, once again below targeted As-levels. Sample G2_MW experienced the same preparation procedure and annealing recipe as previous samples. Witness samples indicated a successful anneal.

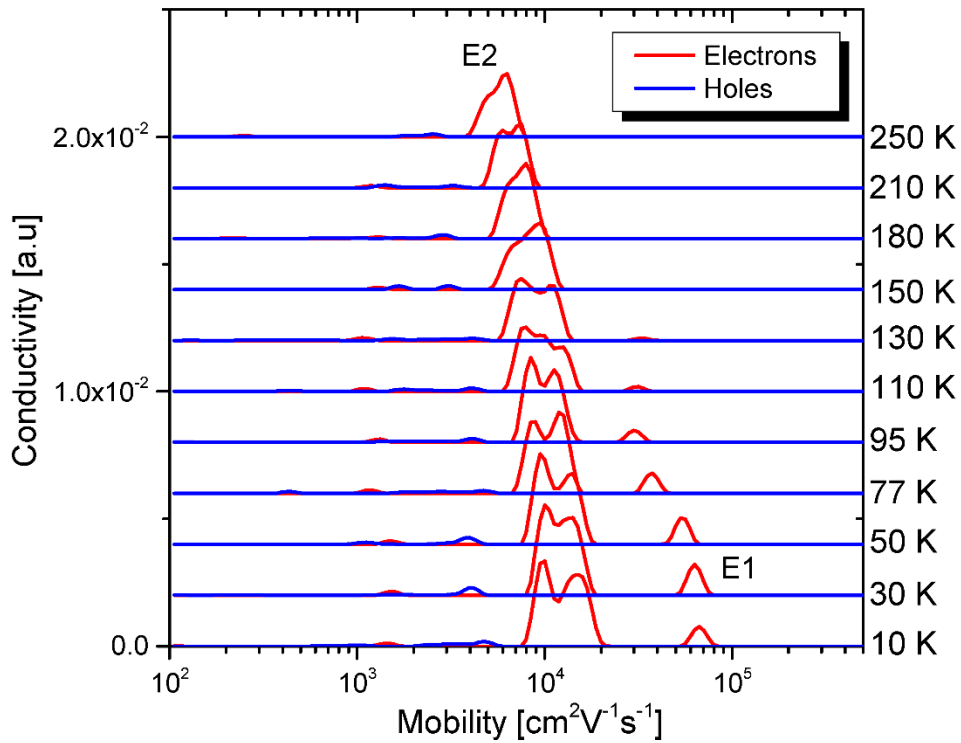


Figure 58: G3_MW mobility spectrum temperature evolution.

An even more noticeable feature in the spectra of G3_MW is the dominant electron (E2) peak $\sim 10,000 \text{ cm}^2\text{V}^{-1}\text{s}^{-1}$. The peak is in fact so conductive that it inhibits the resolution of the bulk electron (E1) species above $\sim 100 \text{ K}$. The sheet concentration of carrier E2 is $\sim 1.7 \times 10^{13} \text{ cm}^{-2}$ throughout the temperature range, showing no activation near room temperature. The carrier represents between 85-90%

of total conduction in sample G3_MW. If carrier E2 was to be distributed evenly throughout the entire epilayer, this would correspond to a concentration of $\sim 4.3 \times 10^{16} \text{ cm}^{-3}$, an order of magnitude higher than In doping levels. Since we are interpreting carrier E1 to be associated with the absorber, this seems very unlikely given that the mobility of E1 is so high at low temperature ($\sim 54,000 \text{ cm}^2\text{V}^{-1}\text{s}^{-1}$ at 50 K).

It is unclear if E2 can be attributed to a surface inversion layer, partial conduction in the cap layer, conduction near the substrate interface, or some combination thereof. Reported values on the sheet concentration at the surface range from low- 10^{11} to low- 10^{12} cm^{-2} [233, 235]. Results on LW layers in this work determined conduction near the substrate interface at levels of approximately $1 \times 10^{12} \text{ cm}^{-2}$. Therefore, the exceedingly high sheet concentration of E2 ($1.7 \times 10^{13} \text{ cm}^{-2}$) cannot be adequately explained by normal behavior in either region. An additional sample from this layer showed no indication of the E2 carrier after cap removal, strong evidence that the carrier resides at the surface, within the cap, or near the depletion region, all of which would have a negative impact on diode performance.

The prominence of the E2 carrier obscures an accurate determination of the bulk electron E1 at all temperatures. Mobility values of E1 are restricted, but MCF was used to characterize low temperature behavior. The mobility is limited mostly by ionized impurity scattering but shows a contribution from dislocation scattering as well. The x-value and doping according to mobility values are roughly $x \sim 0.31$ and $N_d \sim 2 \times 10^{15} \text{ cm}^{-3}$.

The lifetime in the absorber was investigated after chemically etching off the cap layer and CdTe surface passivation. The temperature dependent results are shown in Figure 59. The fitted parameters of $x = 0.285$ and $N_d = 2.2 \times 10^{15} \text{ cm}^{-3}$ produced an excellent fit across the entire temperature range, showing that the lifetime behavior in the absorber is limited by intrinsic mechanisms. Based upon the low temperature MSA mobility and minority carrier lifetime, the absorber material of G3_MW appears to be high quality.

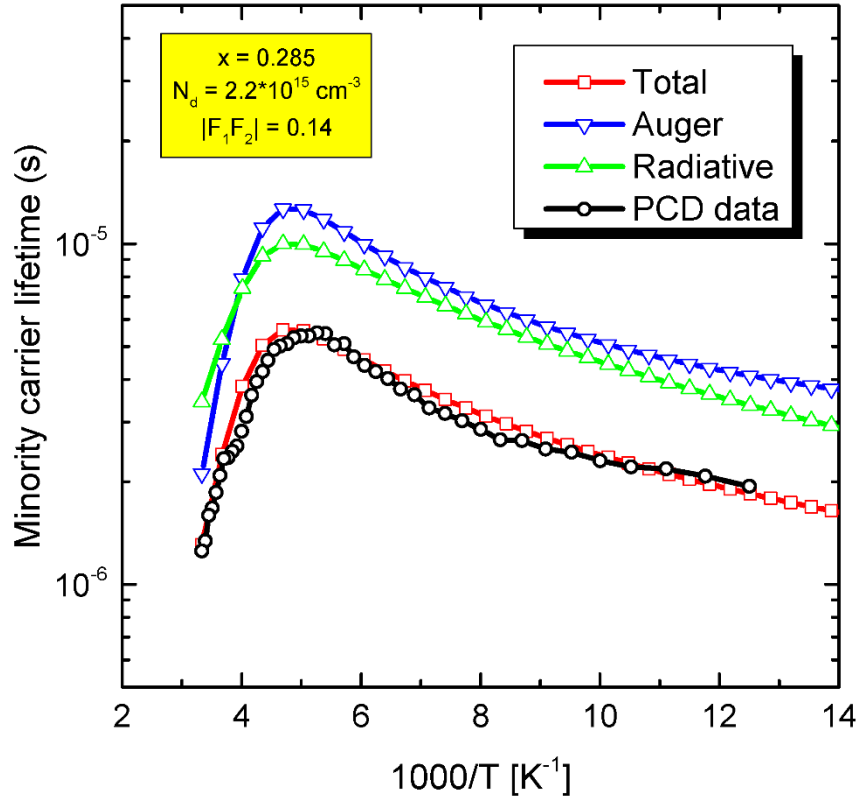


Figure 59: Lifetime versus temperature of G3_MW absorber layer.

A number of mesa diodes were fabricated and tested from sample G3_MW. The overall consistency across tested diodes was very poor suggesting uniformity issues. Dark current at operational bias was seen to spread across roughly four orders of magnitude. The IV curves from two of the best mesa diodes at 162 K show pronounced contributions from tunneling and are shown in Figure 60 (Left: 50 μm circle. Right: 80 μm circle). Both diffusion and GR currents were present. A cut-off of $\lambda_{co} = 4.45\mu\text{m}$ was determined from temperature dependent dark current. Contributions from GR were not expected based upon PCD measurement and may indicate the junction is within the wider-gap cap region. The x-value and doping used in fitting are slightly higher than those used in fitting the lifetime, but are in better agreement with mobility calculations and reverse bias dark current versus temperature. The high degree of non-uniformity of diodes is thought to be linked to the presence of the E2 carrier determined by MSA.

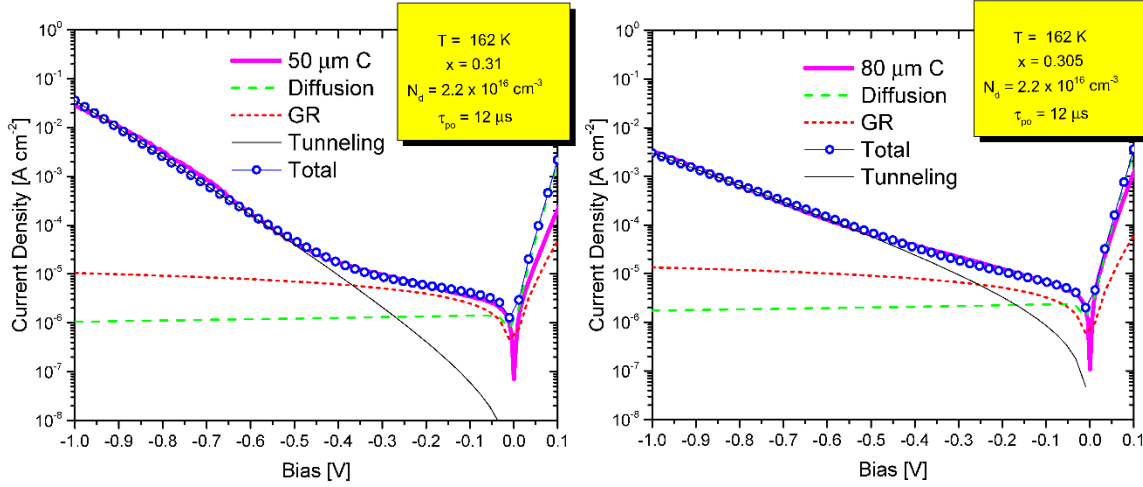


Figure 60: IV characteristics of sample G3_MW mesa diodes. Left figure is for a 50 μm circular diode, while right figure is for an 80 μm circular diode. Pronounced tunneling (thin solid black line) is evident in both diodes. GR (short dash red) and diffusion (long dash green) are also present in both cases at low reverse bias.

4.3.2.3 MCT/CZT

Sample CZT2_MW has a few key differences that separate it from previously analyzed MW heterojunctions in this work. The first is that the layer was grown via liquid-phase epitaxy (LPE) and has a significantly thicker absorber layer (~ 14 μm). As a consequence of LPE growth, the transitional region near the substrate interface is also much wider. While MBE samples in this work have shown transitional regions of approximately 1 - 1.5 μm, sample CZT2_MW has a transitional region of ~3 - 4 μm. Additionally, dislocation density in sample CZT2_MW is not expected to have an impact due to low densities for lattice-matched growth. The SIMS In, As, and compositional profiles are shown in Figure 61. The layer is grown under Hg-rich conditions, and therefore the As dopant is considered to be electrically active as-grown [242].

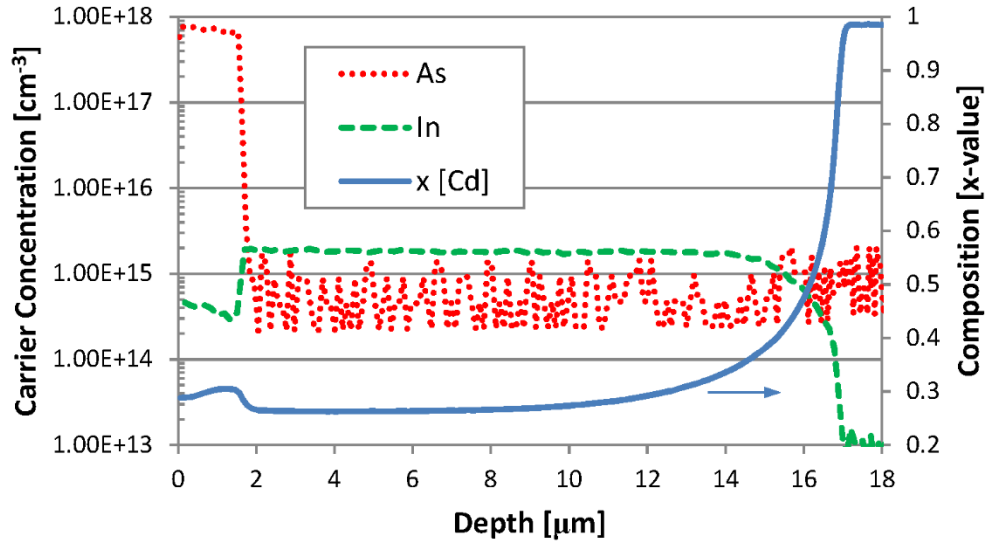


Figure 61: SIMS profiles of CZT2_MW. Indium (dashed line) and arsenic (dotted line) are shown on the primary axis, while composition (solid line) is shown on the secondary axis.

The mobility spectrum temperature evolution of CZT2_MW is shown in Figure 62, with 4 electron carriers and 2 hole carriers identified. The increased amount of electron carriers is likely due to the gradual compositional gradient characteristic of LPE-grown layers, with carriers E2 and E3 attributed to this effect. Carrier E1 remains identified as the bulk electron, while E4 is associated with the surface/substrate-interface. Again, the mobility of the bulk hole carrier in the cap (H2) presents an issue for MSA, with too low of a mobility to accurately quantify. Regardless, based on the conductivity of the hole carrier using MCF, the As appears to be completely electrically active as-grown.

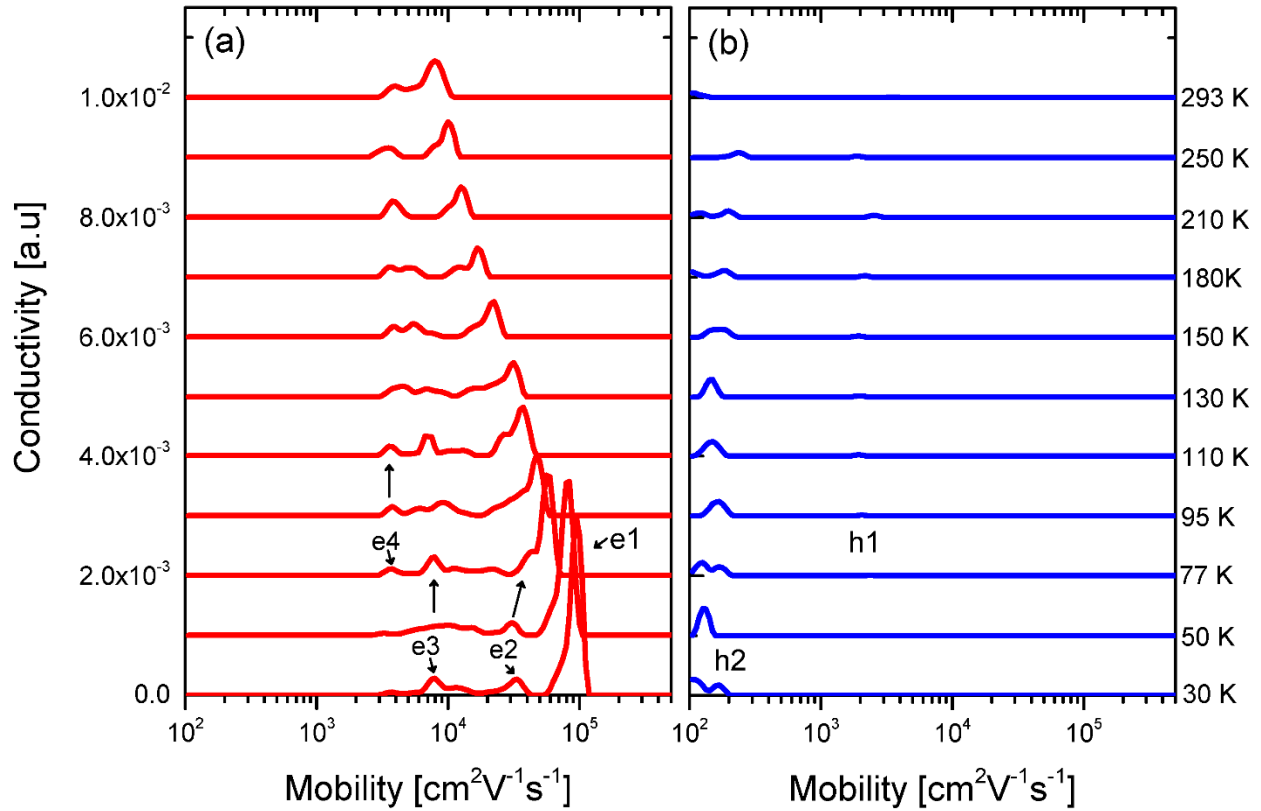


Figure 62: Mobility spectrum temperature evolution of electrons (left) and holes (right) from sample CZT2_MW.

The bandgap of the absorber was determined from measurements performed using the Thermo Nicolet Nexus 870. Bandgap versus temperature for sample CZT2_MW are shown in Figure 63, with fitting according to the Hansen [12] and Lowney [14] expressions. The fitting results are in agreement with one another, determining that $x \sim 0.2815$. The inset of Figure 63 shows the first derivative of the spectral response at 80 K, with the clearly identifiable peak that determines the optical bandgap.

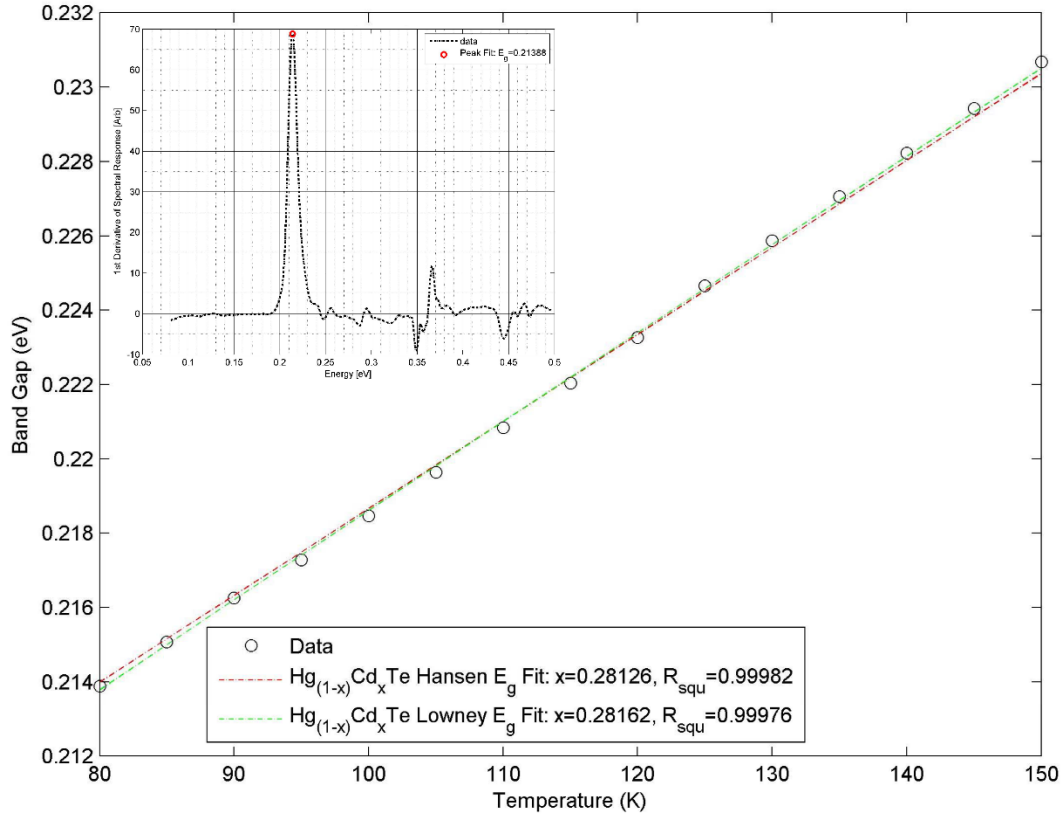


Figure 63: Bandgap versus temperature of sample CZT2_MW absorber as determined from first-derivative of spectral response measurement. Fitting of the bandgap temperature dependence yielded an x-value of ~ 0.2815 . Inset graph shows first derivative of spectral response at 80 K.

The x-value is used to analyze the mobility of the bulk electron. Experimental data and theoretical modelling of scattering mechanisms are shown in Figure 64, with the low temperature mobility limited by ionized impurity scattering. Using MSA derived sheet concentration, the carrier concentration determined from mobility-fitting suggests the bulk electron is localized to only $\sim 3 \mu\text{m}$ worth of absorber material, likely at the onset of the absorber region closest to the junction. Using the same approach, additional carriers E2 and E3 would then correspond to approximately $\sim 3.5 \mu\text{m}$ and $\sim 9 \mu\text{m}$ worth of absorber material, respectively, which agrees very nicely with the overall absorber thickness. The average x-values of these regions reflect the changes of mobility determined by MSA.

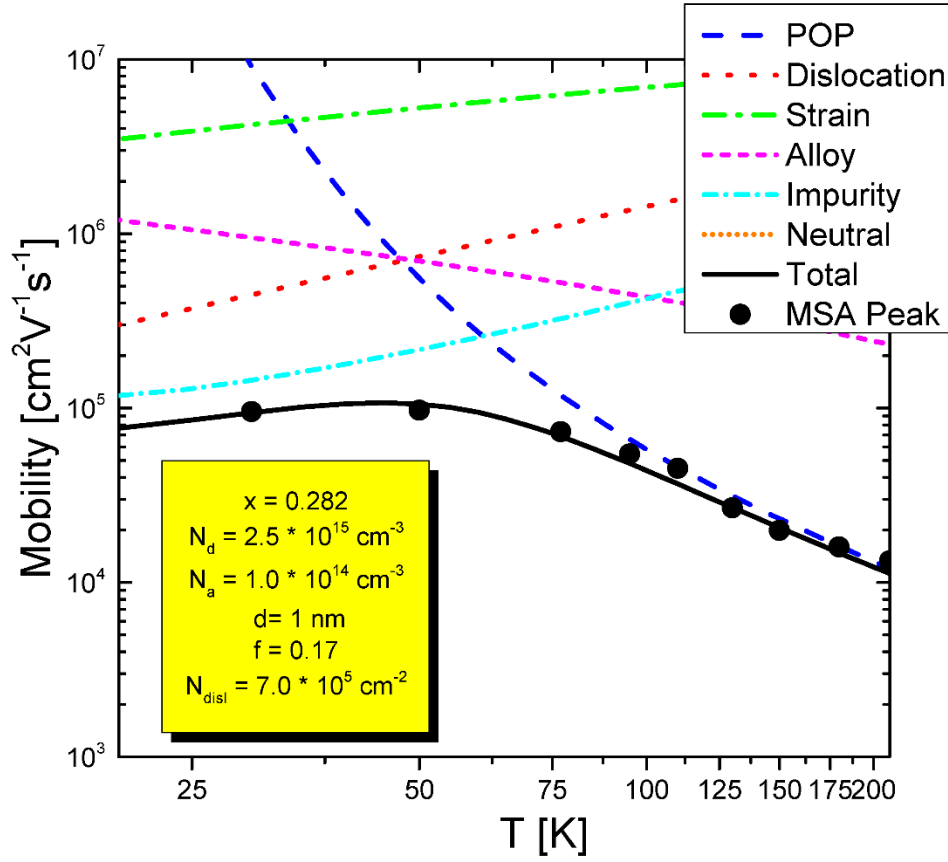


Figure 64: Theoretical fitting of mobility versus temperature on the absorber electron (E1) from sample CZT2_MW.

After cap removal and CdTe passivation the lifetime of sample CZT_MW was measured using a $1.55 \mu\text{m}$ QCL. The temperature dependent results are shown in Figure 65. One set of measurements were taken using a Spectogon narrow bandpass filter while the other employed an Al_2O_3 window. Efforts were undertaken to maintain positioning and experimental procedures between measurements. The main benefit behind using the narrow bandpass filter is the reduction in background flux, which may impact radiative recombination when photon recycling is prevalent. As can be seen, the measurements agree well at higher temperatures but diverge slightly at cryogenic temperature with results using the filter displaying longer lifetimes. Attempts to fit the data using theoretical models were initially unsuccessful. After introducing photon recycling a satisfactory fit was obtained with a radiative lifetime enhancement factor of $\beta = 6.5$ when the Al_2O_3 window was used. Results using the bandpass filter suggest that $\beta > 20$, but an

accurate number cannot be determined from this data set.

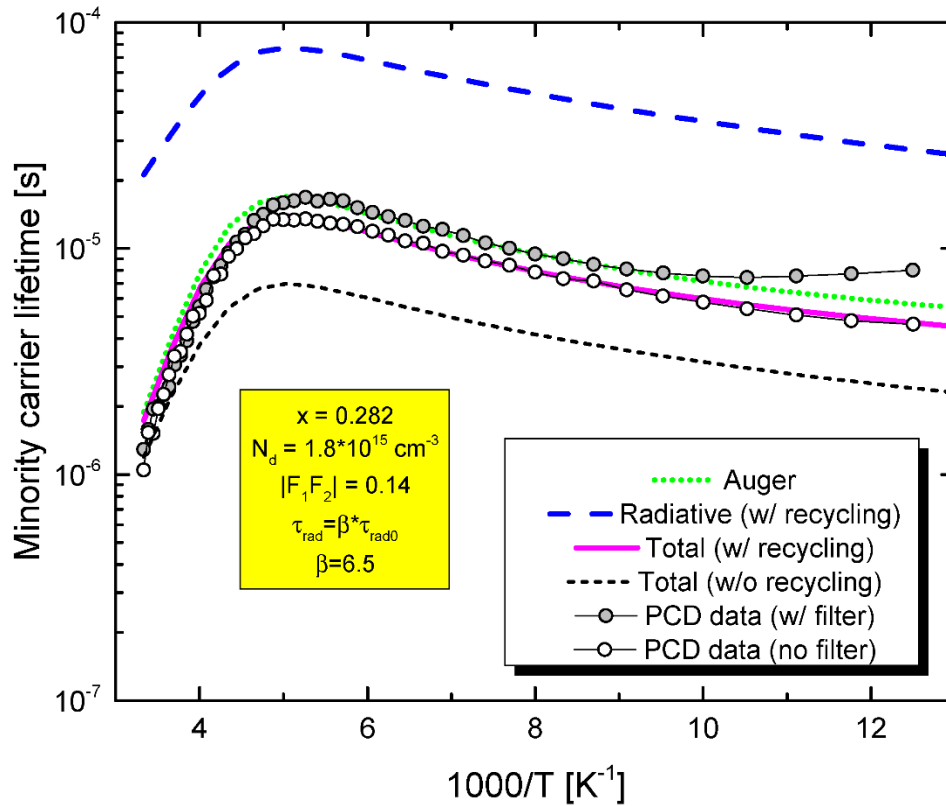


Figure 65: PCD lifetime versus temperature on CZT2_MW absorber. Two sets of PCD data are shown; lifetime with a narrow band-pass filter (filled circles) and lifetime using the same setup but without a filter (open circles). Dashed line represented theoretically intrinsic lifetime using these parameters. As can be seen, a much better fit is obtained after introducing the radiative lifetime enhancement factor $\beta = 6.5$.

A series of lifetime samples were prepared at progressive etch depths to determine if a thickness dependence on photon recycling could be determined. Samples were front-side illuminated and 93.3 % of incoming photons are expected to be photogenerated within 1.5 μm of the surface. The lifetime results at 77 K are shown in Figure 66. Composition (SIMS) is shown on the secondary y-axis for reference. The x-axis represents the total sample thickness during each measurement. As can be seen, the highest lifetime (8 μs) is measured at a sample thickness of 13.8 μm . A decrease in lifetime is observed for measurements on samples 11.3 μm and 8.8 μm thick. At a sample thickness of 8.8 μm , an additional decay, τ_2 , is resolved with a lifetime of $\sim 12 \mu\text{s}$. The second decay time is interpreted as a

characteristically longer lifetime from higher x-value regions. Further etching measurements were unsuccessful due to this mechanism. The data presented here is limited and complicated by the compositional gradient in the layer, but the expected non-linear decrease in lifetime with decreasing thickness agrees with a general photon recycling effect.

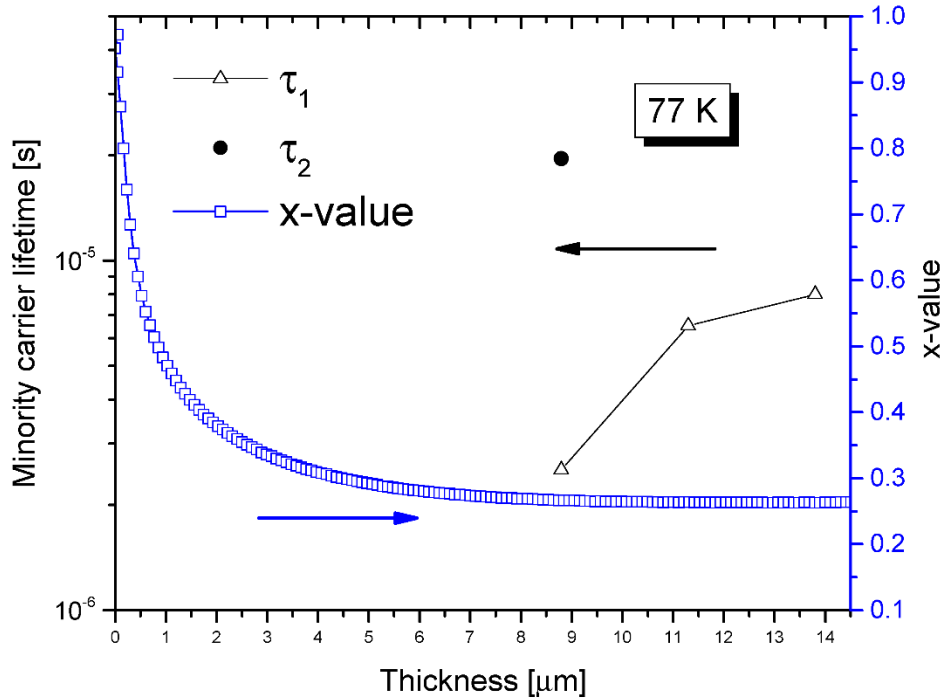


Figure 66: Lifetime results from sample CZT2_MW after various amounts of material were removed. The x-axis reflects the total sample thickness after etching.

Mesa diodes from sample CZT2_MW were generally well-behaved. IV curves from 130 K to 200 K of a 30 μm square diode are shown in Figure 67. The temperature dependence of the dark current at 50 meV reverse bias is found to correspond with a cut-off of $\lambda_{co} = 5.3 \mu\text{m}$, in agreement with spectral measurements. No attempt will be made to fit the IV curves from sample CZT2_MW due to the following complicating factors:

- Compositional gradient in the absorber

- Shallow etch depths coupled with a large diffusion length producing an unknown lateral diffusion contribution
- Unknown quality of passivation and associated surface GR and/or shunt current

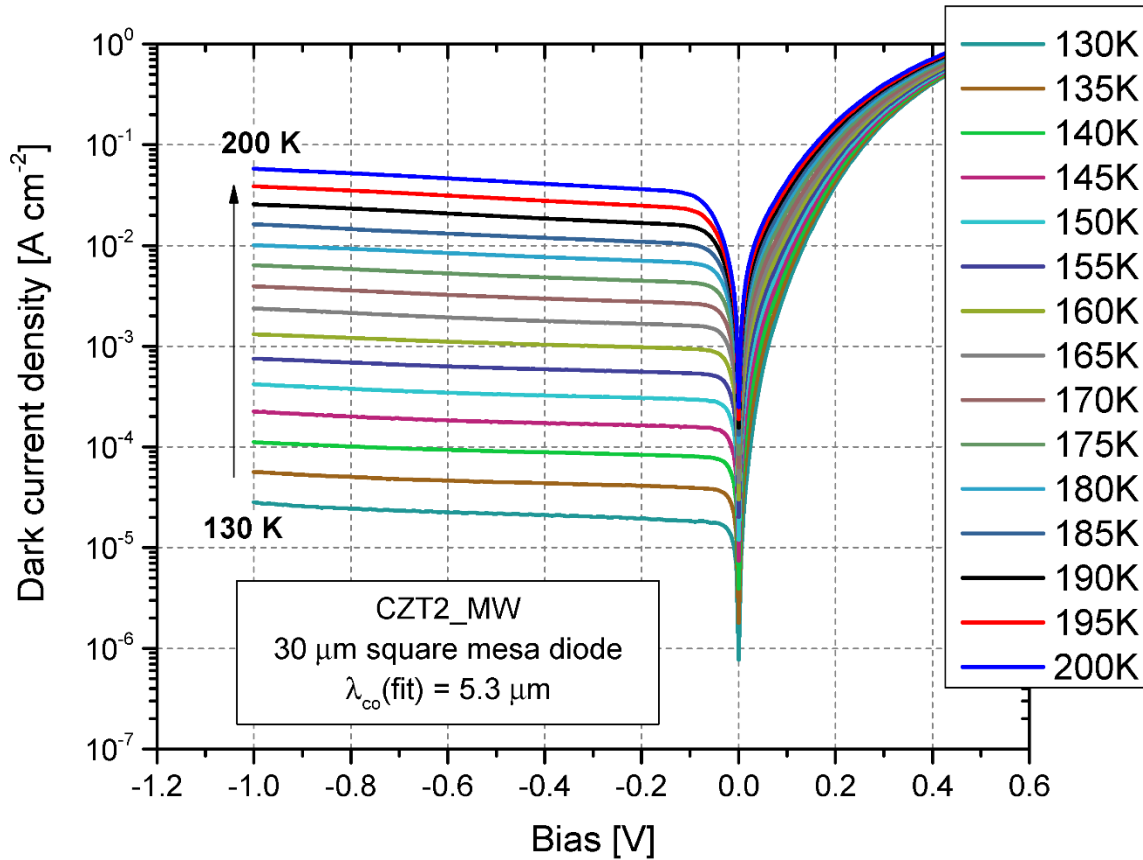


Figure 67: IVT plot for 30 μm square mesa diode from sample CZT2_MW.

QE and EBIC measurements on CZT2_MW both showed excellent results, and are shown in Figure 68. The QE at 4.5 μm was determined to be 62 % for back-side illuminated measurement at 190 K. Electrical defects from EBIC were very low ($< 2 \times 10^3 \text{ cm}^{-2}$), with many corresponding to surface defects identified from SEM, implying little to no junction defects across the sample.

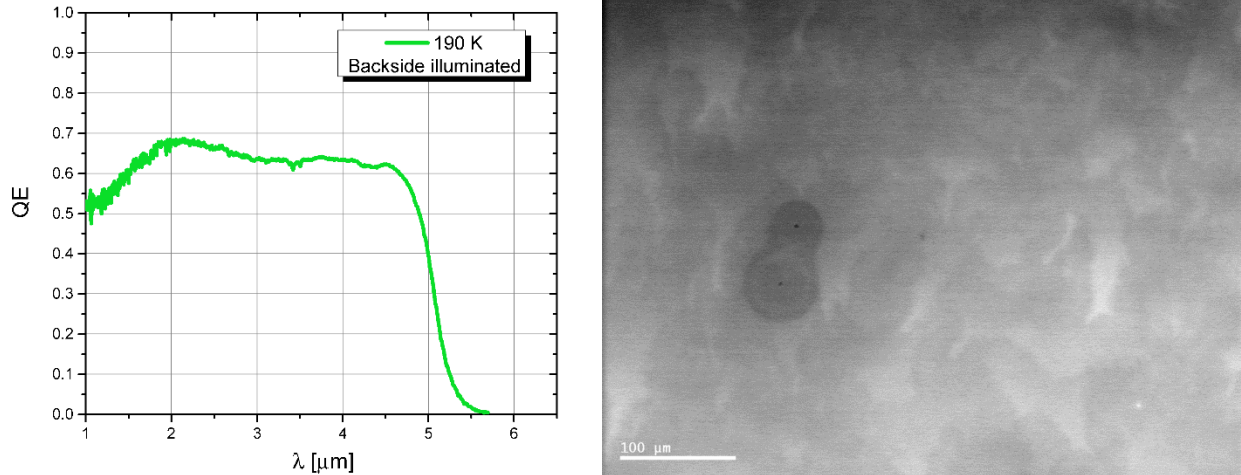


Figure 68: QE (left) and EBIC (right) results from CZT2_MW, indicating excellent diode performance and uniformity.

4.3.3 Discussion

The p-on-n heterojunction results presented in this work are compared to “Rule 07” [9, 10] in Figure 69. Rule 07 is derived from empirical data and has become a common figure of merit in the field representing state-of-the-art performance. From this perspective, we can see that all diodes in this work have performed quite well, although simple comparison to Rule07 can sometimes be misleading without proper scaling. The consistency of CZT2_MW is represented in the tight spacing of diodes in the right figure. S2_MW and G3_MW show significant signs of non-uniformity. The lower diode count for S2_MW was due to an error in processing and/or junction related defects. A more detailed analysis would be necessary in order to fairly compare performance merits and is outside the scope of this work. At first glance it would appear CZT2_MW was the worst performer, but this is not the case. It is worth noting that estimates of lateral diffusion for this diode have increased the dark current by over a factor of 10, so after proper scaling CZT2_MW would display the best performance. The dynamic resistance-area product for all diodes near operating temperature are shown in Figure 70. The maxima observed in the reverse bias dynamic resistance-area for samples S2_MW and G3_MW is the result of TAT current [243]. The resistance area-product around zero-bias may signify the presence of a barrier [244] or series resistance.

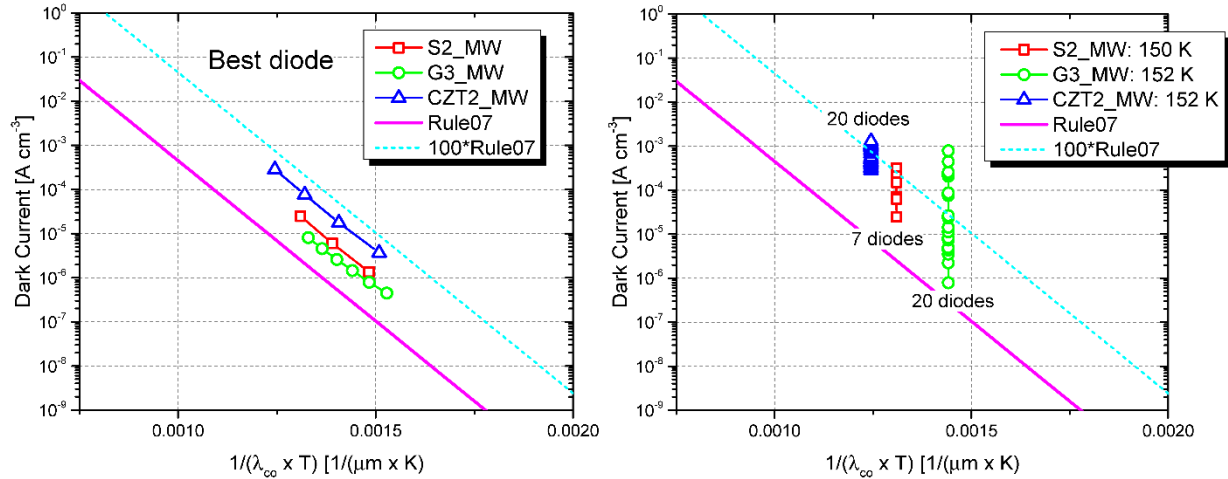


Figure 69: P+/n dark current comparison to Rule 07. Figure on the left shows the best performing diode near operating temperature (no scaling), while the right figure shows spread of dark current across a number of processed diodes.

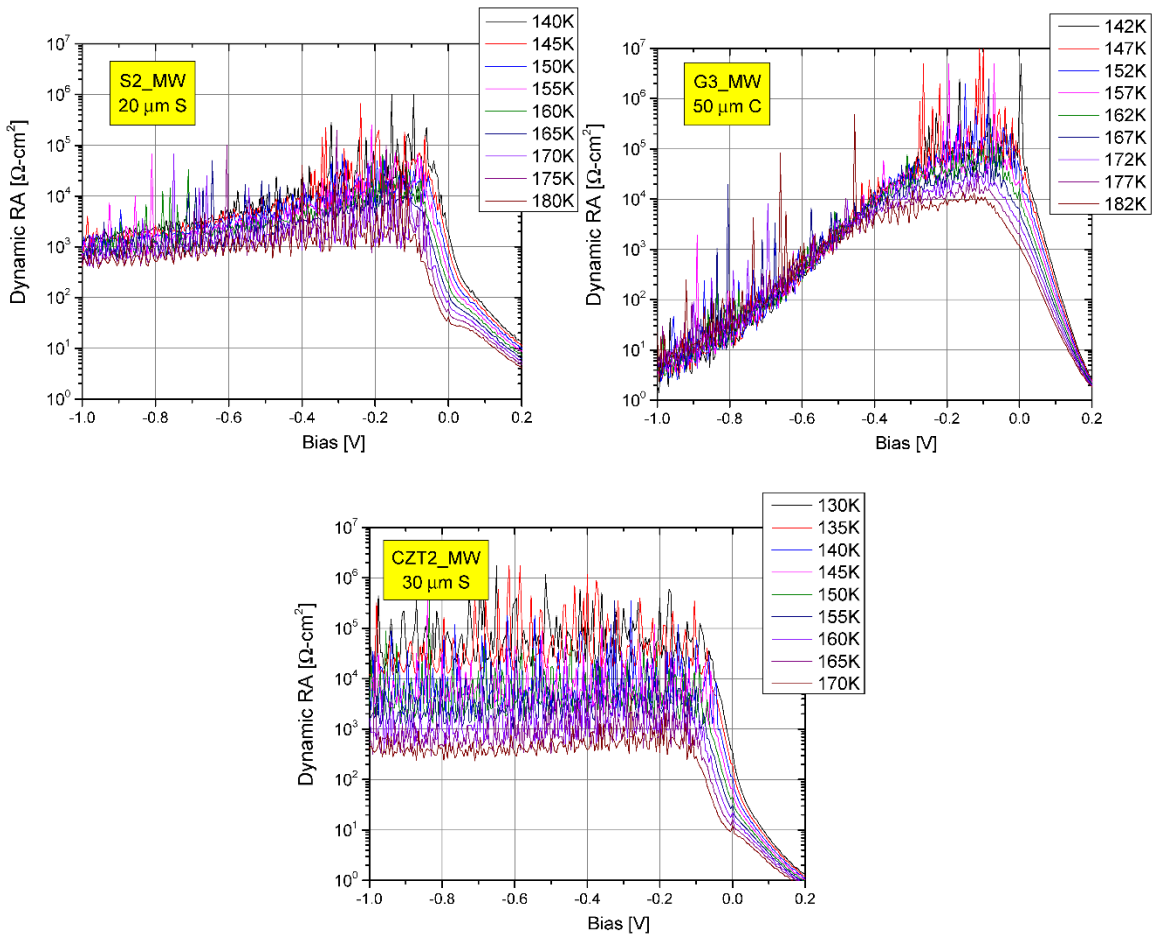


Figure 70: Dynamic resistance-area product curves for diodes in this work near operating temperature.

The MCT heterojunction presents a significantly more sophisticated multi-layer structure for MSA. The number of carriers in all samples was greater than or equal to 5 with mobility values spread across 3 orders of magnitude. Low mobility hole carriers in the *p*-type cap layer were the most challenging to resolve accurately and MCF fitting was found to be the preferred characterization method. Although the complexity of the system placed strain on the analysis many critical properties were still resolved.

MSA did not act as a straight forward predictor of diode performance, but failure analysis was useful as a diagnostic tool in identifying if layers were good candidates for device processing. From this perspective, the utility of MSA on p-on-n HgCdTe heterojunctions can be justified. MSA demonstrated the ability to identify when something had gone awry during growth or annealing, and in particular, was seen to be more sensitive to the impact of dislocations as compared to minority carrier lifetime measurements. Unexpected carriers, such as carrier E2 in sample G3_MW, were easily identified and demonstrated undesirable tunneling/GR currents.

A brief description of results on P+/n samples are summarized here:

S2_MW

- Mobility spectrum well-behaved, low temperature limited by dislocation scattering
- Lifetime intrinsically limited
- Dark current contributions from diffusion and tunneling. Decent diode performance

G2_MW

- Mobility spectrum revealed low *p*-type doping in the cap
- As a result, no successful diodes were processed
- Identified doping issue as growth related

G3_MW

- Mobility spectrum showed pronounced contribution from low mobility electron carrier associated with cap layer

- Able to resolve bulk absorber electron, low temperature limited by ionized impurities and dislocation scattering
- Lifetime intrinsically limited
- Large spread in dark current values, diffusion, GR, and tunneling present.
- Unexpected electron had deleterious impact on performance, specifically excessive tunneling currents and non-uniformity, identified as growth related

CZT2_MW

- Mobility spectrum well-behaved. Multiple carriers found in absorber due to thickness and x-value gradient. Electron mobility limited by ionized impurities.
- *p*-type cap was fully active as-grown
- Lifetime intrinsically limited, evidence of photon recycling
- Excellent diode uniformity and performance

4.4 Summary

MSA approach was successfully used to characterize a number of LW planar and MW P+/n HgCdTe structures, producing a number of interesting results. Dislocation scattering was seen to have a pronounced impact on all layers grown on alternative substrates, and in all cases correlated with excessive tunneling currents. The impact of dislocations on lifetime was apparent in LW material, but minority carrier lifetimes of MW absorbers were largely dominated by intrinsic mechanisms. In this sense, mobility fitting at low temperature may prove to be more sensitive to deleterious effects of dislocations than more traditional lifetime characterization.

Although results for growth on GaAs, Si, and CdZnTe produced fundamentally similar results, HgCdTe/CdZnTe showed superior quality for both device architectures, showing mobility limited by ionized impurity scattering, intrinsically limited lifetimes, and no evidence of tunneling.

Doping concentrations and x-values obtained from MSA for all layers showed good correlation with

SIMS, FTIR, and fitting of lifetime and dark current. Dislocation scattering parameters appeared consistent with both theory and EPD measured values. Additional characterization in the future would be useful in order to better establish dislocation scattering parameters with regards to bandgap and doping concentration.

Despite the maturity of HgCdTe technology, it is clear that many topics of research remain. This section was successful in demonstrating the utility of MSA in that endeavor, but also highlights a number of fundamental limitations. MSA has proved particularly useful as a diagnostic on device structures and as a powerful tool for fundamental investigations, such as LW minority carrier mobility, surface/substrate-interface conduction, *p*-type doping and activation, dislocation scattering, annealing effects, and absorber grading studies. On the other hand, MSA showed marked difficulty in resolving low mobility carriers, a natural ramification tied to maximum magnetic-field strength.

5. III-V studies

This chapter is devoted to III-V materials and related structures, particularly superlattice layers. III-V materials offer an enticing alternative to incumbent HgCdTe technologies and their fundamental transport properties will be explored in this chapter, beginning with bulk binary/ternary materials, and later InAs/GaSb and InAs/InAsSb superlattice layers. Two major issues that impede the development of III-V Sb-based IR materials will be addressed; background carrier concentration and surface passivation. The goal of this chapter is to gain a better understanding of transport in this material system, as well as determination of ways mobility spectrum analysis may aid in the development of this technology.

5.1 Bulk InAs, GaSb, and InAsSb

Unintentionally doped (uid) GaSb, InAs, and InAs_{1-x}Sb_x ($x = 0.09$) layers were grown using MBE to establish a baseline of expected carriers. Te-doped GaSb layers were grown for comparison. GaSb and InAs layers were 3 μm thick while InAs_{1-x}Sb_x was 4 μm thick. GaSb and InAs were grown on lattice-mismatched GaAs substrates while InAsSb was grown on lattice-matched GaSb. All layers were grown with an insulating barrier of AlSb between substrate and epi-layer. The AlSb ensures that conductive substrates will not be present in the mobility spectrum. Contacts were made to the electrically active layers using In and baked at $\sim 158^\circ\text{C}$ to ensure ohmic behavior.

Mobility spectrum at 77 K of uid and Te-doped GaSb are shown in Figure 71. The uid material displayed *p*-type conduction with two primary hole peaks at $\sim 4,000\text{ cm}^2\text{V}^{-1}\text{s}^{-1}$ and $\sim 14,000\text{ cm}^2\text{V}^{-1}\text{s}^{-1}$. The two holes are interpreted as a light hole (LH) and heavy hole (HH), and dominate conduction within the layer, with the HH responsible for 75 % of total conduction at 77 K, and the light hole contributing 15 %. Based on the temperature dependence of the heavy hole mobility, the material does not appear to be compensated [245]. The ratio between the heavy and light hole carrier concentrations does not vary significantly with temperature at an average value of 22.96 from 30 - 293 K. From simple band theory,

this ratio corresponds to a heavy to light hole effective mass ratio of 8.1, in agreement with a theoretically calculated value of 10.7 [246]. The background doping level is quite high, measuring $\sim 8 \times 10^{15} \text{ cm}^{-3}$ at 77 K. The residual acceptors are due to gallium vacancies (V_{Ga}) and gallium antisites (Ga_{Sb}) [247]. The light and heavy hole mobility versus temperature is shown in Figure 72, with values and temperature dependence in agreement with measurements on thick GaSb wafers [248]. At high temperatures, each carrier displays the expected $\sim T^{-3/2}$ behavior indicative of the lattice scattering regime, which is to be expected [245]. No definitive surface carrier was found in the mobility spectrum, but low mobility carriers ($< 1,000 \text{ cm}^2\text{V}^{-1}\text{s}^{-1}$) may be evidence of conduction near the AlSb-GaSb interface, indicating a collection of impurities in that region.

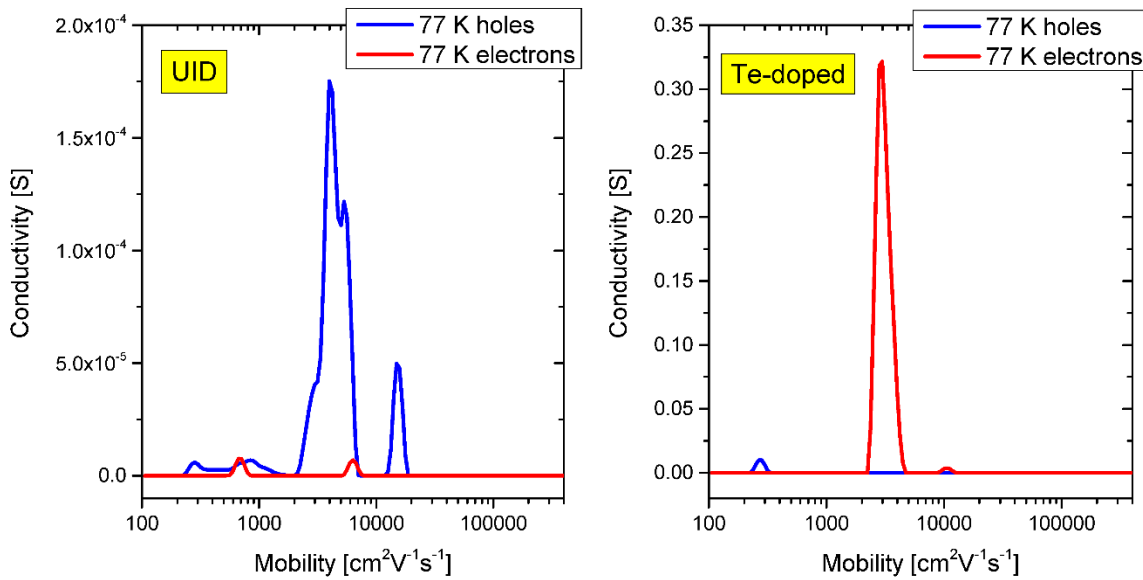


Figure 71: GaSb mobility spectrum at 77 K for uid (left) and Te-doped (right) samples.

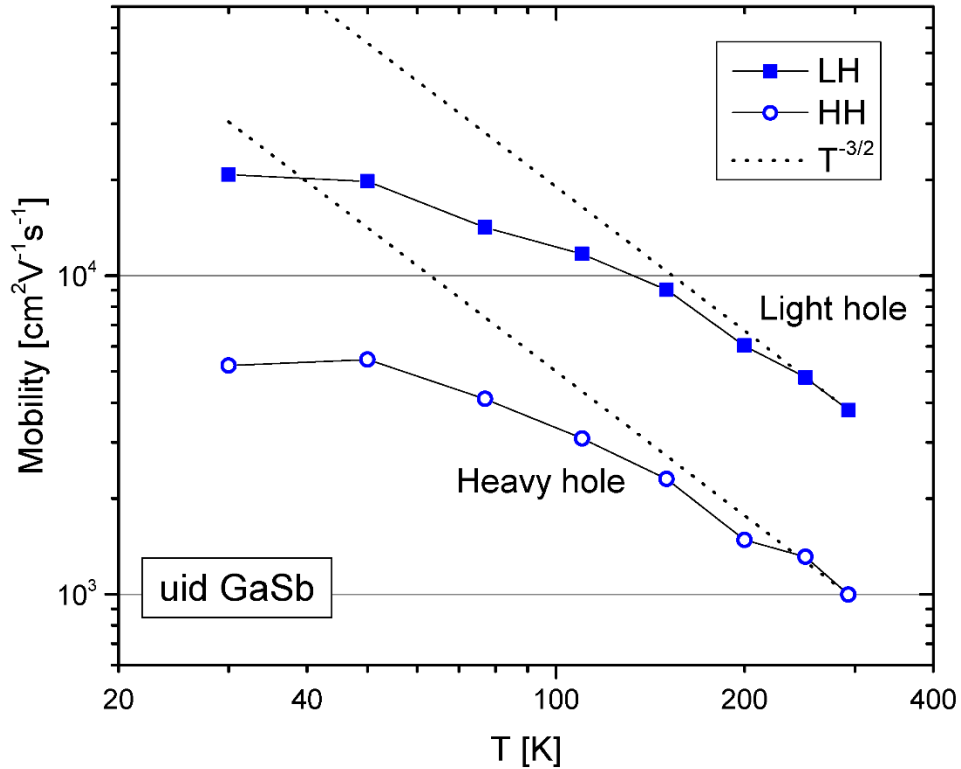


Figure 72: Heavy (open) and light (closed) hole mobility versus temperature for uid GaSb grown on GaAs.

The Te-doped GaSb sample shows one dominant electron peak at $\sim 3,000 \text{ cm}^2\text{V}^{-1}\text{s}^{-1}$ and two minor peaks. The dominant electron peak is a result of the Γ conduction band, contributing 98% of total conduction at 77 K. Although the transport of the Te-doped n -type GaSb appears simple at 77 K, it is actually complex, as contributions from L and X conduction bands are expected at higher temperatures [249]. The mobility of all carriers from the Te-doped sample are shown in Figure 73. At room temperature, 77 % of conductivity is due to the Γ -valley, 12 % due to the L -valley, and 10 % due to the X -valley, with mobility values of 4.78×10^3 , 848, and $114 \text{ cm}^2\text{V}^{-1}\text{s}^{-1}$, respectively, in excellent agreement with previous reports [250]. Additional peaks attributed to defects and a minority hole are also labelled. Low temperature defects may be related to residual compensating acceptors [251]. At room temperature, the sample is expected to be significantly compensated [252], which explains the presence of a minority hole carrier.

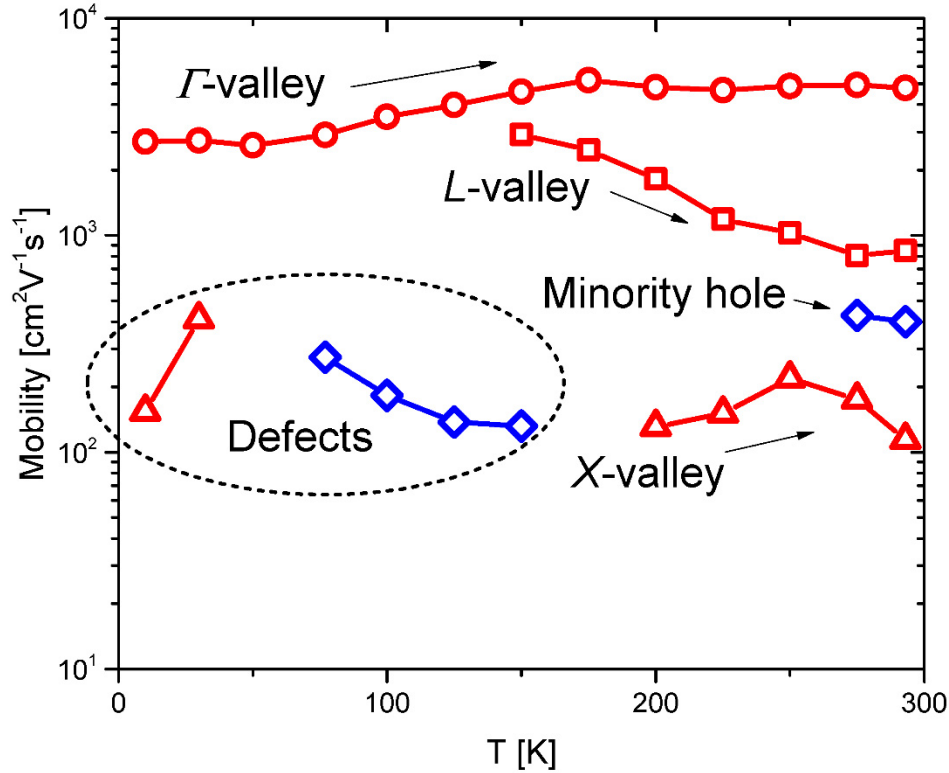


Figure 73: Mobility versus temperature results from Te-doped GaSb sample showing conduction from Γ , L, and X conduction bands.

Mobility spectrum results at 77 K from an undoped InAs sample are shown in Figure 74. The bulk electron mobility is $\sim 45,000 \text{ cm}^2\text{V}^{-1}\text{s}^{-1}$ at 77 K and $\sim 14,000 \text{ cm}^2\text{V}^{-1}\text{s}^{-1}$ at 293 K, in agreement with previous MBE results [253]. A wide and significantly populated peak is observed at $\sim 10,000 \text{ cm}^2\text{V}^{-1}\text{s}^{-1}$, and can readily be assigned to the well-known surface accumulation layer and substrate interface, both of which are expected to show a mobility reduction as compared to the bulk [254]. A surface sheet carrier concentration of $\sim 10^{12} \text{ cm}^{-3}$ is in excellent agreement with high-resolution electron-energy-loss spectroscopy [255, 256] and angle-resolved photoelectron spectroscopy [257] of the InAs surface. The bulk electron displays slight intrinsic activation at elevated temperature and has a carrier concentration of $6.5 \times 10^{15} \text{ cm}^{-3}$ at 293 K. The background doping level in the undoped InAs sample is $\sim 1 \times 10^{15} \text{ cm}^{-3}$ when only the bulk electron is considered.

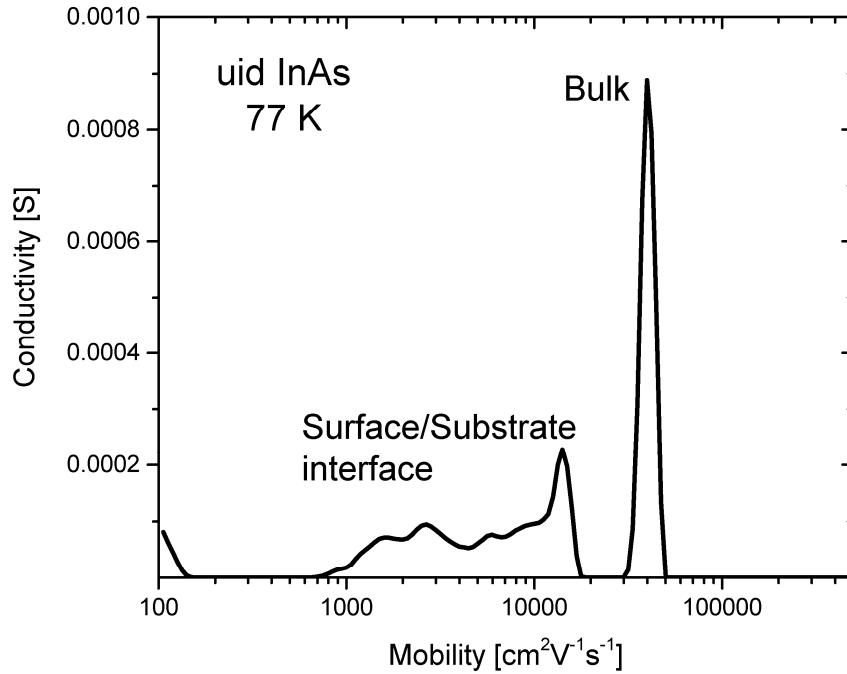


Figure 74: 77 K mobility spectrum of uid InAs sample.

The final bulk layer studied was a ternary $\text{InAs}_{0.91}\text{Sb}_{0.09}$ layer. With $x = 0.09$, the material is nearly lattice matched to the GaSb substrate. InAsSb possesses the narrowest bandgap of bulk III-V materials in this study. The bandgap of InAsSb is known to change as a function of x -value and bowing parameter [258, 259], and the response can be extended past the cut-offs of InAs and InSb. Spectral response measurements and fitting of the bandgap for this layer are shown in Figure 75, with Varshni fitting parameters of $E_0 = 0.319$, $\alpha = 0.0003586$, and $\beta = 270$ providing adequate fit.

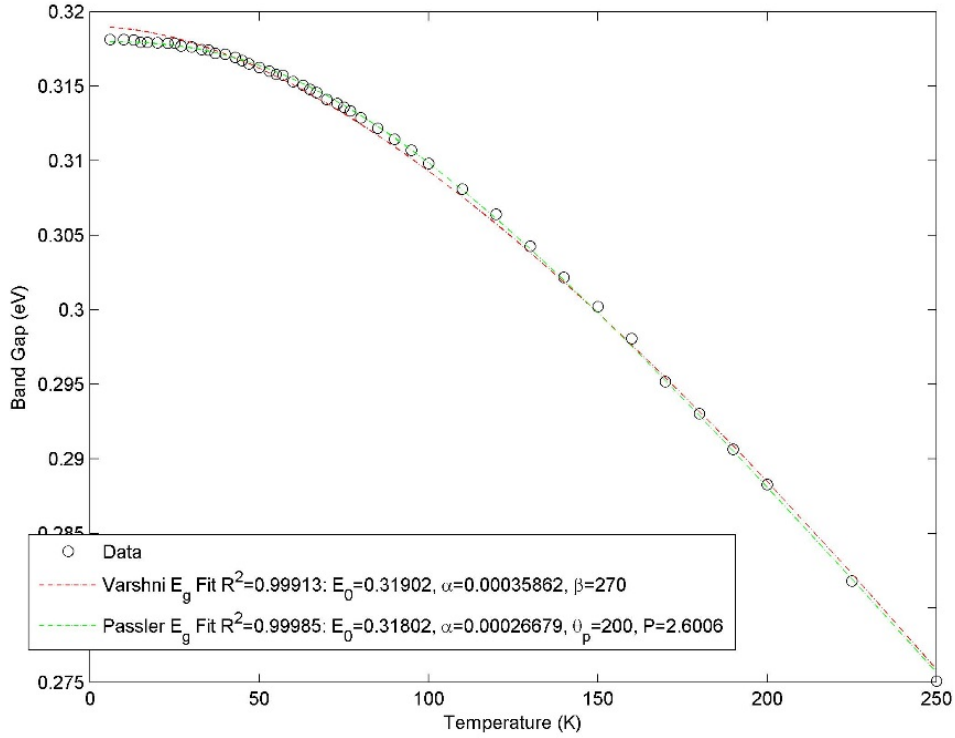


Figure 75: Bandgap versus temperature of InAs_{0.91}Sb_{0.09} layer determined from spectral response.

The mobility spectrum temperature evolution of electrons in the InAs_{0.91}Sb_{0.09} sample is shown in Figure 76. The mobility of the bulk electron is easily the highest of the bulk materials studied in this work, having a mobility $> 10^5 \text{ cm}^2\text{V}^{-1}\text{s}^{-1}$ at low temperature. The other electron peaks are comparatively low conductivity. This material is expected to exhibit Fermi level pinning at the surface similar to InAs. From the temperature dependence of mobility and carrier concentration, the electron mobility peak $\sim 10,000\text{-}15,000 \text{ cm}^2\text{V}^{-1}\text{s}^{-1}$ appears to be surface related. The sheet concentration of the surface carrier is $\sim 5 \times 10^{11} \text{ cm}^{-2}$. The surface peak maintains an average percent conductivity of $\sim 13 \%$ across the temperature range.

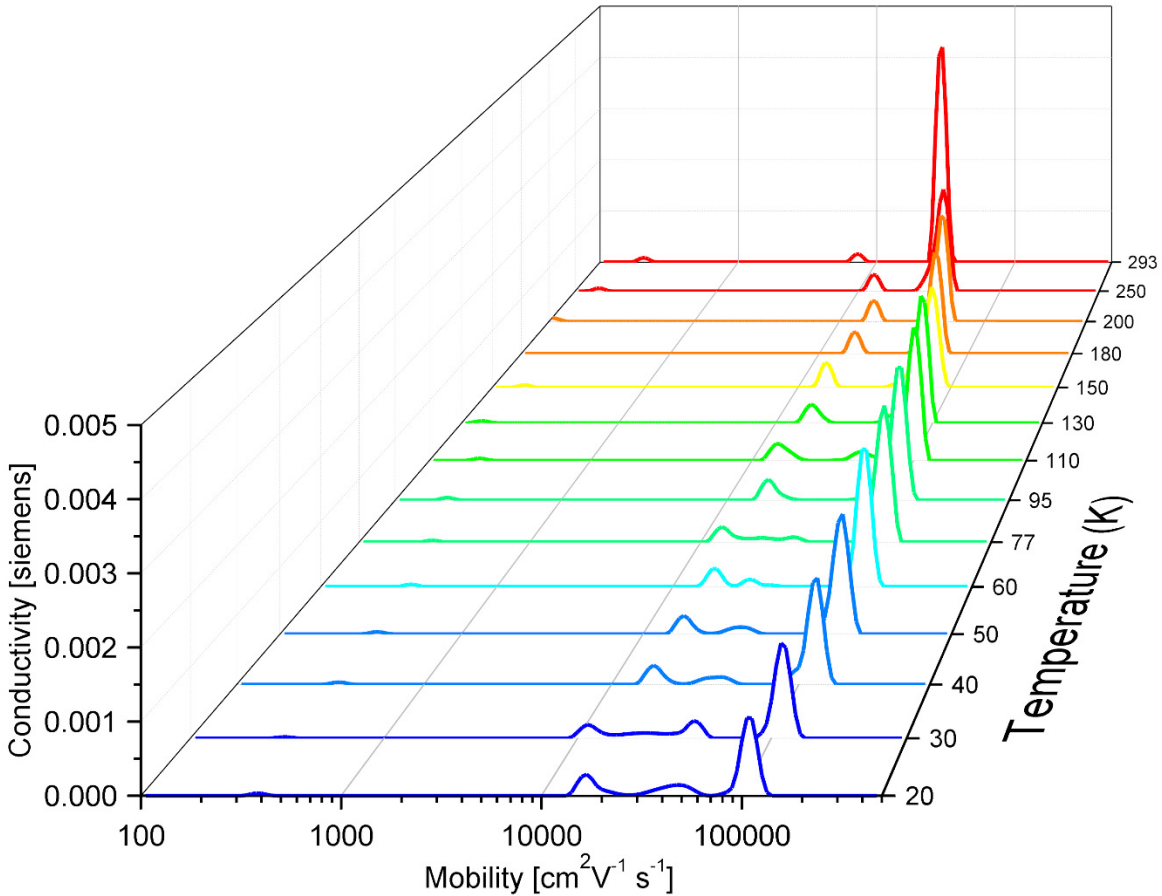


Figure 76: Evolution of electron mobility spectra from InAs_{0.91}Sb_{0.09} layer.

An additional electron peak is observed for $T \leq 77$ K with mobility ranging from $\sim 28,000$ - $48,000$ $\text{cm}^2\text{V}^{-1}\text{s}^{-1}$. The mobility and sheet concentration at 77 K are $34,912$ $\text{cm}^2\text{V}^{-1}\text{s}^{-1}$ and 1.2×10^{11} cm^{-2} , respectively. The conductivity of this carrier drops rapidly with increasing temperature, and may be interpreted as a result of conduction at the barrier-SL interface, in agreement with recent reports employing step-etching and oxide removal to pinpoint the origin of a similar carrier [260]. The mobility versus temperature behavior of all identified carriers for the InAs_{0.91}Sb_{0.09} layer are shown in Figure 77. Lattice scattering behavior of the bulk electron is recovered near room temperature. The low temperature mobility is found to be a result of ionized impurity and alloy scattering, and does not appear to be compensated [261].

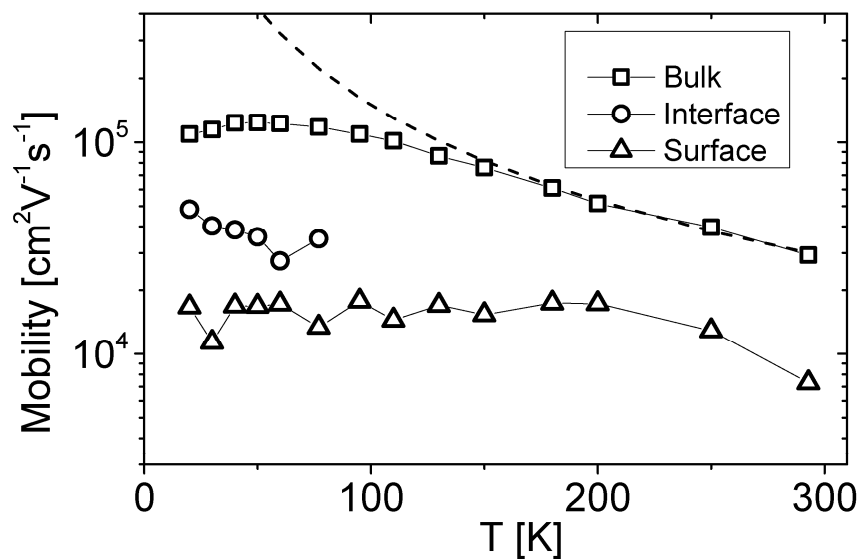


Figure 77: Mobility versus temperature of bulk, surface, and back interface carriers present in $\text{InAs}_{0.91}\text{Sb}_{0.09}$ layer. Dashed line represented lattice scattering.

Figure 78 shows the MSA obtained bulk mobility and concentration versus single-field results. An accurate background doping is only obtained when MSA is used, as the single-field results overestimate residual doping levels even though the bulk electron is responsible for 81 % of conduction at 77 K and 93 % at room temperature. A more accurate value of $\sim 1.4 \times 10^{15} \text{ cm}^{-3}$ is obtained using the MSA approach. The electron shows a shallow activation energy level of 2.7 meV below 150 K, comparable to 1.3 meV obtained from a simple hydrogenic model in InAs.

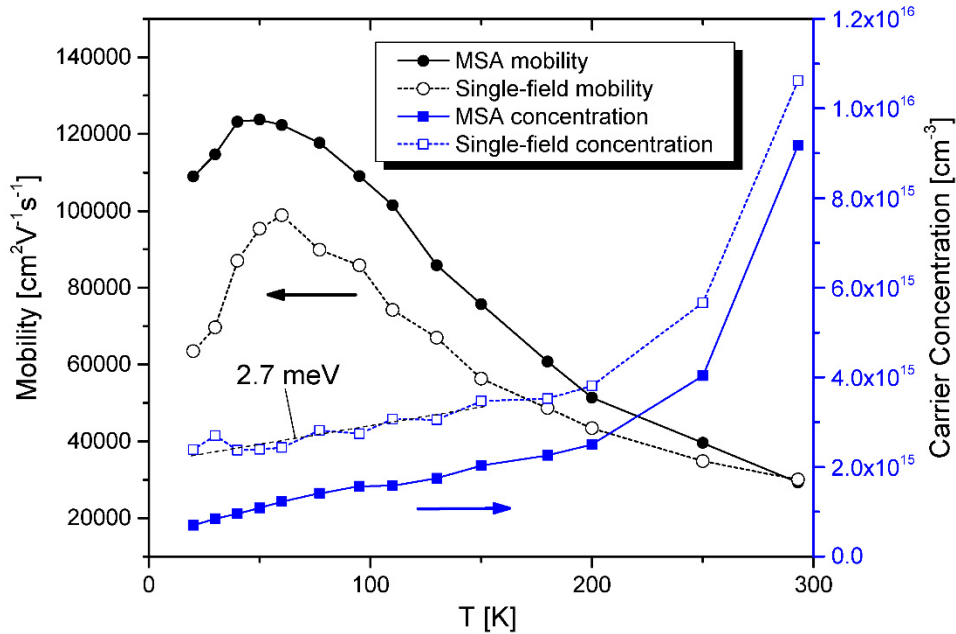


Figure 78: Bulk electron mobility and carrier concentration versus temperature. MSA data (filled) and single-field (open) are shown for comparison.

An attempt was made to measure the bulk lifetime in all uid samples using PCD method. Reliable results were not obtained on GaSb due to rapid recombination (< 80 ns). All lifetime samples displayed a noticeable surface recombination decay. The basic material property results for uid GaSb, uid InAs, and uid InAsSb are shown in Table VIII for reference.

Table VIII: Summary of resolved properties for uid bulk III-V materials

Sample	Substrate	Type	μ [77 K] [$\text{cm}^2\text{V}^{-1}\text{s}^{-1}$]	Background concentration [cm^{-3}]	τ [77 K]
GaSb	GaAs	<i>p</i> -type	$\sim 4,000$	7.6×10^{15}	< 80 ns
InAs	GaAs	<i>n</i> -type	$\sim 45,000$	1.2×10^{15}	~ 400 ns
InAs _{0.91} Sb _{0.09}	GaSb	<i>n</i> -type	$\sim 120,000$	1.4×10^{15}	~ 850 ns

5.2 LW T2SL III-V

A series of doped and undoped SL structures were grown and prepared for in-plane Hall measurement. The results of this section will provide valuable information on background carrier concentration and in-plane transport properties, which could be used to correlate with vertical transport in the future. Samples can be divided based upon their constituent layer materials, namely InAs/GaSb and InAs/InAsSb SL structures. The goal of this section is to present the basic properties of these structures with regards to doping and material choice.

5.2.1 InAs/GaSb

Three binary-binary InAs/GaSb ($42 \text{ \AA} / 21 \text{ \AA}$) LW structures were grown including a *p*-type device structure [262], an undoped layer for PCD/Hall characterization, and a Be-doped *p*-type layer for PCD/Hall characterization. The absorber layer of the device structure and the characterization samples are nominally identical. All structures were grown on (100) GaSb substrates with a 1 \mu m thick insulating buffer layer of AlAsSb to electrically separate the conductive substrate from the LW SL material. The LW absorber recipe was repeated 400 times for an overall absorber thickness of 2.52 \mu m . The device structure consists of a highly doped *p*-type back contact and wide gap highly *n*-type top contact. Both characterization samples have a thin ($\sim 50 \text{ \AA}$) highly *p*-type doped GaSb top contact layer so that ohmic contacts could be made. The undoped and Be-doped LW InAs/GaSb characterization sample layers are shown in Figure 79.

Top Contact	p-GaSb	Be:4.0E+18	50Å
SLS Absorber	InAs/GaSb	Be:1.1E+16 (Sample 2: uid)	2.52μm
Barrier	AlAsSb	uid	1μm
Buffer	GaSb	uid	150nm
	Substrate	n-GaSb	

Figure 79: Characterization sample structure of LW InAs/GaSb SL.

A series of Hall samples were fabricated from all three InAs/GaSb SL structures. The square van der Pauw geometry was used in all cases. A selective sulfuric based wet etch (H₂SO₄/citric acid) solution was used to remove the top contact layer except for small contact pads at the four corners of each sample. The selective etch is a crucial step for successful Hall measurement as it removes the highly conductive pathway of the top contact layer while still allowing ohmic contact formation in the corner regions. Contact pads were kept as small as possible to improve measurement accuracy. Variable-field Hall measurements were performed at 25 magnetic field points across a temperature range of 30 - 293 K.

In order to correctly identify hole carriers in the Be-doped SL layers, samples from the *p*-type device structure containing the absorber+back contact layers and the back contact layer only were measured and compared to the Be-doped characterization sample (absorber layer only). The mobility spectrum of hole carriers is shown in Figure 80. The absorber hole is clearly evident in the absorber+back contact and absorber layer as a peak at a mobility of ~2,500 cm²V⁻¹s⁻¹. The additional peak related to the *p*-type back contact layer is seen across a mobility range of 400-1,000 cm²V⁻¹s⁻¹. A similar identification process was carried out for electron carriers, identifying a substrate-interface electron, a surface electron, and a bulk electron.

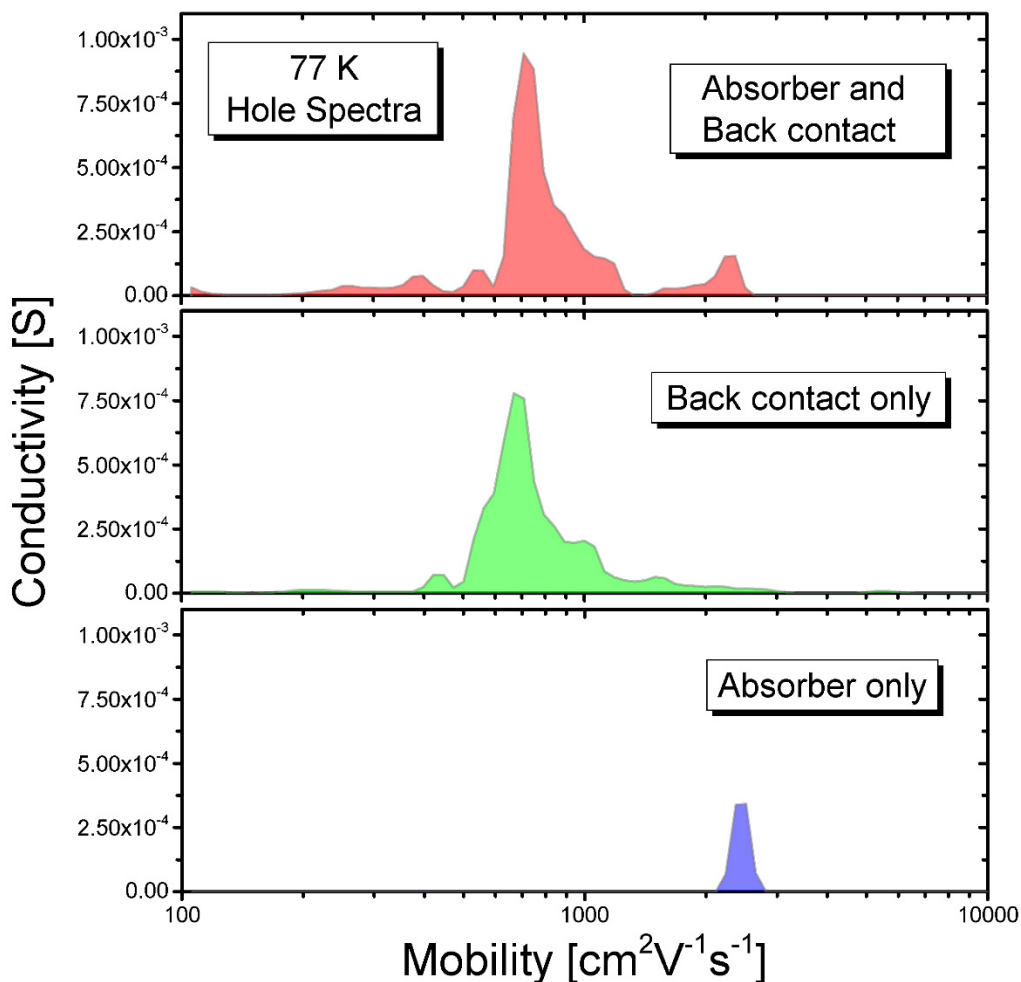


Figure 80: Mobility spectrum of three distinct layers in order to properly identify carriers in the *p*-type SL structure. From top to bottom: Absorber and back contact layers of *p*-type device structure, etched sample containing only the back contact layer, and characterization sample containing only the *p*-type absorber layer.

The mobility spectrum of the Be-doped *p*-type absorber layer is shown in Figure 81, with electron (a) and hole (b) spectra separated. The spectra are linearly spaced but shown on a logarithmic scale to account for intrinsic activation. A total of three electron carriers are identified: carrier e1 (bulk), carrier e2 (surface), and carrier e3 (barrier-SL interface). Carrier e1 begins to emerge in the spectra at $T = 77$ K and quickly becomes the dominate electron species as temperature increases. Alternatively, carrier e2 displays a weak temperature dependence for both mobility and carrier concentration. The carrier concentration of e1 and e2 are normalized to their minima and shown for comparison in Figure 82. The rapid increase in

carrier e1 confirms the carrier is related to the SL bulk, consistent with optical measurements of bandgap. Alternatively, e2 is only weakly temperature dependent, suggesting more 2D-like origin consistent with the surface. Carrier concentration spikes at I. and II. in Figure 82 are a result of the initial emergence of the e1 peak and likely a trickle over effect from the e1 peak as it begins to overwhelming dominate conduction in the layer, respectively.

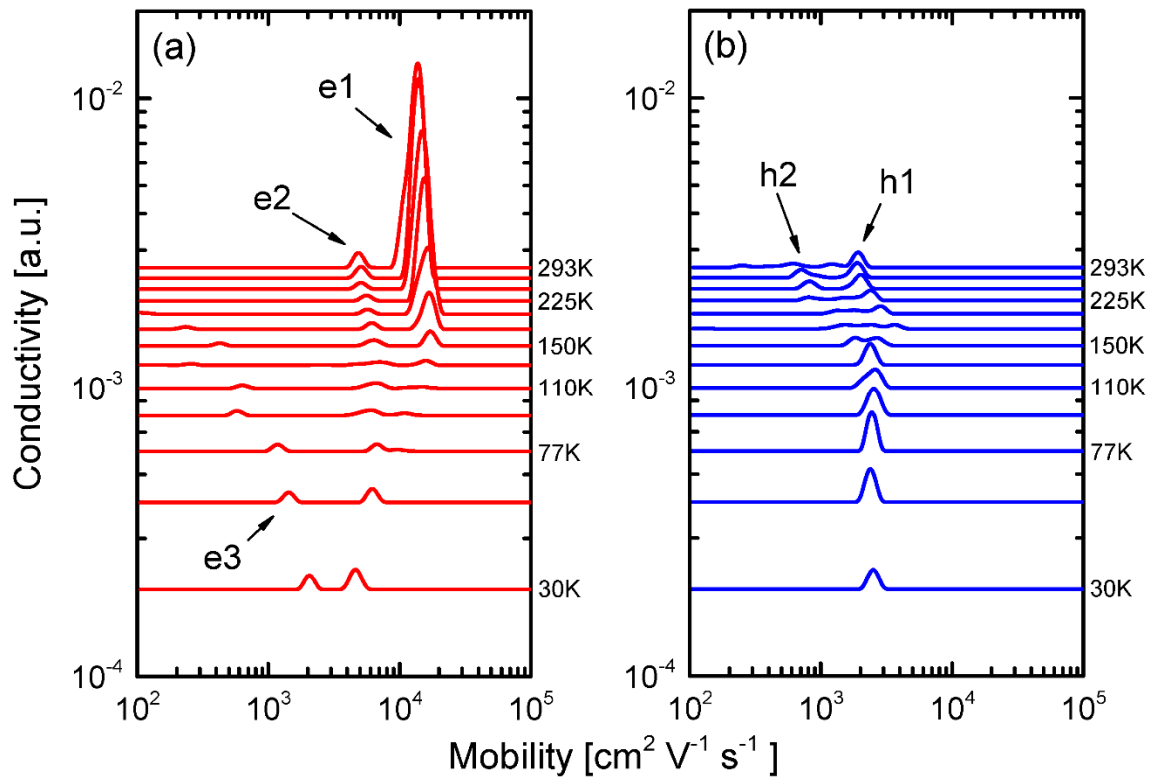


Figure 81: Mobility spectrum temperature evolution of Be-doped LW InAs/GaSb SL structure, with electrons (a) and holes (b).

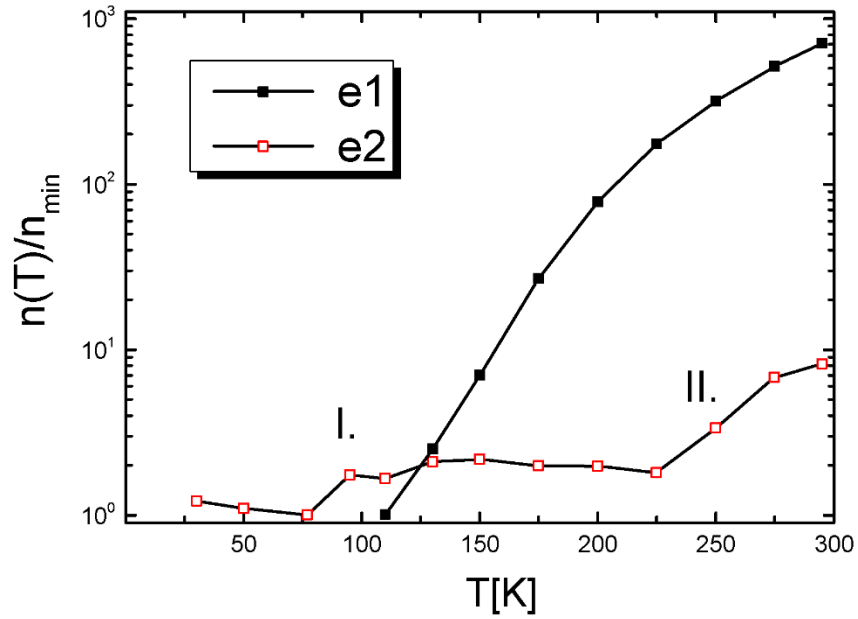


Figure 82: Temperature dependence of carriers e1 and e2 carrier concentration from Be-doped LW InAs/GaSb. Values are normalized to minimum resolved concentration to highlight change with temperature.

The mobility spectrum of the uid LW InAs/GaSb layer is shown in the same manner as above in Figure 83. The most obvious feature changes are the presence of carrier e1 at low temperature, as well as an overall lower conductivity from hole carriers. Carrier e2, e3, and the splitting of the peak h1 at high temperature are consistent between uid and Be-doped samples.

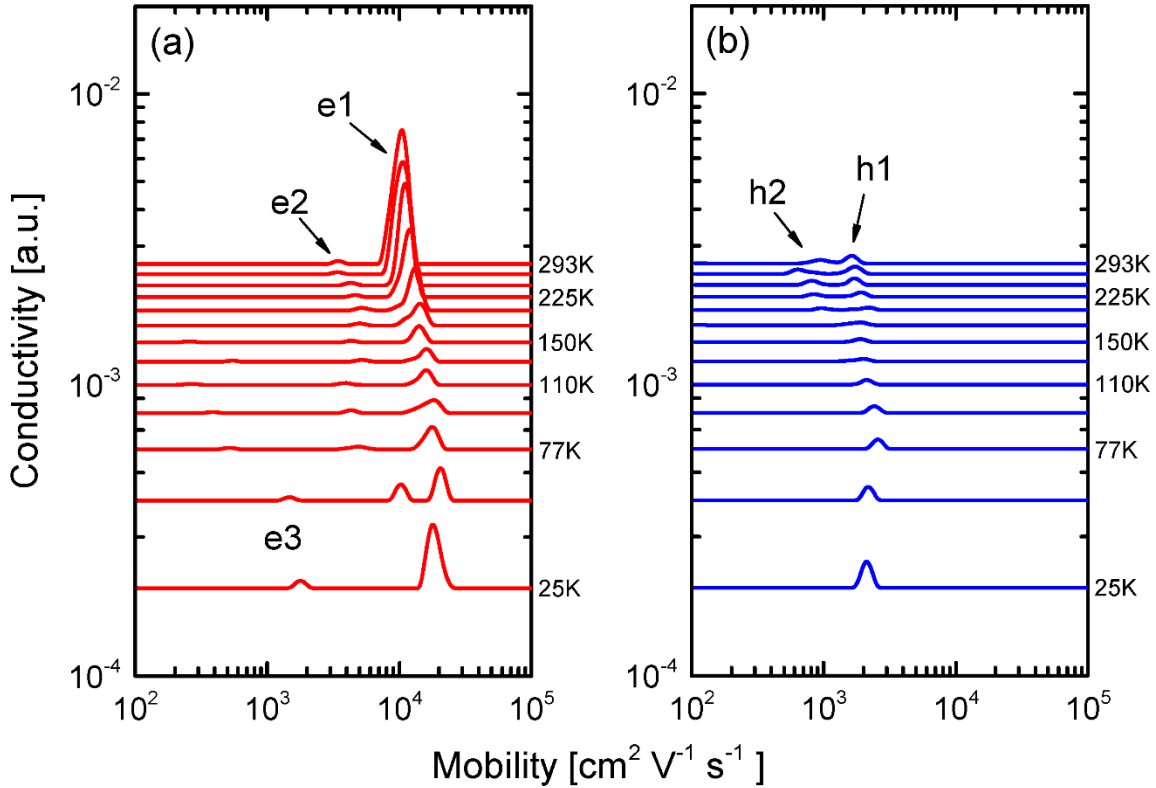


Figure 83: Mobility spectrum temperature evolution of uid LW InAs/GaSb SL structure, with electrons (a) and holes (b).

Figure 84 shows the mobility versus temperature for all carriers resolved in the uid (top) and Be-doped (bottom) samples. Overall, the mobility values of all carriers are quite similar despite the doping difference. The high ($> 10^4 \text{ cm}^2 \text{V}^{-1} \text{s}^{-1}$) electron mobility is limited by IRS in both samples and indicates a low lateral correlation length of interface fluctuation, Λ , estimated to be $\sim 30 \text{ \AA}$ [167]. It is not clear if the drop in low temperature e1 mobility in the Be-doped sample is physical or a result of a low conductivity peak in close proximity with the e2 surface carrier peak, as the mobility of e1 seems drawn to the e2 peak as temperature decreases, which is not seen in the uid case. For each sample, carrier e3 is seen to drop off sharply as temperature increases, and is most likely a result of conduction near the SL-substrate interface [263]. This interpretation is consistent with previous findings of antisite donors at InAs/AlSb interfaces [264].

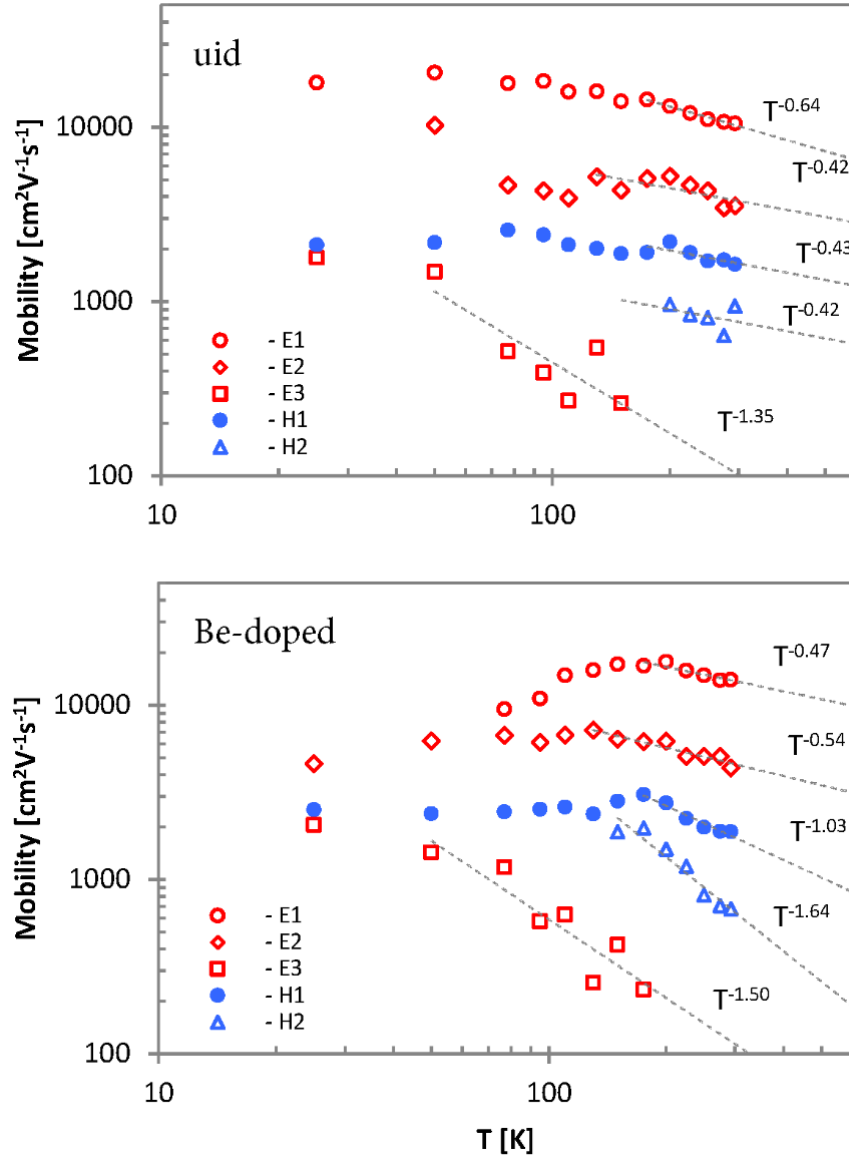


Figure 84: Mobility versus temperature for all resolved carriers in uid LW InAs/GaSb (top) and Be-doped LW InAs/GaSb. Mobility temperature behavior at higher temperatures is included.

The splitting of the h1 hole peak at elevated temperature ($\geq 200\text{K}$) is consistent between samples (including Be-doped device structure) although the precise cause is unknown. The h1 and h2 peaks show slightly different activation energies at high temperature, as shown in Figure 85, but both appear bulk related. The activation energy of h2 (low mobility split-off) is found to be systematically higher.

Interestingly, the hole splitting is seen to coincide with the material becoming near-degenerate

according to calculation of the Fermi level. Furthermore, the splitting is accompanied by a change in the slope of resistivity power-law function of temperature. The splitting may therefore be a result of conduction from carriers deeper down in the band structure which can possess very different effective masses due to band nonparabolicity. Additional complicating factors, such as intrinsic peak broadening [265] and different phonon interactions must also be considered and are worthy of future investigation.

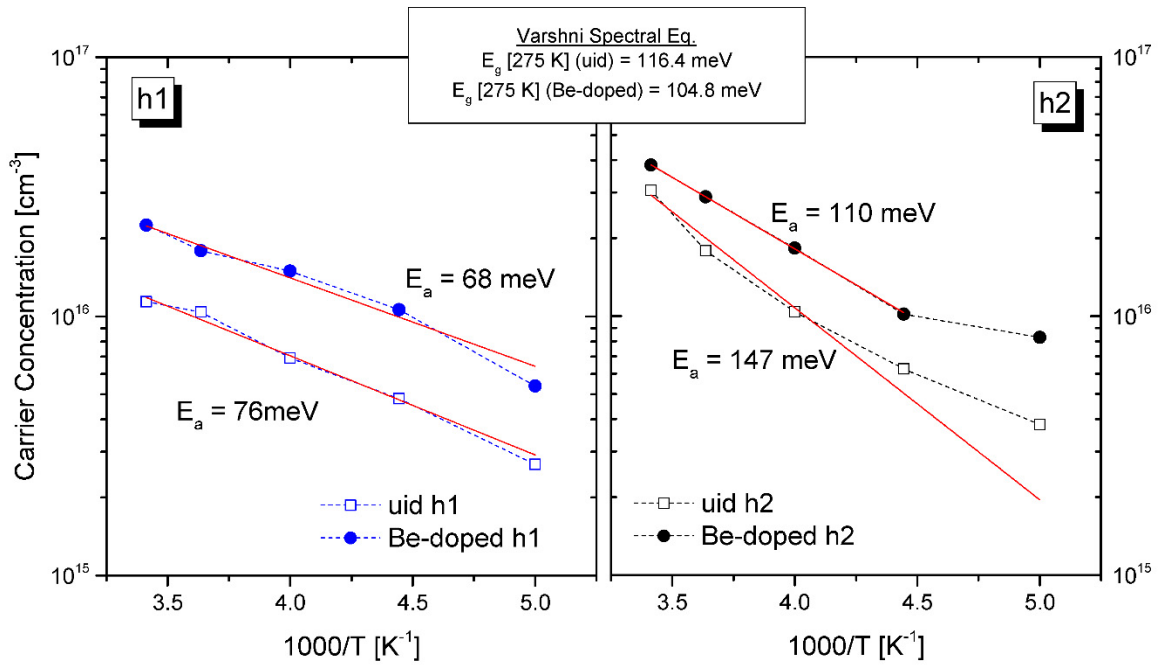


Figure 85: Activation energies of carriers h1 and h2 near room temperature. In both the uid and Be-doped case the activation energy of carrier h2 is larger.

The combined carrier concentration of h1 and h2 can be used to determine n_i as a function of temperature, as can be seen in Figure 86, which shows the concentration of all resolved carriers for the uid (top) and Be-doped (bottom) case. Fitting of n_i gives an effective bandgap of 143 meV for the uid sample and 132 meV for the Be-doped sample. Varshni parameters determined from spectral response measurements for the uid sample are $E_0 = 0.15351$ eV, $\alpha = 0.0002676$, and $\beta = 270$ while the Be-doped sample parameters are $E_0 = 0.1344$ eV, $\alpha = 0.00021312$, and $\beta = 270$. In each case, the bandgap determined from intrinsic fitting agree reasonably well with those obtained from spectral response

measurements.

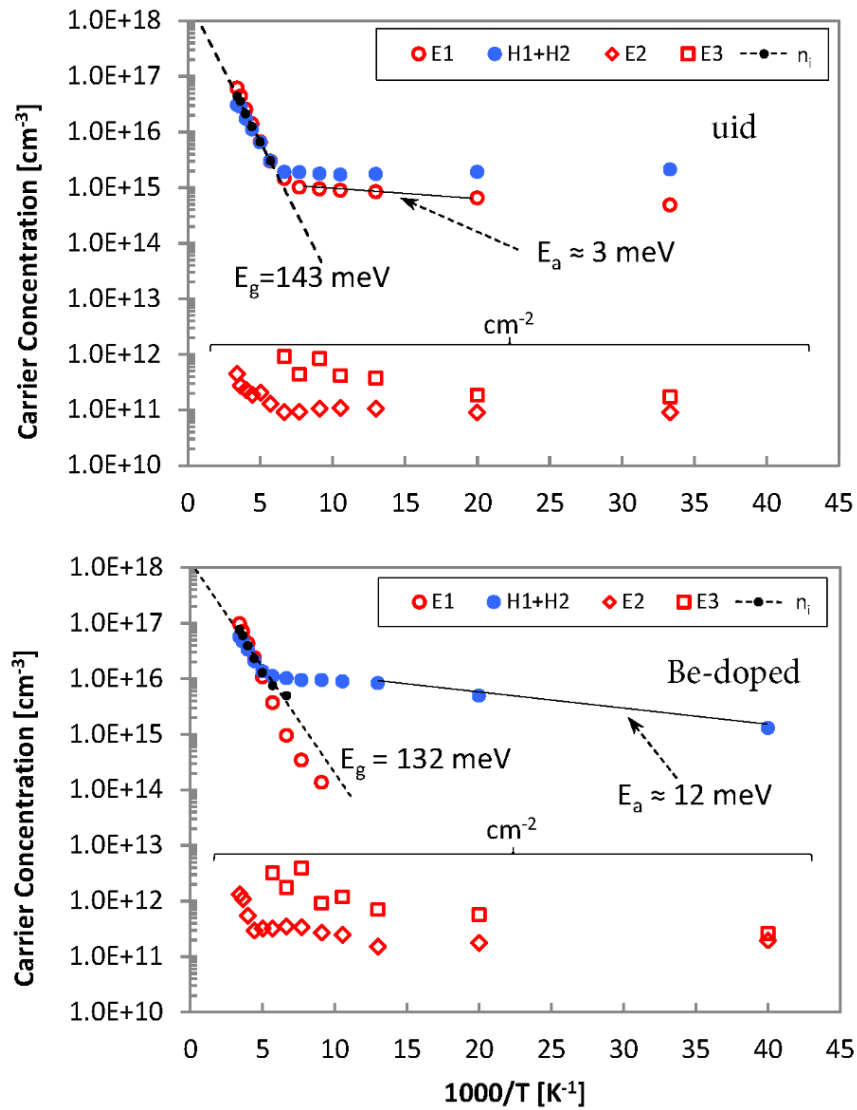


Figure 86: Carrier concentration versus $1000/T$ for all resolved carriers in uid LW InAs/GaSb (top) and Be-doped LW InAs/GaSb. Bulk carriers (E1 and H1+H2) are given in units of cm⁻³ while interfacial carriers (E2 and E3) are expressed as cm⁻². Fitting of bandgap in the intrinsic region and carrier activation at low temperature are included.

The low temperature activation energy of $E_a = 12$ meV in the Be-doped sample is calculated assuming partially compensated material, and is less than half the value of 28 meV previously reported using electroluminescence data on Be-doped MW InAs/GaSb didoes [266]. The activation energy

obtained in this work compares nicely with the binding energies of carbon [267], Si, and Ge [268] in GaSb, which reported values of 12.9 ± 1 meV, 9.4 meV, and 9.5 meV, respectively. The lower value of $E_a = 12$ meV would suggest that the degree of confinement within the LW SL is lower than in the MW layer [269], which does not seem likely due to the increasing separation between adjacent wells. It is worth noting that the activation energy obtained here is in agreement with Be-doped InAs [270] and Be-doped InAs/InAsSb SLs [271].

The power of MSA rests in its ability to quickly determine the relevant conductive carrier species in samples of interest. The bulk electron and bulk hole resolved from the MSA (left column) and Be-doped (right column) samples are shown in comparison to traditional single-field Hall results in Figure 87. The left column are results from the MSA sample, while the right column are from the Be-doped sample. In all figures, red markers indicate electrons, blue holes, and black lines with small circles represent single-field Hall results. Figure 87 (b) and (d) show interesting transitional behavior as the sample switches from p -type to n -type for $T > 175$ K. While the conductivity change is reflected in the single-field results, MSA is able to quantify both carriers throughout the temperature range. Figure 87 (e) and (f) show the electron and hole percent conductivities across the entire layer. For the MSA doped sample (left column), conduction is dominated by the electron carrier at all temperatures due to the lower effective mass. Alternatively, in the Be-doped sample (right column), low T conduction is dominated by hole carriers but quickly transitions to electron-dominated as the electron population rises with temperature. Any interpretation of single-field Hall results on SL material must take into account the relationships outlined in Figure 87, particularly in determining background doping levels.

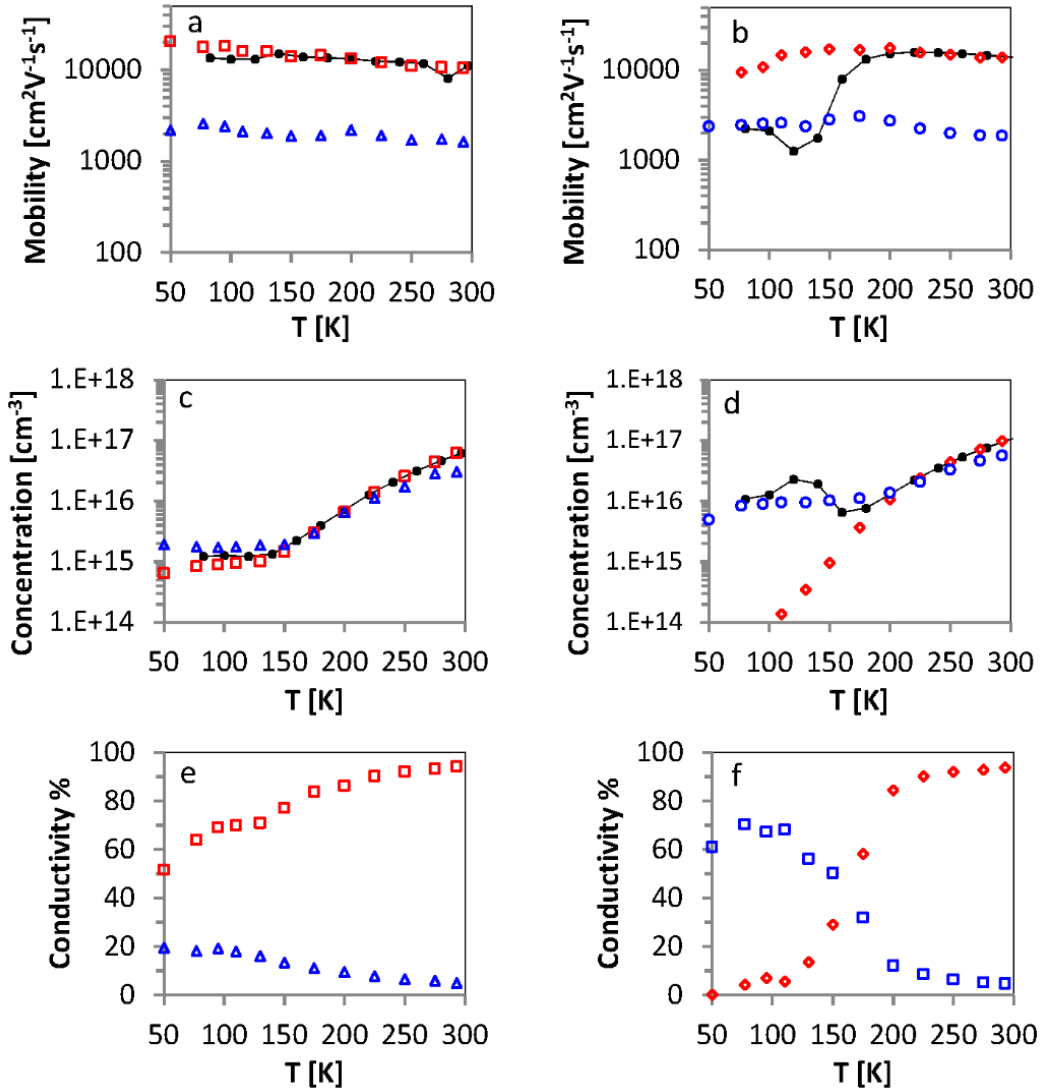


Figure 87: Single-field Hall results (solid black line and circle) are compared to bulk electron (open red markers) and bulk hole (open blue markers) from MSA. The mobility (a and b), carrier concentration (c and d), and conductivity percent (e and f) and shown for undoped LW InAs/GaSb (left column, a, c and e) and Be-doped LW InAs/GaSb (right column, b, d, and e).

5.2.2 InAs/InAsSb

Despite a wealth of optical and lifetime studies of the InAs/InAsSb material system, there has been very little work concerning carrier transport to date. Although there were initial concerns about poor vertical transport [272, 273], more recent measurements find an order of magnitude improvement of vertical hole mobility in InAs/InAsSb material [274] versus similar InAs/GaSb material [204]. Studies to

date have been primarily *n*-type but recent efforts have been made to dope the material *p*-type [275], thus harnessing the higher mobility electron to enhance performance [276]. To the best of the authors' knowledge at the time of writing, MSA of transport in the InAs/InAsSb material system have not been presented in the literature.

To determine fundamental carrier properties a 3.3 μm thick uid LW InAs/InAs_xSb_{1-x} ($x \approx 0.5$) layer was prepared using the same preparation details as outlined for InAs/GaSb SL layers. The material was grown on a GaSb substrate with an Al-containing insulating layer separating absorber and substrate. The desired LW response was confirmed using FTIR spectral measurements. Mobility spectrum temperature evolution results for in-plane transport are shown in Figure 88. Clearly, based upon the mobility spectrum results, the transport within this layer is complex. Four electron and two hole peaks are labelled for convenience. The overall conductivity, including the high mobility bulk electron, of this layer was found to be much higher than uid InAs/GaSb SL results.

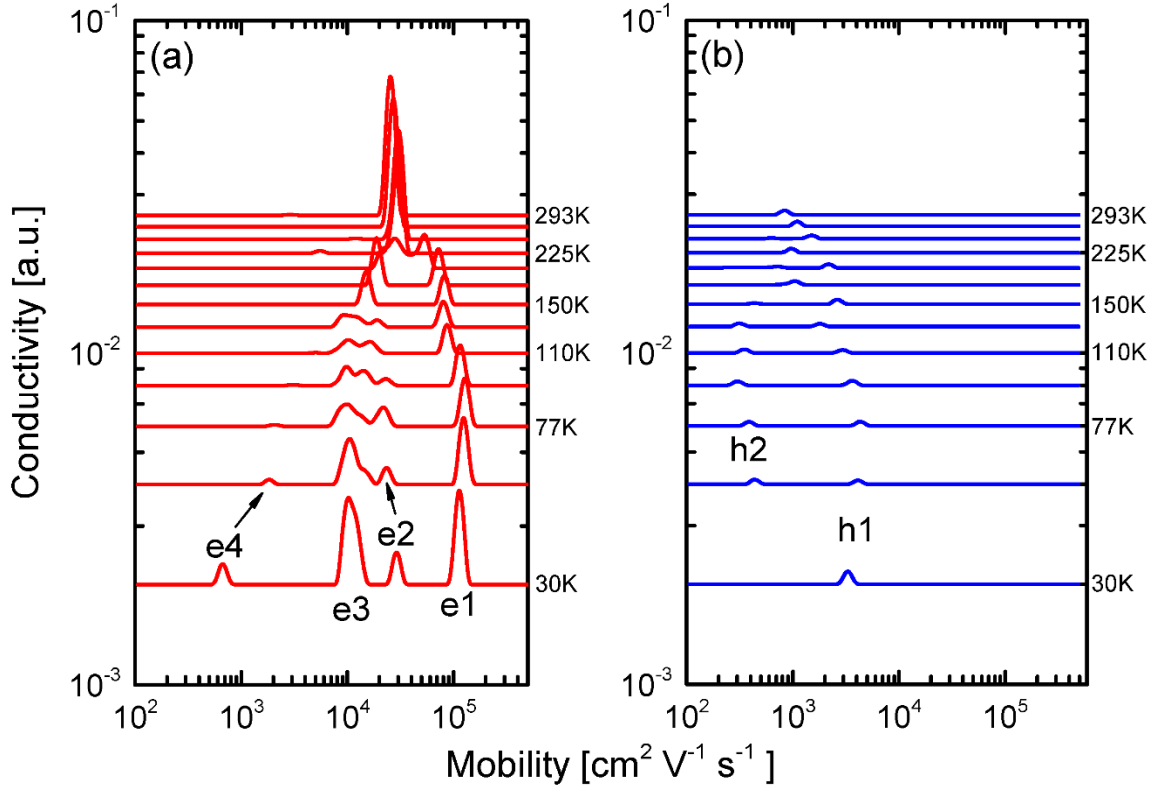


Figure 88: Mobility spectrum temperature evolution of 3.3 μm uid LW InAs/InAsSb SL showing distinct electron (a) and hole (b) peaks.

In the InAs/InAsSb material system, holes are expected to be primarily localized to the InAsSb layers while electrons reside mainly in InAs layers but may penetrate into InAsSb as well. As a result, the uid LW InAs/InAsSb material was determined to be *n*-type, as expected [139]. Mobility and carrier concentration behavior of all peaks are shown in Figure 89, with carrier e2, e3, e4, and h2 listed as sheet concentration since it is unclear if they are bulk-related. The high mobility electron peak e1 and hole peak h1 can intuitively be assigned to the SL bulk due to intrinsic behavior. A bandgap of 89 meV near room temperature was calculated from fitting of the intrinsic carrier concentration, verifying LW behavior.

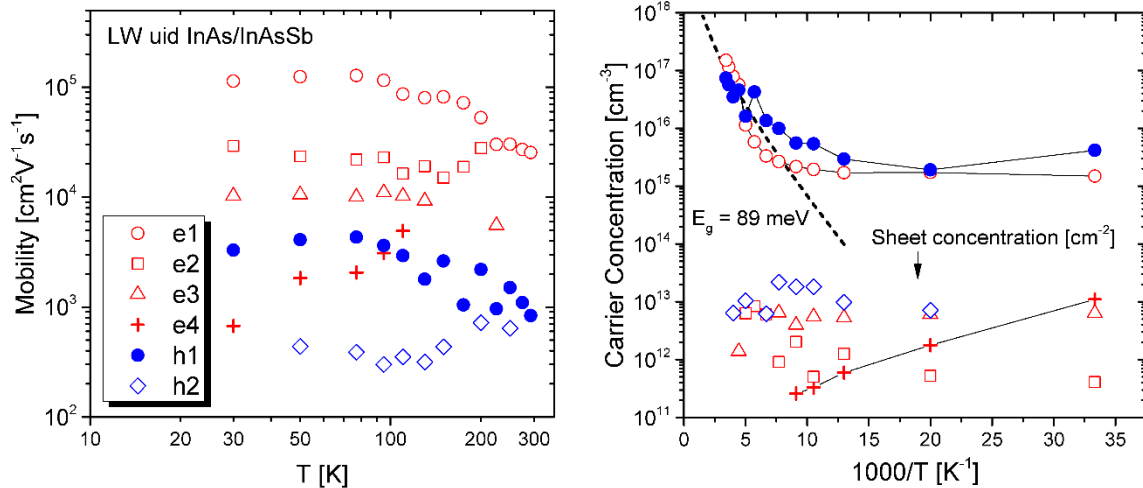


Figure 89: Mobility (left) and concentration (right) of all peaks in uid LW InAs/InAsSb sample.

Carrier e1 has a mobility of $127,810 \text{ cm}^2\text{V}^{-1}\text{s}^{-1}$ at 77 K and a low temperature residual doping of $1.5 \times 10^{15} \text{ cm}^{-3}$ at 30 K. The bulk hole concentration was surprisingly higher, measuring $4.2 \times 10^{15} \text{ cm}^{-3}$ at 30 K. The absorber hole mobility was determined to be $4,307 \text{ cm}^2\text{V}^{-1}\text{s}^{-1}$ at 77 K, comparable to results from LW InAs/GaSb layers, indicating similar in-plane hole effective masses. Alternatively, the absorber electron mobility is notably higher than InAs/GaSb SLs in this work. The magnitude and temperature dependence of the bulk electron mobility is reminiscent of ternary InAsSb material; i.e. mobility governed by ionized impurities and alloy scattering at low temperature and lattice phonon scattering at high temperature. The InAsSb-like properties of the bulk electron are an indication of strong electron wave function leakage into adjacent barriers [277].

The percentage of total conductivity of carriers e2, e3, and e4 are not insignificant, measuring 8.9%, 48.4%, and 5.5%, respectively, at 30 K. In fact, carrier e3 has the largest conductivity contribution of any carrier at 30 K. The percent conductivity versus temperature for electron carriers is shown in Figure 90, and gives a better idea about conduction dynamics in this layer. Spikes at 150 K and 200 K are seen to correspond to MSA peak merging of electron carriers once mobility values become comparable, which also tends to distort the mobility versus temperature smoothness. Despite peak mergers, the dominate peak near room temperature is mostly comprised of the bulk electron population due to thermal

carrier generation.

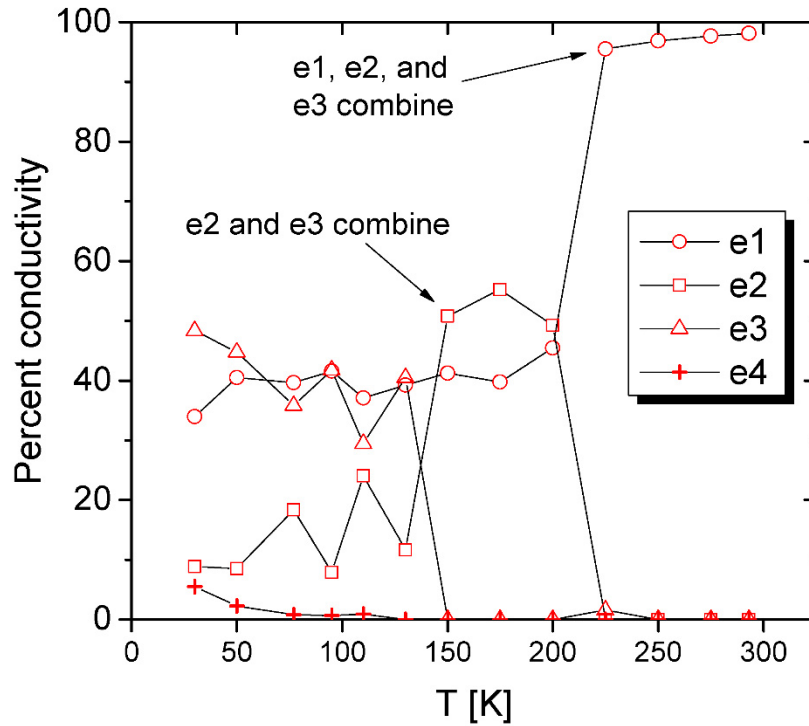


Figure 90: Electron peak percent conductivity to overall conductivity versus temperature in uid LW InAs/InAsSb layer. The graph clearly shows peak mergers at 150 K and 200 K.

In order to better investigate the origin of carriers the following LW InAs/InAsSb samples were grown:

- 0.5 μm thick uid sample
- 1.0 μm thick Be-doped *p*-type sample (target doping level: $2 \times 10^{16} \text{ cm}^{-3}$)

Both samples were grown and prepared under nominally similar conditions. The 0.5 μm thick sample was grown in an effort to determine surface-like contributions by changing sample thickness while the Be-doped sample was simply to investigate *p*-type doping effects. Variable-field measurements were taken on both samples at 77 K for comparison.

MSA revealed the 0.5 μm uid sample to contain four electron peaks and zero hole peaks. The *n*-type background carrier concentration in this layer was determined to be $7.1 \times 10^{15} \text{ cm}^{-3}$, almost a factor

of 5 higher than in the 3.3 μm thick sample. Given the background hole doping in the 3.3 μm sample ($\sim 3 \times 10^{15} \text{ cm}^{-3}$ at 77 K), the absence of hole conduction in this layer is not surprising. The electron mobility spectra from the 3.3 μm and 0.5 μm thick layers are shown side-by-side in Figure 91. Although there are qualitative similarities, little can be concluded from the comparison. A drop in the e1 peak mobility is a result of increased ionized impurity scattering and compensation effects [261], further indication of the InAsSb-like mobility properties governing in-plane scattering in this material. The near factor of 5 change in background concentration between these samples is a major growth concern that has considerable performance implications, and highlights the need for more fundamental growth studies.

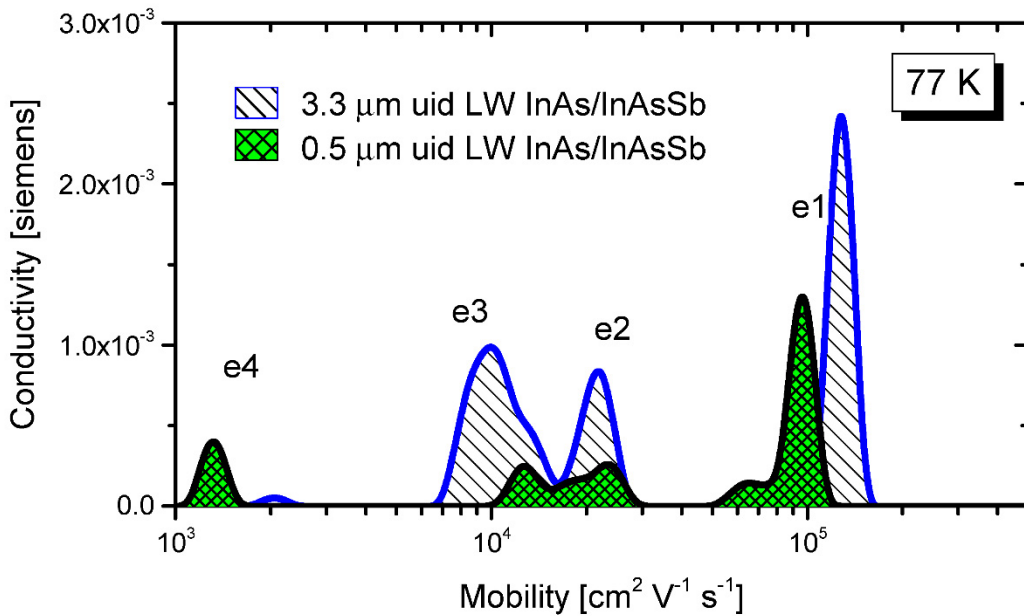


Figure 91: 77 K electron mobility spectrum of 0.5 μm and 3.3 μm thick InAs/InAsSb absorbers.

Peaks e2 and e3 appear at similar mobility but are overall much less conductive, in better agreement with bulk InAsSb results presented earlier. The combined conductivity of peaks e2 and e3 turn out to be a factor of ~ 4 less in the 0.5 μm layer than in the 3.3 μm layer. This finding is an indication that e2 and e3 are not likely found in the bulk of the material. Rather, the variability seen here is probably a result of surface/interface quality; i.e. the 3.3 μm layer appears to possess particularly poor surface and

barrier-interface regions. Future studies should aim to closely monitor material quality near the SL-barrier and surface interfaces, especially with regards to growth conditions and chemical surface treatments. The high conductivities and variability of surface/interface carriers found in this work make a more detailed study paramount.

The 77 K mobility spectrum of the Be-doped InAs/InAsSb sample is shown in Figure 92. Two electrons and two hole carriers were resolved. Be-doping is observed to effectively remove the bulk electron (e1) peak from the mobility spectrum. The hole peak of $3,069 \text{ cm}^2\text{V}^{-1}\text{s}^{-1}$ agrees nicely with the absorber hole resolved in the $3.3 \text{ }\mu\text{m}$ thick sample and does not appear strongly dependent on doping concentration. The carrier concentration of holes in the Be-doped sample was determined to be $6.1 \times 10^{15} \text{ cm}^{-3}$ (target level: $2 \times 10^{16} \text{ cm}^{-3}$). Concentration lower than targeted values may be a result of compensation and/or insufficient dopant activation. Although the sample is *p*-type, single-field Hall results do not yield positive values of R_H until fields are greater than 4 T. A recent study showed type conversion in MW InAs/InAsSb SLS at a Be doping level of $3 \times 10^{16} \text{ cm}^{-3}$ [275]. In that study, samples were measured at 10 K and 0.5 T, conditions under which contributions from the two electron peaks may be expected, suggesting that type conversion may occur at lower doping levels. Although the required doping level to type-convert is likely to vary on a run-to-run basis, it is encouraging that both studies suggest type conversion at low- 10^{16} cm^{-3} levels.

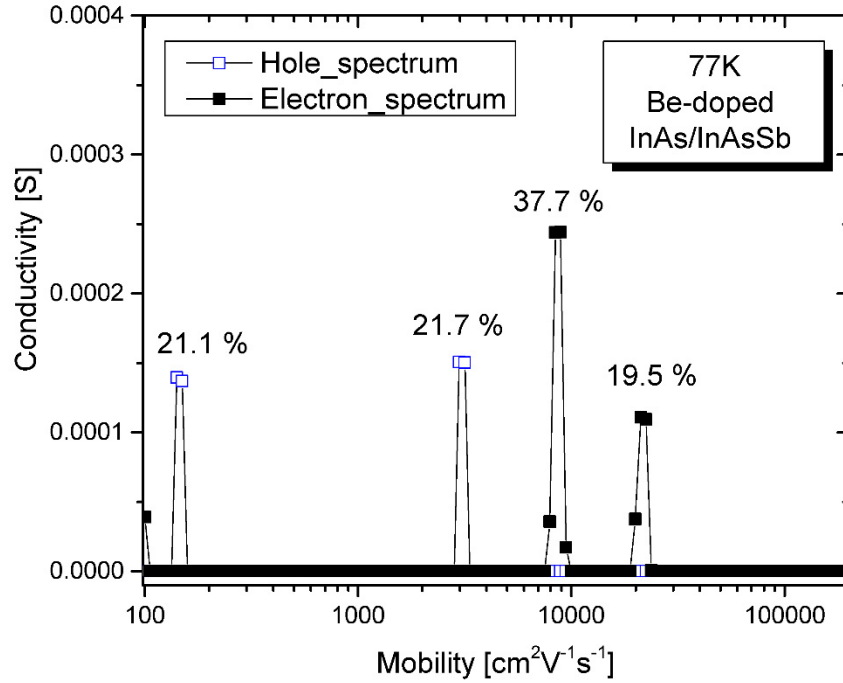


Figure 92: Mobility spectrum of Be-doped InAs/InAsSb at 77 K. Percent of overall conductivity values are included.

The electron (top) and hole (bottom) spectra for the 3.3 μm uid and the 1.0 μm Be-doped samples are shown in Figure 93. The lower mobility hole carrier (h2) displays consistent conductivity between samples despite the changes in absorber thickness and doping. It is interesting to note that the mobility of carrier h2 is consistent with previous findings on the hole mobility in $\text{Al}_x\text{Ga}_{1-x}\text{Sb}$ [278], suggesting this carrier (h2) could be a result of partial conduction within the insulating layer. Further analysis, including temperature dependent behavior, would be required in order to more accurately characterize the h2 carrier.

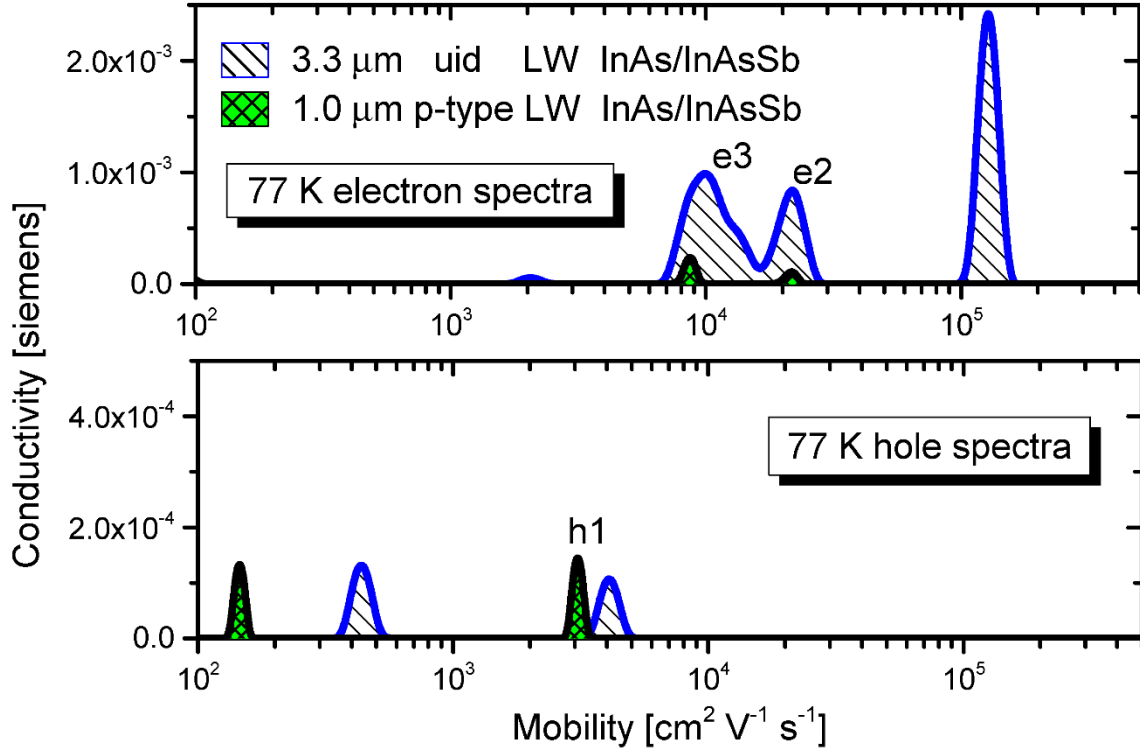


Figure 93: Electron (top) and hole (bottom) spectra comparison between uid and Be-doped InAs/InAsSb absorbers.

The electron peaks in Figure 93, namely the e3 ($\sim 10,000 \text{ cm}^2\text{V}^{-1}\text{s}^{-1}$) and e2 peaks ($\sim 25,000 \text{ cm}^2\text{V}^{-1}\text{s}^{-1}$), are also present in the Be-doped samples but at much lower concentration than the uid SL. Lower surface and barrier-interface sheet concentrations are expected in *p*-type material due to the alignment of the Fermi level. At this point, carrier e3 has consistently been assigned to the surface while e2 attributed to the back SL-barrier interface. While electron peaks e2 and e3 have been found in all three SL samples studied in this section, no consistent behavior concerning sheet concentration has been observed. The mobility and concentration of peaks e2 and e3 for all samples at 77 K are shown in Table IX. The conductivity of e2 and e3 is the lowest in the Be-doped sample, at sheet concentration values of only $3.9 \times 10^{11} \text{ cm}^{-2}$ and $8.3 \times 10^{10} \text{ cm}^{-2}$, respectively. The mobility values are fairly consistent across samples, but sheet concentration values vary significantly, with the apparent outlier being the uid 3.3 μm sample.

Table IX: Summary of surface (e3) and barrier-interface (e2) electron characteristics at 77 K.

Sample	E2 mobility [cm ² V ⁻¹ s ⁻¹]	E2 sheet concentration [cm ⁻²]	E3 mobility [cm ² V ⁻¹ s ⁻¹]	E3 sheet concentration [cm ⁻²]
3.3 μm uid InAs/InAsSb	21,817	1.3 x 10 ¹²	10,000	5.3 x 10 ¹²
0.5 μm uid InAs/InAsSb	23,714	4.6 x 10 ¹¹	12,590	6.3 x 10 ¹¹
1.0 μm Be:2e16 InAs/InAsSb	20,540	8.3 x 10 ¹⁰	8,500	3.9 x 10 ¹¹
InAsSb	34,912	1.2 x 10 ¹¹	13,380	5.7 x 10 ¹¹
InAs	-	-	14,500	1.1 x 10 ¹²

Measurements on the minority carrier lifetime in the 3.3 μm and 0.5 μm uid InAs/InAsSb were found to be ~ 350 ns at 77 K, in agreement with previous results [139]. A reduction in minority carrier lifetime in the Be-doped layer was observed. The Be-doped lifetime at 77 K was measured to be ~120 ns, which gives a concentration lifetime product in close agreement with similar lifetime measurements on Be-doped InAs/InAsSb samples, suggesting an SRH-limited lifetime [279]. The fundamental properties of the InAs/InAsSb material system presented here are very promising and warrant further investigation.

5.3 Residual doping and annealing results

Despite advantages in lateral uniformity, Auger suppression, and reduced B2B tunneling currents, LW InAs/GaSb has not yet reached theoretical performance limits [280]. Unfortunately, high defect-

related SRH centers and high background carrier concentrations limit the lifetime of InAs/GaSb T2SLs [140] and can impact carrier mobility [161]. The background carrier concentration in InAs/GaSb SLs is fundamentally related to transport and is a crucial parameter in design optimization, and must be reduced in order for InAs/GaSb SLs to become a more viable candidate for LW IR detectors [281].

A number of growth studies have shown the importance of growth conditions as related to background doping in InAs/GaSb SLs [145, 282, 283]. Although significant gains in growth quality have been demonstrated, minority carrier lifetimes still remain low (~100 ns). The impact of interface quality has been debated, with most reports showing no correlation with lifetime [138, 284], and others suggesting modest lifetime improvement [285]. Even in reports showing improvement [286], lifetime values were still much lower than desired, suggesting that bulk constituents remain the issue.

Post-growth annealing efforts have been explored in order to improve the quality of T2SL materials [287-289], as well as in bulk III-V materials [290]. Annealing has the potential to improve bulk defects and interface quality if done properly. In this section, we will report on the application of MSA to post-growth annealing studies of bulk InAs and GaSb and LW InAs/GaSb SLs.

Anneals were performed in a closed ampule containing high-purity As. Bulk undoped GaSb and InAs samples (same growth layers as Section 5.1) were annealed at temperatures of 530 °C and 560 °C while undoped and Be-doped LW InAs/GaSb SL samples were annealed at 500 °C. Anneals on InAsSb and InAs/InAsSb layers showed signs of surface sublimation and are therefore not reported on. Ramp up times were short, after which the samples were annealed at temperature for roughly 2 hours. Cool-down was gradual and recorded to take approximately 16 hours. After annealing samples were prepared for Hall and lifetime measurements using standard procedures.

The 77 K single-field Hall results on bulk InAs and GaSb are shown in Table X. A clear degradation in the mobility of the InAs is observed with increasing anneal temperature. Alternatively, no significant change in the mobility or carrier concentration of the GaSb layer is observed. Figure 94 shows the surface morphology of as-grown layers and those after 560 °C anneal, showing severe degradation in both GaSb and InAs.

Table X: Summary of 77 K single-field Hall results on annealed bulk InAs and GaSb.

Anneal	InAs mobility [cm ² V ⁻¹ s ⁻¹]	InAs carrier concentration (n)	Gasb mobility [cm ² V ⁻¹ s ⁻¹]	GaSb carrier concentration (p)
None	19,416	9.34 x 10 ¹⁵	4,910	8.47 x 10 ¹⁵
530 °C	17,852	9.56 x 10 ¹⁵	4,299	1.15 x 10 ¹⁶
560 °C	7,813	1.08 x 10 ¹⁵	4,538	9.30 x 10 ¹⁵

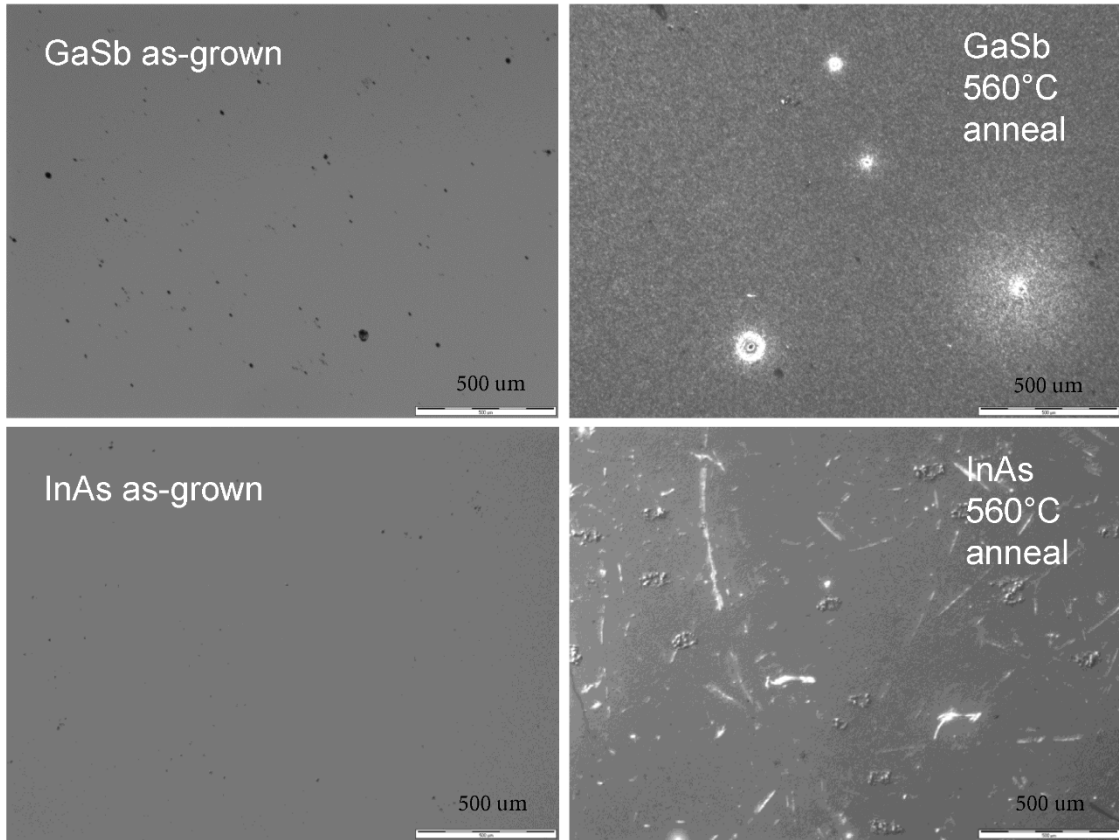


Figure 94: Nomarski images of surface morphology on GaAs (top) and InAs (bottom) samples. As-grown images are shown in the left column, while images after annealing at 560 °C are shown in the right column.

MSA results on bulk annealed samples at 77 K are shown in Figure 95 to better determine what properties are changing within the material. The mobility spectrum for the GaSb returned virtually identical results regardless of treatment, showing the material to be resilient to high temperature annealing. The light hole and heavy hole peaks are unchanged, indicating no material improvement or reduction in background doping levels. The mobility spectrum of the InAs layer shows significant alteration with annealing treatments. After analyzing the conductivity of the layer, we see a slight increase in low mobility carriers ($\sim 1,000\text{-}15,000\text{ cm}^2\text{V}^{-1}\text{s}^{-1}$) and an 18% reduction in the bulk conductivity peak. After 560 °C anneal, an 80% drop in bulk electron conductivity is observed. Low mobility carriers (surface and substrate-interface) are also shifted to lower mobility, signifying degradation in these regions.

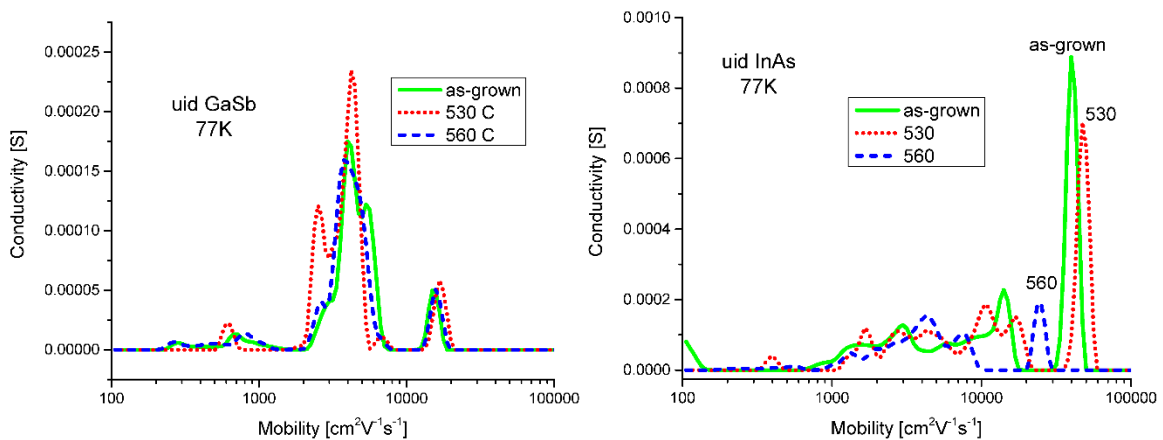


Figure 95: GaSb (left) and InAs (right) mobility spectrum at 77 K for as-grown (solid green), 530 °C annealed (red dot), and 560 °C annealed (blue dash).

Attempts were made to measure the minority carrier lifetime of bulk samples in relation to annealing treatment. As-grown GaSb, as previously mentioned, displayed low ($< 100\text{ ns}$) lifetime and showed no signs of improvement with annealing treatment. On the other hand, the InAs material showed a high degree of sensitivity to annealing treatments. Measurements after 530 °C anneal were plagued with surface recombination (20 ns) and no bulk lifetime could be established. Lifetime measurements on the

560 °C sample possessed exceptionally long lifetimes ($\sim 70 \mu\text{s}$), well above theoretical predictions, a strong indication of deleterious carrier trapping effects.

Overall, the results on bulk materials showed no signs of improvement in mobility, background carrier concentration, or minority carrier lifetime. Surface damage was evident in both samples and InAs material showed a rapid degradation in quality with increasing anneal temperature. For this reason, anneal temperatures of 500 °C will be used on InAs/GaSb SL layers, which is expected to improve photoresponse and mobility [291].

Bulk electron and hole carriers were extracted from temperature dependent MSA on the previously characterized undoped and Be-doped LW InAs/GaSb samples following a 2 hour 500 °C anneal under As overpressure. The annealed and unannealed temperature dependent mobility and carrier concentration of bulk carriers for the undoped LW InAs/GaSb sample are shown in Figure 96. Mobility values near room temperature are in agreement but changes in the low temperature hole and electron are observed. An improvement of the bulk hole after annealing is accompanied by a drop in the bulk electron mobility for temperatures of 30-150 K. For an operating temperature of 77 K, the hole mobility improves from $2,567 \text{ cm}^2\text{V}^{-1}\text{s}^{-1}$ to $3,901 \text{ cm}^2\text{V}^{-1}\text{s}^{-1}$ after annealing, an encouraging improvement. Alternatively, the electron mobility drops from $17,793 \text{ cm}^2\text{V}^{-1}\text{s}^{-1}$ to $11,190 \text{ cm}^2\text{V}^{-1}\text{s}^{-1}$. The low temperature mobility changes are complemented by low temperature changes in carrier concentration, namely a drop in hole population and increase in electron population. As can be seen in Figure 96, the bandgap of the material is preserved after annealing. As a whole, the background doping levels appear to drop after annealing, which should have a positive impact on performance. Furthermore, mobility changes in the material at low temperature should also have a positive influence on performance, as an increase in the hole carrier mobility (minority carrier) could lead to QE improvement.

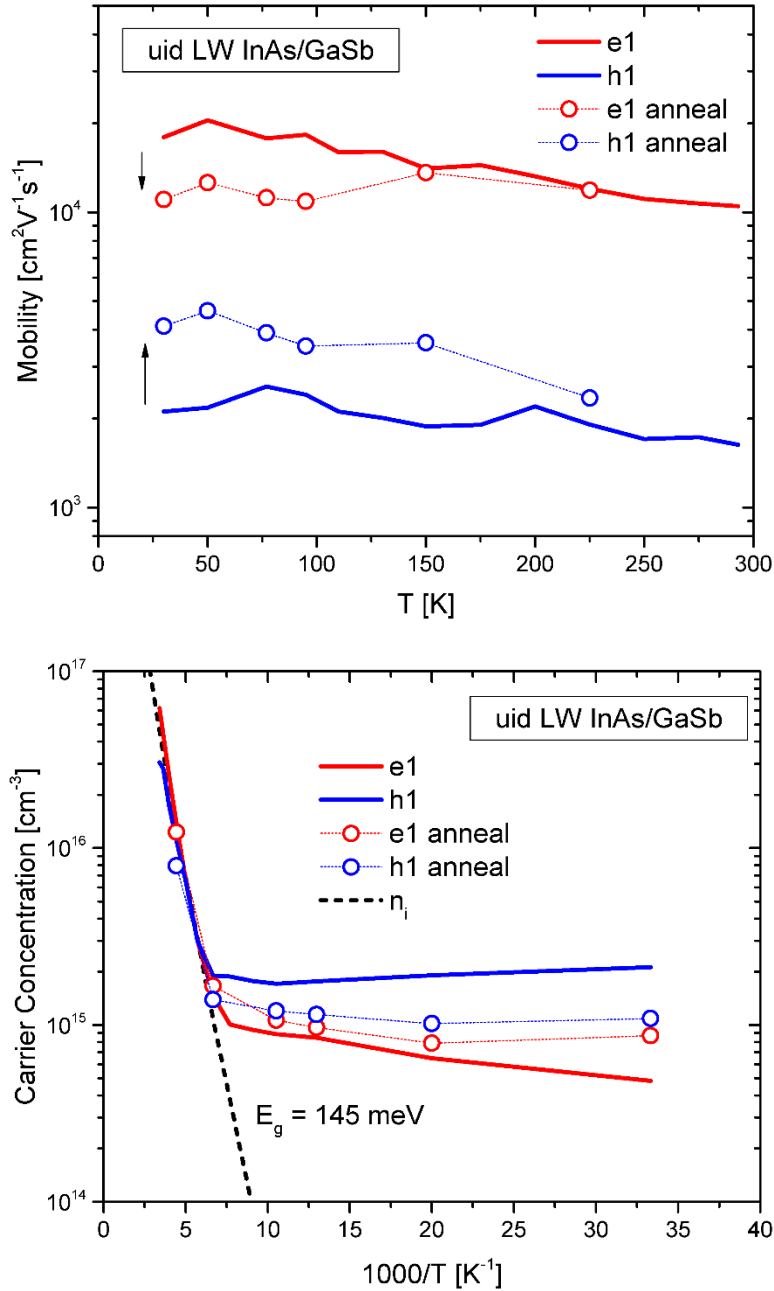


Figure 96: Bulk mobility (top) and concentration (bottom) for absorber electron and hole before and after post-growth anneal at 500 °C in uid LW InAs/GaSb.

The mobility and concentration comparison for the Be-doped LW InAs/GaSb sample are shown in Figure 97. Strong overlap in the mobility and carrier concentration is observed for electron and hole carriers. The bandgap of the material is again unaffected by the annealing treatment. Overall, the Be-doped sample appeared more resilient to post-growth annealing treatments and did not display any

significant changes in MSA. This result may be related to a lowering of the average lattice constant in the SL as a result of Be-doping [292].

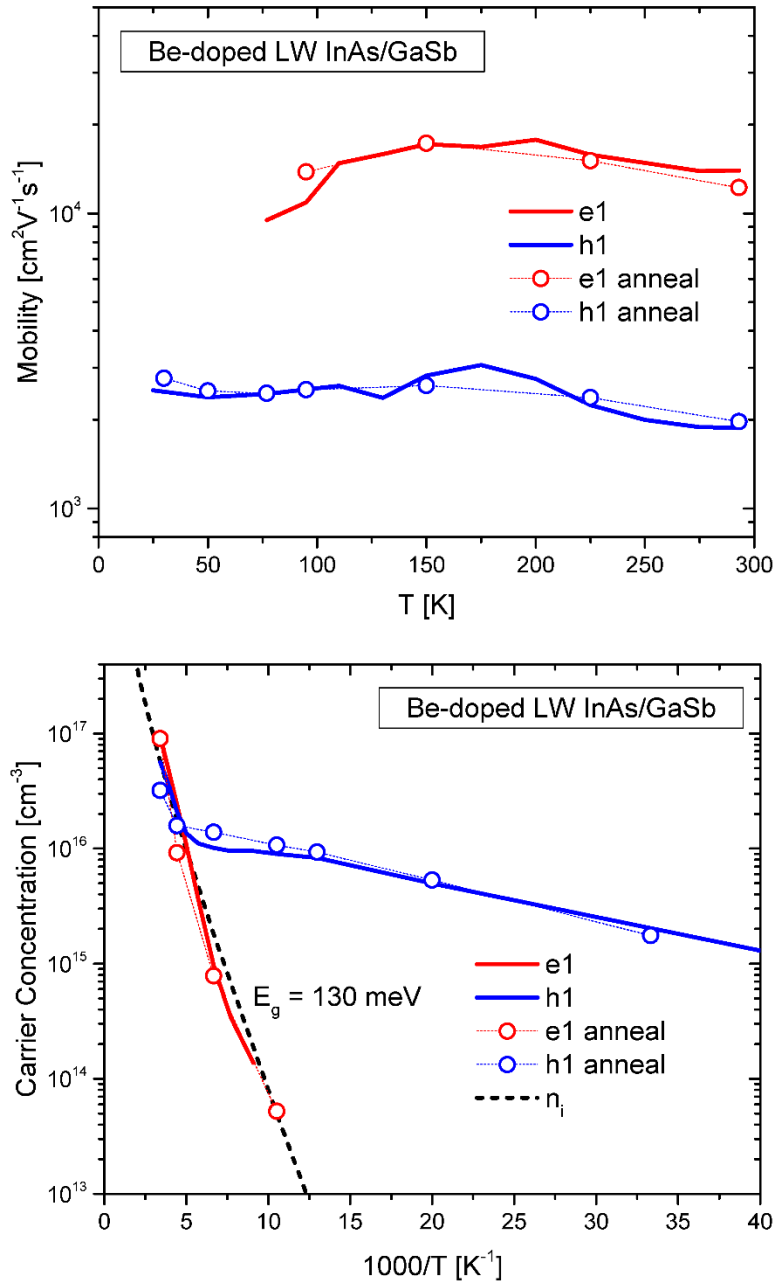


Figure 97: Bulk mobility (top) and concentration (bottom) for absorber electron and hole before and after post-growth anneal at 500 °C in Be-doped LW InAs/GaSb.

In summary, results show that MSA can effectively be applied to the study of residual doping levels in T2SLs. Post-growth temperature annealing was largely ineffective at improving bulk GaSb and InAs material. Care should be exercised in annealing of bulk InAs material, as rapid degradation is observed at temperatures greater than 500 °C. The bandgap of LW SL material was unchanged after annealing at 500 °C for 2 hours. Improvements in background doping level and hole mobility were seen on an undoped LW InAs/GaSb layer, but no significant changes were observed in the Be-doped LW InAs/GaSb, possibly due to crystallographic changes within the SL as a result of doping.

5.4 Surface passivation experiments

An important challenge in the development of LW T2SL devices is the reduction of excessive surface leakage currents due to exposure of mesa sidewalls. The termination of the lattice gives rise to a large number of surface states, and along with the spontaneous formation of native oxides, provides a conductive pathway that increases dark current and limits performance. The issue is especially pronounced in LW devices and has been met with substantial efforts to develop effective and durable passivation techniques. Passivation studies using dielectric SiO₂ [293], (NH₄)₂S [294], sulphur [295, 296], polyimide [297], photoresist SU-8 [298], and atomic layer deposition (ALD) of Al₂O₃ [299] have all been explored as means of passivation. The goal of establishing a long-term passivation technique remains an active area of research in the field.

To analyze the efficacy of passivation treatments, this section proposes the application of MSA to determine the impact of various depositions on SL surface conductivity. Focus will be placed upon heterostructure devices employing *p*-type absorbers, which present potential performance advantages due to the fundamentally high mobility of the minority carrier electrons but is challenging due to excessive surface leakage currents. Previous analysis on Be-doped LW InAs/GaSb revealed an electron carrier (e⁻) with weakly temperature dependent mobility and concentration and identified as a surface electron. Based on Figure 98, we see that the surface carrier percent conductivity maximizes at 30 K. Therefore, to better

assess the impact of surface treatments, all measurements are performed at 30 K. For reference, the unpassivated surface electron has a mobility of $4,620 \text{ cm}^2\text{V}^{-1}\text{s}^{-1}$ and sheet carrier concentration of $1.97 \times 10^{11} \text{ cm}^{-2}$, giving a conductivity of 1.458×10^{-4} siemens at 30 K.

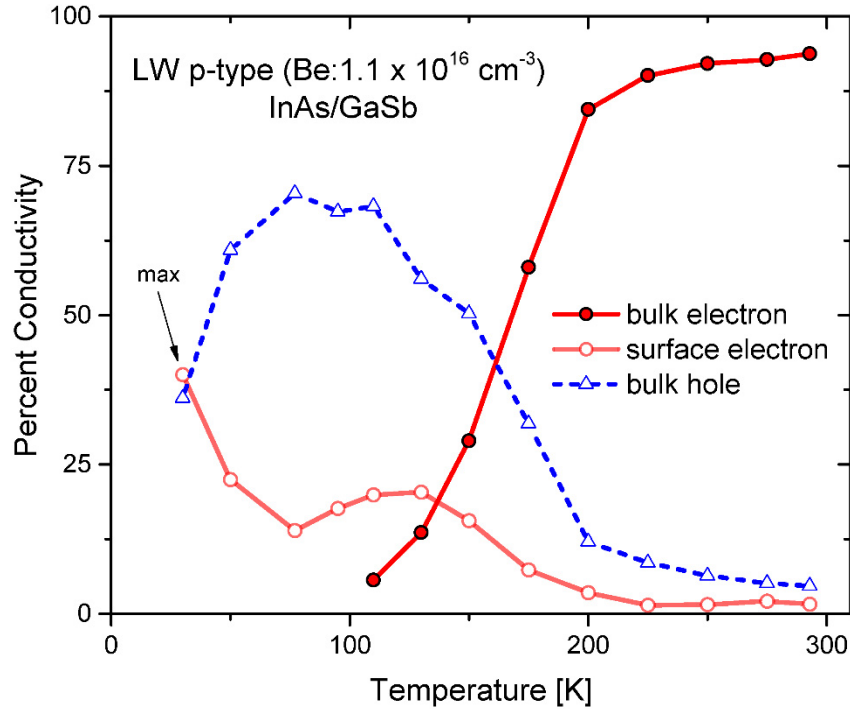


Figure 98: Percent conductivity of bulk electron (closed circle), surface electron (open circle), and bulk hole (open triangle) in Be-doped LW InAs/GaSb layer used for all surface passivation measurements. Surface electron conductivity contribution is seen to maximize at low temperature.

Two passivation approaches were attempted. The first approach consists of dielectric SiO_2 deposition followed by X-ray charging [300, 301], thus forming an SiO_2 -based electret to act as a built-in gated diode, which has been shown to be an effective suppressant of surface leakage [302]. The second approach consists of electrical passivation via thiolated self-assembled monolayer (SAM) deposition followed by a subsequent inorganic (SiO_2 , SiN) physical encapsulate. The electret based approach is appealing because it removes the need for a metal gate contact layer, thus making it more compatible with FPA fabrication. The thiol approach also has many advantages. Thiols consist of a sulfur head, which has

long been used in passivation of III-V materials. Many thiols are commercially available, and may be non-functionalized or functionalized. Functionalized tails may allow for easier bonding of a polymer encapsulate layer. Alternatively, non-functionalized thiols may act as sacrificial layers, preventing oxidation prior to chemical vapor deposition (CVD) of dielectric passivation, thus providing a superior interface.

Surface preparation is a critical procedure for successful passivation deposition. For simplicity, all material etching (delineation/Hall sample preparation) was performed using a H_3PO_4 /citric acid solution. A degrease step consists of sonication in hexane, acetone, and ethanol, following by O_2 plasma ashing. For thiol passivated samples, a rapid H_2SO_4 /citric acid etch was performed prior to deposition since phosphoric acid solutions resulted in poor monolayer formation [303]. Samples used for Hall characterization were wet-etch significantly into the absorber layer, adequately exposing multiple SL periods. Efforts to maintain similar preparation, including sample geometry and etch depth, were conducted.

After etching to expose the SL, ~ 300 nm of SiO_2 were deposited on three measurement samples; a control sample with no charging (bare SiO_2), a sample X-ray charged overnight (-75 V surface), and a sample X-ray charged over multiple charging cycles (-90 V surface). The surface voltage of charged samples was measured before and after Hall measurement. The overnight charge surface measured at -75 V before and -23 V after, while the charge-cycled sample measured at -90 V before and -61 V after.

The mobility spectrum results on electret surface passivation are shown in Figure 99, with inset showing unchanged bulk hole spectra to confirm measurement integrity. Surprisingly, the bare SiO_2 passivation results in nearly an order of magnitude increase in surface conductivity compared to unpassivated as-grown measurement. This may be due to improper deposition or, more likely, the introduction of water moisture during cool-down for Hall measurement leading to the formation of charged trap states [304]. A reduction in surface conductivity is seen for both SiO_2 electret passivations versus bare SiO_2 , but surface conductivity for all SiO_2 layers is higher than in the as-grown sample. The more highly charged electret passivation is encouraging since in theory it shows that surface conduction

can be reduced using this approach. However, the charge stability in these electret layers does not appear tolerable at this point, as severe drops in surface voltage were measured in both layers after Hall measurement and continued to drop when measured a week later. Clearly, for this project to prove successful in the future, a more mature understanding of charge stability is needed, in addition to a more robust charging apparatus, with corona discharge being an excellent candidate.

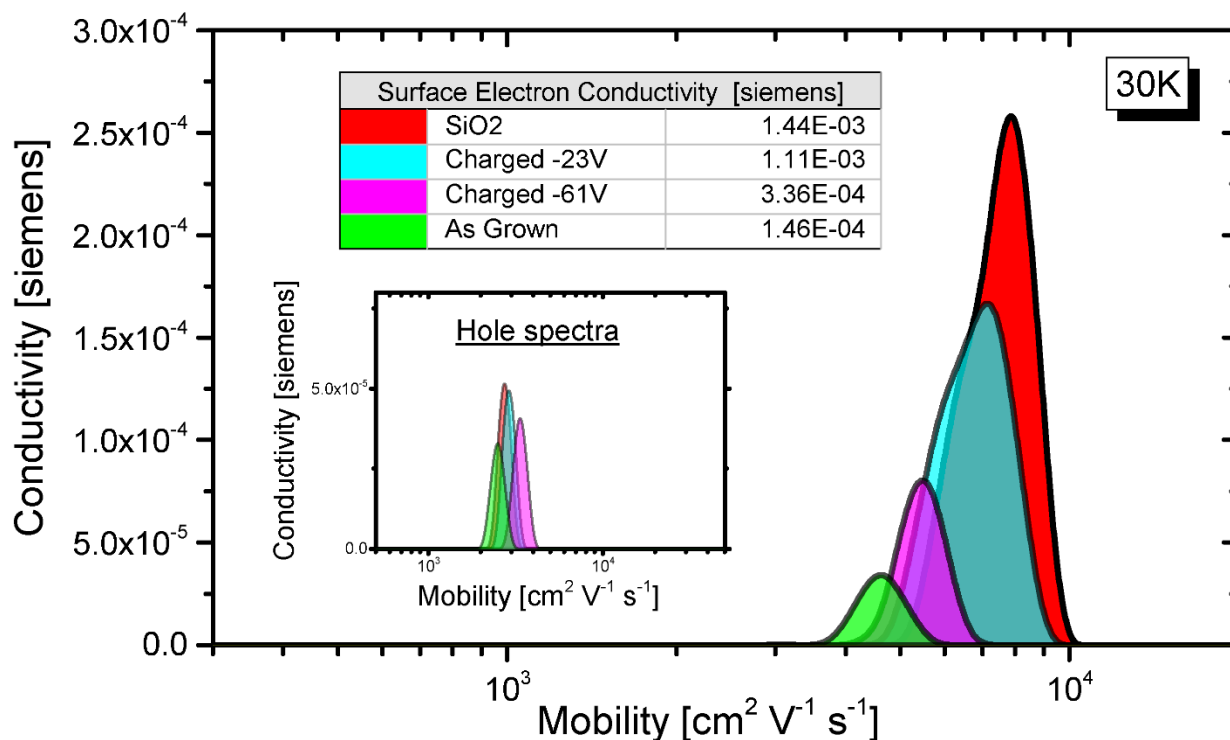


Figure 99: 30 K mobility spectrum of surface electron after SiO₂ passivation with respect to electret charging. As-grown surface conductivity shown for comparison. Inset graph shows consistency of bulk hole spectra to verify measurement integrity.

Thiolated SAMs used in this work were chosen due to commercial availability, affordability, and relative ease of deposition. The non-functionalized alkane thiols in this work are referred to as CXSH, where X denotes the carbon chain length, and include C₆SH (hexanethiol), C₁₂SH (dodecanethiol), and C₁₈SH (octadecanethiol). The increased carbon chain length may provide a more hydrophobic surface to prevent moisture adsorption, but possibly at the expense of thiol density in the monolayer. An additional amine-functionalized thiol, cysteamine, is investigated due to the enhanced potential to bond with a

polymer-based encapsulate for long term chemical and physical stability.

Standard alkane thiol deposition is carried out by sample immersion of 10 mM CXSH in solution with 9:1 ratio of ethanol to NH_4OH . Ammonium hydroxide is intended to promote covalent bonding by de-protonating the thiol molecule [305]. After 24 hr immersion at 40 °C, the sample is rinsed in ethanol and prepared for Hall measurement. The same procedure was used for cysteamine (Cyst1) with the exception of temperature, with immersion at room temperature. An additional cysteamine sample (Cyst2) was deposited in a 100 mM, NH_4OH -free solution at 40 °C for 2 hours in an attempt to avoid unwanted etching [306]. Changes in deposition procedure (time, chemical treatment, temperature) are noted as necessary.

Surface electron conductivities for all thiol passivation treatments are compiled and shown in Figure 100. Due to the remaining conductivity of the bulk hole and SL-barrier interface, the confidence level for resolving carriers rests at $\sim 10^{-6}$ S. All thiol treatments (C6SH, C12SH, C18SH, Cyst1, and Cyst2) are seen to be excellent passivants of the surface electron carrier, showing at least two orders of magnitude reduction in surface conductivity. The true reduction in surface conduction is unfortunately below system limit in some cases and cannot be reported here.

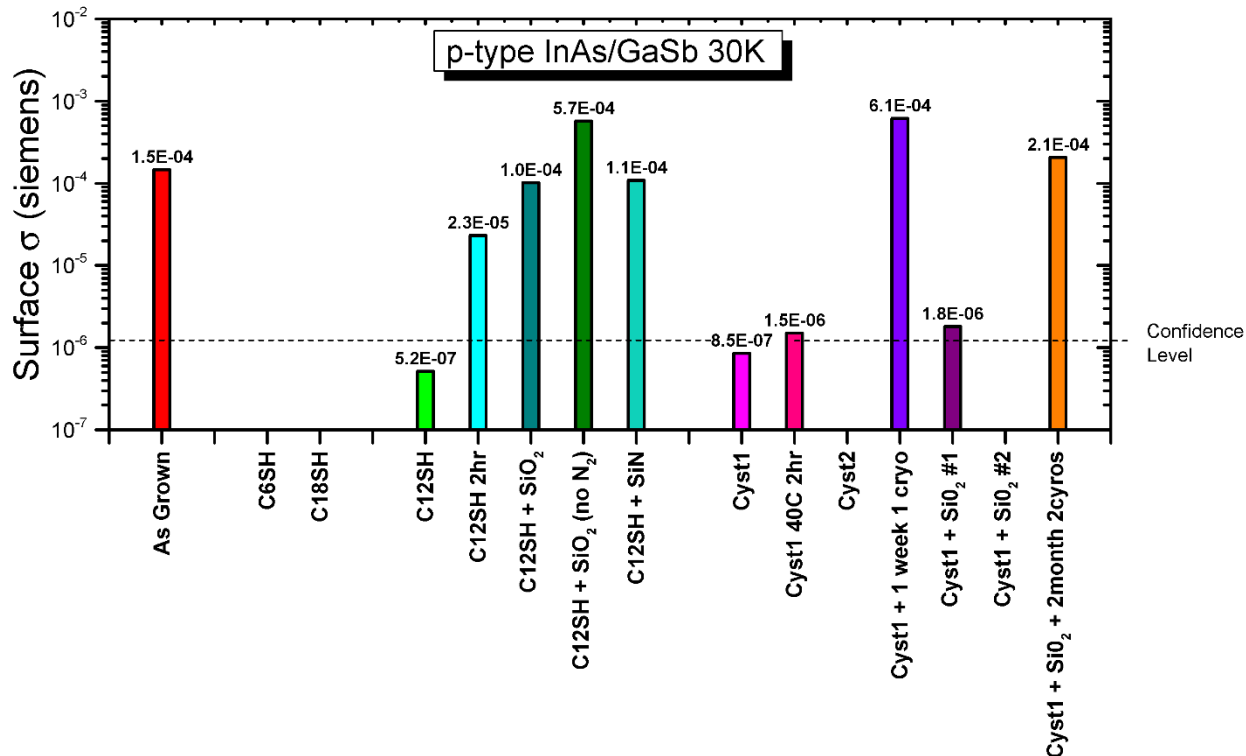


Figure 100: Collection of electron surface conductivity data on all thiol surface treatments in this work. Results include attempts to shorten immersion time in thiol-solution, as well as stability studies after cryo-cycling and time lapse.

In an attempt to alleviate the onerous immersion time, C12SH and Cyst1 samples were prepared and tested after only 2 hours in solution (C12SH 2hr and Cyst1 40C 2hr in Figure 100). Results show that cysteamine binds to the surface at a much faster rate than C12SH, in agreement with deposition rates on InAs. Still, the surface conductivity using cysteamine with a shortened deposition time is worse than standard deposition, suggesting further refinements would need to be made.

Additional samples were prepared to incorporate the dielectric encapsulation layers (C12SH + SiO₂, C12SH + SiO₂ (no N₂), C12SH + SiN_x, Cyst1 + SiO₂ #1, and Cyst1 + SiO₂ #2). All attempts to encapsulate C12SH passivated layers saw an increase in surface conductivity back to as-grown quality levels. The reason for this is not precisely known but provides valuable feedback on deposition procedures. On the other hand, cysteamine encapsulated with SiO₂ repeatedly retained the desired surface passivation. This result is particularly promising for future development of long term passivation using

the two-step chemical and physical passivation approach.

Unfortunately, MSA measurements also show serious issues with surface stability at this stage in development. A bare cysteamine layer was retested after one cryo-cycle and one week later (Cyst1 + 1 week 1 cryo) and showed reversion back to as-grown conductivity levels. The same degradation was observed for a dielectric encapsulated cysteamine layer after 2 cryo-cycles and 2 months (Cyst1 + SiO₂ + 2month + 2cryo). Although the results remain encouraging, this finding highlights the need for further studies in order to properly address this issue.

Diodes were fabricated for successful thiol passivations (C6SH, C12SH, C16SH, Cyst1, and Cyst2) to validate the observed MSA reductions in surface conductivity. The device layer (mentioned earlier) used is a *p*-type barrier structure [262] with an identical *p*-type LW InAs/GaSb absorber, a wide-gap lightly *p*-type doped barrier layer, a wide-gap highly *n*-type top contact, and a highly doped *p*-type back contact layer. Spectral response measurements revealed the desired 9.5 μm cut-off and a low turn-on bias of ~ 50 mV. The 77 K dark current results for all thiol passivations are shown in Figure 101. Unpassivated and shallow etch results are shown for reference, with the shallow etch being indicative of material quality. At an operating bias of – 50 mV, all thiol passivated layers are within an order of magnitude of shallow etched values. C6SH and cysteamine appear to be the best performers, suggesting that smaller molecules provide a highly thiol density leading to better passivation.

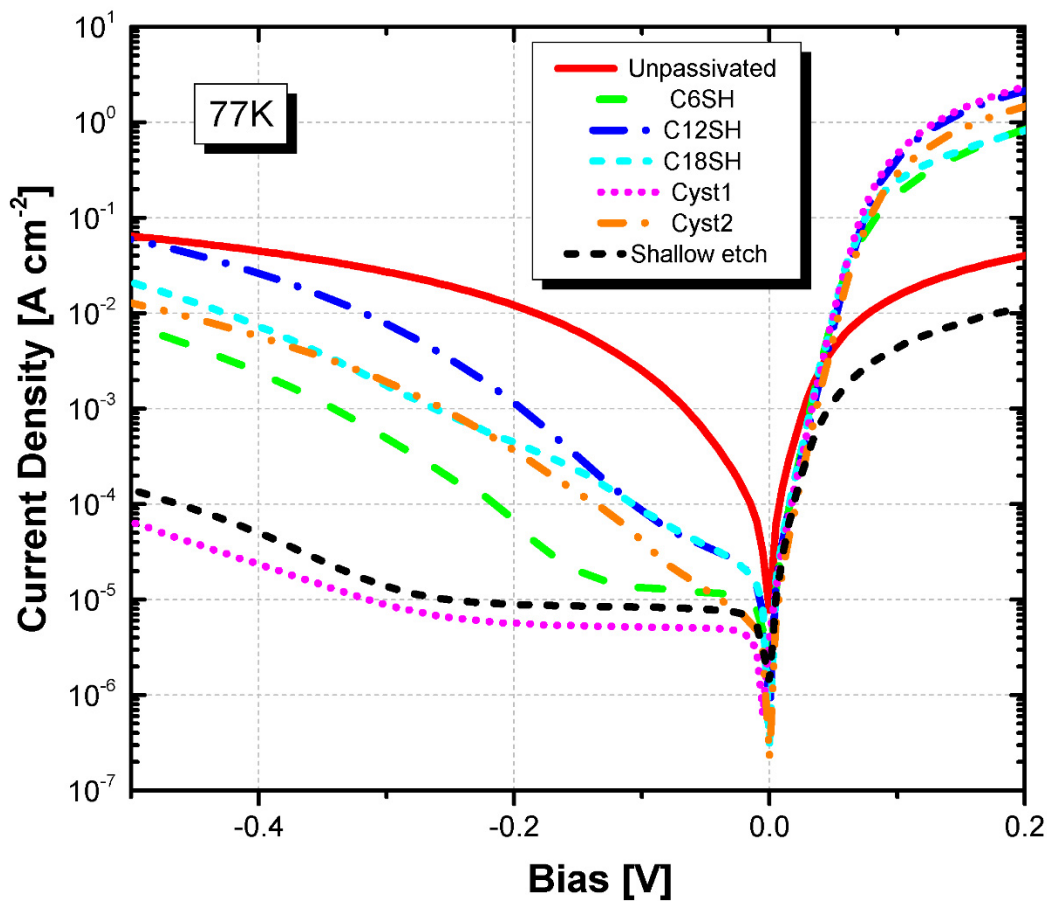


Figure 101: Dark current measurements of thiol passivated *p*-type barrier structure. Unpassivated and shallow etch results are shown for comparison.

Dark current measurements for shorter deposition times (C12SH 2hr and Cyst1 40C 2hr) were significantly worse than those shown in Figure 101, and are not shown here. The poor diode performance of shorter depositions echoes the results seen with MSA. For this reason, no attempts were made to measure dark current on layers incorporating encapsulate layers as MSA indicated further development was necessary.

Perimeter-to-area versus the inverse dynamic resistance-area product on device diodes is shown in Figure 102, with extracted surface resistivity values included. Significant increases in the surface resistivity are observed for all thiol treatments, with the best performer (Cyst1) showing more than three orders of magnitude increase, measuring 103 M Ω ·cm. The surface resistivity value indicates the degree

by which the surface influences diode behavior, showing that thiol passivation is quite effective.

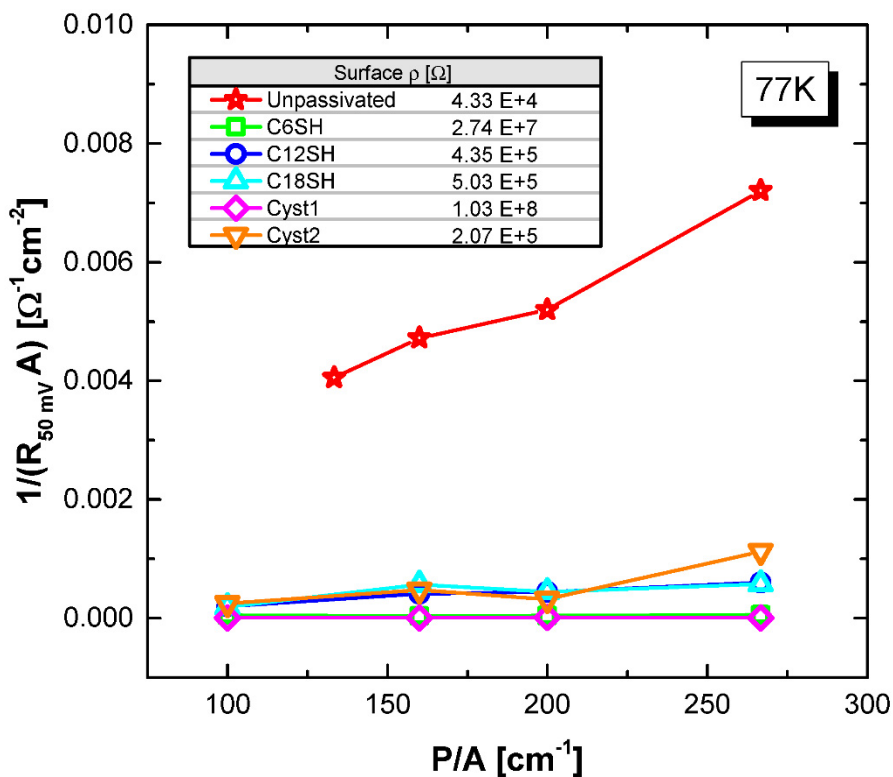


Figure 102: Inverse dynamic resistance-area product versus perimeter-to-area plot for successful thiol passivations. The fitted slope from this data is used to determine the surface resistivity, as shown in inset-table.

A rank plot is shown in Figure 103 to indicate process uniformity. The most consistent, uniform results are obtained from the smallest molecules (Cyst and C6SH). Cyst2 (100 mM NH_4OH -free solution at 40 °C for 2 hours) shows inferior uniformity as compared to the longer 24 hour deposition of Cyst1. C12SH and C18SH show progressively less uniform results, in line with previous assessment on molecular size.

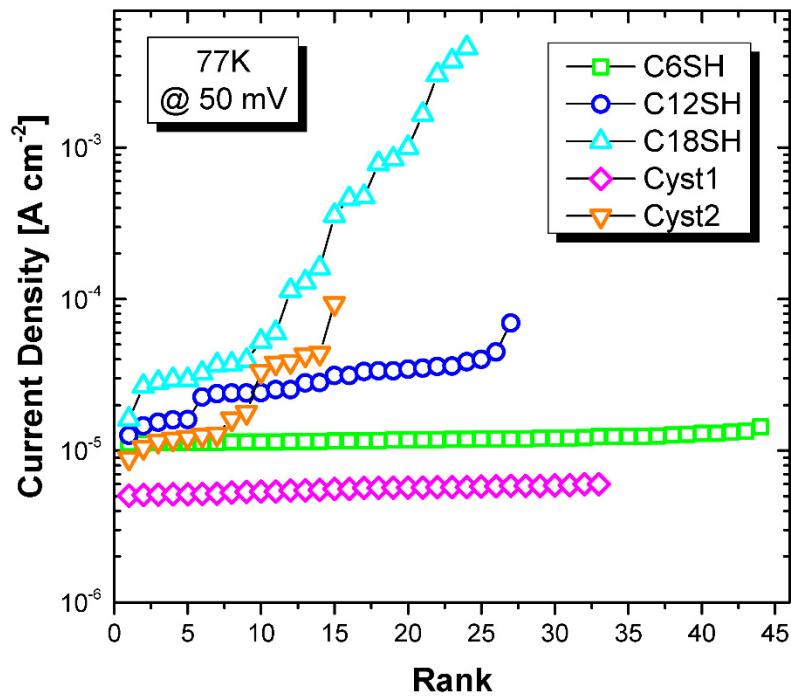


Figure 103: Rank plot of thiol passivated diodes from fabrication lots.

5.5 Summary

Fundamental transport properties of bulk and SL III-V materials were presented in this section with a focus on the most promising materials for future development of LW detectors. The basic transport properties presented in this section are expected to be helpful in future modelling and experimental work on this material system. MSA proved useful in addressing two of the most critical issues for the future of this technology; residual carrier concentrations and surface passivation. Background doping levels were more accurately resolved using a MSA approach and were better monitored with regards to post-growth annealing treatments. It was found that the electrical properties of GaSb could not be improved via thermal treatment. InAs material worsens rapidly at high annealing temperatures and care should be taken if thermal treatments are necessary. Post-growth annealing of an undoped InAs/GaSb T2SLs at 500 °C showed an improvement of hole mobility from $2,567 \text{ cm}^2\text{V}^{-1}\text{s}^{-1}$ to $3,901 \text{ cm}^2\text{V}^{-1}\text{s}^{-1}$ at 77 K, but was accompanied

by a drop in electron mobility. No changes in the background carrier concentration and mobility of carriers in Be-doped InAs/GaSb SLs were observed. Overall, post-growth annealing does not appear to be a viable path forward in reducing background doping levels. The results in this work recommend that more detailed growth studies would contribute more to the knowledge base and have a more dramatic impact on future improvements.

In-plane carrier transport in SL structures were reported for LW InAs/GaSb and LW InAs/InAsSb materials. Background electron and hole concentrations in uid samples were found to be higher in InAs/InAsSb layers, indicating non-optimized growth conditions. The bulk electron (left) and hole mobilities (hole) for all SLs in this work are shown in Figure 104. Very little variance in hole mobility is seen amongst samples, in agreement with similar predicted in-plane effective masses. The largest discrepancies are seen in the electron mobility behavior. Electrons in InAs/GaSb layers were limited by IRS and did not change substantially with doping, measuring $\sim 15,000\text{-}20,000\text{ cm}^2\text{V}^{-1}\text{s}^{-1}$. The electron mobility in InAs/InAsSb layers were much higher, in excess of $10^5\text{ cm}^2\text{V}^{-1}\text{s}^{-1}$, and was governed by ionized impurity and alloy scattering. The high electron mobility in InAs/InAsSb is very promising for the development of *p*-type device structures.

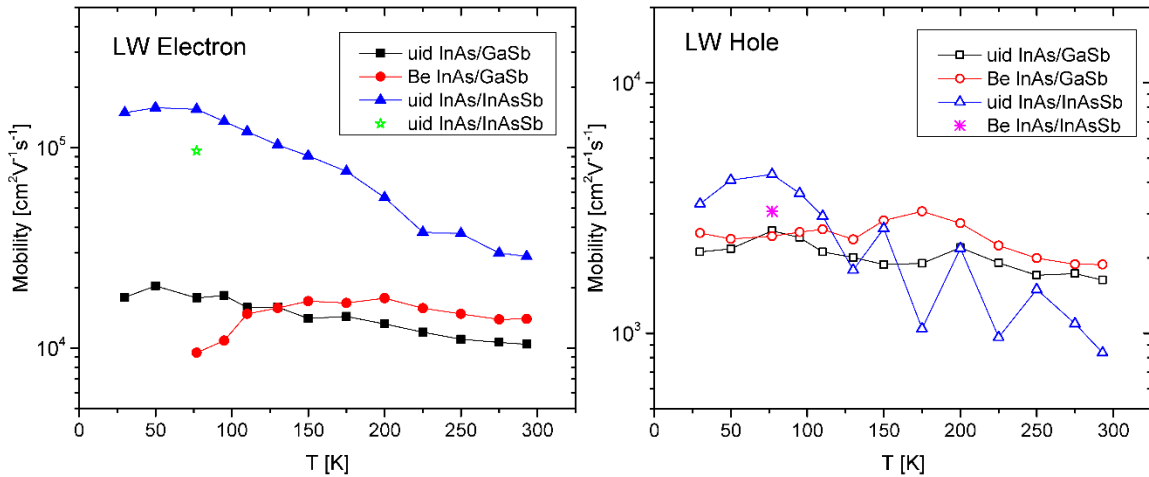


Figure 104: In-plane mobilities of bulk electrons (left figure) and bulk holes for all superlattice measurements.

Passivation experiments using MSA were reported for *p*-type InAs/GaSb. This novel application of MSA clearly demonstrated its utility with regards to assessing surface treatments. The powerful MSA characterization quickly provided reliable indication of passivation quality and was demonstrated to correlate with device performance in all cases.

6. Conclusions and future work

The utility of mobility spectrum analysis with regards to IR device materials has been demonstrated via investigation of HgCdTe and III-V T2SL materials in a variety of studies. This powerful technique has proven adept in characterization of multi-layered structures, extracting critical parameters which are shown to correlate with additional performance metrics. The versatility of MSA ensures that it will remain a valuable tool for future efforts within the IR community.

Limiting mechanisms on LW HgCdTe planar layers varied with choice of substrate, namely, growth on lattice-matched CdZnTe substrates produced intrinsically limited performance while growth on alternative substrates (Si and GaAs) were dominated by extrinsic mechanisms. Dislocation scattering produced a significant reduction in the bulk electron mobility for growth on alternative substrates for $T \leq 77$ K by a factor of $\sim 1.3-1.5$. The occupation rate, f , varied from 0.07-0.101 for LW material, and showed dependences on both x -value and doping concentration. The presence of significant dislocation scattering correlated with SRH-limited minority carrier lifetimes and pronounced tunneling dark current. A factor ~ 5 reduction in minority carrier lifetime was observed in the presence of significant dislocation scattering, with SRH-limited lifetimes of only 30 ns measured at 77 K. With mobility limited by ionized impurity scattering and a lifetime of $\sim 2-3$ μ s at 77 K, it is clear that growth on CdZnTe remains the preferred technology for highest performance LW application.

MSA of MW P+/n heterjunctions provided a number of useful results. It was shown that MSA provides direct measurement of conductivity within the p -type cap layer so that proper growth and annealing conditions may be verified. Examples of poor growth conditions and improper doping incorporation have been reported in this work, both of which are clearly identified by MSA technique. Low temperature mobility was again sensitive to dislocation scattering and in all cases excessive diode tunneling currents were reported. Occupation rate for dislocation scattering ranged from 0.12 to 0.17 for MW material. It is interesting to note that minority carrier lifetime measurement returned intrinsically limited lifetimes for all samples. This may be evidence that temperature dependent MSA is more sensitive

to extrinsic behavior and may serve as a useful performance indicator.

Future work on HgCdTe should be geared towards fundamental studies, such as solidifying dislocation scattering parameters, better understanding of *p*-type dopant incorporation/activation, or further characterization of minority carriers in LW material. With increased layer complexity, the level of insight into each particular material property is sacrificed for information on an increased amount of properties. For this reason, fundamental studies should be performed on the simplest layers possible so that the level of detail may be maximized and conclusions strengthened. On the other hand, this work has undoubtedly shown that MSA can identify when problems arise in dual-layer structures. Therefore, MSA would serve as an effective diagnostic tool for dual-layer or triple-layer growth campaigns, either preventing processing on non-optimal layers or by determining root causes in the event of subpar performance.

Measurements on bulk III-V materials were used to accurately determine background carrier concentration, surface carriers properties, and barrier-interface conduction for GaSb, InAs, and InAsSb layers. Reliable background levels were only obtained with MSA approach for InAs and InAsSb due to significant conduction at the surface and barrier-interface which dramatically altered single-field Hall measurement results. Post-growth annealing results showed InAs to be sensitive to high temperature treatment (> 500 °C) resulting in inferior material properties. GaSb was resilient to all post-growth treatments (500-560 °C), suggesting that material improvements cannot be made using this methodology. InAsSb material displayed the highest mobility ($> 10^5$ cm²V⁻¹s⁻¹ at 77 K) but could not be annealed due to sublimation at the surface. GaSb revealed the highest background doping level and lowest minority carrier lifetime of samples studied in this work.

Annealing of LW InAs/GaSb T2SLs at 500 °C did not alter cut-off wavelength and moderate improvements of the hole mobility were observed for an undoped sample, with mobility improving from 2,567 cm²V⁻¹s⁻¹ to 3,901 cm²V⁻¹s⁻¹ at 77 K. Although some improvements were recorded, post-growth annealing does not ultimately appear viable in improving performance in the InAs/GaSb material system.

In-plane transport properties of undoped and Be-doped InAs/GaSb and InAs/InAsSb LW absorbers were

reported. Hole mobility did not change between material systems or with Be doping level, maintaining temperature independent values of $\sim 2,000\text{-}4,000\text{ cm}^2\text{V}^{-1}\text{s}^{-1}$. Absorber electrons for InAs/GaSb layers were IRS-limited with mobility of $\sim 15,000\text{-}20,000\text{ cm}^2\text{V}^{-1}\text{s}^{-1}$ while electrons in InAs/InAsSb layers were in excess of $10^5\text{ cm}^2\text{V}^{-1}\text{s}^{-1}$ at low temperature and limited by ionized impurity and alloy scattering. The high mobility in InAs/InAsSb layers signify significant electron wave function leakage into adjacent InAsSb layers. Similar hole mobility values are not surprising as comparable hole effective masses are predicted. Overall, background carrier concentrations were highest for the InAs/InAsSb material system, indicating non-optimized growth conditions, which is also reflected in the variance of conductivity at the surface and barrier-interface.

Novel application of MSA towards the study of surface passivation of *p*-type LW InAs/GaSb layers was reported. Successful passivation techniques identified via MSA correlated well with dark current reduction in *p*-type barrier structures. Passivation via charged electret shows promising results, as passivation improved with increasing stored charge, but further refinements are necessary for practical application. Thiolated self-assembled monolayers showed very effective passivation according to MSA and dark current measurements. However, issues regarding long-term stability and encapsulation of thiol depositions were also identified.

A wealth of future studies on III-V bulk and SL materials using MSA remain to be explored, ranging from basic to highly specialized. As stated earlier, growth improvements are still necessary to reduce background carrier concentration levels, particularly in the InAs/InAsSb system, so that transport properties may be improved. The advancement of growth techniques can be accurately monitored using MSA, making this technique an indispensable tool towards that endeavor.

Additional studies regarding surface passivation are required, including demonstration of long-term stability and refinement of encapsulate deposition techniques. Follow-up quantum efficiency (QE) measurements are also necessary to quantify potential performance benefits of *p*-type absorbers. An extension of the passivation work reported here should include Be-doped InAs/InAsSb layers as well, as harnessing the electron mobility of this system could provide a dramatic increase in carrier collection.

MSA techniques will be integral in this development, especially with regards to doping levels necessary to type convert. The reduction in minority carrier lifetime with high p -type doping observed in this work and elsewhere make it desirable for extrinsic doping levels to be kept as low as possible.

The final extension of this work builds upon the techniques and analysis presented here and directs them towards characterization efforts of SL materials in the vertical (growth) direction, which have a much more direct influence on device performance. Vertical conductivity studies using geometrical magnetoresistance could be used to determine limiting transport mechanisms of InAs/GaSb and InAs/InAsSb materials, particularly at low temperature, and to better establish theoretical connections between in-plane and vertical transport. Surface passivation studies in the vertical direction can also be conducted by varying sample size. Measurements on very small samples would more accurately replicate mesa diode sidewalls and act as the ultimate test of passivation efficacy due to increased surface area.

CITED LITERATURE

- [1] W. Herschel, "Experiments on the refrangibility of the invisible rays of the Sun," *Phil. Trans. Roy. Soc. London* 90, 284–292 (1800).
- [2] T.J. Seebeck, "Magnetische Polarisation der Metalle und Erze durch Temperatur-Differenz," *Abh. Deutsch. Akad. Wiss. Berlin*, 265–373 (1822).
- [3] W. Smith, "Effect of light on selenium during the passage of an electric current," *Nature* 7, 303 (1873).
- [4] S.P. Langley, "The bolometer and radiant energy," *Proc. Am. Academy of Arts and Sciences* 16, 342–358 (May 1880 – Jun. 1881).
- [5] J. C. Bose, "Detector for electrical disturbances," U. S. Patent 755,840 (Filed September 30, 1901. Issued March 29, 1904).
- [6] T.W. Case, "Notes on the change of resistance of certain substrates in light," *Phys. Rev.* 9, 305–310 (1917).
- [7] Mercer, Douglas E., and C. Robert Helms. "A diffusion model for the internal photoresponse of PtSi/p-Si Schottky barrier diodes." *Journal of Applied Physics* 65.12 (1989): 5035-5042.
- [8] Ünlü, M. Selim, and Samuel Strite. "Resonant cavity enhanced photonic devices." *Journal of Applied Physics* 78.2 (1995): 607-639.
- [9] Tennant, W. E., et al. "MBE HgCdTe technology: a very general solution to IR detection, described by "Rule 07", a very convenient heuristic." *Journal of Electronic Materials* 37.9 (2008): 1406-1410.
- [10] Tennant, W. E. "'Rule 07' revisited: still a good heuristic predictor of p/n HgCdTe photodiode performance?." *Journal of Electronic Materials* 39.7 (2010): 1030-1035.
- [11] Lawson W D, Nielson S, Putley E H and Young A S 1959 Preparation and properties of HgTe and mixed crystals of HgTe-CdTe *J. Phys. Chem. Solids* 9 325–9.
- [12] Hansen, G. L., J. L. Schmit, and T. N. Casselman. "Energy gap versus alloy composition and temperature in Hg_{1-x}CdxTe." *Journal of Applied Physics* 53.10 (1982): 7099-7101.
- [13] Finkman, E., and S. E. Schacham. "The exponential optical absorption band tail of Hg_{1-x}CdxTe." *Journal of applied physics* 56.10 (1984): 2896-2900.
- [14] Lowney, J. R., et al. "Intrinsic carrier concentration of narrow-gap mercury cadmium telluride based on the nonlinear temperature dependence of the band gap." *Journal of applied physics* 71.3 (1992): 1253-1258.
- [15] Hansen, G. L., and J. L. Schmit. "Calculation of intrinsic carrier concentration in Hg_{1-x}CdxTe." *Journal of Applied Physics* 54.3 (1983): 1639-1640.
- [16] Weiler, M. H. "Magneto-optical properties of Hg_{1-x}CdxTe alloys." *semiconductors and Semimetals* 16 (1981): 119-191.
- [17] Dornhaus, Ralf, Günter Nimtz, and Burghard Schlicht. *Narrow-gap semiconductors*. Springer, 1983.
- [18] Dornhaus, Ralf, Günter Nimtz, and Wolfgang Richter. *Springer tracts in modern physics*. Vol. 78. Springer-Verlag., 1976.
- [19] Liu, Kun, et al. "Measurement of composition in Hg_{1-x}CdxTe epilayers." *Applied physics letters* 64.21 (1994): 2818-2820.
- [20] Hlildek, P., et al. "Refractive index of CdTe: Spectral and temperature dependence." *Journal of Applied Physics* 90.3 (2001): 1672-1674.

- [21] Urbach, Franz. "The long-wavelength edge of photographic sensitivity and of the electronic absorption of solids." *Physical Review* 92.5 (1953): 1324.
- [22] Chu, Junhao, et al. "Empirical rule of intrinsic absorption spectroscopy in Hg_{1-x}Cd_xTe." *Journal of applied physics* 75.2 (1994): 1234-1235.
- [23] Moss, Trevor Simpson, Geoffrey John Burrell, and Brian Ellis. *Semiconductor opto-electronics*. Butterworth-Heinemann, 2013.
- [24] Schacham, S. E., and E. Finkman. "Recombination mechanisms in p-type HgCdTe: Freezeout and background flux effects." *Journal of applied physics* 57.6 (1985): 2001-2009.
- [25] Price, Stephen L., and Phillip R. Boyd. "Overview of compositional measurement techniques for HgCdTe with emphasis on IR transmission, energy dispersive X-ray analysis and optical reflectance." *Semiconductor Science and Technology* 8.6S (1993): 842.
- [26] Chang, Yong, et al. "Narrow gap HgCdTe absorption behavior near the band edge including nonparabolicity and the Urbach tail." *Applied physics letters* 89.6 (2006): 062109.
- [27] Flatté, M. E., et al. "Generalized superlattice K·p theory and intersubband optical transitions." *Physical Review B* 53.4 (1996): 1963.
- [28] Beattie, A. R. and P. T. Landsberg. "Auger effect in semiconductors." *Proc. R. Soc. Lond. A* 249 (1959): 16-29.
- [29] Beattie, A. R. and P. T. Landsberg. "One-dimensional overlap functions and their application to Auger recombination in semiconductors." *Proc. R. Soc. Lond. A* 258 (1960): 486-495.
- [30] J.S. Blakemore, *Semiconductor Statistics* (New York:Pergamon, 1962), Chap. 6.
- [31] Krishnamurthy, S., and T. N. Casselman. "A detailed calculation of the Auger lifetime in p-type HgCdTe." *Journal of Electronic Materials* 29.6 (2000): 828-831.
- [32] Casselman, T. N. "Calculation of the Auger lifetime in p-type Hg_{1-x}Cd_xTe." *Journal of Applied Physics* 52.2 (1981): 848-854.
- [33] Kinch, M. A., et al. "Minority carrier lifetime in p-HgCdTe." *Journal of electronic Materials* 34.6 (2005): 880-884.
- [34] Emelie, P. Y., et al. "Modeling of LWIR HgCdTe Auger-suppressed infrared photodiodes under nonequilibrium operation." *Journal of Electronic Materials* 37.9 (2008): 1362-1368.
- [35] Bertazzi, Francesco, Michele Goano, and Enrico Bellotti. "Calculation of auger lifetimes in HgCdTe." *Journal of electronic materials* 40.8 (2011): 1663-1667.
- [36] Lopes, V. C., A. J. Syllaios, and M. C. Chen. "Minority carrier lifetime in mercury cadmium telluride." *Semiconductor Science and Technology* 8.6S (1993): 824.
- [37] Kinch, M. A., M. J. Brau, and A. Simmons. "Recombination mechanisms in 8–14-μ HgCdTe." *Journal of Applied Physics* 44.4 (1973): 1649-1663.
- [38] Kinch, Michael A. *Fundamentals of infrared detector materials*. Vol. 76. SPIE press, 2007.
- [39] Chang, Y., et al. "Carrier recombination lifetime characterization of molecular beam epitaxially grown HgCdTe." *Applied Physics Letters* 93.19 (2008): 192111.
- [40] Grein, C. H., M. E. Flatte, and Yong Chang. "Modeling of recombination in HgCdTe." *Journal of Electronic Materials* 37.9 (2008): 1415-1419.
- [41] Krishnamurthy, S., et al. "Model for minority carrier lifetimes in doped HgCdTe." *Journal of electronic materials* 34.6 (2005): 873-879.

- [42] Krishnamurthy, S., M. A. Berding, and Z. G. Yu. "Minority carrier lifetimes in HgCdTe alloys." *Journal of electronic materials* 35.6 (2006): 1369-1378.
- [43] Penna, Michele, et al. "Empirical Pseudopotential and Full-Brillouin-Zone $k \cdot p$ Electronic Structure of CdTe, HgTe, and $\text{Hg}_{1-x}\text{Cd}_x\text{Te}$." *Journal of electronic materials* 38.8 (2009): 1717-1725.
- [44] Van Roosbroeck, W., and W. Shockley. "Photon-radiative recombination of electrons and holes in germanium." *Physical Review* 94.6 (1954): 1558.
- [45] Humphreys, R. G. "Radiative lifetime in semiconductors for infrared detection." *Infrared physics* 23.3 (1983): 171-175.
- [46] Humphreys, R. G. "Radiative lifetime in semiconductors for infrared detection." *Infrared physics* 26.6 (1986): 337-342.
- [47] Grein, Christoph H., Henry Ehrenreich, and E. Runge. "Radiative lifetime in semiconductors: Influence of photon recycling." *Photonics West'97*. International Society for Optics and Photonics, 1997.
- [48] Józwiowski, Krzysztof, Małgorzata Kopytko, and Antoni Rogalski. "Numerical Estimations of Carrier Generation-Recombination Processes and the Photon Recycling Effect in HgCdTe Heterostructure Photodiodes." *Journal of electronic materials* 41.10 (2012): 2766-2774.
- [49] Shockley, We, and W. T. Read Jr. "Statistics of the recombinations of holes and electrons." *Physical review* 87.5 (1952): 835.
- [50] Hall, Re N. "Electron-hole recombination in germanium." *Physical Review* 87.2 (1952): 387.
- [51] J. P. Rosbeck, R. E. Starr, S. L. Price, and K. J. Riley, *J. Appl. Phys.* 53(9) , Sept. 1982, p. 6430.
- [52] Scott, Walter. "Electron mobility in $\text{Hg}_{1-x}\text{Cd}_x\text{Te}$." *Journal of Applied Physics* 43.3 (1972): 1055-1062.
- [53] Schmit, Joseph L., and John E. Bowers. "LPE growth of $\text{Hg}_{0.60}\text{Cd}_{0.40}\text{Te}$ from Te-rich solution." *Applied Physics Letters* 35.6 (1979): 457-458.
- [54] Meyer, J. R., and F. J. Bartoli. "Theory for electron mobilities in n-type $\text{Hg}_{1-x}\text{Cd}_x\text{Te}$ and CdTe at low temperatures." *Journal of Vacuum Science & Technology* 21.1 (1982): 237-240.
- [55] Dennis, P. N. J., C. T. Elliott, and C. L. Jones. "A method for routine characterisation of the hole concentration in p-type cadmium mercury telluride." *Infrared Physics* 22.3 (1982): 167-169.
- [56] Gold, M. C., and D. A. Nelson. "Variable magnetic field Hall effect measurements and analyses of high purity, Hg vacancy (p-type) HgCdTe." *Journal of Vacuum Science & Technology A* 4.4 (1986): 2040-2046.
- [57] Leslie-Pelecky, D. L., et al. "New method of characterizing majority and minority carriers in semiconductors." *Applied physics letters* 51.23 (1987): 1916-1918.
- [58] Wijewarnasuriya, P. S., M. Boukerche, and J. P. Faurie. "High-quality p-type HgCdTe grown by molecular beam epitaxy." *Journal of applied physics* 67.2 (1990): 859-862.
- [59] Talipov, N. K., et al. "Method for the characterization of electron, light-and heavy-hole concentrations and mobilities in narrow-gap p-type HgCdTe." *Materials Science and Engineering: B* 44.1 (1997): 278-282.
- [60] Gui, Yongsheng, et al. "Evaluation of densities and mobilities for heavy and light holes in p-type $\text{Hg}_{1-x}\text{Cd}_x\text{Te}$ molecular beam epitaxy films from magnetic-field-dependent Hall data." *Journal of applied physics* 84.8 (1998): 4327-4331.
- [61] Swartz, C. H., et al. "Fundamental materials studies of undoped, In-doped, and As-doped $\text{Hg}_{1-x}\text{Cd}_x\text{Te}$." *Journal of electronic materials* 33.6 (2004): 728-736.

- [62] Rothman, Johan, et al. "Maximum entropy mobility spectrum analysis of HgCdTe heterostructures." *Journal of electronic materials* 35.6 (2006): 1174-1184.
- [63] Grill, R. "Self-consistent calculation of Hall mobilities in the valence band of Hg_{0.8}Cd_{0.2}Te." *Physical Review B* 48.15 (1993): 11398.
- [64] Yadava, R. D. S., A. K. Gupta, and A. V. R. Warriar. "Hole scattering mechanisms in Hg_{1-x}CdxTe." *Journal of electronic materials* 23.12 (1994): 1359-1378.
- [65] Gordon, N. T., et al. "Electron mobility in p-type epitaxially grown Hg_{1-x}CdxTe." *Semiconductor Science and Technology* 8.1S (1993): S221.
- [66] Yoo, Sang Dong, and Kae Dal Kwack. "Analysis of carrier concentration, lifetime, and electron mobility on p-type HgCdTe." *Journal of applied physics* 83.5 (1998): 2586-2592.
- [67] Lacklison, D. E., and G. Duggan. "Determination of the minority carrier mobility of n-type cadmium-mercury-telluride using the Haynes–Shockley method." *Journal of applied physics* 55.12 (1984): 4257-4265.
- [68] Shacham-Diamand, Y., and I. Kidron. "Haynes–Shockley experiment on n-type HgCdTe." *Journal of applied physics* 56.4 (1984): 1104-1108.
- [69] Franc, Jan, et al. "Determination of diffusion lengths of minority carriers in Hg_{1-x}CdxTe (x~ 0.2 to 0.3) by EBIC method." *Material Science and Material Properties for Infrared Optoelectronics*. International Society for Optics and Photonics, 1997.
- [70] Smolin, Oleg V., Eugeny V. Susov, and Eugene B. Yakimov. "EBIC characterization of HgCdTe based photoconductive elements." *Moscow, Russia*. International Society for Optics and Photonics, 2005.
- [71] Jones, C. E., et al. "Status of point defects in HgCdTe." *Journal of Vacuum Science & Technology A* 3.1 (1985): 131-137.
- [72] Finkman, E., and Y. Nemirovsky. "Electrical properties of shallow levels in p-type HgCdTe." *Journal of applied physics* 59.4 (1986): 1205-1211.
- [73] Berding, M. A., A. Sher, and M. Van Schilfgaarde. "Defect modeling studies in HgCdTe and CdTe." *Journal of electronic materials* 24.9 (1995): 1127-1135.
- [74] Gemain, F., et al. "Identification of the double acceptor levels of the mercury vacancies in HgCdTe." *Applied Physics Letters* 98.13 (2011): 131901.
- [75] Boieriu, P., et al. "Effects of hydrogen on majority carrier transport and minority carrier lifetimes in long wavelength infrared HgCdTe on Si." *Applied physics letters* 88.6 (2006): 062106.
- [76] Wijewarnasuriya, P. S., et al. "Carrier recombination in indium-doped HgCdTe (211) B epitaxial layers grown by molecular beam epitaxy." *Journal of applied physics* 75.2 (1994): 1005-1009.
- [77] Berding, M. A., and A. Sher. "Amphoteric behavior of arsenic in HgCdTe." *Applied physics letters* 74.5 (1999): 685-687.
- [78] Capper, P., and D. Shaw. "Activation of arsenic in epitaxial Hg_{1-x}CdxTe (MCT)." *SPIE Optics+ Photonics*. International Society for Optics and Photonics, 2006.
- [79] Lee, T. S., et al. "Correlation of arsenic incorporation and its electrical activation in MBE HgCdTe." *Journal of Electronic Materials* 29.6 (2000): 869-872.
- [80] Sivananthan, S., et al. "Mode of arsenic incorporation in HgCdTe grown by MBE." *Journal of Electronic Materials* 26.6 (1997): 621-624.
- [81] Grein, C. H., et al. "Arsenic incorporation in MBE grown Hg_{1-x}Cd_xTe." *Journal of electronic materials* 28.6 (1999): 789-792.

- [82] Almeida, L. A. "Doping of molecular beam epitaxy HgCdTe using an arsenic cracker source (As₂)." *Journal of electronic materials* 31.7 (2002): 660-663.
- [83] Garland, James W., Christoph Grein, and Sivalingam Sivananthan. "Arsenic p-Doping of HgCdTe Grown by Molecular Beam Epitaxy (MBE): A Solved Problem?." *Journal of electronic materials* 42.11 (2013): 3331-3336.
- [84] Biquard, X., I. Alliot, and P. Ballet. "Extended x-ray absorption fine structure study of arsenic in HgCdTe: p-type doping linked to nonsubstitutional As incorporation in an unknown AsHg {sub 8} structure." *Journal of Applied Physics* 106.10 (2009).
- [85] Gemain, F., et al. "Arsenic complexes optical signatures in As-doped HgCdTe." *Applied Physics Letters* 102.14 (2013): 142104.
- [86] Skauli, T., and T. Colin. "Accurate determination of the lattice constant of molecular beam epitaxial CdHgTe." *Journal of crystal growth* 222.4 (2001): 719-725.
- [87] Dhar, N. K., et al. "Heteroepitaxy of CdTe on {211} Si using crystallized amorphous ZnTe templates." *Journal of Vacuum Science & Technology B* 14.3 (1996): 2366-2370.
- [88] Rujirawat, S., et al. "High quality large-area CdTe (211) B on Si (211) grown by molecular beam epitaxy." *Applied physics letters* 71.13 (1997): 1810-1812.
- [89] Dexter, D. L., and F. Seitz. "Effects of dislocations on mobilities in semiconductors." *Physical Review* 86.6 (1952): 964.
- [90] Pödör, B. "Electron mobility in plastically deformed germanium." *physica status solidi (b)* 16.2 (1966): K167-K170.
- [91] Shin, S. H., et al. "Effect of the dislocation density on minority-carrier lifetime in molecular beam epitaxial HgCdTe." *Applied physics letters* 59.21 (1991): 2718-2720.
- [92] Gopal, Vishnu, and Sudha Gupta. "Effect of dislocations on minority carrier lifetime in HgCdTe." *Journal of applied physics* 95.5 (2004): 2467-2472.
- [93] Johnson, S_M, et al. "Effect of dislocations on the electrical and optical properties of long-wavelength infrared HgCdTe photovoltaic detectors." *Journal of Vacuum Science & Technology B* 10.4 (1992): 1499-1506.
- [94] Everson, W. J., et al. "Etch pit characterization of CdTe and CdZnTe substrates for use in mercury cadmium telluride epitaxy." *Journal of electronic materials* 24.5 (1995): 505-510.
- [95] Benson, J. D., et al. "Topography and Dislocations in (112) B HgCdTe/CdTe/Si." *Journal of electronic materials* 38.8 (2009): 1771-1775.
- [96] Arias, J. M., et al. "Dislocation density reduction by thermal annealing of HgCdTe epilayers grown by molecular beam epitaxy on GaAs substrates." *Journal of Vacuum Science & Technology B* 9.3 (1991): 1646-1650.
- [97] Chen, Y., et al. "Dislocation reduction in CdTe/Si by molecular beam epitaxy through in-situ annealing." *Journal of Crystal Growth* 310.24 (2008): 5303-5307.
- [98] Brill, G., et al. "Dislocation reduction of HgCdTe/Si through ex situ annealing." *Journal of Electronic Materials* 39.7 (2010): 967-973.
- [99] Stoltz, A. J., et al. "Reduction of dislocation density in HgCdTe on Si by producing highly reticulated structures." *Journal of electronic materials* 40.8 (2011): 1785-1789.
- [100] Benson, J. D., et al. "In-situ spectroscopic ellipsometry of HgCdTe." *Journal of Electronic Materials* 25.8 (1996): 1406-1410.

- [101] Almeida, L. A., et al. "HgCdTe heteroepitaxy on three-inch (112) CdZnTe/Si: Ellipsometric control of substrate temperature." *Journal of Electronic Materials* 29.6 (2000): 754-759.
- [102] Johs, B., et al. "Development of a parametric optical constant model for Hg_{1-x}Cd_xTe for control of composition by spectroscopic ellipsometry during MBE growth." *Thin Solid Films* 313 (1998): 137-142.
- [103] Fujiwara, H., et al. "Assessment of effective-medium theories in the analysis of nucleation and microscopic surface roughness evolution for semiconductor thin films." *Physical Review B* 61.16 (2000): 10832.
- [104] Kinch, Michael A. "HDVPTM FPA technology at DRS." *Proc. SPIE*. Vol. 4369. 2001.
- [105] Sze, Simon M., and Kwok K. Ng. *Physics of semiconductor devices*. John Wiley & Sons, 2006.
- [106] Lindmayer, Joseph, and Charles Y. Wrigley. *Fundamentals of semiconductor devices*. van Nostrand, 1965.
- [107] McKelvey, John P. "Solid state and semiconductor physics." (1966).
- [108] Sah, Chih-Tang, Robert Noyce, and William Shockley. "Carrier generation and recombination in pn junctions and pn junction characteristics." *Proceedings of the IRE* 45.9 (1957): 1228-1243.
- [109] Choo, S. C. "Carrier generation-recombination in the space-charge region of an asymmetrical p-n junction." *Solid-State Electronics* 11.11 (1968): 1069-1077.
- [110] Abramowitz, Milton, and Irene A. Stegun. "Handbook of mathematical functions." *Applied Mathematics Series* 55 (1966): 62.
- [111] Yang, Q. K., et al. "Investigation of trap-assisted tunneling current in InAs/(GaIn)Sb superlattice long-wavelength photodiodes." *Applied physics letters* 81.25 (2002): 4757-4759.
- [112] Riley, K. J., and A. H. Lockwood. "HgCdTe hybrid focal-plane arrays." *1980 Los Angeles Technical Symposium*. International Society for Optics and Photonics, 1980.
- [113] Wang, C. C. "Mercury cadmium telluride junctions grown by liquid phase epitaxy." *Journal of Vacuum Science & Technology B* 9.3 (1991): 1740-1745.
- [114] Esaki, Leo, and Ray Tsu. "Superlattice and negative differential conductivity in semiconductors." *IBM Journal of Research and Development* 14.1 (1970): 61-65.
- [115] Smith, D. L., T. C. McGill, and J. N. Schulman. "Advantages of the HgTe-CdTe superlattice as an infrared detector material." *Applied Physics Letters* 43.2 (1983): 180-182.
- [116] Grein, C. H., P. M. Young, and H. Ehrenreich. "Minority carrier lifetimes in ideal InGaSb/InAs superlattices." *Applied physics letters* 61.24 (1992): 2905-2907.
- [117] Grein, C. H., et al. "Long wavelength InAs/InGaSb infrared detectors: Optimization of carrier lifetimes." *Journal of Applied Physics* 78.12 (1995): 7143-7152.
- [118] Sai-Halasz, G. A., R. Tsu, and L. Esaki. "A new semiconductor superlattice." *Applied Physics Letters* 30.12 (1977): 651-653.
- [119] Schulman, J. N., and T. C. McGill. "The CdTe/HgTe superlattice: Proposal for a new infrared material." *Applied Physics Letters* 34.10 (1979): 663-665.
- [120] Reno, J., et al. "HgTe-CdTe superlattices: Experimental and theoretical curves of band gap versus HgTe layer thickness." *Applied physics letters* 49.2 (1986): 106-108.
- [121] Arch, David K., J. L. Staudenmann, and J. P. Faurie. "Layer intermixing in HgTe-CdTe superlattices." *Applied physics letters* 48.23 (1986): 1588-1590.

- [122] Chang, Yia-Chung, and J. N. Schulman. "Interband optical transitions in GaAs-Ga_{1-x}Al_xAs and InAs-GaSb superlattices." *Physical Review B* 31.4 (1985): 2069.
- [123] Smith, D. L., and C. Mailhot. "Proposal for strained type II superlattice infrared detectors." *Journal of Applied Physics* 62.6 (1987): 2545-2548.
- [124] Miles, R. H., et al. "Infrared optical characterization of InAs/Ga_{1-x}In_xSb superlattices." *Applied Physics Letters* 57.8 (1990): 801-803.
- [125] Chow, D. H., et al. "Type II superlattices for infrared detectors and devices." *Semiconductor Science and Technology* 6.12C (1991): C47. DL Smith Private Communication.
- [126] Youngdale, E. R., et al. "Auger lifetime enhancement in InAs-Ga_{1-x}In_xSb superlattices." *Applied Physics Letters* 64.23 (1994): 3160-3162.
- [127] Herres, N., et al. "Effect of interfacial bonding on the structural and vibrational properties of InAs/GaSb superlattices." *Physical Review B* 53.23 (1996): 15688.
- [128] Walther, M., et al. "Growth of InAs/GaSb short-period superlattices for high-resolution mid-wavelength infrared focal plane array detectors." *Journal of Crystal growth* 278.1 (2005): 156-161.
- [129] Wei, Y., et al. "High-performance type-II InAs/GaSb superlattice photodiodes with cutoff wavelength around 7 μm." *Applied Physics Letters* 86.9 (2005): 091109.
- [130] Vurgaftman, I., et al. "Graded band gap for dark-current suppression in long-wave infrared W-structured type-II superlattice photodiodes." *Applied physics letters* 89.12 (2006): 121114.
- [131] Gautam, N., et al. "Performance improvement of longwave infrared photodetector based on type-II InAs/GaSb superlattices using unipolar current blocking layers." *Applied Physics Letters* 96.23 (2010): 231107.
- [132] Wei, Y., et al. "Advanced InAs/GaSb superlattice photovoltaic detectors for very long wavelength infrared applications." *Applied physics letters* 80.18 (2002): 3262-3264.
- [133] Hood, Andrew, et al. "On the performance and surface passivation of type II InAs/GaSb superlattice photodiodes for the very-long-wavelength infrared." *Applied Physics Letters* 87.15 (2005): 1113.
- [134] Maimon, S., and G. W. Wicks. "nBn detector, an infrared detector with reduced dark current and higher operating temperature." *Applied Physics Letters* 89.15 (2006): 1109.
- [135] Ting, David Z-Y., et al. "A high-performance long wavelength superlattice complementary barrier infrared detector." *Applied Physics Letters* 95.2 (2009): 3508.
- [136] Nguyen, Binh-Minh, et al. "Dark current suppression in type II InAs/GaSb superlattice long wavelength infrared photodiodes with M-structure barrier." *Applied Physics Letters* 91.16 (2007): 3511.
- [137] Vurgaftman, I., et al. "Graded band gap for dark-current suppression in long-wave infrared W-structured type-II superlattice photodiodes." *Applied physics letters* 89.12 (2006): 121114.
- [138] Svensson, S. P., et al. "Growth of type II strained layer superlattice, bulk InAs and GaSb materials for minority lifetime characterization." *Journal of Crystal Growth* 334.1 (2011): 103-107.
- [139] Steenbergen, E. H., et al. "Significantly improved minority carrier lifetime observed in a long-wavelength infrared III-V type-II superlattice comprised of InAs/InAsSb." *Applied physics letters* 99.25 (2011): 251110.
- [140] Donetsky, Dmitry, et al. "Minority carrier lifetime in type-2 InAs-GaSb strained-layer superlattices and bulk HgCdTe materials." *Appl. Phys. Lett* 97.5 (2010): 052108.

- [141] Connelly, Blair C., et al. "Direct minority carrier lifetime measurements and recombination mechanisms in long-wave infrared type II superlattices using time-resolved photoluminescence." *Applied Physics Letters* 97.25 (2010): 251117.
- [142] Olson, B. V., et al. "Time-resolved optical measurements of minority carrier recombination in a mid-wave infrared InAsSb alloy and InAs/InAsSb superlattice." *Applied Physics Letters* 101.9 (2012): 092109.
- [143] Aytac, Y., et al. "Effects of layer thickness and alloy composition on carrier lifetimes in mid-wave infrared InAs/InAsSb superlattices." *Applied Physics Letters* 105.2 (2014): 022107.
- [144] Bürkle, L., et al. "Control of the residual doping of InAs/(GaIn) Sb infrared superlattices." *Applied Physics Letters* 77.11 (2000): 1659-1661.
- [145] Haugan, H. J., et al. "Growth optimization for low residual carriers in undoped midinfrared InAs/GaSb superlattices." *Journal of Applied Physics* 104.7 (2008): 073111.
- [146] Da Silva, E. C. F., et al. "Influence of residual impurity background on the nonradiative recombination processes in high purity InAs/GaSb superlattice photodiodes." *Applied physics letters* 89.24 (2006): 3517.
- [147] Kroemer, Herbert. "The 6.1 A family (InAs, GaSb, AlSb) and its heterostructures: a selective review." *Physica E: Low-dimensional Systems and Nanostructures* 20.3 (2004): 196-203.
- [148] Nguyen, Binh-Minh, et al. "Demonstration of midinfrared type-II InAs/GaSb superlattice photodiodes grown on GaAs substrate." *Applied Physics Letters* 94.22 (2009): 223506.
- [149] Varshni, Y. P. "Temperature dependence of the energy gap in semiconductors." *Physica* 34.1 (1967): 149-154.
- [150] Pässler, R. "Parameter sets due to fittings of the temperature dependencies of fundamental bandgaps in semiconductors." *physica status solidi(b)* 216.2 (1999): 975-1007.
- [151] Ting, David Z-Y., et al. "Type-II superlattice infrared detectors." *Advances in Infrared Photodetectors* 84 (2011): 1-57.
- [152] Lumb, M. and J. Meyer. (2011). NRL Bands [Computer Software]. Washington, D.C.: Naval Research Laboratory.
- [153] Chandola, A., R. Pino, and P. S. Dutta. "Below bandgap optical absorption in tellurium-doped GaSb." *Semiconductor science and technology* 20.8 (2005): 886.
- [154] Klipstein, P. C., et al. "Modeling InAs/GaSb and InAs/InAsSb Superlattice Infrared Detectors." *Journal of Electronic Materials* 43.8 (2014): 2984-2990.
- [155] Höglund, L., et al. "Influence of radiative and non-radiative recombination on the minority carrier lifetime in midwave infrared InAs/InAsSb superlattices." *Applied Physics Letters* 103.22 (2013): 221908.
- [156] Olson, B. V., et al. "Identification of dominant recombination mechanisms in narrow-bandgap InAs/InAsSb type-II superlattices and InAsSb alloys." *Applied Physics Letters* 103.5 (2013): 052106.
- [157] Höglund, L., et al. "Minority carrier lifetime in mid-wavelength infrared InAs/InAsSb superlattices: Photon recycling and the role of radiative and Shockley-Read-Hall recombination mechanisms." *Applied Physics Letters* 105.19 (2014): 193510.
- [158] Gold, A. "Electronic transport properties of a two-dimensional electron gas in a silicon quantum-well structure at low temperature." *Physical Review B* 35.2 (1987): 723.
- [159] Meyer, J. R., et al. "Interface roughness limited electron mobility in HgTe-CdTe superlattices." *Applied physics letters* 58.22 (1991): 2523-2525.

- [160] Sakaki, H., et al. "Interface roughness scattering in GaAs/AlAs quantum wells." *Applied physics letters* 51.23 (1987): 1934-1936.
- [161] Szmulowicz, F., et al. "Carrier mobility as a function of carrier density in type-II InAs/GaSb superlattices." *Journal of Applied Physics* 105.7 (2009): 074303.
- [162] Hoffman, C. A., et al. "Interface roughness scattering in semiconducting and semimetallic InAs-Ga_{1-x}In_xSb superlattices." *Applied physics letters* 63.16 (1993): 2210-2212.
- [163] Szmulowicz, F., et al. "Demonstration of interface-scattering-limited electron mobilities in InAs/GaSb superlattices." *Journal of applied physics* 101.4 (2007): 043706.
- [164] Szmulowicz, F., et al. "Calculation of vertical and horizontal mobilities in InAs/GaSb superlattices." *Physical Review B* 84.15 (2011): 155307.
- [165] Umana-Membreno, G. A., et al. "Vertical minority carrier electron transport in p-type InAs/GaSb type-II superlattices." *Applied Physics Letters* 101.25 (2012): 253515.
- [166] Swartz, C. H., and T. H. Myers. "Method for the simultaneous determination of vertical and horizontal mobilities in superlattices." *Physical Review B* 89.7 (2014): 075305.
- [167] Szmulowicz, F., et al. "Calculation of the temperature dependence of the vertical and horizontal mobilities in InAs/GaSb superlattices." *Infrared Physics & Technology* 56 (2013): 76-79.
- [168] Conwell, E., and V. F. Weisskopf. "Theory of impurity scattering in semiconductors." *Physical review* 77.3 (1950): 388.
- [169] Brooks, H. "Scattering by ionized impurities in semiconductors." *Physical Review*. Vol. 83. No. 4. ONE PHYSICS ELLIPSE, COLLEGE PK, MD 20740-3844 USA: AMERICAN PHYSICAL SOC, 1951.
- [170] Dingle, R. B. "XCIV. Scattering of electrons and holes by charged donors and acceptors in semiconductors." *The London, Edinburgh, and Dublin Philosophical Magazine and Journal of Science* 46.379 (1955): 831-840.
- [171] Ridley, B. K. "Reconciliation of the Conwell-Weisskopf and Brooks-Herring formulae for charged-impurity scattering in semiconductors: Third-body interference." *Journal of Physics C: Solid State Physics* 10.10 (1977): 1589.
- [172] Luong, Mark, and Alan W. Shaw. "Quantum Transport Theory of Impurity-Scattering-Limited Mobility in n-Type Semiconductors Including Electron-Electron Scattering." *Physical Review B* 4.8 (1971): 2436.
- [173] Rode, D. L. "Low-field electron transport." *Semiconductors and semimetals* 10 (1975): 1-89.
- [174] Takimoto, Noboru. "On the screening of impurity potential by conduction electrons." *Journal of the Physical Society of Japan* 14.9 (1959): 1142-1158.
- [175] Selar, N. "Ionized impurity scattering in nondegenerate semiconductors." *Physical Review* 104.6 (1956): 1548.
- [176] Schenk, A. "Spatially Variable Drift Mobility Model for Hg_{1-x}Cd_xTe Diodes I. Analytical Base and Fit to Hall Data." *physica status solidi (a)* 122.1 (1990): 413-425.
- [177] Dubowski, J. J., et al. "Electron scattering in Cd_xHg_{1-x}Te." *Journal of Physics and Chemistry of Solids* 42.5 (1981): 351-362.
- [178] Talwar, D. N., and M. Vandevyver. "Vibrational properties of HgCdTe system." *Journal of applied physics* 56.6 (1984): 1601-1607.
- [179] Howarth, D. J., and E. Ho Sondheimer. "The theory of electronic conduction in polar semiconductors." *Proceedings of the Royal Society of London A: Mathematical, Physical and Engineering Sciences*. Vol. 219. No. 1136. The Royal Society, 1953.

- [180] Stratton, Robert. "The influence of interelectronic collisions on conduction and breakdown in polar crystals." *Proceedings of the Royal Society of London A: Mathematical, Physical and Engineering Sciences*. Vol. 246. No. 1246. The Royal Society, 1958.
- [181] Ehrenreich, H. "Electron scattering in InSb." *Journal of Physics and Chemistry of Solids* 2.2 (1957): 131-149.
- [182] Nordheim, Lothar. "Zur Elektronentheorie der Metalle. I." *Annalen der Physik* 401.5 (1931): 607-640.
- [183] Makowski, L., and M. Glicksman. "Disorder scattering in solid solutions of III–V semiconducting compounds." *Journal of Physics and Chemistry of Solids* 34.3 (1973): 487-492.
- [184] Hass, K. C., H. Ehrenreich, and B. Velický. "Electronic structure of Hg $1-x$ Cd x Te." *Physical Review B* 27.2 (1983): 1088.
- [185] Kossut, J. "The disorder scattering in zincblende narrow-gap semiconducting mixed crystals." *physica status solidi (b)* 86.2 (1978): 593-601.
- [186] Erginsoy, Cavid. "Neutral impurity scattering in semiconductors." *Physical Review* 79.6 (1950): 1013.
- [187] McGill, T. C., and R. Baron. "Neutral impurity scattering in semiconductors." *Physical Review B* 11.12 (1975): 5208.
- [188] Ng, H. M., et al. "The role of dislocation scattering in n-type GaN films." *Applied physics letters* 73.6 (1998): 821.
- [189] Egan, R. J., V. W. L. Chin, and T. L. Tansley. "Dislocation scattering effects on electron mobility in InAsSb." *Journal of applied physics* 75.5 (1994): 2473-2476.
- [190] Bonch-Bruевич, L., and V. B. Glasko. "To theory of dislocations-related electronic transitions." *Sov. Phys. Solid State* 3 (1961): 36-52.
- [191] Pödör, B. "Electron mobility in plastically deformed germanium." *physica status solidi (b)* 16.2 (1966): K167-K170.
- [192] Carmody, M., et al. "Role of dislocation scattering on the electron mobility of n-type long wave length infrared HgCdTe on silicon." *Journal of Electronic Materials* 36.8 (2007): 1098-1105.
- [193] Weimann, Nils G., et al. "Scattering of electrons at threading dislocations in GaN." *Journal of Applied Physics* 83.7 (1998): 3656-3659.
- [194] H. Belincourt, *Phys. Rev.* 129, 1009 (1963).
- [195] Wan, C. F., et al. "Piezoelectric effects in HgCdTe devices." *Journal of electronic materials* 24.9 (1995): 1293-1297.
- [196] Fedders, Peter A. "Strain scattering of electrons in piezoelectric semiconductors." *Journal of Applied Physics* 54.4 (1983): 1804-1807.
- [197] Meyer, J. R., F. J. Bartoli, and C. A. Hoffman. "Majority-carrier mobility in p-type Hg $_{1-x}$ Cd x Te." *Journal of Vacuum Science & Technology A* 5.5 (1987): 3035-3039.
- [198] Chen, M. C., and L. Colombo. "The majority carrier mobility of n-type and p-type Hg $_0.78$ Cd $_0.22$ Te liquid phase epitaxial films at 77 K." *Journal of applied physics* 73.6 (1993): 2916-2920.
- [199] Shih, C. K., and W. E. Spicer. "Determination of a natural valence-band offset: The case of HgTe-CdTe." *Physical review letters* 58.24 (1987): 2594.
- [200] Costato, M., and L. Reggiani. "Scattering probabilities for holes I. Deformation potential and ionized impurity scattering mechanisms." *physica status solidi (b)* 58.2 (1973): 471-482.

- [201] Bolognesi, C. R., H. Kroemer, and J. H. English. "Interface roughness scattering in InAs/AlSb quantum wells." *Applied physics letters* 61.2 (1992): 213-215.
- [202] Gottinger, R., et al. "Interface roughness scattering and electron mobilities in thin GaAs quantum wells." *EPL (Europhysics Letters)* 6.2 (1988): 183.
- [203] Nag, B. R., Sanghamitra Mukhopadhyay, and Madhumita Das. "Interface roughness scattering-limited electron mobility in AlAs/GaAs and Ga_{0.5}In_{0.5}P/GaAs wells." *Journal of applied physics* 86.1 (1999): 459-463.
- [204] Olson, B. V., et al. "All-optical measurement of vertical charge carrier transport in mid-wave infrared InAs/GaSb type-II superlattices." *Applied Physics Letters* 102.20 (2013): 202101.
- [205] Seiler, D. G., S. Mayo, and J. R. Lowney. "Hg_{1-x}Cd_xTe characterization measurements: current practice and future needs." *Semiconductor Science and Technology* 8.6S (1993): 753.
- [206] Hall, Edwin H. "On a new action of the magnet on electric currents." *American Journal of Mathematics* 2.3 (1879): 287-292.
- [207] van der PAUW, L. J. "A method of measuring specific resistivity and Hall effect of discs of arbitrary shape." *Philips Res. Rep.* 13 (1958): 1-9.
- [208] Wong, T. M.Sc. Thesis, MIT, 1974.
- [209] Lou, L. F., and W. H. Frye. "Hall effect and resistivity in liquid-phase-epitaxial layers of HgCdTe." *Journal of applied physics* 56.8 (1984): 2253-2267.
- [210] Beck, W. A., and J. R. Anderson. "Determination of electrical transport properties using a novel magnetic field-dependent Hall technique." *Journal of applied physics* 62.2 (1987): 541-554.
- [211] Dziuba, Z., and M. Gorska. "Analysis of the electrical conduction using an iterative method." *Journal de Physique III* 2.1 (1992): 99-110.
- [212] Antoszewski, J., et al. "Magneto-transport characterization using quantitative mobility-spectrum analysis." *Journal of electronic materials* 24.9 (1995): 1255-1262.
- [213] Meyer, J. R., et al. "Quantitative mobility spectrum analysis of multicarrier conduction in semiconductors." *Journal of applied physics* 81.2 (1997): 709-713.
- [214] Vurgaftman, I., et al. "Improved quantitative mobility spectrum analysis for Hall characterization." *Journal of applied physics* 84.9 (1998): 4966-4973.
- [215] Chwang, Ronald, B. J. Smith, and C. R. Crowell. "Contact size effects on the van der Pauw method for resistivity and Hall coefficient measurement." *Solid-State Electronics* 17.12 (1974): 1217-1227.
- [216] Koon, Daniel W. "Effect of contact size and placement, and of resistive inhomogeneities on van der Pauw measurements." *Review of Scientific Instruments* 60.2 (1989): 271-274.
- [217] Smith, Stewart. *Sheet resistance and electrical linewidth test structures for semiconductor process characterisation*. Diss. University of Edinburgh, 2004.
- [218] David, J. M., and M. G. Buehler. "A numerical analysis of various cross sheet resistor test structures." *Solid-State Electronics* 20.6 (1977): 539-543.
- [219] De Mey, Gilbert. "Potential calculations in Hall plates." *Advances in electronics and electron physics* 61 (1983): 1-61.
- [220] Arnaudov, B., et al. "Multilayer model for Hall effect data analysis of semiconductor structures with step-changed conductivity." *Physical Review B* 67.4 (2003): 045314.
- [221] Stevenson, Donald T., and Robert J. Keyes. "Measurement of carrier lifetimes in germanium and silicon." *Journal of Applied Physics* 26.2 (1955): 190-195.

- [222] Bubulac, L. O. "Defects, diffusion and activation in ion implanted HgCdTe." *Journal of Crystal Growth* 86.1 (1988): 723-734.
- [223] Daraselia, M., et al. "In-Situ monitoring of temperature and alloy composition of Hg_{1-x}Cd_xTe using FTIR spectroscopic techniques." *Journal of electronic materials* 28.6 (1999): 743-748.
- [224] Sporcken, R., et al. "Molecular beam epitaxial growth of CdTe and HgCdTe on Si (100)." *Applied Physics Letters* 55.18 (1989): 1879-1881.
- [225] Wijewarnsuriya, P. S., et al. "MBE P-on-n Hg_{1-x}Cd_xTe heterostructure detectors on silicon substrates." *Journal of electronic materials* 27.6 (1998): 546-549.
- [226] Arias, J. M., et al. "Infrared diodes fabricated with HgCdTe grown by molecular beam epitaxy on GaAs substrates." *Applied Physics Letters* 54.11 (1989): 1025-1027.
- [227] Lennon, C. M., et al. "Real-Time In Situ Monitoring of GaAs (211) Oxide Desorption and CdTe Growth by Spectroscopic Ellipsometry." *Journal of electronic materials* 41.10 (2012): 2965-2970.
- [228] De Lyon, T. J., et al. "Molecular-beam epitaxial growth of CdTe (112) on Si (112) substrates." *Applied physics letters* 66.16 (1995): 2119-2121.
- [229] Carmody, M., et al. "Recent progress in MBE growth of CdTe and HgCdTe on (211) B GaAs substrates." *Journal of electronic materials* 41.10 (2012): 2719-2724.
- [230] Benson, J. D., et al. "Structural analysis of cdte hetero-epitaxy on (211) si." *Journal of Electronic Materials* 37.9 (2008): 1231-1236.
- [231] Almeida, L. A., et al. "Improved morphology and crystalline quality of MBE CdZnTe/Si." *Journal of electronic materials* 30.6 (2001): 608-610.
- [232] Koestner, R. J., et al. "Improved structural quality of molecular-beam epitaxy HgCdTe films." *Journal of Vacuum Science & Technology A* 7.2 (1989): 517-522.
- [233] Chen, M. C. "Inverted surface effect of p-type HgCdTe." *Applied physics letters* 51.22 (1987): 1836-1838.
- [234] Tsen, G. K. O., et al. "Magneto-transport characterization of p-type HgCdTe." *Journal of Electronic Materials* 36.8 (2007): 826-831.
- [235] Umana-Membreno, G. A., et al. "Investigation of Multicarrier Transport in LPE-Grown Hg_{1-x}Cd_xTe Layers." *Journal of Electronic Materials* 39.7 (2010): 1023-1029.
- [236] Chen, M. C., and R. A. Schiebel. "Observation of a deep level in p-type Hg_{0.78}Cd_{0.22}Te with high dislocation density." *Journal of applied physics* 71.10 (1992): 5269-5271.
- [237] Arias, J. M., et al. "Planar p-on-n HgCdTe heterostructure photovoltaic detectors." *Applied physics letters* 62.9 (1993): 976-978.
- [238] Grimbergen, C. A. "The influence of geometry on the interpretation of the current in epitaxial diodes." *Solid-State Electronics* 19.12 (1976): 1033-1037.
- [239] DeWames, R., et al. "Electro-optical characteristics of a MWIR and LWIR planar hetero-structure P+ n HgCdTe photodiodes limited by intrinsic carrier recombination processes." *SPIE Defense, Security, and Sensing*. International Society for Optics and Photonics, 2011.
- [240] Moll, John L. *Physics of semiconductors*. McGraw-Hill, 1964.
- [241] Vilela, M. F., et al. "Higher Dislocation Density of Arsenic-Doped HgCdTe Material." *Journal of Electronic Materials* 43.8 (2014): 3018-3024.
- [242] Kalisher, M. H. "The behavior of doped Hg_{1-x}Cd_xTe epitaxial layers grown from Hg-rich melts." *Journal of Crystal Growth* 70.1 (1984): 365-372.

- [243] Singh, S. K., et al. "An analysis of the dynamic resistance variation as a function of reverse bias voltage in a HgCdTe diode." *Semiconductor science and technology* 15.7 (2000): 752.
- [244] Weiler, M. H., and M. B. Reine. "Effect of a valence-band barrier on the quantum efficiency and background-limited dynamic resistance of compositionally graded HgCdTe P-on-n heterojunction photodiodes." *Journal of electronic materials* 24.9 (1995): 1329-1339.
- [245] Dutta, P. S., et al. "Carrier compensation and scattering mechanisms in p-GaSb." *Journal of applied physics* 80.5 (1996): 2847-2853.
- [246] P. Lawaetz, *Phys. Rev. B* 4, 3460 (1971).
- [247] Baxter, Ronald Dale, R. T. Bate, and F. J. Reid. "Ion-pairing between lithium and the residual acceptors in GaSb." *Journal of Physics and Chemistry of Solids* 26.1 (1965): 41-48.
- [248] Kala, Hemendra, et al. "Heavy and light hole transport in nominally undoped GaSb substrates." *Applied Physics Letters* 106.3 (2015): 032103.
- [249] Dutta, P. S., H. L. Bhat, and Vikram Kumar. "The physics and technology of gallium antimonide: An emerging optoelectronic material." *Journal of Applied Physics* 81.9 (1997): 5821-5870.
- [250] Lee, Hyung Jae, and John C. Woolley. "Electron transport and conduction band structure of GaSb." *Canadian Journal of Physics* 59.12 (1981): 1844-1850.
- [251] Baxter, R. D., F. J. Reid, and A. C. Beer. "Electron mobility in GaSb at 77 K." *Physical Review* 162.3 (1967): 718.
- [252] Chin, V. W. L. "Electron mobility in GaSb." *Solid-state electronics* 38.1 (1995): 59-67.
- [253] Kubiak, R. A. A., et al. "The morphology and electrical properties of heteroepitaxial InAs prepared by MBE." *Applied Physics A* 35.1 (1984): 61-66.
- [254] Washburn, H. A., J. R. Sites, and H. H. Wieder. "Electronic profile of n-InAs on semi-insulating GaAs." *Journal of Applied Physics* 50.7 (1979): 4872-4878.
- [255] Noguchi, M., K. Hirakawa, and T. Ikoma. "Intrinsic electron accumulation layers on reconstructed clean InAs (100) surfaces." *Physical review letters* 66.17 (1991): 2243.
- [256] Bell, Gavin R., Tim S. Jones, and Chris F. McConville. "Accumulation layer profiles at InAs polar surfaces." *Applied physics letters* 71.25 (1997): 3688-3690.
- [257] Olsson, L. Ö., et al. "Charge accumulation at InAs surfaces." *Physical review letters* 76.19 (1996): 3626.
- [258] Yen, M. Y., et al. "Molecular beam epitaxial growth and optical properties of InAs_{1-x}Sb_x in 8–12 μm wavelength range." *Applied physics letters* 50.14 (1987): 927-929.
- [259] Svensson, S. P., et al. "Band gap of InAs_{1-x}Sb_x with native lattice constant." *Physical Review B* 86.24 (2012): 245205.
- [260] Svensson, S. P., et al. "Background and interface electron populations in InAs_{0.58}Sb_{0.42}." *Semiconductor Science and Technology* 30.3 (2015): 035018.
- [261] Chin, Vincent WL, R. J. Egan, and T. L. Tansley. "Electron mobility in InAs_{1-x}Sb_x and the effect of alloy scattering." *Journal of applied physics* 69.6 (1991): 3571-3577.
- [262] Baril, Neil, et al. "Low operating bias InAs/GaSb strain layer superlattice LWIR detector." *Infrared Physics & Technology* (2014).
- [263] Rao, TV Chandrasekhar, et al. "Electrical transport in InAs/GaSb superlattice: role of surface states and interface roughness." *Semiconductor Science and Technology* 27.10 (2012): 105025.

- [264] Tuttle, Gary, Herbert Kroemer, and John H. English. "Effects of interface layer sequencing on the transport properties of InAs/AlSb quantum wells: Evidence for antisite donors at the InAs/AlSb interface." *Journal of Applied Physics* 67.6 (1990): 3032-3037.
- [265] Jolley, Greg, et al. "Intrinsic broadening of the mobility spectrum of bulk n-type GaAs." *New Journal of Physics* 16.11 (2014): 113033.
- [266] Hoffman, Darin, et al. "Electroluminescence of InAs-GaSb heterodiodes." *Quantum Electronics, IEEE Journal of* 42.2 (2006): 126-130.
- [267] Wiersma, R. D., et al. "Electrical and optical properties of carbon-doped GaSb." *Physical Review B* 67.16 (2003): 165202.
- [268] Jakowetz, W., D. Barthruff, and K. W. Benz. "Gallium Arsenide and Related Compounds." *Inst. Phys. Conf. Ser.* No. 33a. 1977.
- [269] de Dios-Leyva, M., et al. "Excitonic and shallow-donor states in semiconducting quantum wells: a fractional-dimensional space approach." *Journal of Physics: Condensed Matter* 9.40 (1997): 8477.
- [270] Averett, KL, "Characteristics of InAs-based materials and bipolar devices grown by molecular beam epitaxy," dissertation, University of Rochester. (2002).
- [271] Steenbergen, Elizabeth H., et al. "Impact of Be-doping on the material properties of InAs/InAsSb type-II superlattices for infrared detection." *SPIE OPTO*. International Society for Optics and Photonics, 2013.
- [272] Kim, H. S., et al. "Long-wave infrared nBn photodetectors based on InAs/InAsSb type-II superlattices." *Applied Physics Letters* 101.16 (2012): 161114.
- [273] Connelly, Blair C., et al. "Time-resolved photoluminescence study of carrier recombination and transport in type-II superlattice infrared detector materials." *SPIE Defense, Security, and Sensing*. International Society for Optics and Photonics, 2013.
- [274] Zuo, Daniel, et al. "Direct minority carrier transport characterization of InAs/InAsSb superlattice nBn photodetectors." *Applied Physics Letters* 106.7 (2015): 071107.
- [275] Steenbergen, E. H., et al. "Carrier transport properties of Be-doped InAs/InAsSb type-II infrared superlattices." *Applied Physics Letters* 104.1 (2014): 011104.
- [276] Hoang, A. M., et al. "High performance photodiodes based on InAs/InAsSb type-II superlattices for very long wavelength infrared detection." *Applied Physics Letters* 104.25 (2014): 251105.
- [277] Lackner, D., et al. "InAs/InAsSb strain balanced superlattices for optical detectors: Material properties and energy band simulations." *Journal of Applied Physics* 111.3 (2012): 034507.
- [278] Ramelan, Ari Handono, and E. M. Goldys. "Hole mobility in Al_xGa_{1-x}Sb grown by metalorganic chemical vapor deposition." *Journal of applied physics* 92.10 (2002): 6051-6056.
- [279] Lin, Y., et al. "Minority Carrier Lifetime in Beryllium-Doped InAs/InAsSb Strained Layer Superlattices." *Journal of Electronic Materials* 43.9 (2014): 3184-3190.
- [280] Grein, C. H., J. Garland, and M. E. Flatte. "Strained and unstrained layer superlattices for infrared detection." *Journal of electronic materials* 38.8 (2009): 1800-1804.
- [281] Pellegrino, J., and R. DeWames. "Minority carrier lifetime characteristics in type II InAs/GaSb LWIR superlattice n⁺ p⁺ photodiodes." *SPIE Defense, Security, and Sensing*. International Society for Optics and Photonics, 2009.
- [282] Bürkle, L., et al. "Control of the residual doping of InAs/(GaIn) Sb infrared superlattices." *Applied Physics Letters* 77.11 (2000): 1659-1661.

- [283] Khoshakhlagh, A., et al. "Background carrier concentration in midwave and longwave InAs/GaSb type II superlattices on GaAs substrate." *Applied Physics Letters* 97.5 (2010): 051109.
- [284] Murray, L. M., et al. "Effects of growth rate variations on carrier lifetime and interface structure in InAs/GaSb superlattices." *Journal of Crystal Growth* 386 (2014): 194-198.
- [285] Zuo, Daniel, et al. "Direct observation of minority carrier lifetime improvement in InAs/GaSb type-II superlattice photodiodes via interfacial layer control." *Applied Physics Letters* 102.14 (2013): 141107.
- [286] Klein, Brianna, et al. "Carrier lifetime studies in midwave infrared type-II InAs/GaSb strained layer superlattice." *Journal of Vacuum Science & Technology B* 32.2 (2014): 02C101.
- [287] Miles, R. H., et al. "Midwave infrared stimulated emission from a GaInSb/InAs superlattice." *Applied physics letters* 66.15 (1995): 1921-1923.
- [288] Haugan, H. J., et al. "Exploring optimum growth for high quality InAs/GaSb type-II superlattices." *Journal of Crystal Growth* 261.4 (2004): 471-478.
- [289] Haugan, H. J., et al. "Growth optimization for low residual carriers in undoped midinfrared InAs/GaSb superlattices." *Journal of Applied Physics* 104.7 (2008): 073111.
- [290] Ling, C. C., et al. "Nature of the acceptor responsible for p-type conduction in liquid encapsulated Czochralski-grown undoped gallium antimonide." *Applied Physics Letters* 85.3 (2004): 384-386.
- [291] Haugan, H. J., et al. "Post growth annealing study on long wavelength infrared InAs/GaSb superlattices." *Journal of Applied Physics* 111.5 (2012): 053113.
- [292] Sankowska, I., et al. "Role of beryllium doping in strain changes in II-type InAs/GaSb superlattice investigated by high resolution X-ray diffraction method." *Applied Physics A* 108.2 (2012): 491-496.
- [293] Gin, Aaron, et al. "Passivation of type II InAs/GaSb superlattice photodiodes." *Thin Solid Films* 447 (2004): 489-492.
- [294] Gin, A., et al. "Ammonium sulfide passivation of Type-II InAs/GaSb superlattice photodiodes." *Applied physics letters* 84.12 (2004): 2037-2039.
- [295] Bessolov, V. N., and M. V. Lebedev. "Chalcogenide passivation of III-V semiconductor surfaces." *Semiconductors* 32.11 (1998): 1141-1156.
- [296] Plis, Elena, et al. "Electrochemical sulphur passivation of InAs/GaSb strain layer superlattice detectors." *Electronics Letters* 42.21 (2006): 1248-1249.
- [297] Hood, Andrew, et al. "Near bulk-limited R0A of long-wavelength infrared type-II InAs/GaSb superlattice photodiodes with polyimide surface passivation." *Applied physics letters* 90.23 (2007): 3513.
- [298] Kim, H. S., et al. "Reduction of surface leakage current in InAs/GaSb strained layer long wavelength superlattice detectors using SU-8 passivation." *Applied Physics Letters* 97.14 (2010): 143512.
- [299] Salihoglu, Omer, et al. "Atomic layer deposited Al₂O₃ passivation of type II InAs/GaSb superlattice photodetectors." *Journal of Applied Physics* 111.7 (2012): 074509.
- [300] Leonov, Vladimir, et al. "Charge injection and storage in single-layer and multilayer inorganic electrets based on SiO₂ and Si₃N₄." *Dielectrics and Electrical Insulation, IEEE Transactions on* 19.4 (2012): 1253-1260.
- [301] Hagiwara, Kei, et al. "Electret charging method based on soft X-ray photoionization for MEMS transducers." *Dielectrics and Electrical Insulation, IEEE Transactions on* 19.4 (2012): 1291-1298.
- [302] Chen, G., et al. "Elimination of surface leakage in gate controlled type-II InAs/GaSb mid-infrared photodetectors." *Applied Physics Letters* 99.18 (2011): 183503.

- [303] Henry, Nathan C., et al. "Chemical and physical passivation of type II strained-layer superlattice devices by means of thiolated self-assembled monolayers and polymer encapsulates." *Infrared Physics & Technology* (2014).
- [304] Nicollian, E. H., et al. "Electrochemical charging of thermal SiO₂ films by injected electron currents." *Journal of Applied Physics* 42.13 (1971): 5654-5664.
- [305] Stine, R., and D. Y. Petrovykh. "Oriented self-assembled monolayers of bifunctional molecules on InAs." *Journal of Electron Spectroscopy and Related Phenomena* 172.1 (2009): 42-46.
- [306] Losurdo, Maria, et al. "Cysteamine-based functionalization of InAs surfaces: Revealing the critical role of oxide interactions in biasing attachment." *Langmuir* 28.2 (2011): 1235-1245.

VITA

Alexander Earl Brown

EDUCATION:

B.S., Physics, Allegheny College, Meadville, PA, 2009

M.S., Physics, University of Illinois at Chicago, Chicago, IL, 2012

Ph.D., Physics, University of Illinois at Chicago, Chicago, IL, 2015

AWARDS and HONORS:

2015 William E. Spicer and Thomas N. Casselman Best Student Paper Award – 2015 II-VI Workshop, “Bulk and surface carrier transport of III-V materials and superlattice structures”.

PUBICATIONS:

In print

1. Lennon, C. M., L. A. Almeida, R. N. Jacobs, J. K. Markunas, P. J. Smith, J. Arias, A. E. Brown, and J. Pellegrino. "Real-Time In Situ Monitoring of GaAs (211) Oxide Desorption and CdTe Growth by Spectroscopic Ellipsometry." *Journal of electronic materials* 41, no. 10 (2012): 2965-2970.
2. Brown, A. E., M. Jaime-Vasquez, L. A. Almeida, J. Arias, C. M. Lennon, R. N. Jacobs, J. Pellegrino, and S. Sivananthan. "Variable-Field Hall Measurement and Transport in LW Single-Layer n-Type MBE Hg_{1-x}Cd_xTe." *Journal of electronic materials* 42, no. 11 (2013): 3224-3230.
3. Stoltz, A. J., J. D. Benson, M. Jaime-Vasquez, P. J. Smith, L. A. Almeida, R. Jacobs, J. Markunas, K. Brogden, A.E. Brown, C. Lennon, P. Maloney, and N. Supola. "A Review of the Characterization Techniques for the Analysis of Etch Processed Surfaces of HgCdTe and Related Compounds." *Journal of Electronic Materials* 43, no. 9 (2014): 3708-3717.
4. Baril, Neil, Sumith Bandara, Linda Hoeglund, Nathan Henry, Alexander Brown, Curtis Billman, Patrick Maloney, Eric Nallon, Meimei Tidrow, and Joseph Pellegrino. "Low operating bias InAs/GaSb strain layer superlattice LWIR detector." *Infrared Physics & Technology* (2014).

Submitted/Pending

1. Henry, N.C., Brown, A.E., Knorr, D.B, Baril, N., Nallon, E., Lenhart, J.L., Tidrow, M., Bandara, S. "A study on the surface conductivity of InAs/GaSb strained layer superlattice infrared detectors treated with thiolated Self Assembled Monolayers (SAMs). *Applied Physics Letters*.
2. A.E. Brown, N. Henry, M. Jaime-Vasquez, L.A. Almeida, J. Arias, S. Bandara, and S. Sivananthan. "Bulk and surface carrier transport of III-V materials and superlattice structures". *Journal of Electronic Materials*.

PRESENTATIONS:

1. "Variable-Field Hall Measurement and Carrier Properties of HgCdTe layers". A.E. Brown, M. Jaime-Vasquez, L.A. Almeida, J. Arias, C.M. Lennon, R.N. Jacobs, and S. Sivananthan. II-VI Workshop, Seattle, WA, 2012.
2. "A Review of the Characterization Techniques for the Analysis of Etch Processed Surfaces of HgCdTe and Related Compounds", Stoltz, A. J., J. D. Benson, M. Jaime-Vasquez, P. J. Smith, L. A. Almeida, R. Jacobs, J. Markunas, K. Brogden, A.E. Brown, C. Lennon, P. Maloney, and N. Supola. II-VI Workshop, Chicago, IL, 2013
3. "New developments in Sb-based III-V infrared detector materials", M. Tidrow, S. Bandara, N. Baril, N. Henry, A.E. Brown, E. Nallon, K.S. Williams, D. Knorr, J.L. Lenhart, J.W. Andzelm, SPIE Photonic West, San Francisco, CA, February 2015.
4. "Optimization of Type-II Superlattice Heterojunction Infrared Detectors", S. Bandara, N. Baril, P. Maloney, C. Billman, N. Henry, A.E. Brown, E. Nallon, J. Pellegrino, and M. Tidrow, SPIE, Baltimore, MD, April 2015.
5. "Bulk and surface carrier transport of III-V materials and superlattice structures", A.E. Brown, N. Henry, M. Jaime-Vasquez, L.A. Almeida, J. Arias, S. Bandara, and S. Sivananthan, II-VI Workshop, Chicago, IL, October 2015.